1290

UNIVERSIDADE Đ
COIMBRA

Rafael Luiz Galvão de Oliveira

EXPERIMENTAL AND NUMERICAL THERMOMECHANICAL CHARACTERIZATION OF REFRACTORY MASONRIES

Tese no âmbito do Doutoramento em Engenharia de Segurança ao Incêndio orientada pelo Professor Doutor João Paulo Correia Rodrigues da Universidade de Coimbra e pelo Doutor João Miguel Pereira da Universidade do Minho e apresentada ao Departamento de Engenharia Civil da Faculdade de Ciência e Tecnologia da Universidade de Coimbra.

Abril de 2022

Faculdade de Ciências e Tecnologia
da Universidade de Coimbra

EXPERIMENTAL AND NUMERICAL THERMOMECHANICAL CHARACTERIZATION OF REFRACTORY MASONRIES

Rafael Luiz Galvão de Oliveira

Tese no âmbito do Doutoramento em Engenharia de Segurança ao Incêndio orientada pelo Professor Doutor João Paulo Correia Rodrigues da Universidade de Coimbra e pelo Doutor João Miguel Pereira da Universidade do Minho e apresentada ao Departamento de Engenharia Civil da Faculdade de Ciência e Tecnologia da Universidade de Coimbra.

Abril de 2022

1 2 9 0

UNIVERSIDADE Ð
COIMBRA

ACKNOWLEDGEMENTS

First of all, I am sincerely grateful to my supervisor Professor João Paulo Correia Rodrigues and my co-supervisor Doctor João Miguel Pereira, for their expertise, guidance and constructive suggestions over the last years. I am also grateful to my secondments mentors Professor Marc Huger and Doctor Hans Ulrich Marschall. I would like to thank Professor Paulo Lourenço for his help during the development of this work.

I would also like to thank the University of Coimbra, the University of Minho, the University of Limoges and the RHI-Magnesita Technology Centre Leoben for providing the necessary facilities and the technical support during the development of the thesis.

Several wonderful people have supported me on this journey. Their help was fundamental and without them I would not be able to finish my thesis. First and foremost, I would like to express my deep and sincere appreciation to my daughter, Ana Luiza, and to my wife, Priscila Sposito. I also would like to thank my mother, Marcia Oliveira, and my sister, Amanda Azevedo.

To the laboratory staff members, I thank their support for assistance with the design, fabrication, preparation and testing the specimens.

To all my colleagues that investigate in the University of Coimbra (Ruben Lopes, Aline Camargo, Fabricio Bolina and Thiago Brazeiro) my gratitude for their help in this work. I also would like to express my gratitude to my ATHOR colleagues (Diana Vitiello, Robert Kaczmarek, Farid Asadi, Camille Raynaert, Ilona Kieliba, Efstathios Kyrilis, Vahid Tadaion, Hung Nguyen, Lucas Teixeira, Mahmoud Ali, Sina Darban, Thais Soares, Soheil Samadi and Pratik Gajjar) and to the ATHOR staff, specially to Glyn Derrick.

I would like to thank the support of European Commission under the framework of Marie Skłodowska-Curie Actions Innovative Training Networks, project ATHOR - Advanced THermomechanical multiscale mOdelling of Refractory linings 764987 Grant.

ABSTRACT

The manufacturing process of several materials adopted in industry, in civil construction and in our daily life has processes performed at high temperatures, such as melting and heat treatments. Thus, these production processes require products that resist to high temperatures, maintaining their physical and chemical properties in service. Refractory ceramics, due to their properties, have been used for this purpose, having crucial importance in high temperature processes. Refractory linings (composed of refractory ceramics) are used in industrial vessels to produce steel, iron, cement, non-ferrous metals, glass, metallic alloys, in melting process, in petrochemical industry, in incinerators, in mineral processing, in power plants and many other applications. The service temperature of these vessels is around 1650ºC for the steel ladles and 1450 ºC for the cement kilns, however, some processes may reach 2000ºC.

In spite of the economic importance of the refractory ceramics, there are few researches on the thermomechanical behaviour of such structures at large scales. Due to the elevated prices of the products and the high costs of large scale tests, the biggest part of the experimental campaigns are focused on small specimens. Nevertheless, the experimental campaigns in large scale specimens are required to calibrate and validate the numerical models developed to simulate the industrial linings.

The focus of this study is to fully characterize the thermomechanical behaviour of dry stacked refractory masonry under diversified situations. Therefore, a large experimental campaign was performed covering the behaviour of the brick, the behaviour of the joints and the behaviour of the masonry panels.

The refractory bricks are injected into the moulds, pressed and then fired during their production processes. Consequently, the ceramics present an anisotropic behaviour. Therefore, the material was characterized using specimens extracted from different types of bricks and from different directions in the same bricks. It was observed that the bricks present a higher compressive strength in the direction of the pressing. The compressive strength of the material was characterized both at room and elevated temperature (600 ºC, 800ºC and 1000 ºC).

The dry joints formed between the stacked bricks play an important role on the thermomechanical behaviour of the masonry panel. The presence of joints reduces the stiffness of the masonry, therefore, the compressive stresses developed in the linings during the heating of the vessels are reduced. The bricks' shape imperfections were found to have the largest influence on the dry joints behaviour, therefore, a statistical analysis of the distribution of the bricks' shape imperfections was carried out. Several studies were carried out on the normal behaviour of the joints: classical joint closure test; bed joint closing action in a masonry wallet measured with a DIC; effects of brick's height imperfections on its loadbearing capacity; effects of brick's height imperfections on the wall's behaviour at ambient and high temperatures and a comparison between the bed and head joints behaviour. To characterize the joint's tangential behaviour at high temperatures a novel device was developed and successfully used.

Aiming to assess the behaviour of the masonry panels a large experimental campaign was developed. The main purpose was to fully characterize the masonry walls at different temperatures and different loading conditions. Several aspects that may influence the behaviour of these walls have been tested, namely the loadbearing capacity, the behaviour under cyclic loading and the restrained thermal elongation. Masonry panels were tested under uniaxial and biaxial loading conditions at ambient and elevated temperatures. The experimental results allowed to identify the effects of the stress concentrations caused by brick's height imperfections in the mechanical behaviour of the bricks and in the loadbearing capacity of the specimens, the evolution of the wall's stiffness with the load application, the developed crack patterns and the mechanical behaviour of the specimens at ambient and high temperatures. The effects of the viscoplastic strains developed due to creep and relaxation were also investigated.

Finally, numerical models were also developed to simulate the behaviour of the walls under different testing conditions and a good agreement with the experimental results was obtained. The concrete damaged plasticity model, using a micro-modelling approach, proved to be suitable for representing the behaviour of these walls at ambient and intermediate temperatures. For temperatures above 1000 ºC, creep effects starts to raise and the Norton-Bailey creep law was successfully used to represented the material behaviour.

Keywords: Refractory; masonry walls; Ambient and high temperature testing; Thermomechanical modelling; Dry-stacked masonry;

RESUMO

O processo de fabricação de diversos materiais adotados na indústria, na construção civil e no nosso dia a dia possui processos realizados em altas temperaturas, como fusão e tratamentos térmicos. Portanto, esses processos produtivos exigem produtos que resistam a temperaturas ainda mais altas, mantendo suas propriedades físicas e químicas em serviço. Cerâmicas refratárias, devido às suas propriedades, têm sido utilizadas para esse fim, tendo importância crucial nestes processos produtivos. Revestimentos refratários são usados em aplicações industriais para produzir aço, ferro, cimento, metais não ferrosos, vidros, ligas metálicas, em processos de fusão, na indústria petroquímica, em incineradores, no processamento de minerais, em usinas de energia e diversas outras aplicações. A temperatura de serviço nestas aplicações é em torno de 1650 ° C para as panelas de fundição e 1450 ° C para os fornos de cimento, porém, alguns processos podem chegar a 2.000 ° C.

Apesar da importância económica das cerâmicas refratárias, existem poucas pesquisas sobre o comportamento termomecânico dessas estruturas em larga escala. Devido aos preços elevados dos produtos e aos altos custos dos testes em larga escala, a maior parte das campanhas experimentais é desenvolvida com pequenos provetes. No entanto, as campanhas experimentais em provetes de maior escala são necessárias para calibrar e validar os modelos numéricos desenvolvidos para simular os revestimentos industriais.

O foco deste estudo é caracterizar completamente o comportamento termomecânico de alvenaria refratária de junta seca em situações diversificadas. Portanto, uma grande campanha experimental foi realizada com o objetivo de estudar o comportamento do bloco, o comportamento das juntas e o comportamento dos painéis de alvenaria. Os blocos refratários são injetados nos moldes, prensados e queimados durante seu processo de produção. Consequentemente, as cerâmicas apresentam comportamento anisotrópico. Portanto, o material foi caracterizado a partir de amostras extraídas de diferentes tipos de blocos e de diferentes direções nos mesmos blocos. Observou-se que os blocos apresentam maior resistência à compressão na direção da prensagem. A resistência à compressão do material foi caracterizada em temperatura ambiente e elevada (600 ºC, 800 ºC e 1000 ºC).

As juntas secas formadas entre os blocos empilhados desempenham um papel importante no comportamento termomecânico do painel de alvenaria. A presença de juntas reduz a rigidez da alvenaria, portanto, as tensões de compressão desenvolvidas nos revestimentos refratários durante o aquecimento são reduzidas. Constatou-se que as imperfeições de forma dos blocos têm a maior influência no comportamento das juntas secas, portanto, foi realizada uma análise estatística da distribuição das imperfeições na forma dos blocos. Vários estudos foram realizados sobre o comportamento normal das juntas: teste clássico de fechamento de juntas; influência do fechamento da junta em um painel de alvenaria medida com DIC; efeitos de imperfeições de altura do bloco na sua capacidade de carga; efeitos das imperfeições de altura do bloco no comportamento da parede em temperatura ambiente e em altas temperaturas e uma comparação entre o comportamento das juntas horizontais e verticais. Para caracterizar o comportamento tangencial da junta em altas temperaturas, um novo dispositivo foi desenvolvido e usado com sucesso.

Com o objetivo de avaliar o comportamento dos painéis de alvenaria foi desenvolvida uma grande campanha experimental. O objetivo principal era caracterizar completamente as paredes de alvenaria em diferentes temperaturas e diferentes condições de carregamento. Vários aspetos que podem influenciar o comportamento dessas paredes foram testados, nomeadamente a capacidade de carga, o comportamento sob carregamento cíclico e o alongamento térmico restringido. Os painéis de alvenaria foram testados sob condições de carregamento uniaxial e biaxial em temperaturas ambiente e elevadas. Os resultados experimentais permitiram identificar os efeitos das concentrações de tensões causadas por imperfeições em altura do bloco no comportamento mecânico dos blocos e na capacidade de suporte dos provetes, a evolução da rigidez da parede com a aplicação de carga, os padrões de fissuras desenvolvidos e o comportamento mecânico das amostras em temperatura ambiente e em altas temperaturas. Os efeitos das deformações visco plásticas desenvolvidas devido à fluência e relaxamento também foram investigados.

Finalmente, também foram desenvolvidos modelos numéricos para simular o comportamento das paredes sob diferentes condições de teste e uma boa concordância com os resultados experimentais foi obtida. O modelo de CDP, utilizando uma abordagem de micro-modelação, mostrou-se adequado para representar o comportamento dessas paredes em temperaturas ambiente e intermediárias. Para temperaturas acima de 1000 ºC, os efeitos de fluência começam a aumentar e a lei de fluência de Norton-Bailey foi usada com sucesso para representar o comportamento do material.

Palavras-chave: Refratário; paredes de alvenaria; teste em temperatura ambiente e alta; modelagem termomecânica; alvenaria de junta seca;

SUMMARY

LIST OF FIGURES

LIST OF TABLES

1 INTRODUCTION

This chapter introduces the current state of knowledge on the refractory ceramics used in the coating of industrial vessels, focusing on dry-stacked masonry linings. The main problems and difficulties in this area, as well as the objectives and methods of this doctoral research are described in this chapter. The problem definitions and motivation are being presented. The difficulties of the numerical simulations of refractory linings are addressed and the ATHOR Project is introduced. In addition, the economic aspects, the impact of the refractories on iron and steel making, the most important issues and challenges in this field of knowledge that motivated the development of this doctoral thesis are also discussed. Finally, the objectives of this research and the methods used to achieve them are described.

The manufacturing process of several materials adopted in industry, in civil construction and in our daily life has processes performed at high temperatures, such as melting and heat treatments. Thus, these production processes require products that resist to high temperatures, maintaining their physical and chemical properties in service. Refractory ceramics, due to their properties, have been used for this purpose, having crucial importance in high temperature processes. Refractory linings (composed of refractory ceramics) are used in industrial vessels to produce steel (**Figure 1-1**a), iron, cement (**Figure 1-1**b), non-ferrous metals, glass, metallic alloys, in melting process, in petrochemical industry, in incinerators, in mineral processing, in power plants and many other applications. The service temperature of these vessels is around 1650ºC for the steel ladles and 1450 ºC for the cement kilns, however, some processes may reach 2000ºC (Poirier and Rigaud, 2017; Khlifi, 2019).


a) b)

Figure 1-1 – Refractory linings: a) steel ladle (Seven Refractories, 2021); b) rotary cement kiln (ZKG, 2021)

The refractory linings used in industrial furnaces and vessels perform different functions (Poirier and Rigaud, 2017):

- Barrier function: the refractory layers must guarantee personnel safety and protect the steel shell and the adjacent industrial facilities when operating at high temperatures.

- Container function: the lining shall confine solid, liquid or gaseous substances in the containers without altering their chemical composition.

- Thermal insulation function: the refractory linings shall contain the heat within the vessels and limit heat losses, contributing to the thermal efficiency of the industrial processes.

1.1 Problem definition and motivation

The extensive use of refractories in industrial processes highlights the key economic importance of these ceramics, and the mass production of refractories is fundamental for many economics sectors (Poirier and Rigaud, 2017). **Figure 1-2** shows the consumption of refractories in steel plants in Europe. It is possible to observe that the specific consumption of refractories depends on the geographical areas, nevertheless, in both cases the iron and steel making industries are the major consumer of refractories.

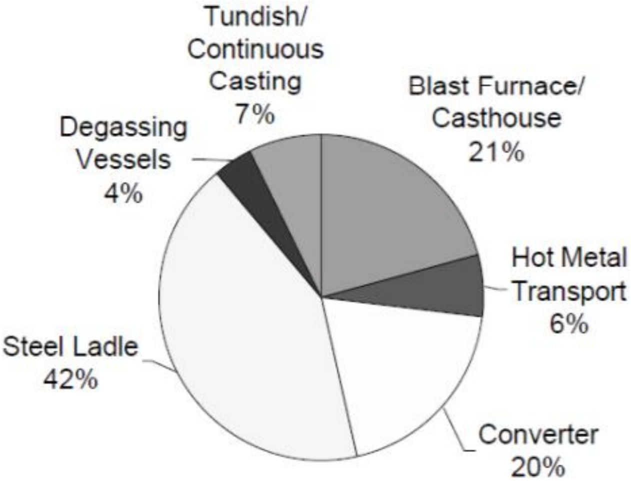

Figure 1-2 - Percent distribution of refractory consumption in different iron & steelmaking equipment, for the integrated European mills. Reprinted from Madias (2018)

As major consumers, the steel industry is the main driver for requiring improvements in the technology of refractory materials (Sugita, 2008). In fact, it is possible to see a decrease in the average of refractories` consumption (kg of refractories required to produce 1 ton of steel) in the iron and steel industry over the years (Figure 1-3), as a result of the improvements in refractories' technology (Rigaud, 2004). However, the continuous increasing of world´s steel production (Figure 1-4) and the increasing of the added value of the new refractories keep the refractory market profitable. The estimated global refractory market is around 23,2 billion dollars a year.

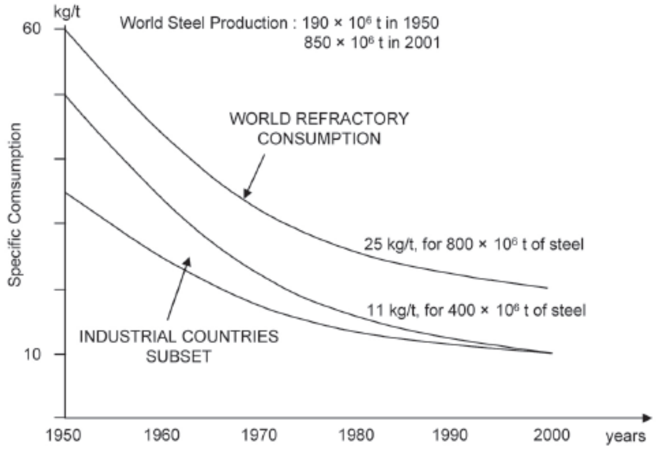

Figure 1-3 – Specific average refractories consumption in the iron and steel industry from 1950 to 2000 (Rigaud, 2004)

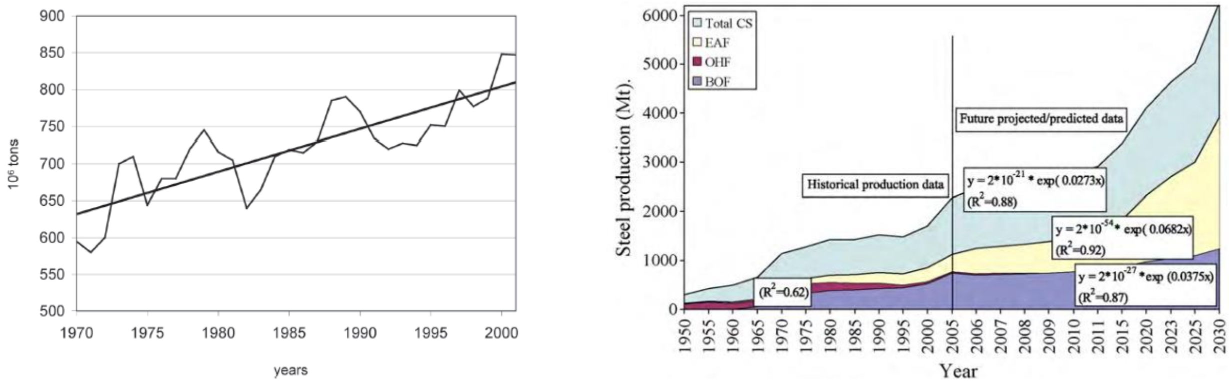

a) b)

Figure 1-4 – World crude steel production: a) from 1970 to 2000 (Rigaud, 2004); b) from 1950 to 2005 and projection (Yellishetty *et al*, 2009)

The industrial requests for more efficient products, with better insulation and better mechanical and chemical resistance, led to significant improvements in refractory ceramics (Sugita, 2008; Rigaud, 2004). However, improvements in modern refractory technologies are not only based on material technology, but also shifted into an integrated system technology that includes heat engineering, monitoring techniques, furnace and lining design and construction, and furnace operation (Sugita, 2008).

Within the steelmaking industry, the steel ladle forms the hearth of the steel making process (**Figure 1-5**) and represents the major source of refractory usage, as it accounts for about 25% of all refractory consumption within a steel making facility (Buhr and Lachmund, 2016). In fact, the impact of such industrial installation is relevant, as it is shown that different choices in refractory design could lead to a loss reduction of 3 up to 20 degrees Celsius in the steel ladles temperature, which constitutes €0.6 million to €4.0 million per year. Also, the increased production capacity of a steel ladle, by being designed with thinner refractory layers, gives a value in use cost reduction of €0.4 million per year (for a 7.3MT production site) (Sinnema *et al*, 2017).

a)

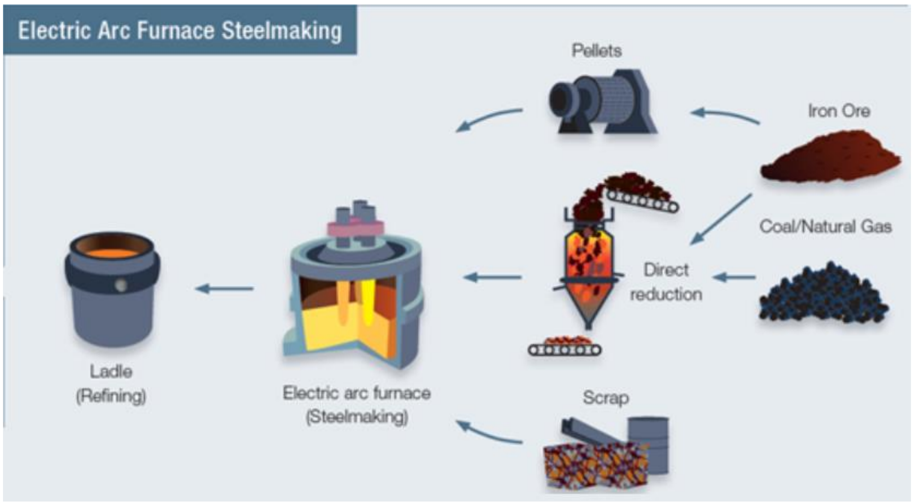

b)

Figure 1-5 - Flowchart of the steelmaking process: a) Blast furnace; b) Electric Arc Furnace (ATHOR, 2021)

The impact of the steel ladle can be demonstrated by the relative short lifespan of some components of the refractory lining. The working lining (also called wear lining and metal lining) of steel ladles works in contact with molten steel and slag, therefore, it is prone to corrosion, wear, thermal shock, spalling and creep. Due to the harsh working environment, the lifespan of the slagline and the bottom of a typical steel ladle is around 75 heats, and the life span of the wall (also called barrel) is around 150 heats. A typical ladle passes through several heats per day; thus, the lining may last for less than a week.

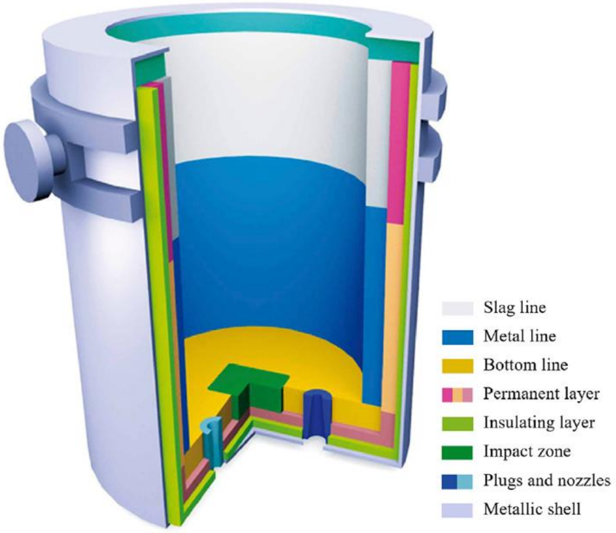

Figure 1-6 – Steel ladle components. Reprinted from (Santos *et al*, 2018).

Consequently, the linings of the steel ladle must be repaired or replaced frequently. The lining process is time consuming and has a considerable impact on the price of the steel. Before the repairing process, the ladle must be cooled, the damaged linings could be repaired using gunning mix or replaced by new ones. After this, the steel ladle must be checked, approved, and pre-heated before returning to the production process. The pre-heating needs to be relatively slow, to avoid potential damage on the material caused by thermal shock. Despite the high maintenance costs of refractory linings, this process is essential, as failures of the ladle are often catastrophic (**Figure 1-7**).

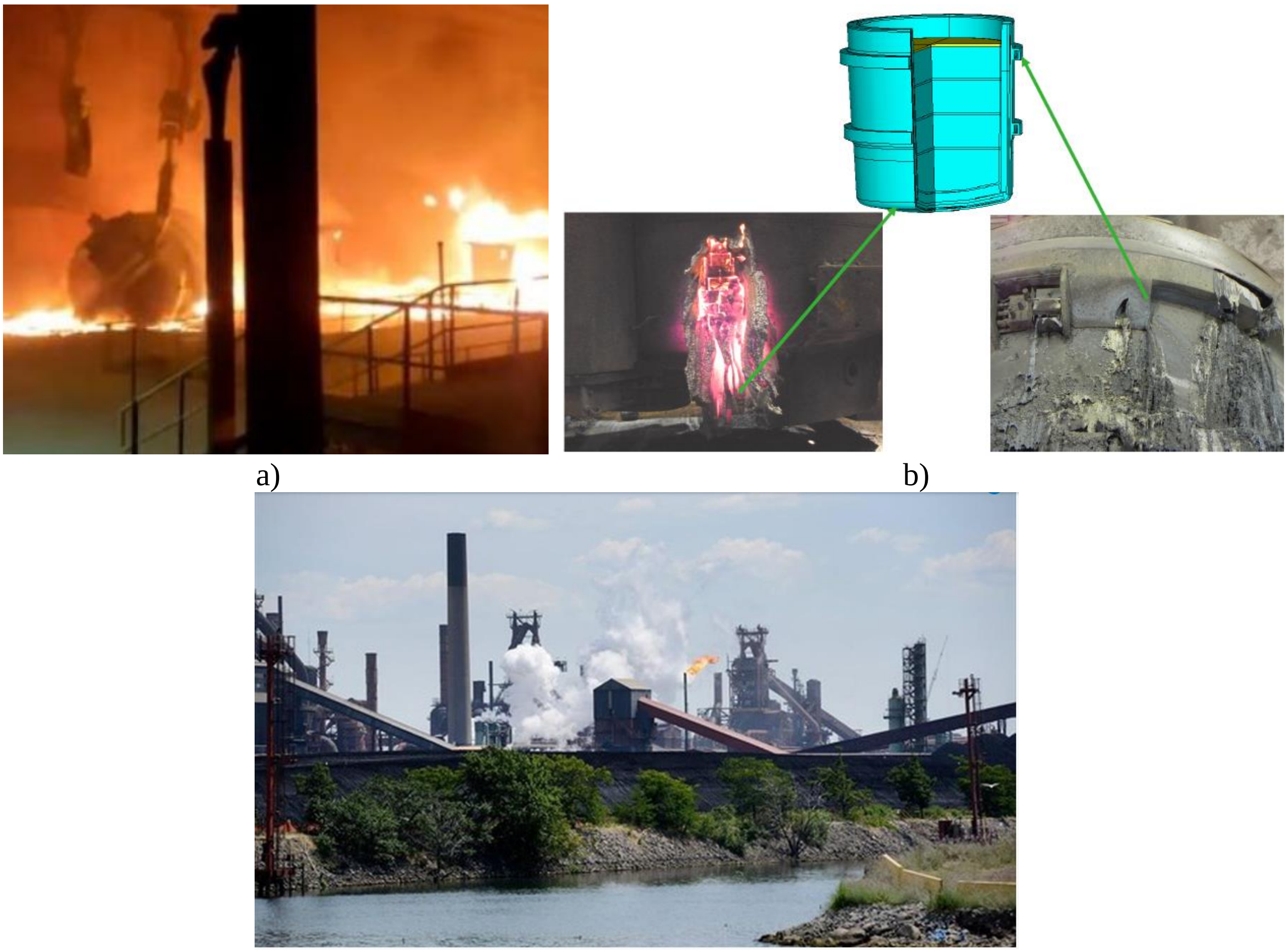
a) b)

c)

Figure 1-7 – Examples of catastrophic accidents in industrial vessels and furnaces: a) Steel plant in India (Sakshi); b) Failures at the bottom and at the top of an steel ladle (TataSteel); c) Blast furnace failure (The spec)

Concerning the thermomechanical behaviour of refractory linings a few studies have been reported in the literature. Only a few experimental studies have been performed, most of them in temperatures far from the service temperatures of steel vessels and in small structures different from the large dimensions of industrial vessels. The thermal and mechanical response of a refractory linings in a steel vessel is very different from the behaviour of a single brick, and even more different from the performance of small specimen extracted from the brick. Therefore, further experimental researches are necessary to better understand: *i*) the bricks' mechanical properties; *ii*) the joints normal behaviour and its influence on the wall performance; *iii*) the joints tangential behaviour and its impact on the stability of linings, *iv*) the behaviour of refractory masonries at ambient and high temperatures under uniaxial compression; *v*) the effects of biaxial compression in the structural response of masonry wallets; *vi*) the behaviour of masonry wallets under creep (uniaxial and biaxial) and under relaxation.

Significant advances were observed in the numerical studies in the recent years. The increasing of the performance of computers, the developments of new constitutive models and the improvements of the homogenization techniques allowed the numerical studies to move from simplified bi-dimensional models to advanced three-dimensional simulations that comprises different non-linearities involved in the process. Nevertheless, the results provided by further experimental campaigns will allow the development, calibration and validation of novels and better numerical models.

The cost involved in the experimental campaigns on sub-systems, such as masonry wallets and pilot industrial vessels are high, as a large laboratorial infrastructure and a huge energy consumption is required. Nevertheless, this investment is justified by the economic importance of refractory linings in industrial processes. The results of this study are being used in the development of new techniques for the design of linings, and consequently in the optimization of these structures.

1.2 ATHOR Network

The challenges present when dealing with such materials and applications led to the development of a research network in the scientific field of refractory ceramics – the ATHOR network. ATHOR (Advance THermomechanical multiscale mOdelling of Refractory linings) is a network firstly dedicated to train researchers in several fields required for a better understanding of the thermomechanical behaviour of refractory linings used industrial applications. The consortium comprises 7 academic poles: *i*) University of Limoges (France); *ii*) AGH University of Science & Technology (Poland); *iii*) University of Aachen (Germany); *iv*) Montanuniversität Leoben (Austria); *v*) University of Orléans (France) ; *vi*) University of Minho (Portugal); and *vii*) University of Coimbra (Portugal) and 8 industrial partners: *i*) Altéo Alumina (France); *ii*) Imerys Refractory Minerals (Austria); *iii*) RHI-Magnesita (Austria); *iv*) Pyrotek Scandinavia AB (Sweden); *v*) Saint-Gobain France); *vi*) TataSteel (Netherlands); *vii*) FIRE (Canada); and *viii*) Safran (France).

The ATHOR Network has a multiscale approach, from the microstructure of the material up to the characterization of industrial vessels. The project is focused in both experimental characterization and numerical modelling. Additionally, improvements on measurement devices and new characterization techniques are being developed. This doctoral thesis comprises the experimental characterization and the numerical modelling of masonry sub-systems. The overall scope of the ATHOR Network is shown in **Figure 1-8**, highlighting (in red) the scope of the research developed within this doctoral thesis.

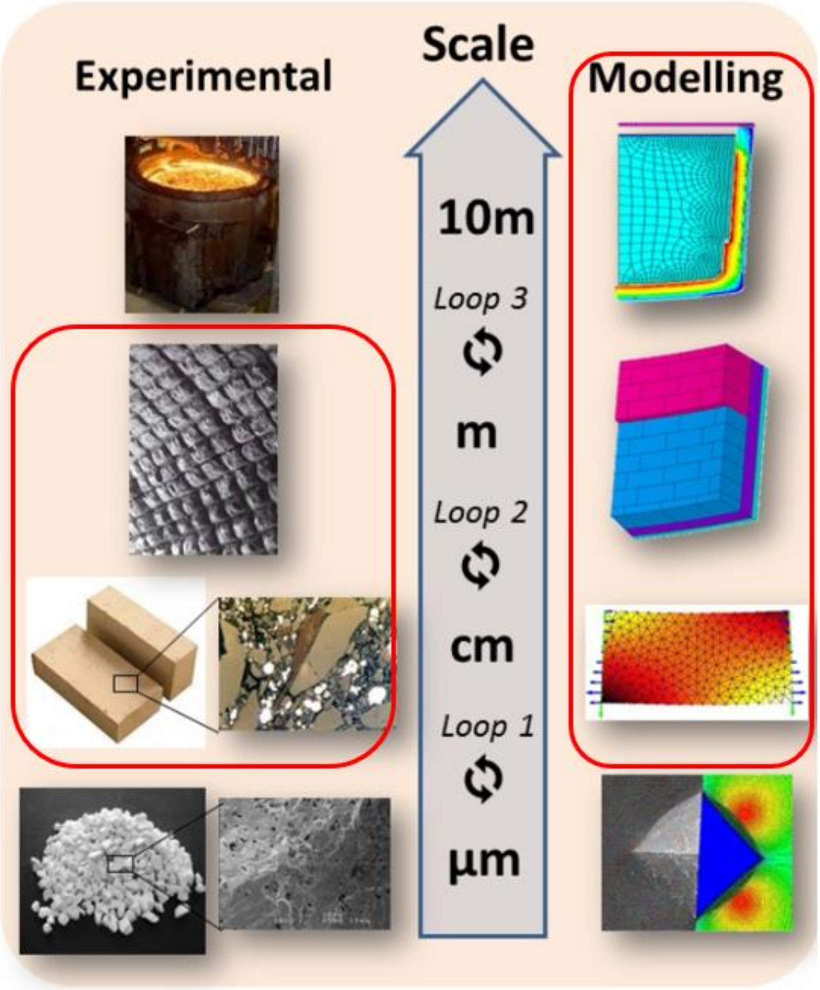

Figure 1-8 – Overall scope of the ATHOR Network, highlighting the scale of the research present in this work

1.3 Research Objectives and Methodology

The overall purpose of this research was to investigate the behaviour of dry-stacked refractory masonry at high temperatures, aiming to contribute to the advance of technology, to improve the understanding of the behaviour of refractory masonry and provide data for the development and validation of numerical models of industrial vessels, fulfilling the current knowledge gaps. Another important goal of this research was to provide valuable experimental results for the development of advanced numerical models based on homogenization techniques. In order to achieve the research's objectives, a large experimental program and advanced numerical simulations were planned and carried out at the Department of Civil Engineering (DEC) of the University of Coimbra, in Portugal, and at the

Technology Centre Leoben (TCL) of the RHI-Magnesita (industrial partner of the ATHOR Project), in Austria.

The experimental phase is divided in three parts: *i*) Characterization of bricks and joints; *ii*) Characterization of dry-stacked refractory masonry under uniaxial compression; and *iii*) Characterization of dry-stacked refractory masonry under biaxial compression. Concerning phase *i*, the goal of the experimental research was to assess the compression strength of the bricks at ambient and high temperatures, evaluate the isotropic behaviour of the material, characterize the normal behaviour of the joints (joint closure curves) and characterize the tangential behaviour of the joints at ambient and high temperatures. To accomplish this task, several compressive tests were performed in cylindrical specimen extracted from bricks in different conditions, joint closure tests were carried-out and slip tests were conducted at ambient and high temperatures. Additionally, a few numerical simulations were carried out to help understanding the joints behaviour.

Concerning the phase *ii*, the goal of the experimental research was to assess the thermomechanical behaviour of dry-stacked masonry wallets at ambient and high temperatures under uniaxial conditions. Five series of tests were performed at the laboratory of the Department of Civil Engineering (DEC) of the University of Coimbra, in Portugal. The tests were planned to evaluate the loadbearing capacity and the response of masonry under cyclic loads at ambient temperature. Additionally, the thermomechanical behaviour of the specimens under constant load level, under restrained thermal elongation and with a higher slenderness ratio was evaluated in fire conditions.

Regarding the phase *iii*, the experimental research aimed to evaluate the thermomechanical response of dry-stacked masonry wallets at ambient and high temperatures under biaxial compression. Six test-series were carried-out at the Technology Centre Leoben (TCL) of the RHI-Magnesita, in Austria. The biaxial response of the masonry wallet was evaluated at ambient temperature considering different loading directions. At high temperatures, uniaxial and biaxial creep tests and biaxial relaxation tests were performed.

Besides the extensive experimental focus of this research, numerical analyses were also performed, at different scales (from a couple of bricks to steel ladles). These were based on micro modelling approach (see additional details in following sections). With calibrated numerical models it was possible to conduct different parametric studies aiming at gathering knowledge outside of the conditions possible within the experimental campaigns.

The specific objectives of this research can be highlighted as:

- ➢ Gather a comprehensive experimental characterization of the thermomechanical properties for refractory masonry elements and masonry components at different temperature regimes and different loading conditions:

  - To evaluate the mechanical strength of alumina spinel bricks at ambient and high temperatures and its anisotropic behaviour.
  - To analyse and characterize the mechanical behaviour of the dry joints: a) The joint closure curve and b) the friction coefficient between the bricks.
  - To study the failure loads, failure modes, failure times and temperatures distribution of masonry wallets.
  - To evaluate the creep and relaxation behaviour of the lining.

- To develop accurate finite element models capable of simulating the thermomechanical behaviour of dry-stacked refractory masonry at ambient and high temperatures and the interactions between bricks and different surrounding elements:
  - To develop numerical models using the micro-modelling technique aiming to represent the behaviour of dry-stacked masonry.
  - To test the Concrete Damage Plasticity (CDP) model applied to refractory ceramics at room and elevated temperatures.
  - To validate the developed numerical models by comparison against the experimental results.
  - To perform simplified analysis of an industrial vessel.

To contribute to the ATHOR Network, providing valuable experimental results for the development and validation of advanced numerical models based on micro-modelling and homogenization techniques.

- To validate the developed numerical models by comparison against the experimental results.
- To simulate a simplified steel ladle during an operational cycle based on the finite element models developed and validated in this research.
- To provide valuable data for developing of a suitable analytical guidance or a new simplified method for the design of refractory linings.
- To propose issues for good practice in the area of the refractory engineering.

1.4 Thesis content

Besides this introductory chapter, this doctoral thesis is organized into six additional chapters, each contributing to a particular subject in this field.

Chapter 2, Refractory masonry: A State of the Art, gathers the most relevant concepts needed to properly understand the work performed in this field. This chapter presents different materials, production techniques, definitions and industrial application of refractory ceramics. Besides presenting the main topics necessary to understand the work performed within this thesis, the most relevant investigations conducted by previous researchers on related topics are also presented and described.

Chapter 3, Characterization of Alumina Bricks and Joints, presents several tests and some numerical studies carried out aiming to analyse the behaviour of the masonry units and joints. The mechanical and thermal properties of the material are presented. Several compression tests were performed at ambient and high temperatures aiming to assess the compressive strength of the brick and study its anisotropic behaviour. The joints normal behaviour was assessed based on an experimental test and numerical simulations. The joints tangential behaviour was evaluated at ambient and high temperatures by means of an innovative device specifically developed for this research. The test specimens, test set-ups, test program, test procedure and the experimental results are addressed and discussed in Chapter 3.

Chapter 4, Experimental Tests on Refractory Masonry Walls under Uniaxial Compression, addresses a series of compression tests on refractory masonry walls at ambient temperature and high temperature. Five test series were performed aiming to evaluate the loadbearing capacity and the response of masonry walls under cyclic loads at ambient temperature and the thermomechanical behaviour of the specimens under a constant load level, under restrained thermal elongation and with a higher slenderness ratio in fire conditions. The experimental results are critically analysed. In this chapter, the test specimens, test set-up, the test program, the test procedures and results are presented and discussed in detail.

Chapter 5, Experimental Tests on Refractory Masonry Walls under Biaxial Compression, addresses a series of biaxial compression tests on masonry walls at ambient temperature and under high temperatures. Six test series were performed aiming to evaluate the structural response of masonry walls under cyclic loading at ambient and high temperatures. The improvements on the biaxial press, the test specimens, the test set-up, the program, the procedure and the experimental results are addressed and discussed in this chapter.

Chapter 6, Numerical Simulations, reports on an extensive numerical study concerning the thermomechanical behaviour of dry-stacked refractory masonry at ambient and high temperatures. The finite element models developed to simulate the thermal and mechanical response of these structures were addressed in this chapter. The finite element software, the mesh, the material constitutive model, the analyses criteria and assumptions, the boundary and loading conditions, the contact formulation of the joints, the analyses procedure and the validation of the finite element models are presented in this chapter. Moreover, numerical models of a steel ladle are also developed, presented and discussed.

Chapter 7, Conclusions and Future Work, provides an overview of the developed research and summarizes its most significant findings. This chapter also presents some suggestions for possible future work related to dry-stacked refractory masonry. Considerations related to the design of refractory linings of industrial vessels and good practice for the lining's construction are also addressed in this chapter, aiming to improve the performance of the linings in service.

Finally, Appendix A and Appendix B present additional information on the industrial applications of refractory ceramics and the summary of standards for the characterization of these materials, respectively.

2 REFRACTORY MASONRY: A STATE OF THE ART

Refractory linings may be composed by masonry (bricks laid with or without mortar) or castables, forming a monolithic structure. Often, both solutions are used in the same industrial application, but in different sections. According to ISO EN 1402-1 (2004), the refractories may be classified based on their shape as pre-formed shapes (also called shaped) and unshaped:

- Unshaped refractory materials: mixtures consisting of aggregates and one or more binders, prepared ready to use directly or after the addiction of suitable liquids;

- Pre-formed shapes refractory materials: shapes made from unshaped refractory materials, casted or moulded and pre-treated by the manufacturer, so that they can be directly placed in service.

The shaped (pre-formed) refractories may range from simple regular bricks to more complex tubes or rods for specific applications. Figure 2-1 presents the usual shapes of pre-formed refractories.

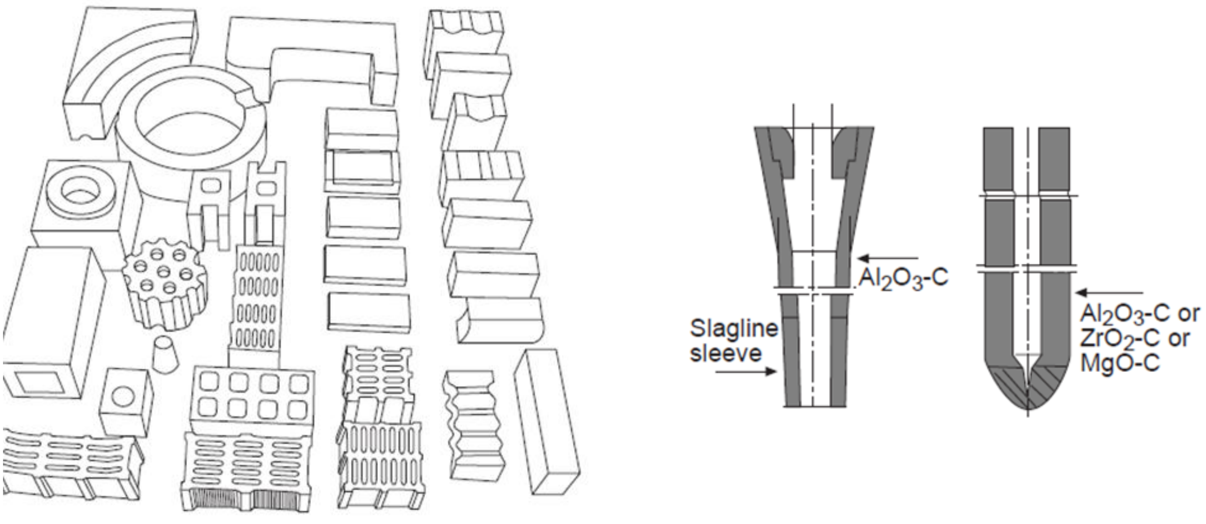

a) b)

Figure 2-1 – Shaped refractories: a) Bricks and shapes; b) More complex tubes and rods (Fruehan and Wakelin, 1998)

The unshaped refractories cure to form a monolithic structure after application. Refractory mortars are available in compositions that approximate the brick’s composition. Alternatively, mortars with thermal elongation similar to the brick may be used as well. The goal is to build a lining as close as possible to a monolithic and continuous structure (Fruehan and Wakelin, 1998). The unshaped refractory materials have some advantages, such as not requiring expansion joints, constructive ease, suitability for various geometries, and reduced material losses during installation. However, they need to go through the curing process after installation (Fruehan and Wakelin, 1998) and the relining process may take longer. The unshaped refractories may be mortars, castables, plastics and mixes as summarized in Table 2-1.

Table 2-1 – Types and Descriptions of Refractories (Heller and Bullock, 2001)

Type	Definition
	Shaped Refractories
Bricks	Shaped refractories used to line furnaces, kilns, glass tanks, incinerators, etc
Insulating firebrick	Low thermal conductivity firebrick
	Unshaped Refractories (Monolithic)
Mortar	Materials for bonding bricks in a lining. The three types of mortar—heat-setting, air-setting, and hydraulic-setting—have different setting mechanisms.
Castable	Refractories for which raw materials and hydraulic-setting cement are mixed. They are formed by casting and used to line furnaces, kilns, etc.
Plastics	Refractories in which raw materials and plastic materials are mixed with water. Plastic refractories are roughly formed, sometimes with chemical additives
Gunning mixes	Refractories that are sprayed on the surface by a gun
Ramming mixes	Granular refractories that are strengthened by gunning formulation of a ceramic bond after heating. Ramming mixes have less plasticity and are installed by an air rammer.
Slinger mixes	Refractories installed by a slinger machine.
Patching materials/ coating materials	Refractories with properties similar to refractory mortar. However, patching materials have controlled grain size for easy patching or coating.
Lightweight castable	Refractories in which porous lightweight materials and hydraulic cement are mixed. They are mixed with water and formed by casting. Lightweight castable are used to line furnaces, kilns, etc.

The focus of this study is the steel ladle. Steel ladles are widely used to carry out metallurgical reactions in steel making plants, because of it is cost-efficiency. The steel ladle is usually lined with three layers of refractories: *i*) working layer; *ii*) the safety layer, and *iii*) the insulating layer. In general, the working lining of steel ladles are composed by mortarless masonry (Gasser *et al,* 2004; Nguyen *et al,* 2009; Ali *et al,* 2020), the coating of cement kiln (Shubin, 2001; Ramanenka *et al,* 2014) and torpedo ladles (Andreev and Zinngrebe, 2009) are also composed by dry-stacked bricks.

The manufacturing process of refractory ceramics has a significant impact on its mechanical properties (Samadi *et al,* 2020; Samadi *et al,* 2021). Several aspects, such as ejection force, type of pressing, spatial arrangement of grains, shape of aggregates, the position of the bricks in the kiln during firing, specimen preparation and pressing direction may affect their thermomechanical properties, and consequently the performance of the refractory linings (Gruber and Harmuth, 2010; Melo *et al,* 2018; Hubalkova and Stoyan, 2003; Heindl and Mong, *1936*; Stuppfler *et al,* 2015; Dahlem *et al,* 2015;

Czechowski *et al*, 2015). Therefore, an elevated technological control is required in the production process.

The manufacturing process of refractory ceramics begins with the extraction and treatment of several types of raw materials, involving the phases of crushing, sorting by size, calcination and drying. Then the chemical and mineral components are combined, aiming to guarantee thermal stability, corrosion resistance, creep resistance, a small coefficient of thermal expansion and other desired physical and chemical qualities. All components undergo strict technological controls, as small deviations in the concentration of the components or in the granulometry distribution of the product can result in greater porosity, greater permeability and consequently lower mechanical resistance. The following steps depend on the type of refractory to be made, the components are shaped, burned (if applicable) and follow for the final processing and transportation (Heller and Bullock, 2001). The flowchart of the manufacturing process is shown in Figure 2-2.

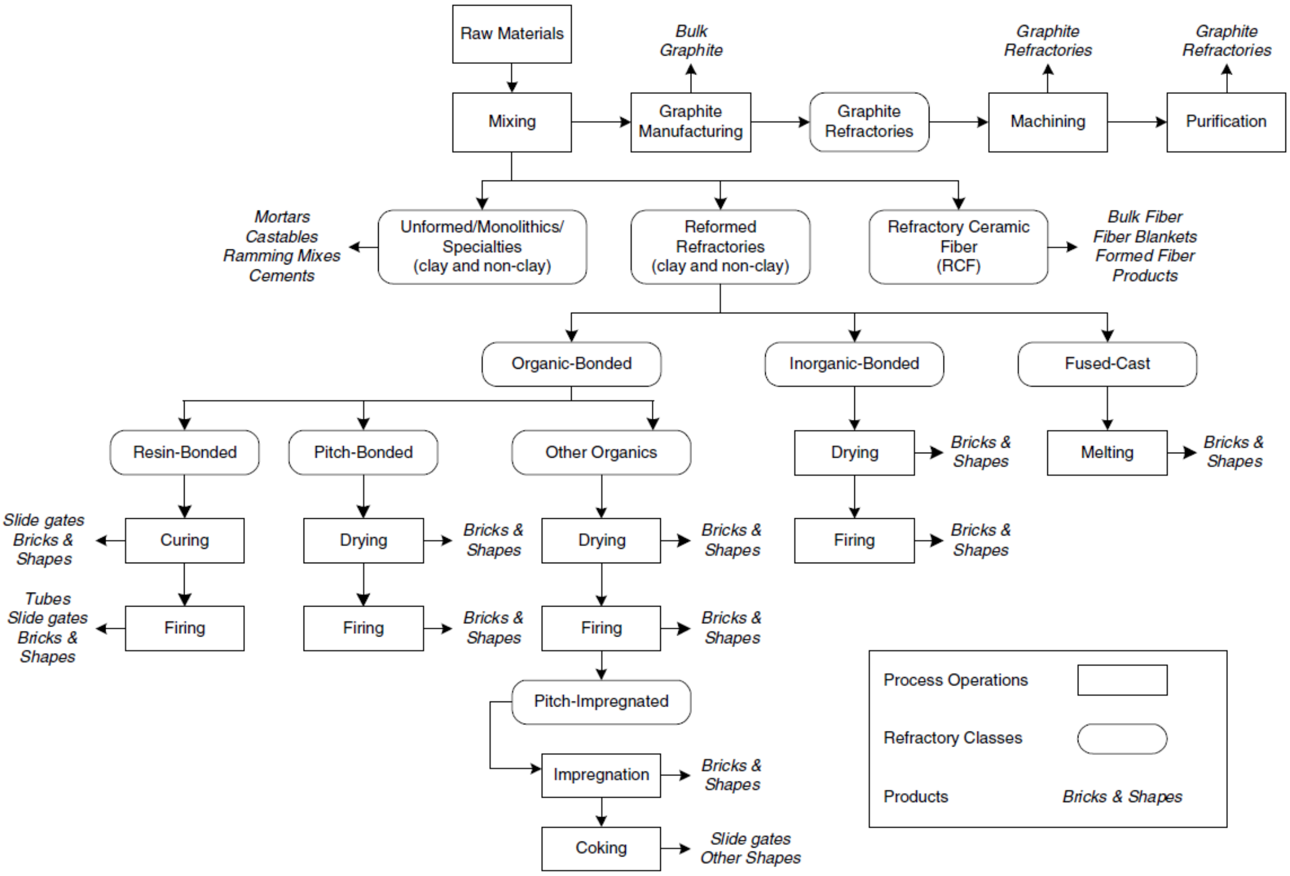

Figure 2-2 - Flowchart of the manufacturing process (Heller and Bullock, 2001)

Due to the extreme service conditions of refractory linings, the design of these structures is very complex. The refractory linings are subjected to high temperatures, consequently, creep, wear, corrosion, spalling and fractures may occur. Therefore, a highly nonlinear behaviour is observed. To properly design and optimize the performance of the linings, advanced numerical models must be developed. The models must account for the joints' closure and reopening, the nonlinear elastic-viscoplastic behaviour of the material, the changes on the thermomechanical properties of the material with the temperature, suitable boundary conditions and many other aspects.

In the recent past, significant developments were made regarding the numerical simulation of industrial vessels. The predictions of the thermal fields and the optimization of the insulation have evolved from simple steady-state two-dimensional models to advanced transient three-dimensional analysis (Xia and Ahokainen, 2001; Yilmaz, 2003; Glaser *et al,* 2011; Santos *et al,* 2018; Ali *et al,* 2020).

The mechanical simulation of dry-stacked refractory masonry have evolved from the simulation of simplified models of masonry wallets (Gasser *et al,* 2004; Nguyen *et al,* 2009), passing by the simulation of small parts of the industrial vessels such as the bottom of a steel ladle and the Ruhrstahl Heraeus snorkel (Gasser *et al,* 2013; Jin *et al,* 2016), to the three-dimensional simulations of an entire ladle comprising all the non-linearities of the process (Ali *et al,* 2020; Ali *et al,* 2021). Nevertheless, further improvements of these models are necessary to increase the reliability, accuracy and the efficiency of these simulations. Experimental and numerical campaigns on the thermomechanical behaviour of dry-stacked refractory are required to fulfil the gaps on the knowledge. The valuable experimental results generated will be used in the development, calibration and validation of advanced numerical models. Appendix A presents the industrial applications and the main properties of several refractory ceramics.

2.1 Material characterization

Alumina-spinel bricks are being increasingly used in for industry applications, especially in the working lining of steel ladles, due to the requirements of ultralow carbon content metallurgy (Poirier et Rigaud, 2017). High-alumina bricks are also used in the lining of rotary cement kilns (Ramanenka *et al,* 2014; Ramanenka *et al,* 2017). Thus, this material was chosen for the experimental campaign presented in this doctoral thesis.

The production process of the refractory bricks involves complex processes that include shaping process (pressing) and thermal treatments (firing). As reported in the literature, the position of the bricks in the furnace during firing affects their mechanical properties (Heindl and Mong, 1936). The pressing procedure has also an impact on the mechanical properties, as the cold crushing strength and refractoriness under load (RUL) of specimens extracted from the direction of pressing are different from the ones obtained perpendicular to the pressing direction (Stuppfler and Dahlem, 2015; Dahlem *et al*, 2015; Czechowski *et al*, 2015). The creep properties of refractories have also a significant scatter depending on the direction of the loading and on the position of the specimen inside the brick (Samadi *et al*, 2020; Bakunov and Belyakov, 2000).

2.1.1 Mechanical properties

The variation of the Young's modulus with the temperature (measured by ultrasonic pulse velocity tests) and the thermal elongation of the material were measured by Kaczmarek *et al.* (2019), as shown in **Figure 2-3**. According to the authors, the increasing of the Young's modulus from ambient temperature to 1100 ºC is a result of cracks' closure caused by thermal expansion. From 1100ºC to 1500ºC a possible formation of viscous phases is responsible for the reduction of the Young's modulus. The dwell time led to an increase in the Young's modulus and specimen elongation as a result of the increasing of the spinel content. At the cooling stage, an increase of the Young's modulus is observed from 1500ºC to 700ºC due to an increasing of the glassy phase within the microstructure of the material. From 700 ºC to ambient temperature, the decrease in the Young's modulus is caused by the development of microcracks as evidenced by the acoustic activity of the specimen. After the heating and cooling cycle, a permanent linear change in the dimension of the specimen is observed. The thermal coefficient expansion is similar in pressing and perpendicular to pressing directions.

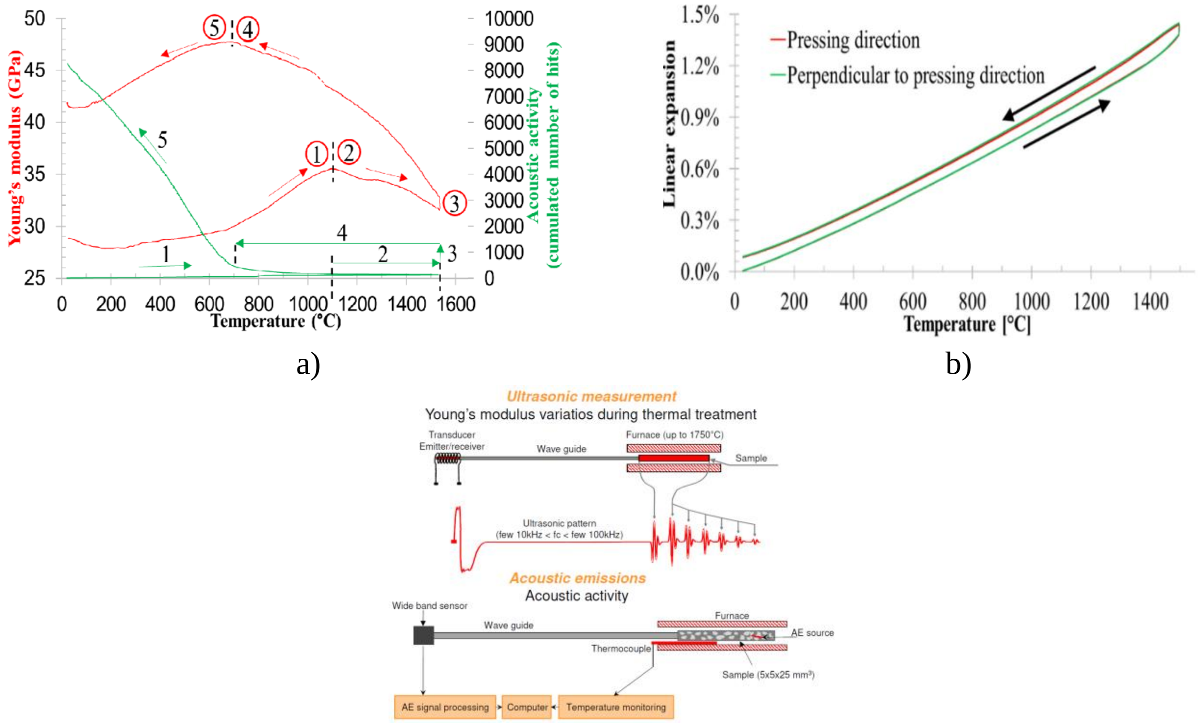

a) b)

c)

Figure 2-3 – Mechanical properties: a) Young's modulus and acoustic activity; b) Thermal elongation; c) Schematics of the test (Kaczmarek *et al*, 2019)

The tensile strength measured by Kaczmarek *et al*, (2019) using direct and indirect methods (Brazilian test) are given in **Figure 2-4**. In the direct tensile test, the specimen is fixed in the testing machine by two clampers and two extensometers are used to measure the strains. In the indirect method (Brazilian test), the specimen is diametrically compressed and tensile stresses are developed in the specimen, the strains are measured by DIC. The schematic of both tests are shown in **Figure 2-4**.

The tensile strength obtained at the direct tensile test at ambient temperature is 1.57 MPa, however the Brazilian test provided a higher value at ambient temperature (3.44 MPa). At 1200 ºC, the tensile strength measured by the Brazilian test was 1.12 MPa.

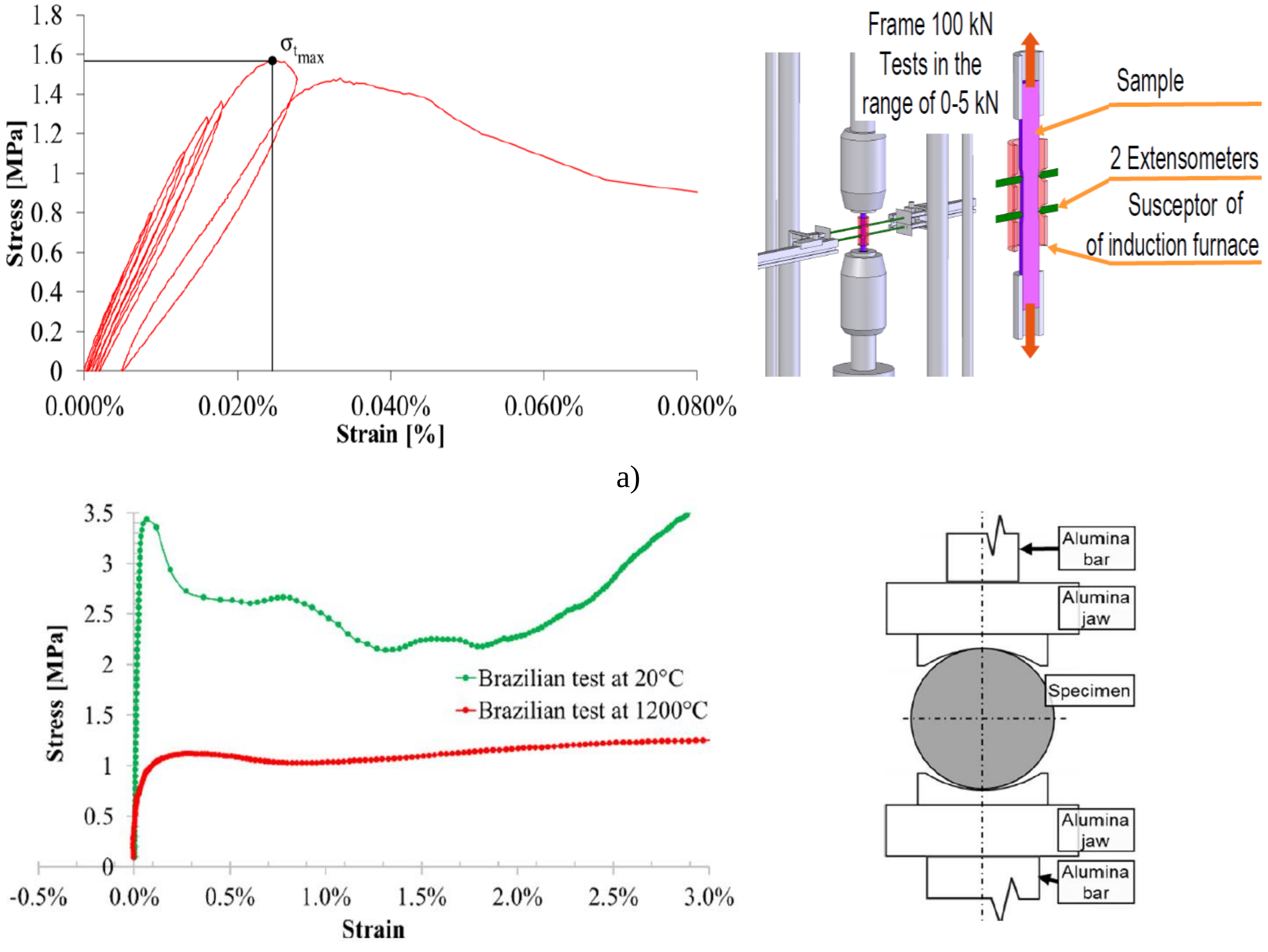

a)

b)

Figure 2-4 – Tensile strength: a) Direct tensile test; b) Brazilian test (Kaczmarek *et al*, 2019)

2.1.2 Thermal properties

The thermal conductivity and the specific heat of the studied material are presented in **Figure 2-5** (Vitiello, 2021). The thermal conductivity was measured based on the laser flash technique. The specific heat was theoretically calculated based on the chemical composition of the material (Knacke *et al*, 1977). A reduction of the thermal conductivity is observed within increasing temperature, while an increasing of the specific heat is detected in the same condition.

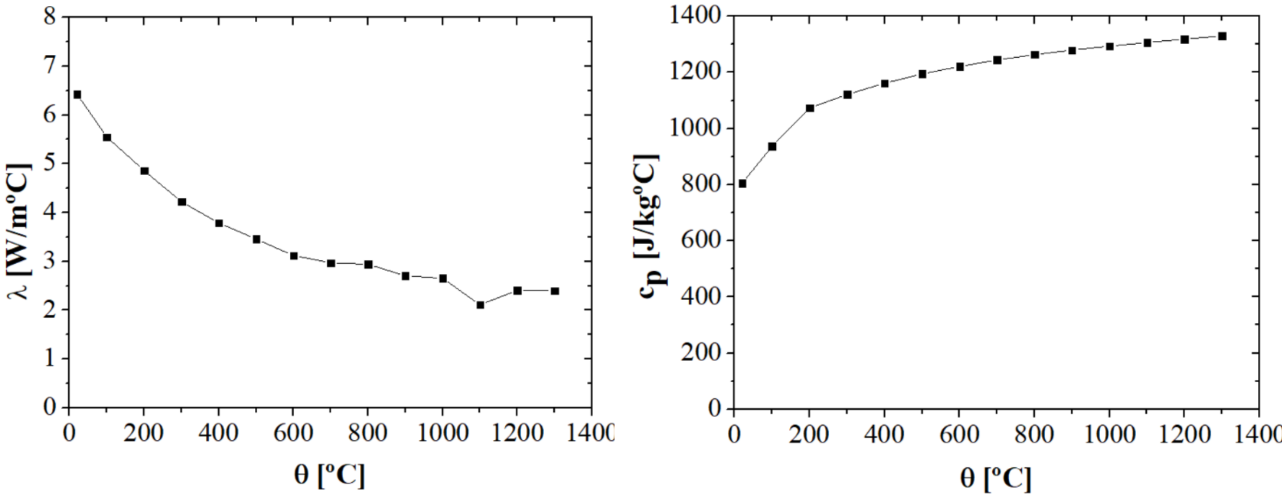

a) b)

Figure 2-5 – Thermal properties: a) Thermal conductivity; b) Specific heat (Vitiello, 2021)

The principle of the laser flash technique is to apply an energy pulse to the front face of the specimen, the absorbed heat diffuses through the material and the resulting time dependent temperature of the opposite face is detected. If the density and the specific heat capacity are known, the thermal conductivity may be calculated (Vitiello *et al*, 2019). The schematic of the laser flash method is shown in **Figure 2-6**.

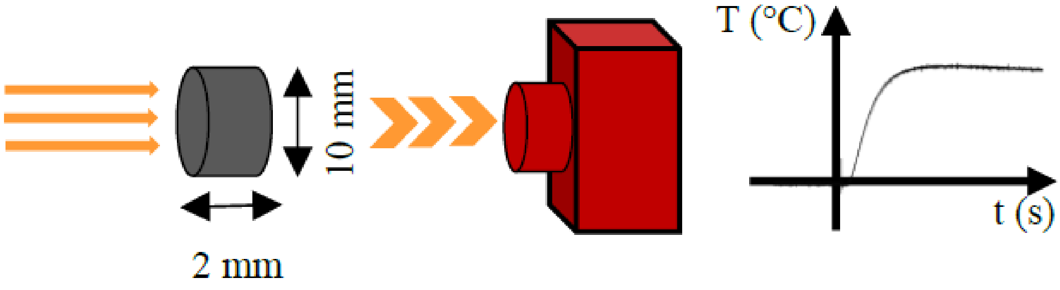

Figure 2-6 – Schematic of the laser flash method (Vitiello *et al*, 2019)

2.1.3 Creep properties

The creep has a significant impact on the thermomechanical behaviour of the industrial vessels, reducing the stresses developed in the refractory linings (Ali *et al*, 2021). The creep properties shall be accurately determined to simulate the performance of the linings. The typical creep strain curves are presented in Figure 2-7, where it is possible to identify the three following creep stages:

- Primary creep: the strain rate is not constant and the acceleration of creep strain is negative.
- Secondary creep: the strain rate is constant and the acceleration of creep strain is zero.
- Tertiary creep: the strain rate is not constant and the acceleration of creep strain is positive.

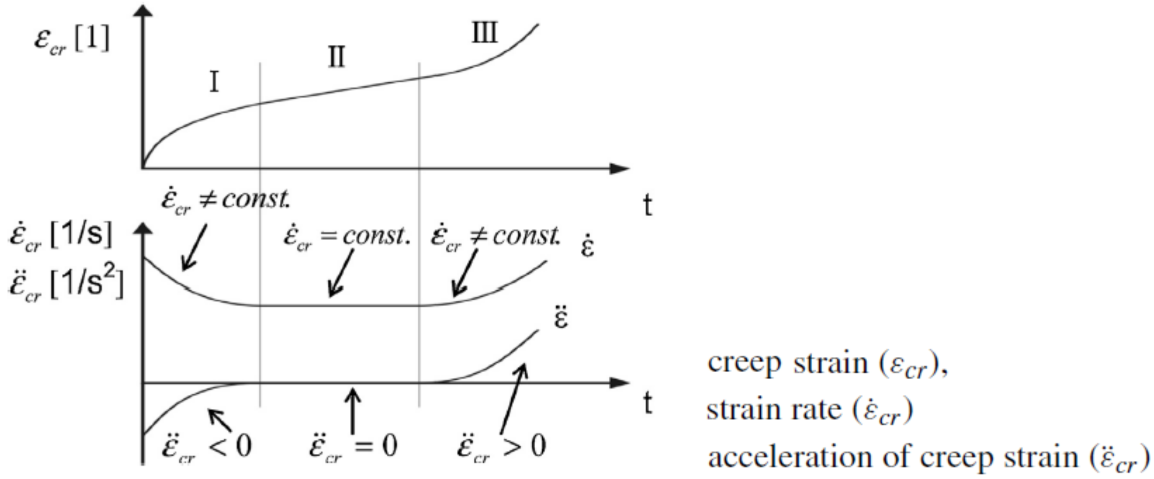

Figure 2-7 – Creep strain curves. (I) primary creep, (II) secondary creep, (III) tertiary creep. Reprinted from (Jin *et al*, 2014)

The European standard EN 993-9 (1997) prescribes a compressive load of 0,2 MPa for the characterization of the creep properties of refractory ceramics. However, according to Jin *et al* (2014) this value is far from the compression stresses usually obtained in refractory linings. Thus, aiming to identify the Norton-Bailey´s strain hardening creep law parameters, Jin *et al* (2014) have developed a device for the characterization of the compressive creep properties, in which the compression stress may reach up to 20 MPa. Figure 2-8 presents the schematic diagram of the testing machine. The procedure developed by the authors allows the characterization of the creep behaviour of shaped and unshaped refractories at elevated loads.

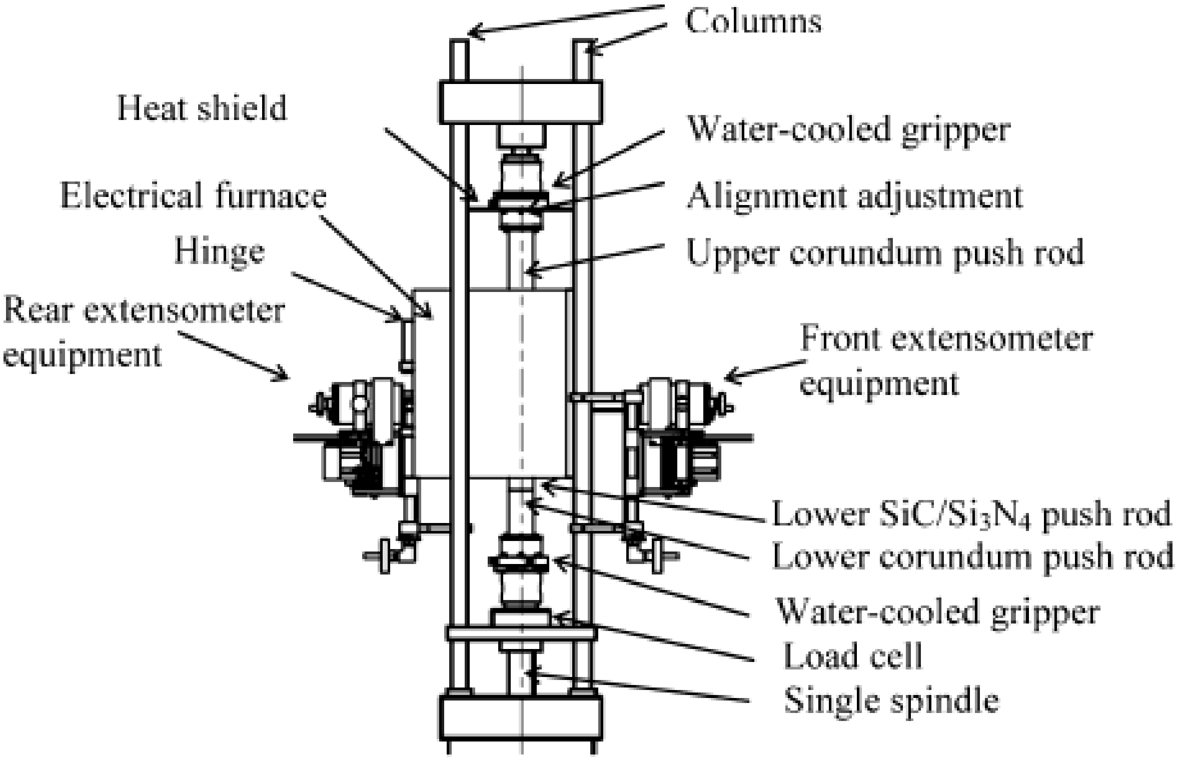

Figure 2-8 – Schematic diagram of the testing machine. Reprinted from (Jin *et al*, 2014)

Samadi *et al* (2020) have used the equipment developed by (Jin *et al,* 2014) to characterize the alumina spinel bricks used in this doctoral research. The results of compression creep tests with different load levels and temperatures are given **Figure 2-9**. As observed, the creep properties of refractories have a significant scatter (Samadi *et al,* 2020; Bakunov and Belyakov, 2000). It is possible to identify the three creep stages in the curves.

Teixeira *et al* (2020) have characterized the tensile creep behaviour of these bricks using a specific machine, similar to the one developed by Jin *et al* (2014). The comparison of the compression and tensile creep curves at 1300 ºC is given in **Figure 2-10**. In the tensile creep curves with load level of 0.20 MPa it is possible to identify primary and secondary creeps, that happens relatively quickly in less than one hour. For the load level of 0.25 MPa, only secondary creep is observed.

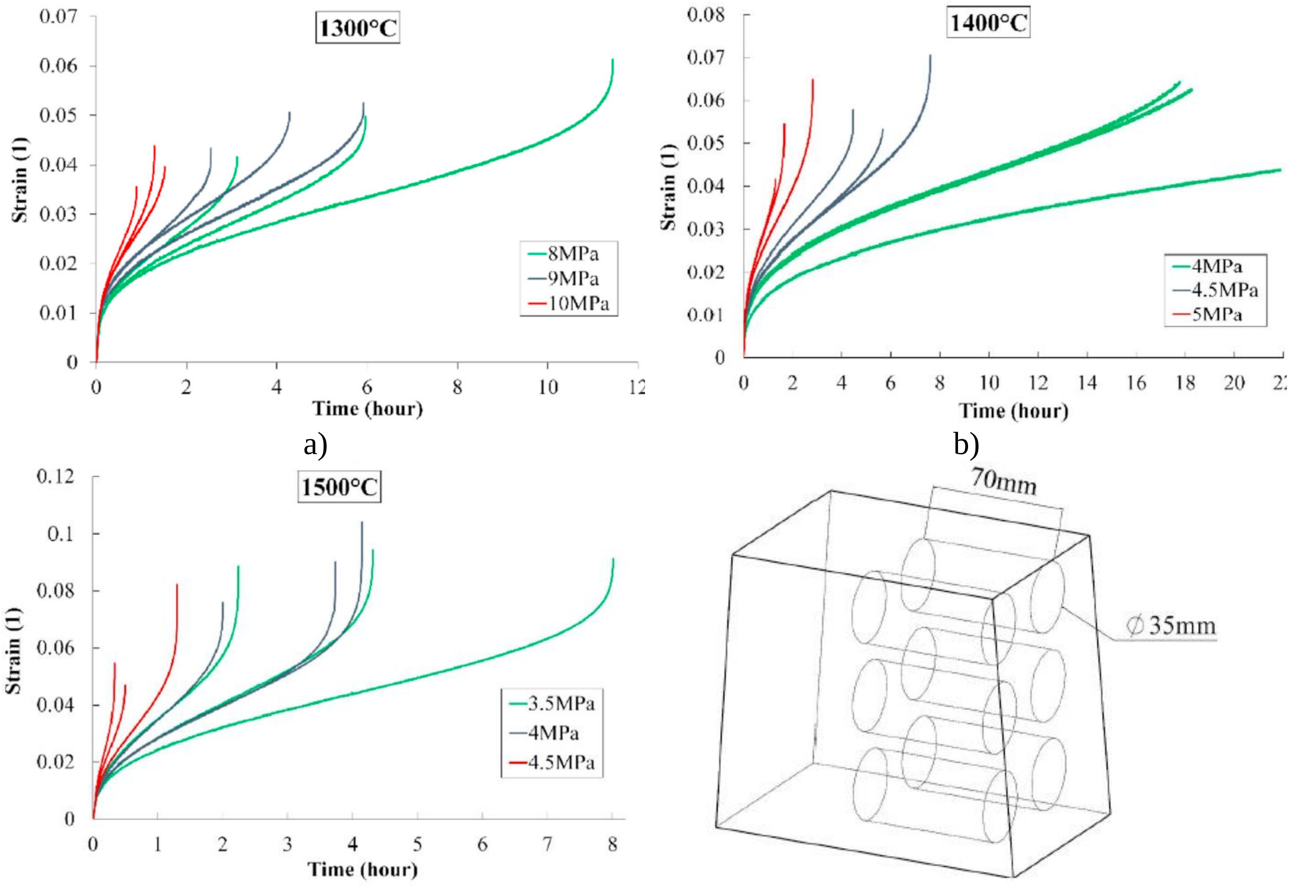

a) b)

c) d)

Figure 2-9 – Compression creep curves: a) 1300 ºC; b) 1400 ºC; c) 1500 ºC; d) S**pecimens** dimensions. Reprinted from (Samadi *et al*, 2020)

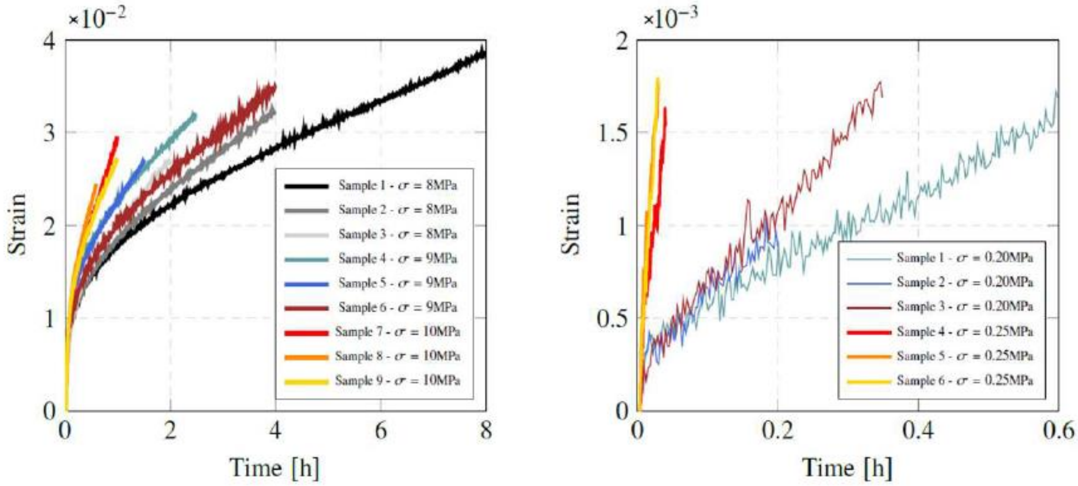

a) b)

Figure 2-10 – Creep curves at 1300 ºC: a) Compression; b) Tensile. Reprinted from (Teixeira *et al*, 2020)

2.2 Dry joint behaviour

In dry-stacked masonry there is no mortar layer to correct the brick shape imperfections. Consequently, the behaviour of mortarless masonry is significantly different from the behaviour of ordinary masonry, as its compression stress-strain curve is non-linear at the beginning of the loading stage (Gasser *et al*, 2004; Andreev *et al*, 2012). Two geometric imperfections are fundamental for the observed behaviour: the height imperfection between different bricks (ΔH) (Ngapeya *et al,* 2018) and the roughness of the bricks' surface (Δh) (Zahra and Dhanasekar, 2018). The behaviour of dry-stacked masonry is addressed in this section.

2.2.1 Joints normal behaviour

Gasser *et al* (2004) performed an experimental study on the behaviour of refractory brick's dry joints. The goal of this research was to evaluate the bricks and joint' properties and define a homogenised material able to simulate the behaviour of the linings. The bricks' Young's modulus was obtained in compression tests, while the joint normal behaviour was obtained by a compression test performed in two stacked bricks (**Figure 2-11**a). The force-displacement curve obtained experimentally for the stacked bricks (**Figure 2-11**b) shown two different stages: *i*) a non-linear part: corresponding to the joint closure; and *ii*) a linear part: corresponding to the brick's behaviour. The joint thickness can be estimated from this curve. According to the authors, the relative dispersion obtained experimentally shown that crushing is affected not only by the surfaces' roughness but also by the brick shape imperfections, such as non-flatness or non-parallelism of the faces.

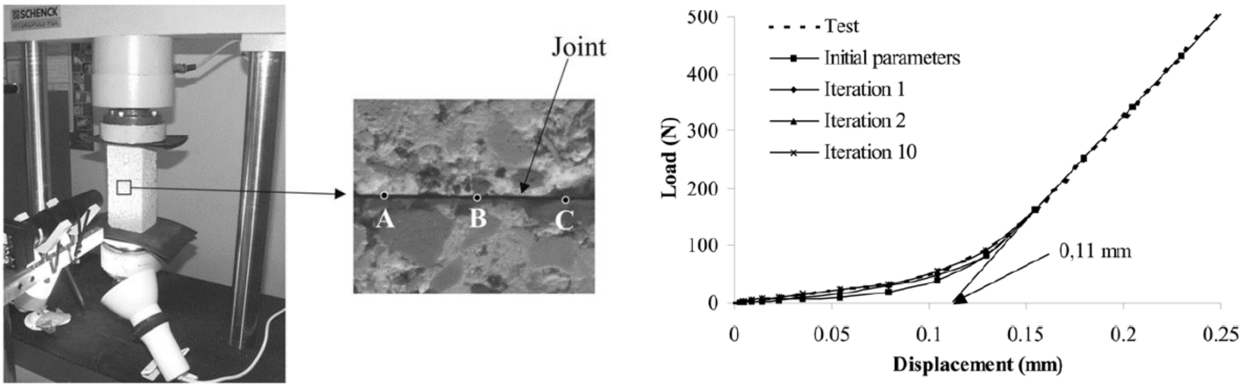

a) b)

Figure 2-11 – Experimental research: a) Test set-up; b) Load displacement-curve. Modified from (Gasser *et al,* 2004)

The behaviour obtained by Gasser *et al* (2004) was also observed by Jaafar *et al* (2006). Thanoon *et al* (2008) proposed a mathematical model to describe the nonlinear compressive stresses in mortarless masonries in terms of joint closure (**Figure 2-12** and **Eq. 1**):

$$\sigma_n = a\, d_n^{\,b} + c\, d_n \tag{1}$$

Where σ_n is the normal compressive stress (N/mm^2), d_n is the gap or closing deformation (mm) and a, b and c are constants determined from experimental results. The normal tangent stiffness of the joint, k_n, may be obtained by differentiating **Eq. 1**, as shown in **Eq. 2**:

$$k_n = ab\, d_n^{\,b-1} + c \tag{2}$$

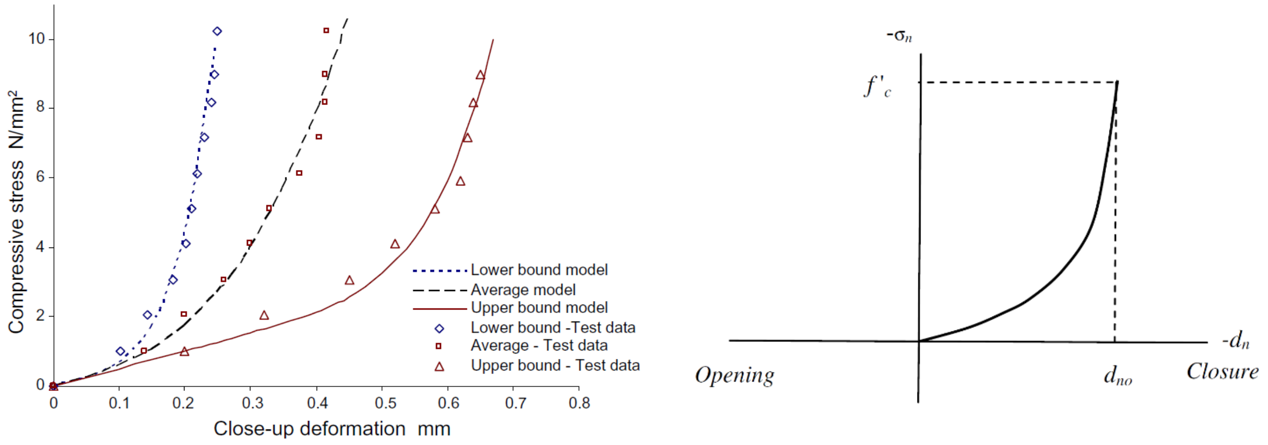

a) b)

Figure 2-12 – Dry joint behaviour: a) Displacement versus compressive stress, b) Criterion for closure of dry joints. Modified from (Thanoon *et al*, 2008)

Andreev *et al* (2012) also characterized the compressive behaviour of dry joints in refractory masonries using the aid of the Digital Image Correlation (DIC) technique. The authors performed compressive tests in prisms formed by magnesia-carbon and magnesia-chromite bricks in a wide temperature range (**Figure 2-13**a). They highlighted that the exponential form of the joint closure curve is a result of the gradual crushing of initially non-parallel surfaces (**Figure 2-13**b). The tests have shown that the temperature influences the joint closure by changing the stiffness of the material and reducing the initial gap by thermal elongation. The contact area between the bricks was found to be proportional to the applied stress (**Figure 2-13**c). The authors observed that the joint thickness is not constant along the joint due to surface roughness, bricks' shape variations and non-parallelism of faces (**Figure 2-13**d).

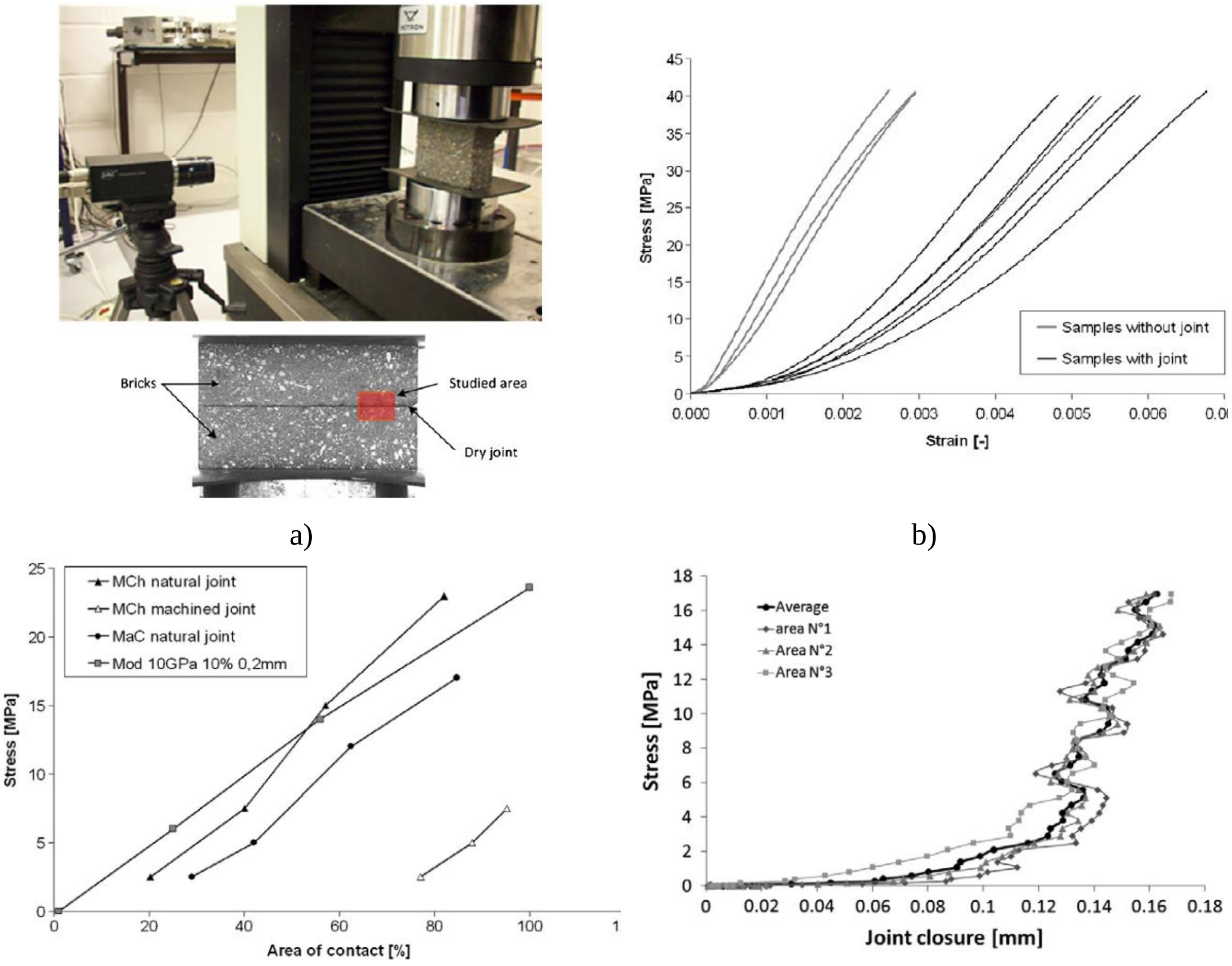

a) b)

c) d)

Figure 2-13 – Experimental research: a) Experimental set-up, b) Effects of joints in the materials behaviour; c) Increasing of contact area with load; d) Scattering in joint closure. Reprinted from (Andreev *et al*, 2012)

Allaoui *et al* (2018) expanded the research performed by Andreev *et al* (2012). The experimental set-up used by the authors is shown in **Figure 2-14**a. The authors evaluated the roughness of the bricks' surface and found the arithmetical mean roughness was about 12 ± 2 µm and the maximum height of the profile between successive peaks and valleys was about 85 ± 15 µm. The results shown that the gap between bricks is caused mainly by the lack of planarity of the brick surfaces. The authors highlighted that the process of joint closure involves roughness crushing and adjustment of surfaces, which is a strongly heterogeneous, orthotropic and a nonlinear process. **Figure 2-14**b presents the joint measurements at different positions of the brick for three different tests and it is possible to identify a significant scatter in the results. This scattering is also observed in the strain fields plotted at **Figure 2-14**c. The authors observed local joint opening during the first stage of the global joint closure in one specimen, caused by rigid body motion that induced rotation of the contacting bricks as shown in the strain fields of **Figure 2-14**d.

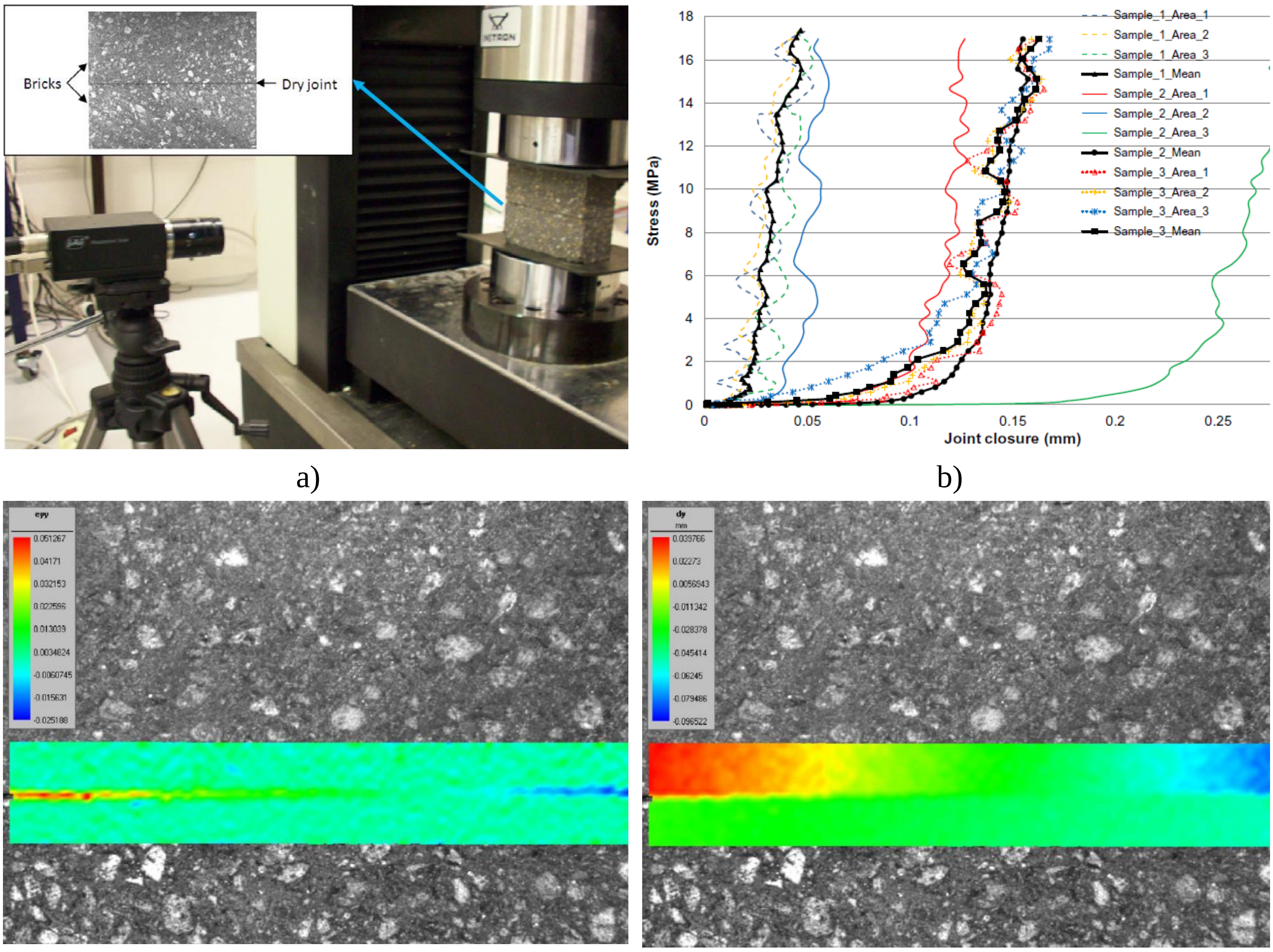

a) b)

c) d)

Figure 2-14 – Experimental research: a) Experimental set-up; b) Scattering of results; c) strain fields at the joints; d) displacement fields at the joint. Reprinted from (Allaoui *et al*, 2018)

Zahra and Dhanasekar (2018) evaluated the effects of contact surface unevenness on the behaviour of dry-stackable concrete blocks used in civil construction, mostly caused by the presence of random interstices and coarse aggregates in the blocks' surface. The experimental set-up is shown in **Figure 2-15**a. Matrix based tactile surface sensors (MBTSS) were used to precisely determine the contact pressure at the brick interfaces (**Figure 2-15**b), which exhibited several high-pressure points over the contact surfaces, leading to a non-uniform stress distribution (**Figure 2-15**c). The high-pressure points are observed even for higher loads, most likely caused by high strength coarse aggregates that are not crushing during the test (**Figure 2-15**d). The authors proposed techniques to mitigate the unevenness contact conditions, however, these techniques seem less interesting in the case of refractory masonries due to the high temperatures in service.

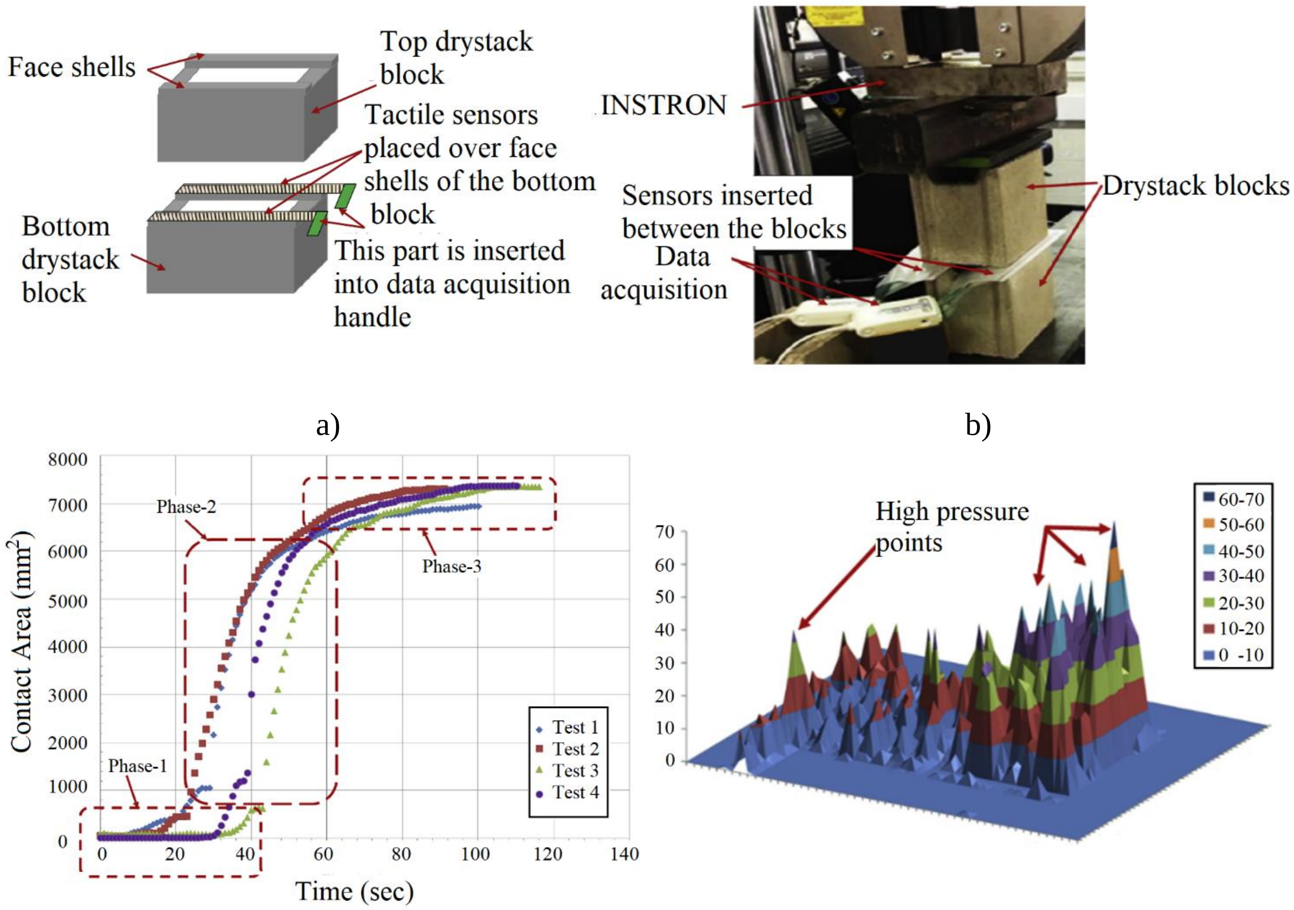

a)

b)

c)

d)

Figure 2-15 – Experimental research: a) Experimental set-up; b) Scattering of results; c) strain fields at the joints; d) displacement fields at the joint. Reprinted from (Zahra and Dhanasekar, 2018)

Ngapeya *et al* (2018) evaluated the effects of bricks' height imperfection on the behaviour of dry-stacked masonry. As observed by Agaajani (2015), the bricks' height imperfections follow a Gaussian law. The tolerances of production of the bricks studied were ± 2 mm. The bricks' height imperfections led to an uneven stress distribution in the wall, as the loading and support conditions of the bricks were not perfect. Due to the unevenness stress distribution in the bricks, the authors defined five load cases for a single brick depending on the support and loading conditions (**Figure 2-16**). In load case 1, the bricks is loaded and supported along its entire surface, consequently it can develop 100% of its loadbearing capacity. For the load cases 2, 3, 4 and 5 the bricks can withstand 40%, 13%, 40% and 30% of its loadbearing capacity, respectively.

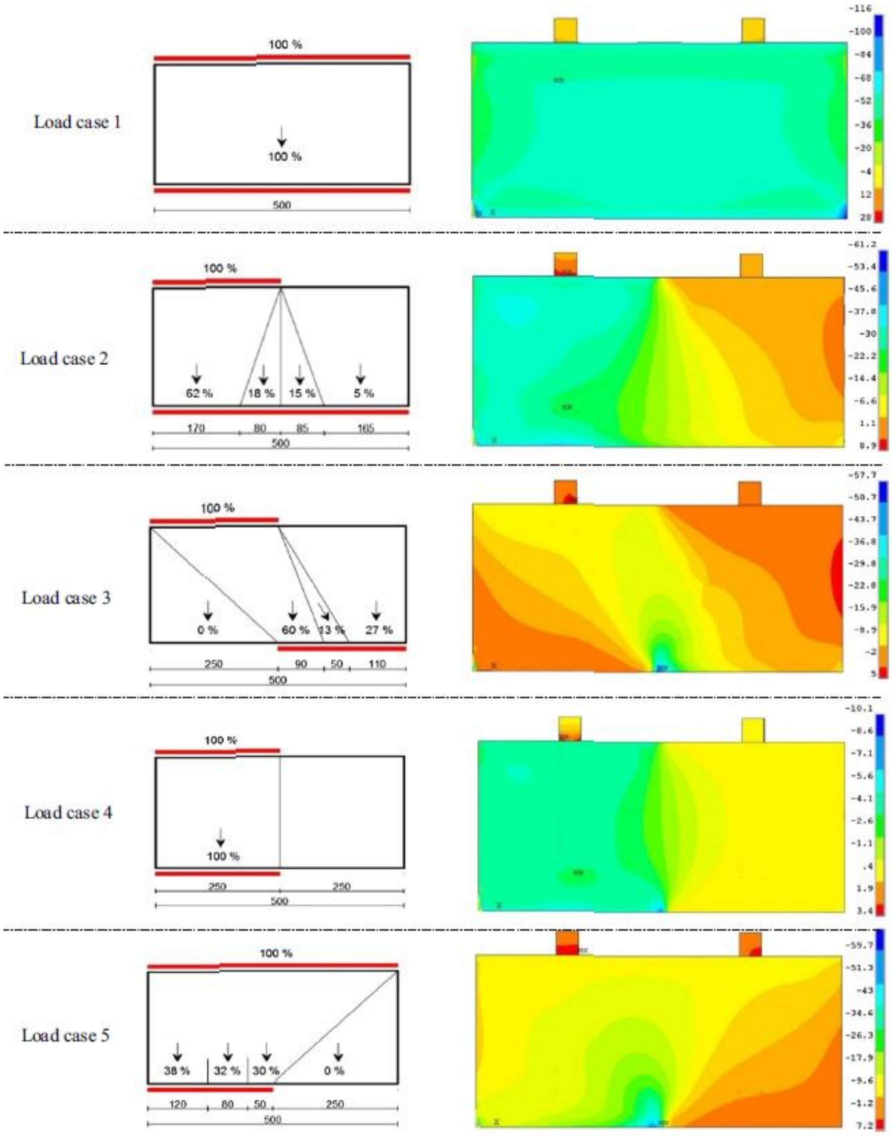

Figure 2-16 – Different support and loading conditions for a brick (Ngapeya *et al*, 2018)

When the bricks are dry-stacked, their shape imperfections lead to a significant non-homogeneous distribution of stresses in the wall. **Figure 2-17** shows the stress distribution for two walls composed by bricks with different shape imperfections randomly distributed in the wall. The load percolation path can be easily identified. The uneven stress distribution of the wall led to a significant reduction on its loadbearing capacity, the ultimate load of wall A and B were 260 kN and 60 kN, respectively.

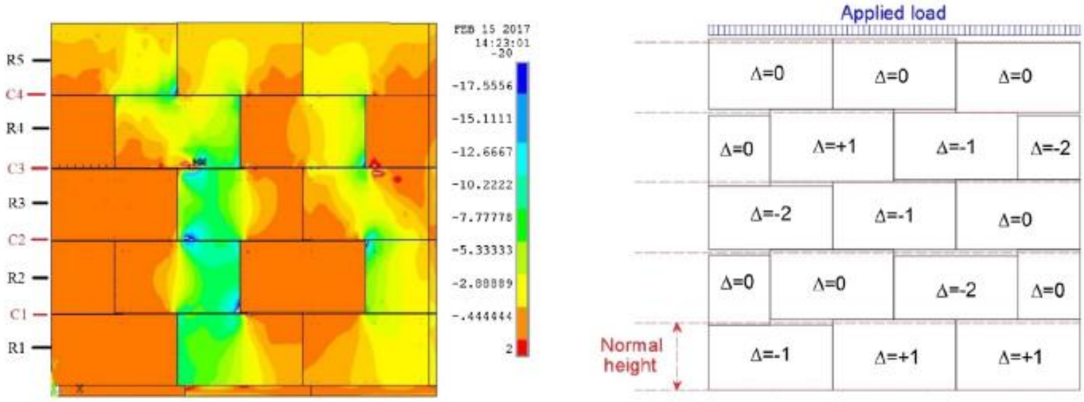

a) Wall A

Height variation of masonry blocks of wall A

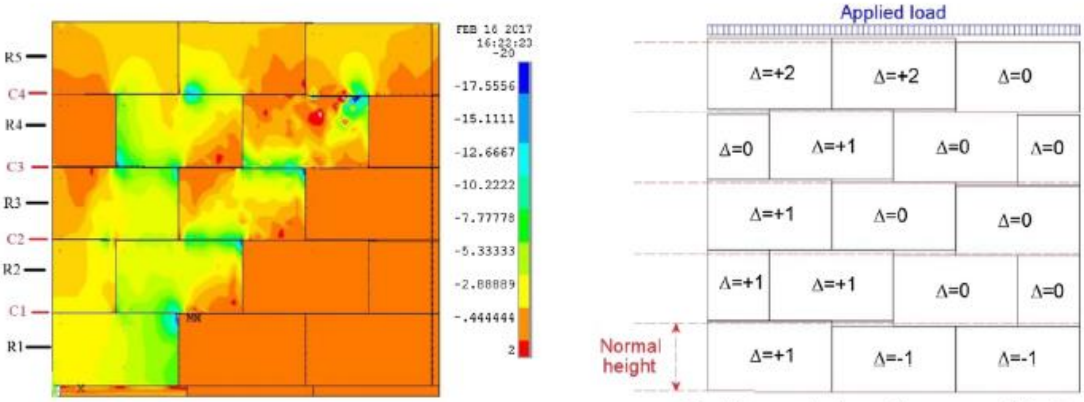

b) Wall B

Height variation of masonry blocks of wall B

Figure 2-17 – Numerical study: a) Stress distribution [MPa] in wall A; b) Stress distribution [MPa] in wall B (Ngapeya *et al*, 2018)

2.2.2 Joints tangential behaviour

The tangential behaviour of joints in masonry is ruled by the Coulomb friction law (Gasser *et al*, 2004; Nguyen *et al*, 2009). The shear strength depends on the normal stress applied to the interface and may be obtained by **Eq.3**:

$$f(\tau,\sigma_n,\Phi) = |\tau| - c + \sigma_n \tan(\Phi) \tag{3}$$

where τ is the shear stress, σ_n is the normal stress, c is the cohesion of the interface and Φ is the internal angle of friction. For masonries with mortar, the Mohr-Coulomb failure criterion with tensile cut-off may be used (Abdou *et al*, 2006; Brulin *et al*, 2020), as shown in **Eq. 4**.

$$f(\sigma_n, f_t) = \sigma_n, - f_t \tag{4}$$

where f_t is the tensile strength of the interface.

The European standard EN 1052-3 (2002) is widely used to determine the initial shear strength at ambient temperature for joints with mortar. Additionally, different test set-ups have been used to characterize the shear strength of joints, as shown in **Figure 2-18** (Abdou *et al*, 2006). However, it is a challenge to perform these kind of tests at high temperatures, as they require the application of loads in two perpendicular directions. Usually, the laboratory furnaces are not prepared for this having only one opening for load application.

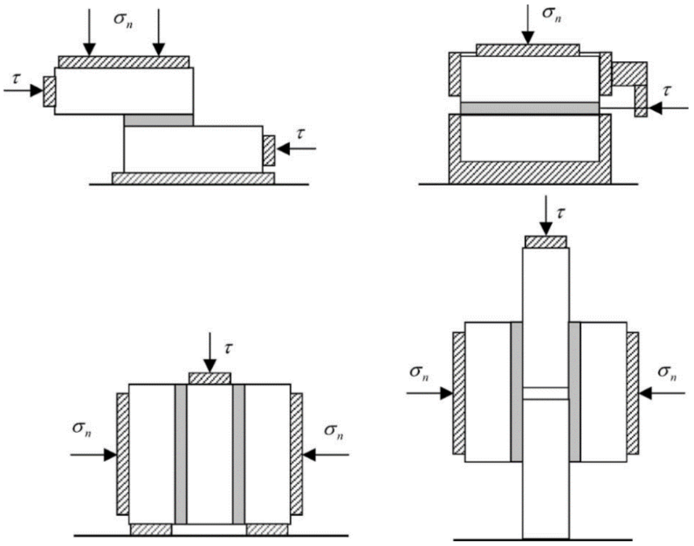

Figure 2-18 – Specimens used for the study of the shear behaviour of the bed joints. Reprinted from (Abdou *et al*, 2006)

The Slant Shear test was successfully used to characterize the brick/mortar interface at ambient and high temperatures (Brulin *et al*, 2020). The schematics and the specimens of this test are shown in **Figure 2-19**. The concept of the test is to perform compression tests in a prism composed by bricks sticked with mortar. The compressive force results in a normal and a tangential stress at the interface. Testing specimens with different angle (α) allows to identify the cohesion and friction angle of the joint. However, the slant shear test can’t be used in the case of dry joints

When dealing with mortarless masonry, only the friction coefficient (or friction angle) needs to be identified. A simple test is the use of an inclined plane, with increasing rotation, which makes possible to determine the initial angle of sliding (Gasser *et al*, 2004). This test can be easily performed at high temperatures.

The friction between bricks plays an important role in the stabilization of the lining, mainly in cold conditions. In cement furnaces, the movement of refractory bricks causes opening of the joints and, as a consequence, individual bricks or even sections of the lining may fall out (Shubin, 2001; Ramanenka *et al,* 2017). In numerical simulations of mortarless masonries, the friction coefficient between bricks is usually taken as a temperature independent parameter (Gasser *et al,* 2004; Nguyen *et al,* 2009; Ramanenka *et al,* 2017; Gasser *et al,* 2013; Ali *et al,* 2019; Ali *et al* 2020). As there is a lack of data in the literature related to the evaluation of the friction coefficient at high temperatures.

a) b)

Figure 2-19 – Slanted test: a) Schematics; b) Specimens tested at 1080 ºC. Reprinted from (Brulin *et al*, 2020)

2.3 Refractory masonry behaviour

Several studies have been conducted on the behaviour of ordinary masonry at elevated temperatures (Byrne, 1979; Lawrence and Gnanakrishnan, 1987; Shields, 1988; O'Meagher, 1991; Dhanasekar *et al*, 1994; Nadjai *et al*, 2003; Nadjai *et al*, 2003; Al Nahhas *et al*, 2007; Nguyen and Meftah, 2012; Nguyen and Meftah, 2014; Andreini *et al*, 2015; Kumar and Kodur, 2017; Lopes, 2017; Lopes *et al*, 2017). Nevertheless, few researches were published on the behaviour of refractory masonries. This section presents and summarizes the most important studies used in the development of this thesis.

2.3.1 Experimental investigations

Prietl (Prietl, 2006) developed a dedicated device to test refractory masonry under biaxial compression. This experimental setup was developed at RHI company and was designed to test refractory wallets from ambient temperature up to 1200ºC (**Figure 2-20**a). A reaction frame was used to fix two hydraulic jacks in perpendicular positions. The bottom of the press was coated by refractory materials (**Figure 2-20**b). The plungers were lined with creep resistant refractory bricks. The specimen as was placed on the test field (**Figure 2-20**c) and corundum tubes connected to LVDTs were used to measure the displacements in the wall (**Figure 2-20**d). The LVDTs system was composed by two concentric tubes made out of corundum, which allowed the measurements of relative displacements in the test field.

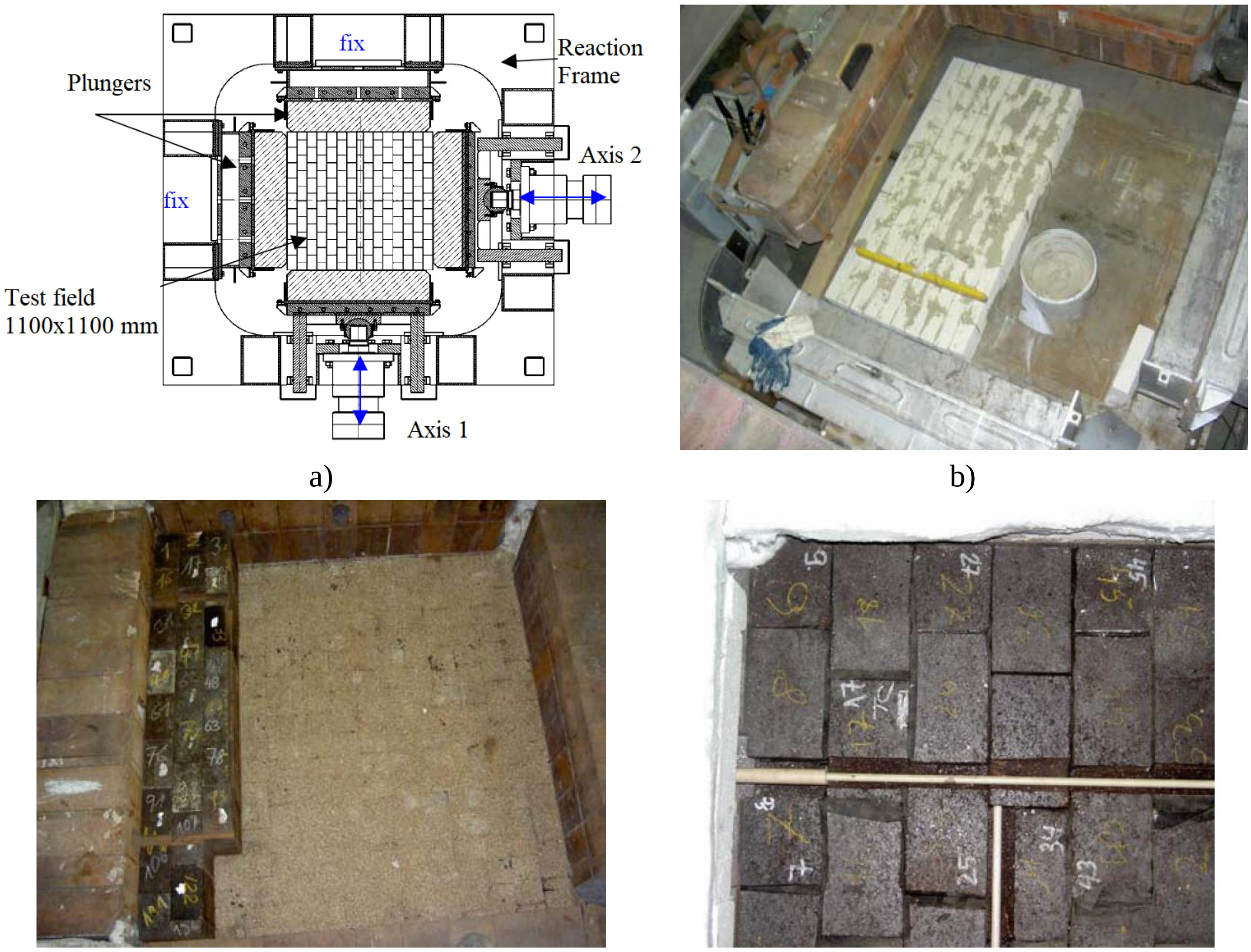

a) b)

c) d)

Figure 2-20 – Experimental setup: a) Schematic; b) Details of insulation; c) Specimen construction; d) Details of Instrumentation. Reprinted from (Prietl, 2006)

A heating hood was used in the tests performed at high temperatures (**Figure 2-21**a). The hood was designed to withstand up to 1400ºC, thus it was built by a 8 mm steel shell and a 200 mm thick ceramic wool lining was used for thermal insulation. A gas burner was used to heat the specimen (**Figure 2-21**b). The experimental setup used by Prietl (2006) was enhanced and improved in the scope of this doctoral research, as detailed in Chapter 5.

The author has carried-out biaxial compressive tests at ambient temperature, 600ºC and 1200ºC in dry-stacked refractory wallets composed by magnesia-chrome bricks. The displacements were measured using LVDT´s connected to the specimen by corundum tubes (**Figure 2-20**d) and the applied loads were measured by pressure gauges installed on the hydraulic jacks. The results of the experiments performed at ambient and high temperatures are shown in **Figure 2-22** and **Figure 2-23**, respectively.

a) b)

Figure 2-21 – Biaxial press: a) Experimental setup; b) Gas burner (Prietl, 2006)

A small scattering was observed in the experimental results at ambient temperature, as expected for dry-stacked masonry. It is possible to observe an increasing of the stiffness of the wall in both directions for the second load cycle (E_{K1}) when compared to the first loading cycle (E_{K0}). It is caused by the crushing of initially non-plane surfaces of the bricks, increasing the contact area between the bricks. The strains in the direction of the bed joints are higher than the strains in the direction of the head joints. This is caused not only by the number of joints in each direction, but also by the different behaviour of bed and head joints, as discussed in 3.2.8.

Comparing the results of the tests performed at 600ºC with the ones at ambient temperature, it is possible to identify a similar behaviour. At this temperature, the mechanical properties of the material are not significantly reduced. Due to the temperature range of the tests, it was not possible to identify viscoplastic strains in the test results.

The result of the test performed at 1200 ºC is very interesting. The viscoplastic strains caused by creep are clearly observed. The residual strains after the first load cycle is significantly higher than the strains obtained at ambient temperature and 600ºC due to the viscoplastic stains.

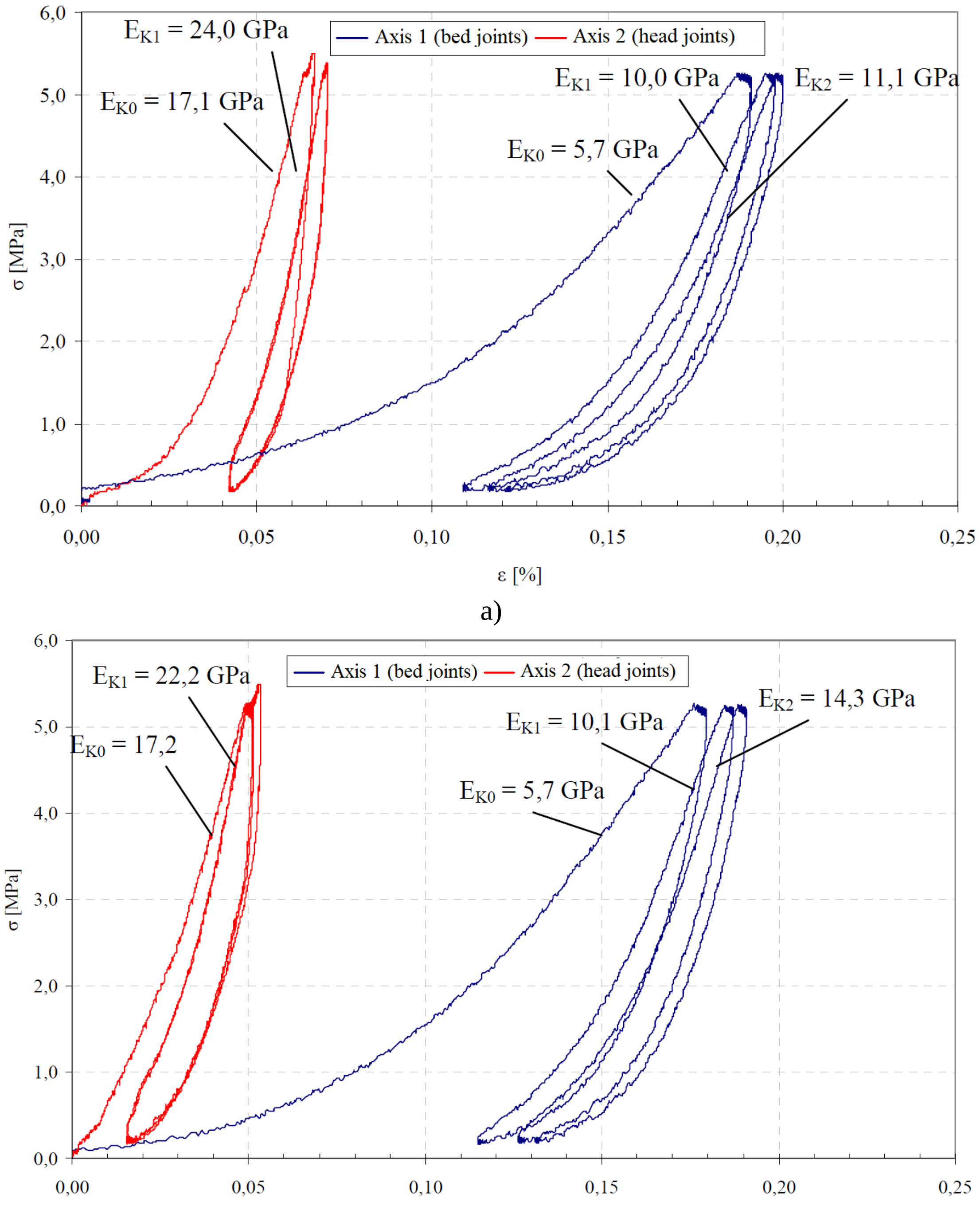

a)

b)

Figure 2-22 – Experimental results at ambient temperature: a) test #1; b) test #2. Adapted from (Prietl, 2006)

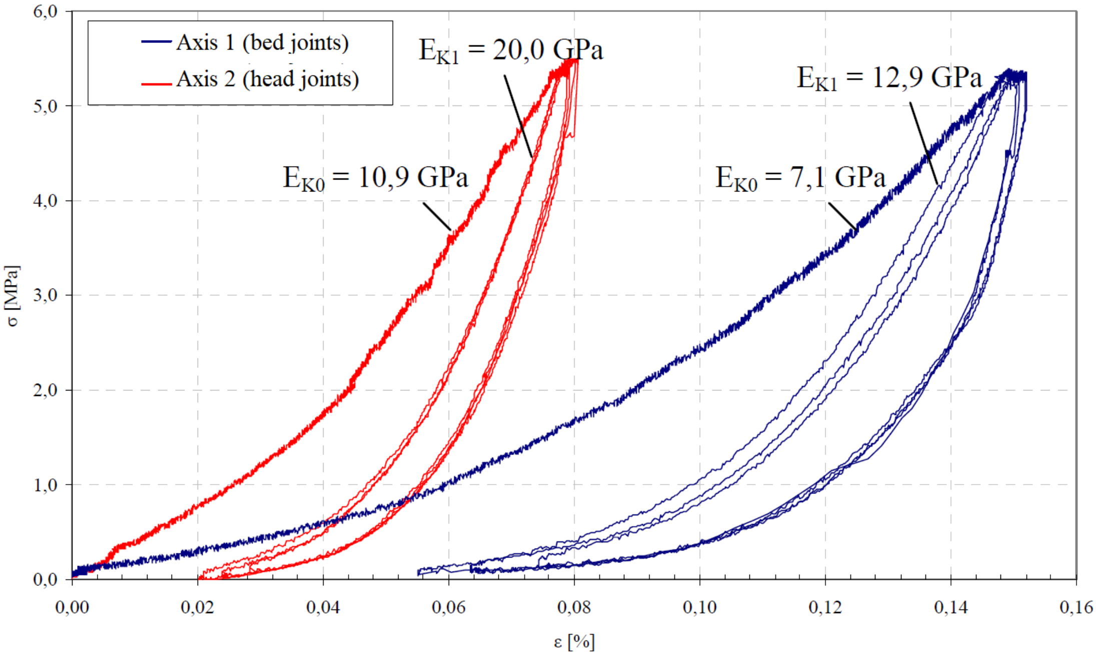

a)

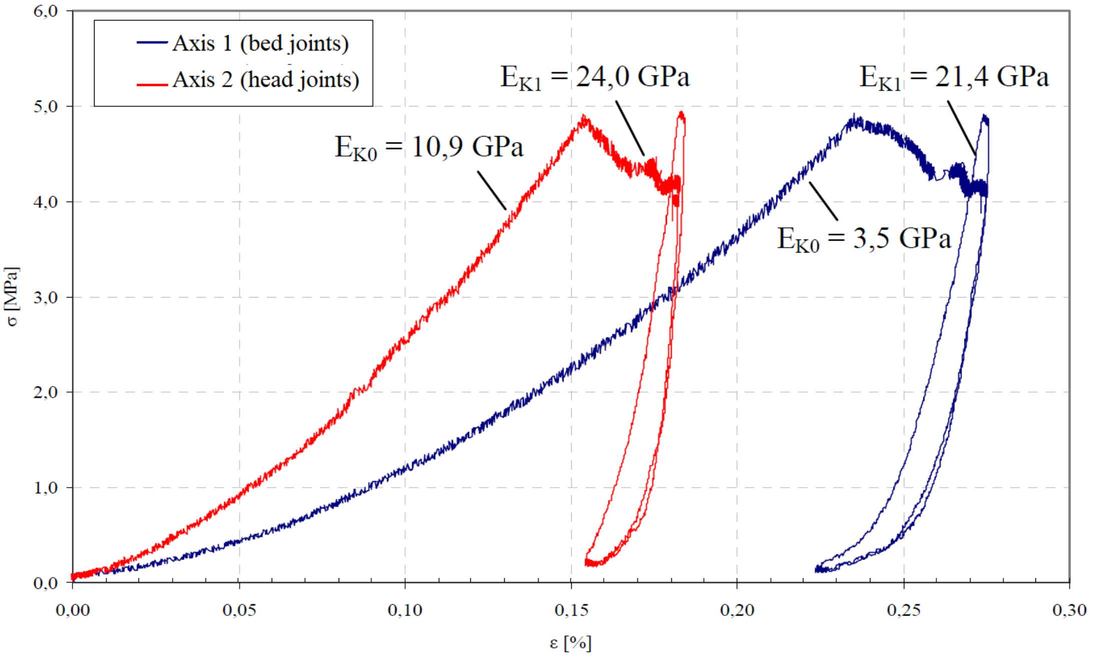

b)

Figure 2-23 – Experimental results at high temperatures: a) 600ºC; b) 1200ºC. Adapted from (Prietl, 2006)

2.3.2 Numerical investigations

Gasser *et al* (2004). proposed a homogenization technique for refractory dry-stacked masonry based on the experimental results presented in the previous section. In the homogenization technique the masonry is replaced by an equivalent material that has the same behaviour as masonry. The representative elementary cell (REC) is used to obtained the homogenized equivalent properties, as shown in **Figure 2-24**. The REC is a part of the masonry that represents the periodicity of the structures and has no joints on its edges. The equivalent material was considered orthotropic, elastic and non-linear and depending on joint opening or closure. Their properties were defined by an inverse method, from different loads simulated on a component model, composed by bricks and joints. The model proposed by the authors was validated based on thermomechanical tests performed in a real structure (Themines, 1994).

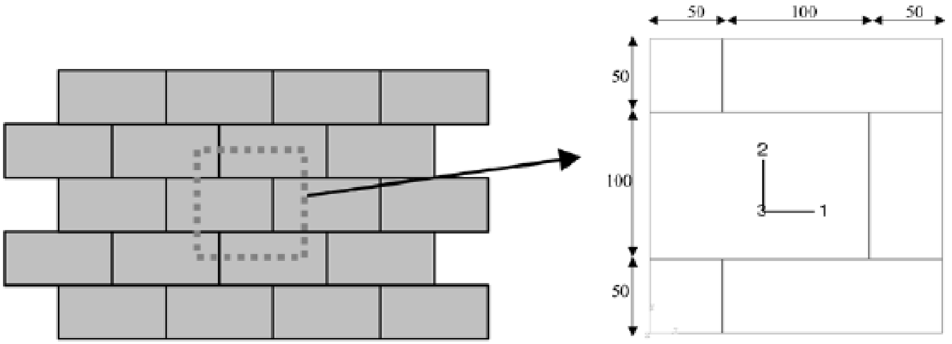

Figure 2-24 – Representative elementary cell. Reprinted from (Gasser *et al*, 2004)

Nguyen *et al* (2009) extended the research performed by (Gasser *et al*, 2004) studying the mechanical homogenization of a mortarless masonry wall. The use of equivalent materials instead of a model with all bricks and joints is necessary when dealing with large-sized masonry structures. The properties of the equivalent material depend on the bricks' material and on the opening and closure mechanism of the joints. The authors have identified four joint states corresponding to the combination of open/closed states of bed and head joints, which are:

a) joints are open in two directions: the structure is totally discrete (Figure 2-25a);

b) joints are closed in two directions: the structure is fully homogeneous (Figure 2-25b);

c) head joints are open and bed joints are closed: the structure is a media containing distributed cracks (Figure 2-25c);

d) head joints are closed, and bed joints are open: the structure is an array of separated bands. (Figure 2-25d)).

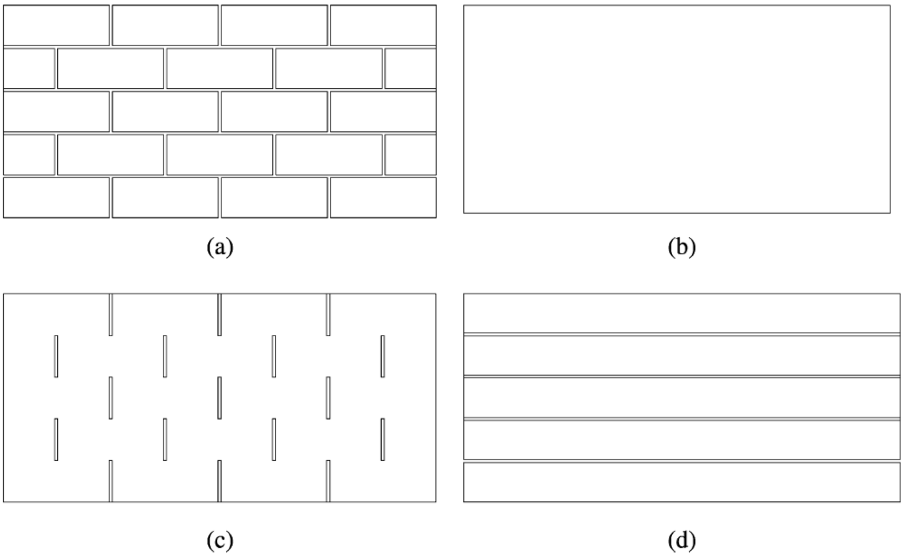

Figure 2-25 – Four periodical structures corresponding to four joint states. Reprinted from (Nguyen *et al*, 2009)

The numerical predictions were validated against the experimental results provided by Prietl (2006). A good correlation was obtained as shown in **Figure 2-26**. The use of homogenization techniques rather than the micro-modelling technique reduces the computation requirements for the analysis without compromising the accuracy of the results. Recent improvements were done in homogenized models to account viscoplastic strains (Rekik, *et al* 2015; Rekik *et al*, 2016; Rekik and Gasser, 2016; Ali *et al*, 2021). Therefore, the use of homogenization techniques is a good approach when dealing with large masonry structures, such as the industrial vessels.

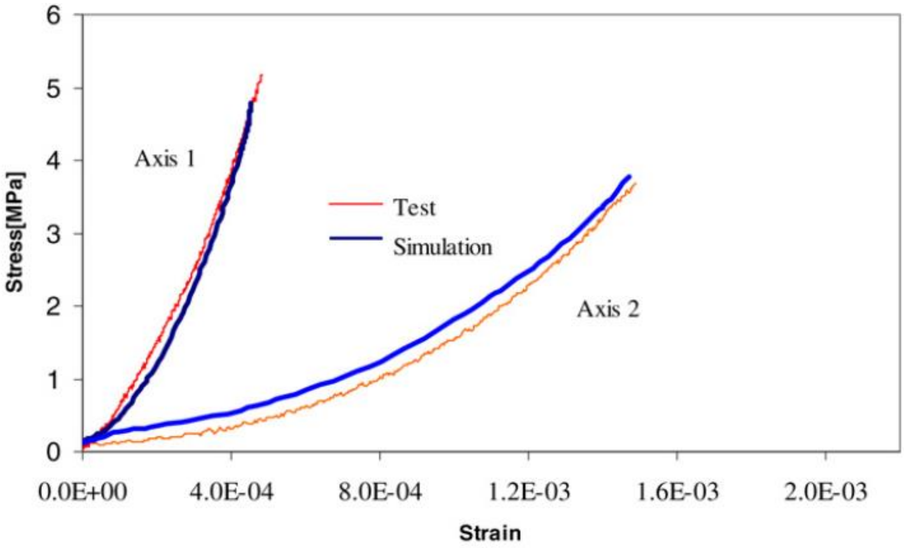

Figure 2-26 – Validation of the numerical results. Reprinted from (Nguyen *et al*, 2009)

2.4 The simulation of refractory linings and industrial vessels

Xia and Ahokainen (2001) developed a numerical model to analyse the transient heat transfer of a steel ladle in the course of the holding period. The refractory layers (working, safety and insulation) and the steel shell were bi-dimensionally modelled (**Figure 2-27**a). The heat losses in the steel shell, in the molten steel and in the exposed faces of the refractory layers was considered (**Figure 2-27**b). The numerical predictions were validated against the temperatures measured in a pilot ladle. The study was focused only in the heat transfer analysis; the mechanical behaviour of the steel ladle was not considered.

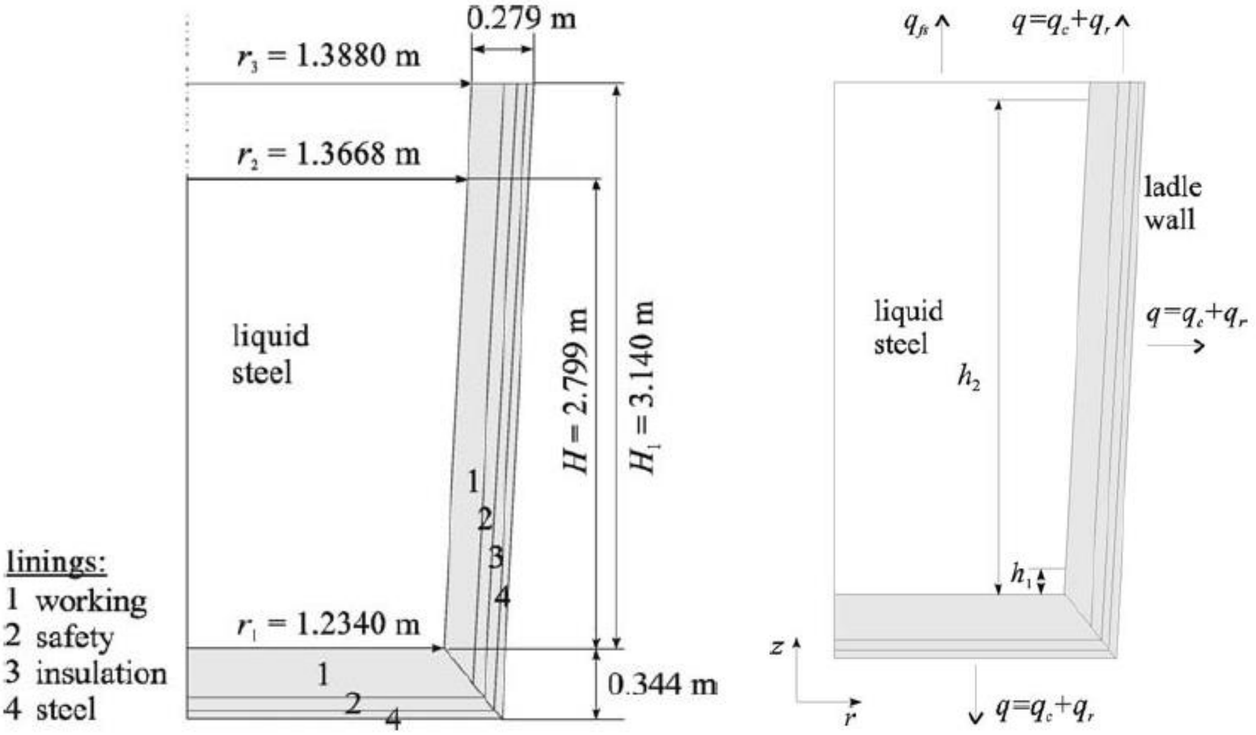

a) b)

Figure 2-27 – Schematics: a) Physical ladle; b) Numerical model. Adapted from (Xia and Ahokainen, 2001)

Glaser *et al* (2011) carried out a study similar to the one performed by (Xia and Ahokainen, 2001) to analyse the fluid flow and the heat transfer in a steel ladle. The authors also have used a two dimensional model to predict the temperature fields in the molten steel and in the components of the steel ladle (**Figure 2-28**). The model was validated against industrial measurements using infrared cameras. The authors highlighted that the insulation layer plays the major role limiting the heat losses.

Only the thermal fields were being analysed in this study, the mechanical behaviour of the steel ladle components was not analysed.

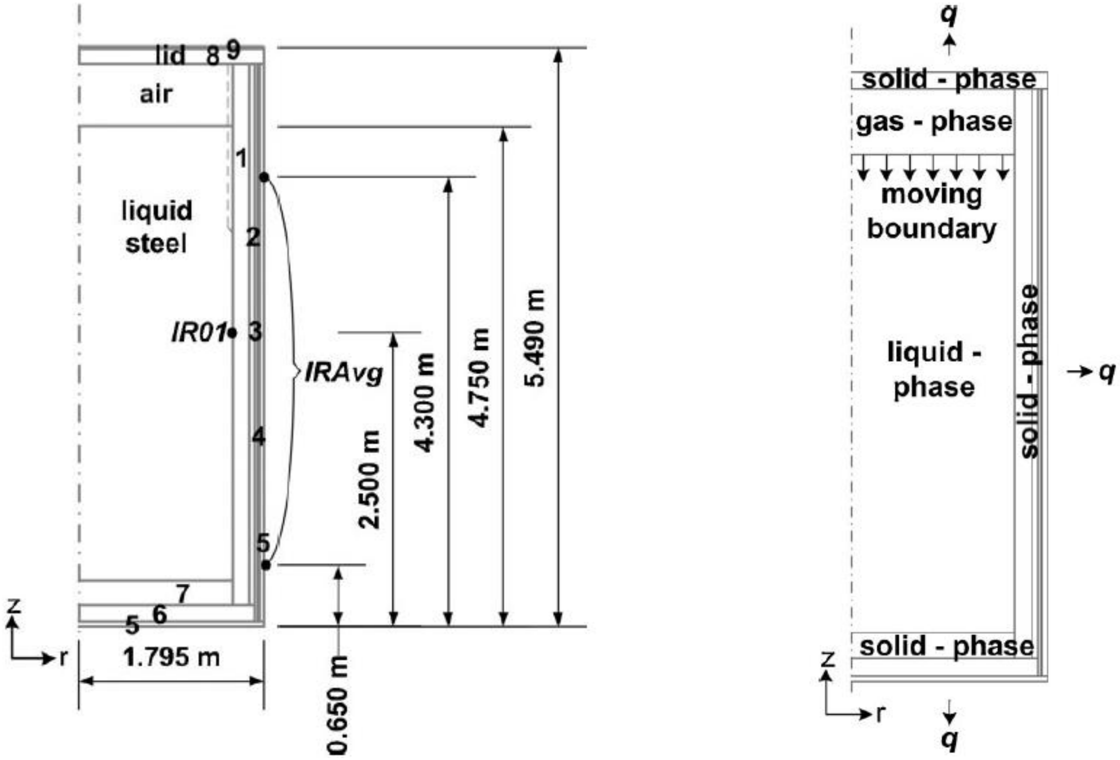

a) b)

Figure 2-28 – Schematics: a) Physical ladle; b) Numerical model. Adapted from (Glaser *et al,* 2011)

Although innovative results were presented by (Xia and Ahokainen, 2001; Glaser *et al,* 2011), the mechanical simulation of the vessel was not performed. In service, the refractory linings are prone to creep, corrosion, abrasion and fracture. The restrained elongation results in elevated compression stresses in the linings and tensile stresses in the steel shell. The accurate prediction of the strain and stresses are crucial for the correct design of the equipment.

Yilmaz (2013) extended the previous studies (Xia and Ahokainen, 2001; Glaser *et al,* 2011) incorporating the analysis of the mechanical fields on the numerical models. The authors have used a two-dimensional axisymmetric model. The simulation was carried-out using a sequentially coupled heat transfer-structural analysis. The geometry of the steel ladle was composed by a wear lining with different thickness at the barrel and at the slag line, one safety lining, one insulating lining and one steel shell. The mechanical boundary condition considered the ladle lifted by a crane, as usual in the steelmaking process. Temperature-dependent mechanical and thermal properties were considered for the materials. The displacement fields were calculated; the author have identified the biggest displacement in the bottom of the steel ladle, caused by the weight of the molten steel and the refractory lining.

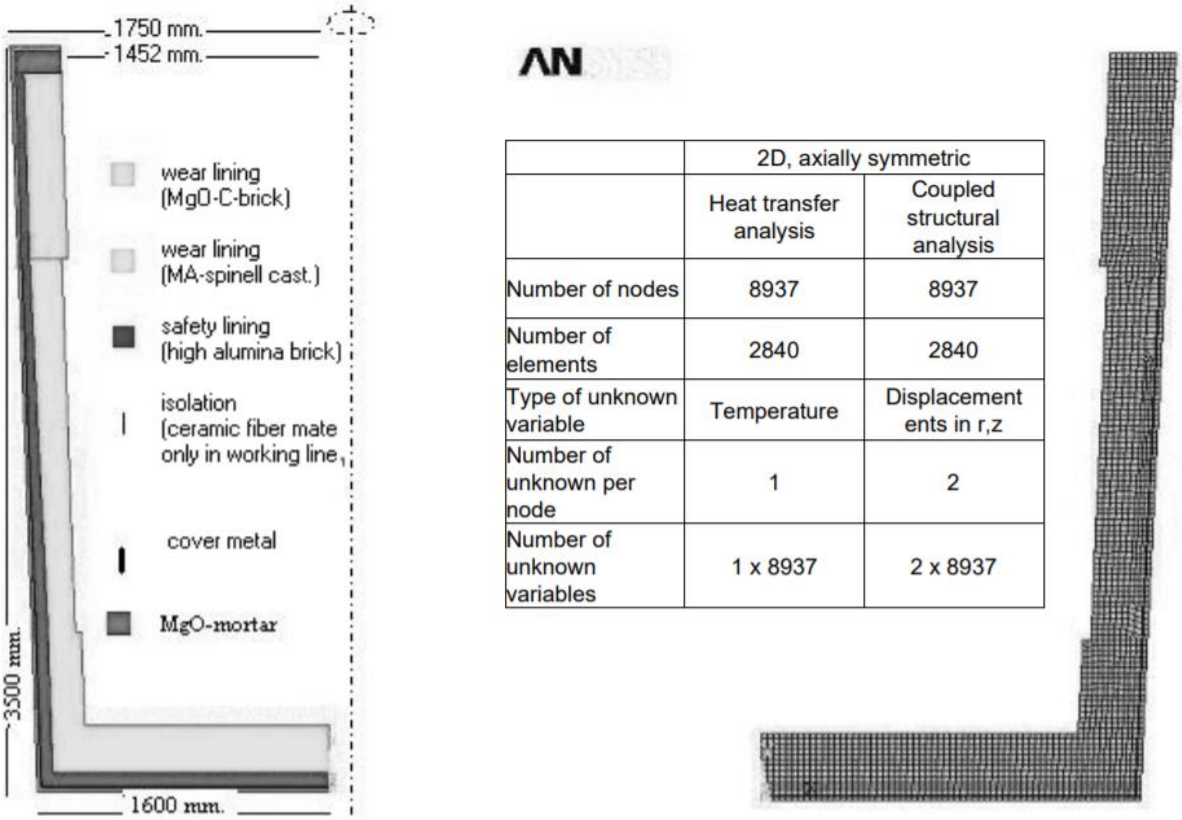

	2D, axially symmetric	
	Heat transfer analysis	Coupled structural analysis
Number of nodes	8937	8937
Number of elements	2840	2840
Type of unknown variable	Temperature	Displacement ents in r,z
Number of unknown per node	1	2
Number of unknown variables	1 x 8937	2 x 8937

a) b)

Figure 2-29 – Schematics: a) Physical ladle; b) Numerical model. Adapted from (Yilmaz, 2013)

The model presented by the author was innovative, nevertheless, it did not take into account the transient heat flow of the process, as a steady-state analysis was performed to identify the temperature fields. Additionally, the author did not consider the viscoplastic strains in the refractory linings caused by relaxation.

Gasser *et al* (2013) used the homogenization techniques previously developed in (Gasser *et al*, 2004; Nguyen *et al* 2009) to evaluate the influence of different masonry designs of the bottom of the linings (**Figure 2-30**a). The homogenization techniques reduces significantly the computational effort required to run the simulations, thus, it is possible to use more detailed three-dimensional models in the numerical simulations (**Figure 2-30**b). Different masonry designs may be used in the bottom of the steel ladle, the most used are the parallel, fish bone and radial. The authors aimed to benchmark the performance of these designs in terms of stress level and displacement in the steel shell. Therefore, homogenized models of steel ladles with different bottom designs were developed. The thermomechanical properties of the materials were taken as temperature dependent. The authors have also evaluated the influence of the presence of the joints and the influence of the joint thickness. It was observed that the presence of joints reduces significantly the stresses generated in the steel shell, moreover, it was noticed that the radial design led to the smallest stress amplitudes in the steel shell (**Figure 2-30**c).

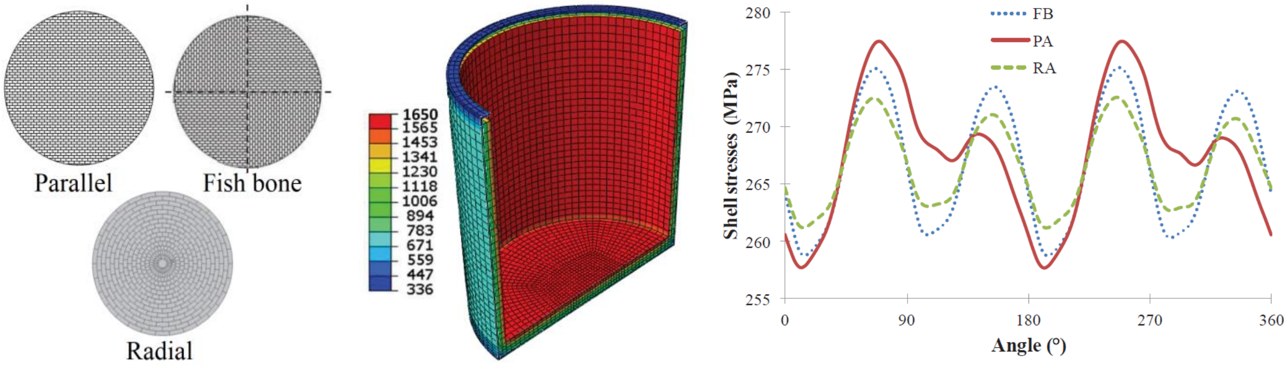

a) b) c)

Figure 2-30 – Influence of different masonry bottom designs.: a) Designs; b) Thermal fields; c) Stresses in the steel shell along its circumference: parallel (PA), fish bone (FB) and radial (RA). Adapted from (Gasser *et al*, 2013)

The results provided by the authors have proved the applicability of homogenization techniques in the design of steel vessels, replacing the very computational onerous micro-modelling strategy. However, the authors have not taken into account the viscoplastic strains in the refractory linings.

Jin *et al* (2016) used a different approach to simulate and optimize a Ruhrstahl Heraeus snorkel (**Figure 2-31**a). Instead of using two-dimensional models or homogenization techniques, the authors have modelled a three-dimensional slice of the equipment (**Figure 2-31**b). The goal of the study was to investigate the thermomechanical failure mechanics of the lining. To authors have included visco-plasticity into the model: the Drucker-Prager´s constitutive model, the Drucker-Prager´s creep model and fictitious crack models were considered to simulate creep and failure. The material properties were obtained experimentally in wedge split tests, modified shear tests and compressive creep tests carried-out at ambient and high temperatures. The numerical results allowed to identify tensile failures in the hot face of the lower refractory lining prior to shear or creep failures. The wear lining did not experience shear failure due to the viscous strains caused by creep. The authors evidenced that the joint normal behaviour (joint opening) is affected by shear failure and creep. Additionally, it was proved that the use less brittle refractories can mitigate the hot thermal shock.

The slice modelling approach used by Jin *et al* (2016) overcomes the requirements of large computational resource of the micro-modelling techniques. Additionally, it is an alternative to the use of homogenization techniques. The drawback of this solution is that it is only applicable for axisymmetric structures. Furthermore, the thickness of the slice shall be big enough to account the head joints, in case of linings composed by dry-stacked masonry.

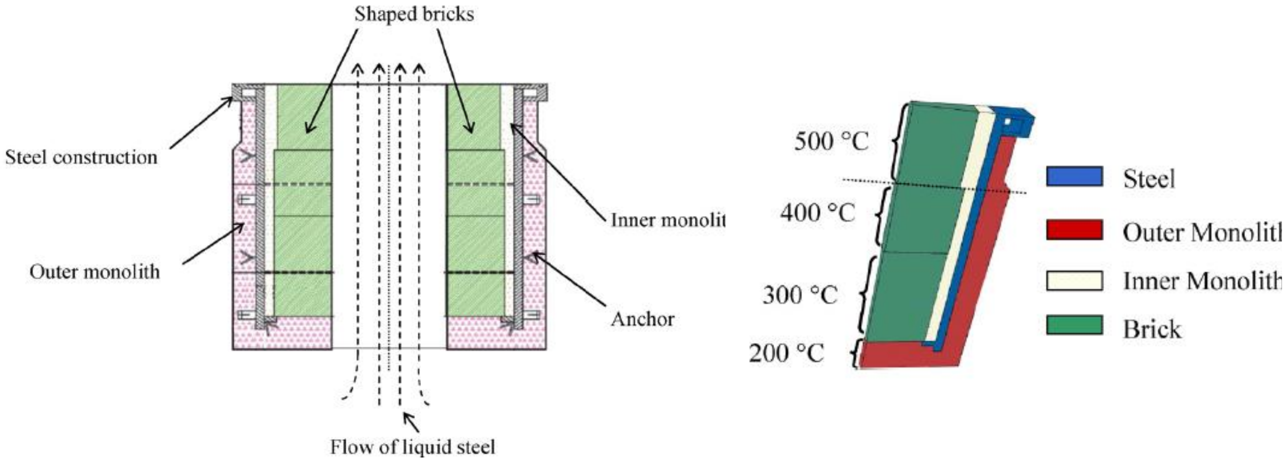

a) b)

Figure 2-31 – Schematics: a) Physical snorkel; b) Numerical model. Adapted from (Jin *et al*, 2016)

The energy efficiency of steelmaking factories is deeply dependent on the thermal insulation properties of the refractory linings. Santos *et al* (2018) carried-out transient heat transfer simulations to evaluate the thermal losses in different design of steel ladles, four configurations were tested. The authors have evaluated the average heat flux in the hot face of the working lining during the holding stage to calculate the energy losses and the lining efficiency. A two-dimensional model was used, as done by (Yilmaz, 2013; Glaser *et al*, 2011). The materials thermal and mechanical properties were taken as temperature dependent. The authors simulated six operational cycles, including the pre-heating of the first cycle.

The research only simulated the heat transfer problem in the steel ladle, the mechanical analysis was not considered. Nevertheless, the numerical results highlight the applicability of the FEM simulations to optimize the design of refractory vessels in terms of energy efficiency.

Hou *et al* (2018) carried-out numerical simulations to optimize the design of a steel ladle in terms of energy efficiency and mechanical behaviour. The Taguchi method was used combined to the finite element models. The authors have used the slice modelling approach, as done by (Jin *et al*, 2016), the reference and optimized steel ladles are shown in **Figure 2-33**. The authors have found two optimized lining concepts with commercially available materials. These concepts have shown a significant increasing in the thermal efficiency of the vessels and reductions in the stresses developed in the working lining.

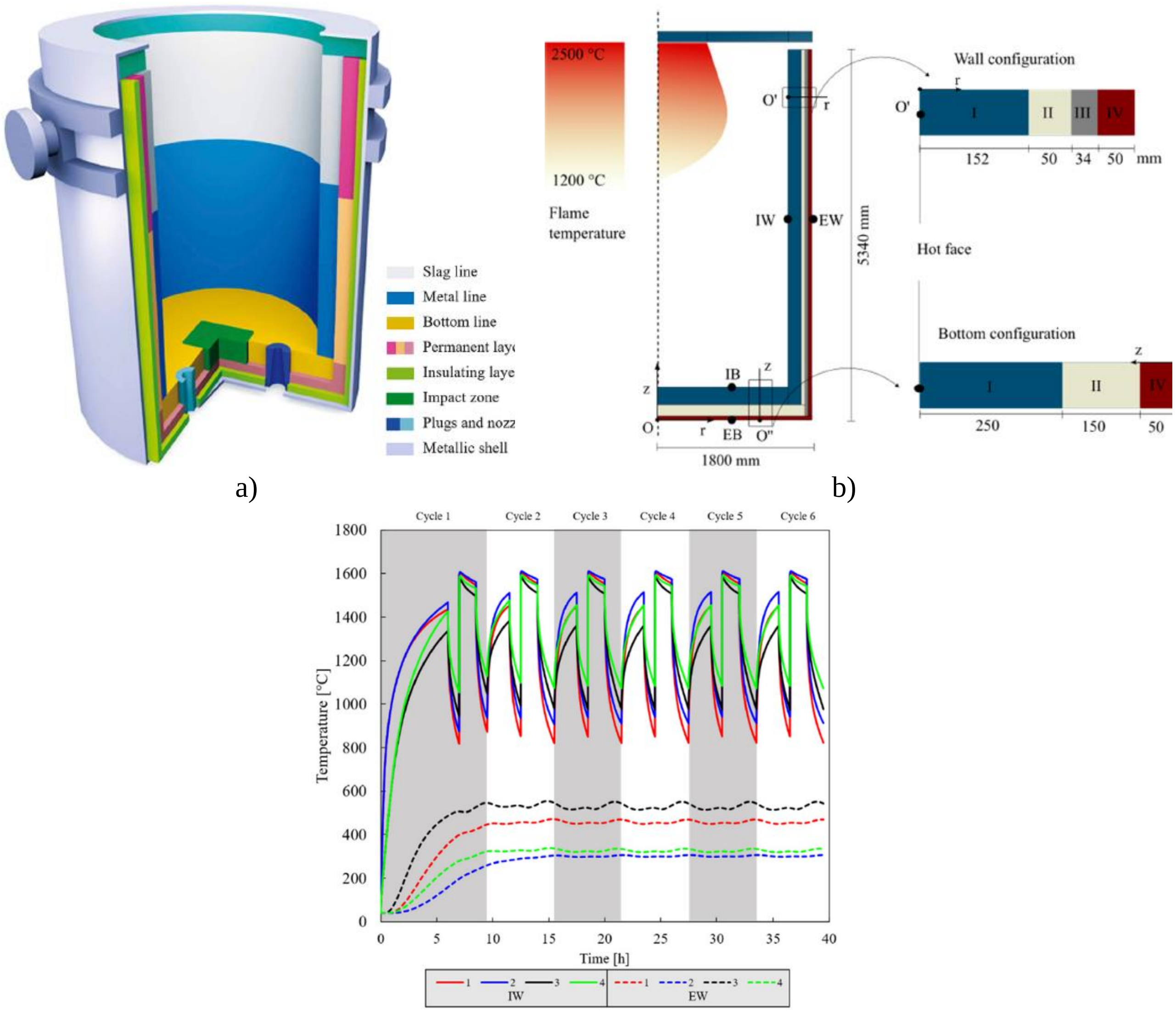

a)

b)

c)

Figure 2-32 – Schematics: a) Physical ladle; b) Numerical model. c) Temperatures in the internal (IW) and external (EW) walls Adapted from (Santos *et al*, 2018)

Ali (2020) have improved the homogenization models previously presented (Gasser *et al*, 2004; Nguyen *et al*, 2009; Gasser *et al*, 2013). The developed constitutive model was validated against experimental results (Prietl, 2006), a good agreement was observed. The homogenization technique developed was used to simulate the transient thermomechanical behaviour of an steel ladle (Figure

2-34a). Three cycles operational cycles were simulated, the predicted temperatures are shown in Figure 2-34b.

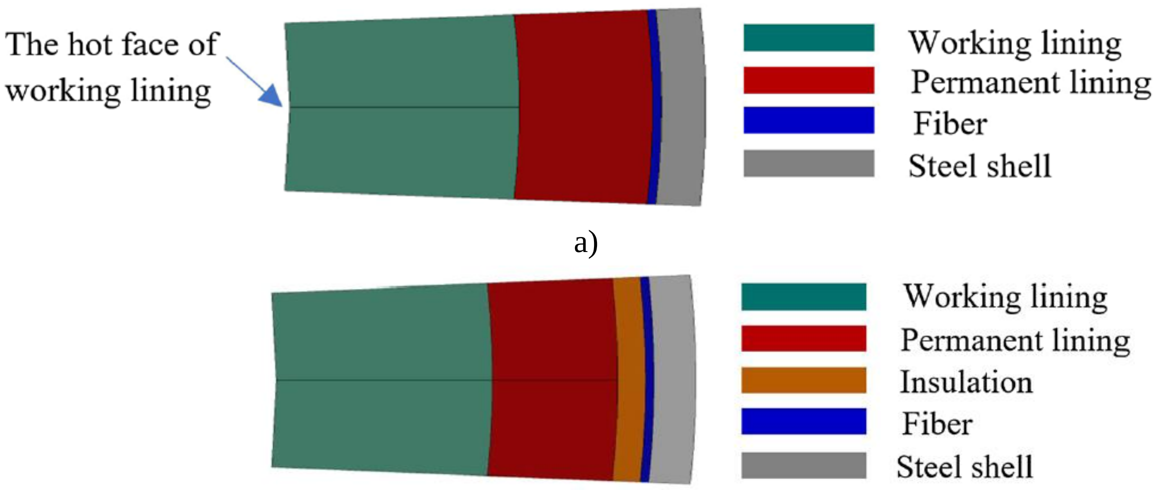

a)

b)

Figure 2-33 – Two dimensional models: a) Refence steel ladle; b) Optimized steel ladle. Adapted from (Hou *et al*, 2018)

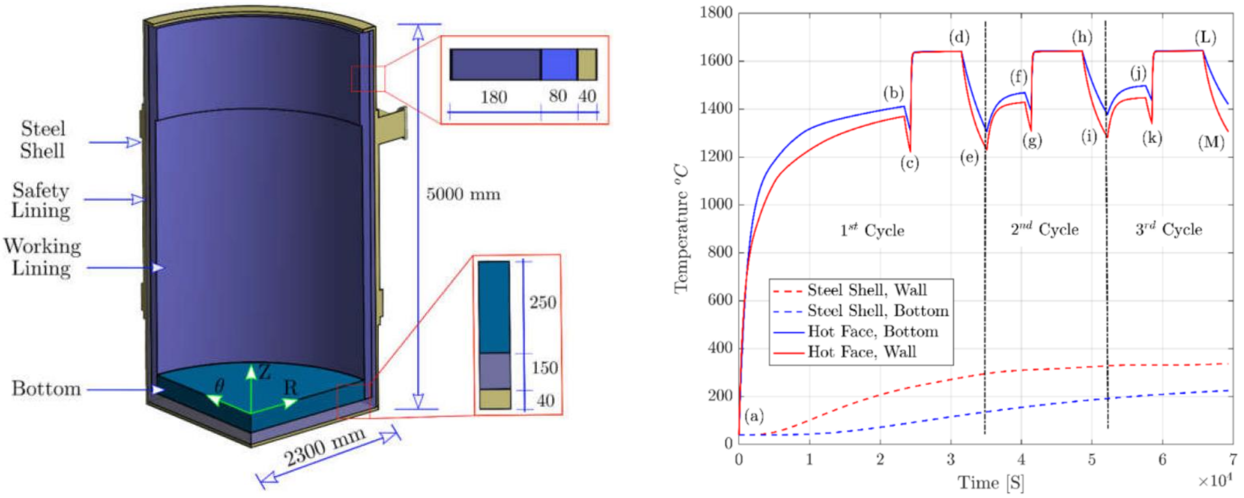

a) b)

Figure 2-34 – Simulated steel ladle: a) Schematics; b) Temperature fields. Adapted from (Ali *et al*, 2020)

The authors have performed a parametric study to analyse the impact of joint presences and joint thickness in the overall behaviour of the ladle. An isotropic model (without joints) and models with different joint thickness (0.1 mm, 0.3 mm and 0.5 mm) were studied. The predicted stresses in the bottom and in the wall surface are shown in **Figure 2-35** and **Figure 2-36**. The numerical predictions shown an orthotropic and nonlinear thermomechanical behaviour. The stresses originated from the restrained thermal elongation of the refractory lining decrease with the increase in the joint thickness.

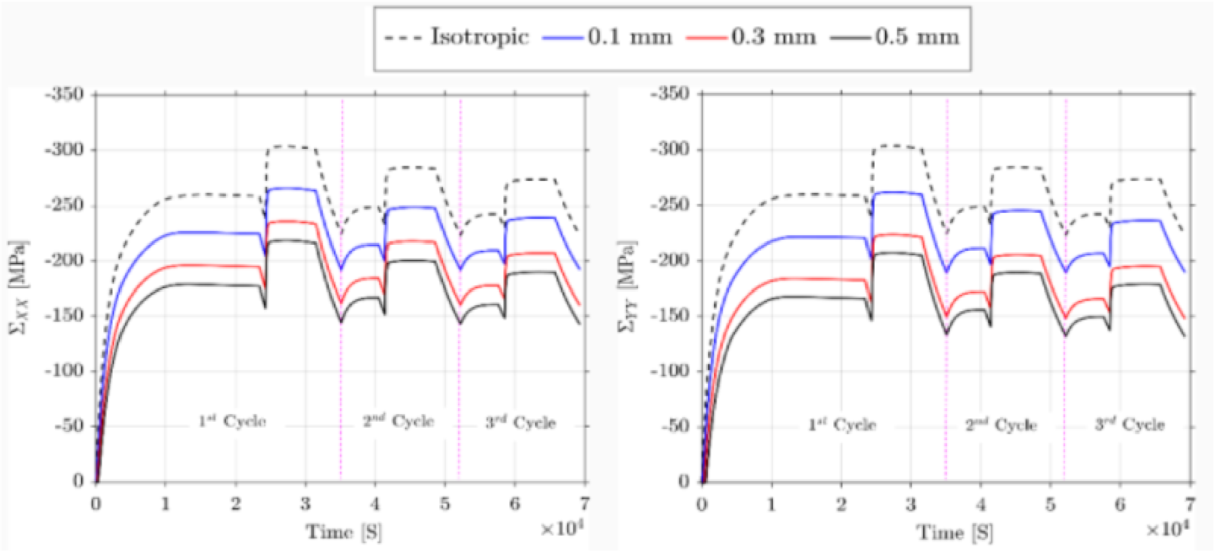

a) b)

Figure 2-35 – Predicted stresses at the bottom surface: a) direction X; b) direction Y (Ali *et al*, 2020)

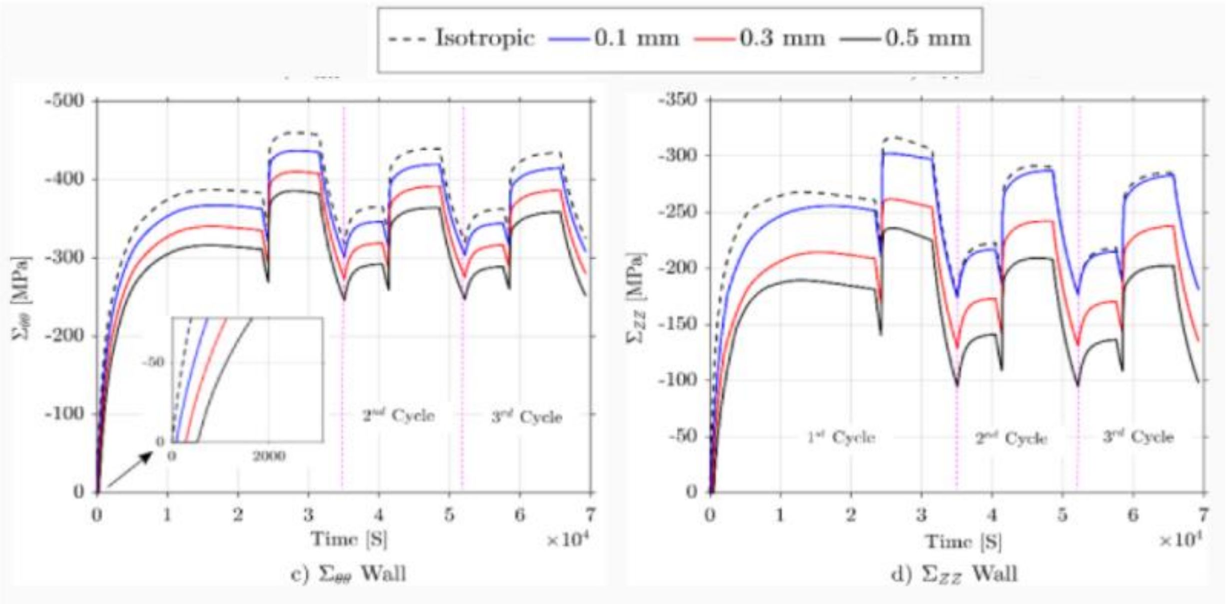

a) b)

Figure 2-36 – Predicted stresses at the wall surface: a) direction X; b) direction Y (Ali *et al*, 2020)

The authors did not consider the viscoplastic strains in the working lining, consequently the stresses predicted in the refractory masonry was significantly higher than the ones expected in the refractory linings. Nevertheless, the developed numerical model allowed the study of the overall behaviour of the steel ladle, including the refractory layers and the steel shell.

The studies presented in this sub-section (Xia and Ahokainen, 2001; Glaser *et al,* 2011; Yilmaz, 2013; Gasser *et al,* 2013; Jin *et al,* 2016; Santos *et al,* 2018; Hou *et al,* 2018; Ali *et al,* 2020) highlighted the development and the enhancement of the numerical models used to represent the industrial vessels over the recent years. The models raised from simplified two-dimensional steady-state models to advanced three-dimensional transient model that comprises the heat transfer and the mechanical analysis. However, there is still room for improvements, the development of further experimental campaigns would generate valuable data for the development, calibration and validation of novel advanced numerical models.

2.5 Final remarks

In spite of the economic importance of refractory ceramics, few researches have been conducted on the behaviour of dry-stacked refractory masonry. The joints in dry-stacked masonry play an important role reducing the compressive stresses generated in the linings by their restrained thermal elongation. Interesting researches have been performed on the normal behaviour of dry joints and its influence on the walls behaviour (Gasser *et al,* 2004; Thanoon *et al,* 2008; Andreev *et al,* 2012; Allaoui *et al,* 2018; Zahra and Dhanasekar, 2018; Ngapeya *et al,* 2018). The tangential behaviour of the joints has been studied for mortared masonry at ambient and high temperatures (Brulin *et al,* 2020), however, the tangential behaviour of dry-stacked joints have been studied only at ambient temperature (Gasser *et al,* 2004) (Nguyen *et al,* 2009). Thus, there is a lack of knowledge on the behaviour of dry joints.

There is only one significant experimental study on the behaviour of dry-stacked refractory masonry taking into account the structure effect. Prietl (Prietl, 2006) had developed a specific device to test refractory wallets at ambient and high temperature under biaxial compression. The press is composed by a steel frame in which hydraulic jacks are connected. Refractory lined plungers are used to support and to load the specimen. The specimen is placed inside the test field, the instrumentation is installed and a gas burner was used to heat the system. The experimental developed by the author was able to test refractory masonries (mortared and dry-stacked) in temperatures up to 1200 ºC. This temperature is still far from the service conditions, however, the experimental results provided by the author have been used by many authors to develop and validated numerical simulations (Nguyen *et al,* 2009; Gasser *et al,* 2013; Ali *et al,* 2020; Ali *et al,* 2021). This experimental setup was improved and used in the experimental campaign of this doctoral thesis, as presented in Chapter 5.

Significant developments have been observed in the numerical simulations of refractory vessels. The models evolved from simplified two-dimensional simulations (Xia and Ahokainen, 2001; Glaser *et al,* 2011; Yilmaz, 2013) to advanced three-dimensional models able to represent the heat transfer and the mechanical nature of the problems with a non-linearities involved, including temperature-dependent parameters, visco-plastic effects and material and geometry non-linearities (Gasser *et al,* 2013; Jin *et al,* 2016; Santos *et al,* 2018; Ali *et al,* 2020). However, experimental tests in conditions similar to the service ones are required for the validation of these numerical models and for the development of new techniques.

Therefore, the performed literature review allowed to identify the lacks on the knowledge of refractory masonries used in the linings of industrial vessels. The presented researches are being used as background to this doctoral thesis.

3 CHARACTERIZATION OF ALUMINA BRICKS AND MASONRY DRY JOINTS

Dry-stacked refractory masonry is composed of refractory units stacked on the top of each other. The absence of mortar influences the behaviour of the structure; as dry joints are created on the interfaces of the bricks. The bricks' geometric imperfections (such as non-parallelism, non-planarity and manufacturing tolerances) are the main contributors for the normal behaviour of the joint, while the bricks' surface roughness has a secondary role. The dry joints have a small thickness but they play a crucial role on reducing the stresses generated in the refractory linings, as they are able to reduce the stiffness of the lining and, consequently, they reduce significantly the stresses caused by the restrained thermal elongation (Allaoui *et al*, 2018; Gasser *et al*, 2004; Andreev *et al*, 2012; Ali *et al*, 2020). In dry-stacked masonry, two geometric imperfections are fundamental for its observed behaviour: the height imperfection between different bricks (ΔH) and the roughness of the bricks' surface (Δh) (Ngapeya *et al*, 2018; Zahra and Dhanasekar, 2018). Despite the importance of the dry joints in the performance of the refractory masonry linings, there is limited literature available on this topic. To tackle this gap in the literature, several experimental campaign were developed and are described in this chapter.

Moreover, the understanding of the joint's behaviour is necessary to properly interpret the experimental results obtained in the following sections (Chapter 4 and 5) as well as to develop the numerical models in Chapter 6. This chapter is the first phase of a large experimental program on the characterization of dry-stacked refractory masonry. A statistical study of the brick shape imperfections is presented in this section. The compressive strength of masonry units is characterized at ambient and high temperatures. The normal behaviour of joints is studied at ambient temperature, and the results of the classical joint closure test in two stacked is compared with the joint closure curves obtained in a wallet. Additionally, numerical simulations were performed to analyse the effects of the brick's height imperfection on the loadbearing capacity of a panel and its overall behaviour. The joints' tangential behaviour was experimentally studied at ambient and high temperatures, using an innovative test set-up.

3.1 Alumina bricks

The first aspect to be tackled is the characterization of the units: alumina bricks. The chemical composition of the bricks used in this research is presented in **Table 3-1**. The material is composed by tabular alumina grains (up to 3 mm) and an alumina spinel matrix. It was fully characterized within the scope of the ATHOR Project (Samadi *et al,* 2020; Teixeira *et al,* 2020; Oliveira *et al,* 2019; Kaczmarek *et al,* 2019; Samadi *et al,* 2020; Teixeira *et al,* 2019; Vitiello, 2021). The brick's density was 3.13 g/cm^3 and its apparent porosity measured according to EN 993-1 (2018) was 19%. The mechanical and thermal properties of the alumina spinel brick is presented in sections 2.1.1 and 2.1.2, respectively. The creep characterization of the material is given in section 2.1.3. Further characterization of bricks (compressive strength, anisotropic behaviour, bricks' shape imperfections) and the characterization of the joints performed within the scope of this doctoral is presented in this chapter.

Table 3-1 – Chemical composition of alumina-spinel bricks according to EN ISO 12677 (2014)

Al_2O_3	Fe_2O_3	SiO_2	MgO
94.0%	0.1%	0.3%	5.0%
Determination on fired substance (1025 ºC / 1877 ºF)			

The microstructure of the material obtained by SEM (Scanning Electron Microscope) is shown in **Figure 3-1** (Kaczmarek *et al*, 2019). The phase equilibrium diagram of MgO and Al_2O_3 is shown in **Figure 3-2**.

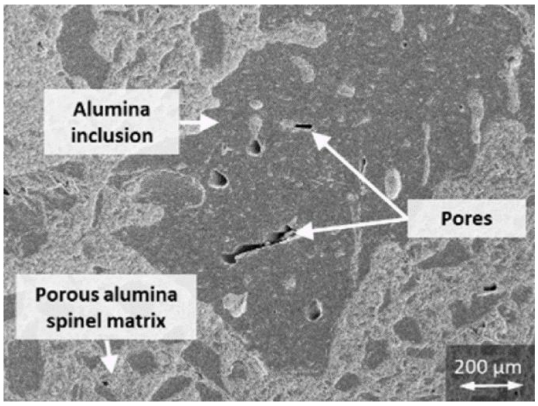

Figure 3-1 – Microstructure of the material. Reprinted from (Kaczmarek *et al*, 2019)

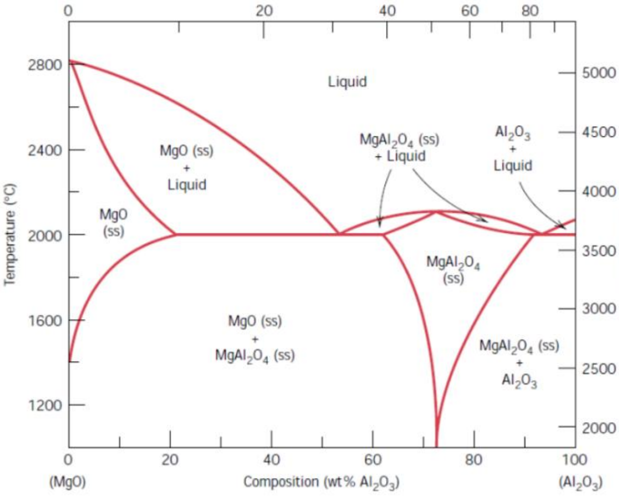

Figure 3-2 – Phase equilibrium diagram MgO – Al_2O_3. Reprinted from (Kaczmarek *et al*, 2019)

Three different bricks, using the same composition, produced for different industrial applications were used in this study (**Figure 3-3**). Brick *A* has an edged shape to fit the circular shape of industrial vessels, it is commercially produced and widely used in steel ladles. Bricks *B* and *C* have rectangular shape, being used in tunnel kilns (*e.g.* for ceramic or glass industries). Brick *C* was used to build the wallets for the compressive tests of masonry panels presented in Chapter 4 and 5.

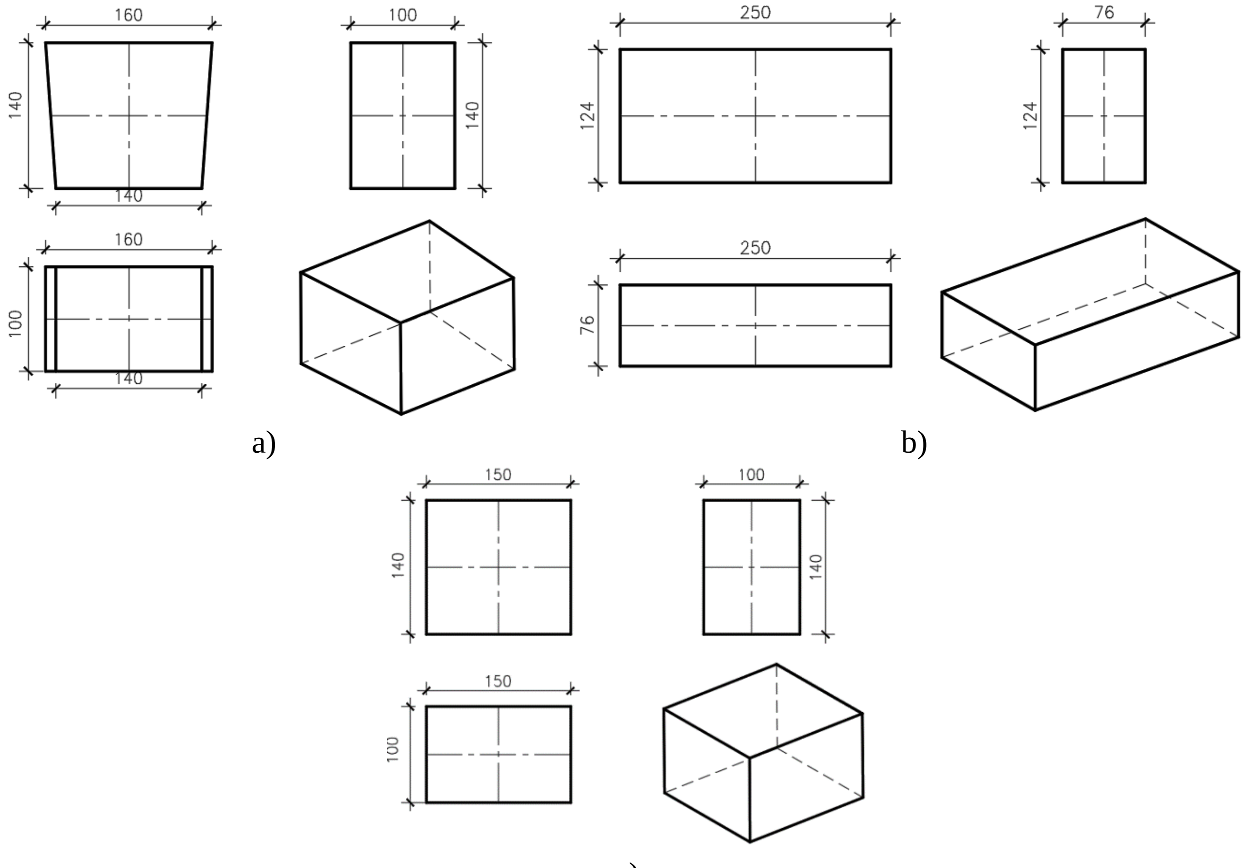

a)

b)

c)

Figure 3-3 – Brick shapes: a) Brick *A*; b) Brick *B*; c) Brick *C* [all measurements in mm]

3.1.1 Unit's shape imperfections

As reported in literature, the units' shape imperfections play the most important role in the dry joint behaviour (Allaoui *et al*, 2018; Gasser *et al*, 2004; Andreev *et al*, 2012; Ngapeya *et al*, 2018). Agaajani (2015) observed that bricks' dimension deviations follow a statistic distribution of a Gaussian curve.

The bricks' dimensions were evaluated for all directions of the brick *C* (Figure 3-3c). The bricks' dimensions were evaluated for all directions of the brick using a calliper rule. A total of fifty bricks were measured. Three measurements were performed for all directions and the mean value was taken.

The imperfections (defined by the differences between the measured and the prescribed dimension) are reported in Figure 3-4. In the directions perpendicular to the pressing during the shaping of the brick (directions X and Y), the imperfections vary from -1.1 mm up to +0.8 mm in good correlation with the fabrication tolerances indicated by the supplier (± 1.0 mm), with a small standard deviation (maximum is σ = 0.41 mm). In the direction of pressing (direction Z), the fabrication tolerances are higher (± 2.0 mm) and higher imperfections were observed, ranging from -2.4 mm up to +1.4 mm, with a higher standard deviation (σ = 0.84 mm). The deviations in the pressing direction are highly influenced by the procedure and by the amount of the material placed in the moulds.

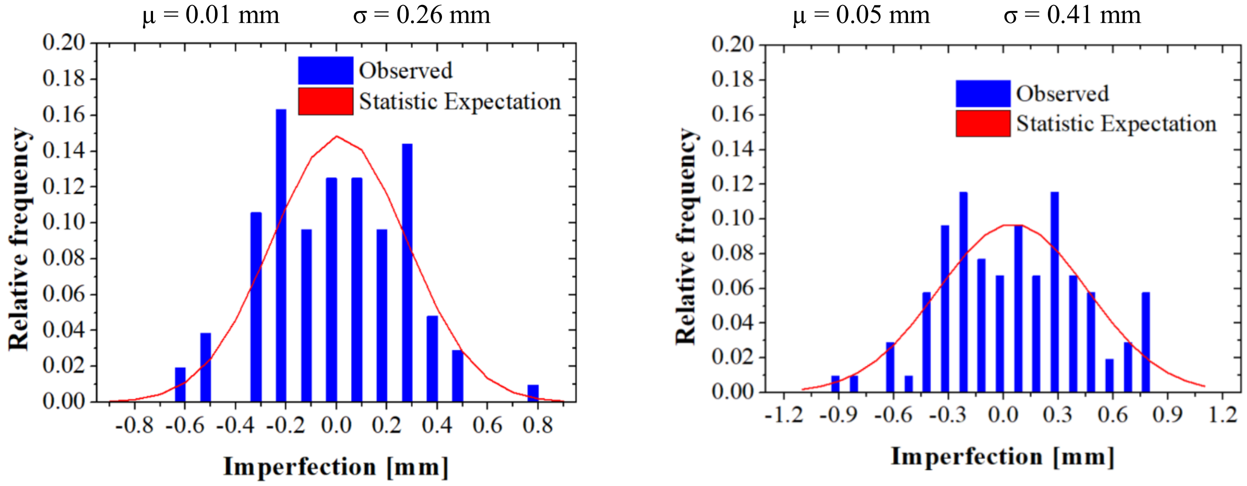

a) Perpendicular to pressing / Direction X (100 mm)

b) Perpendicular to pressing / Direction Y (140 mm)

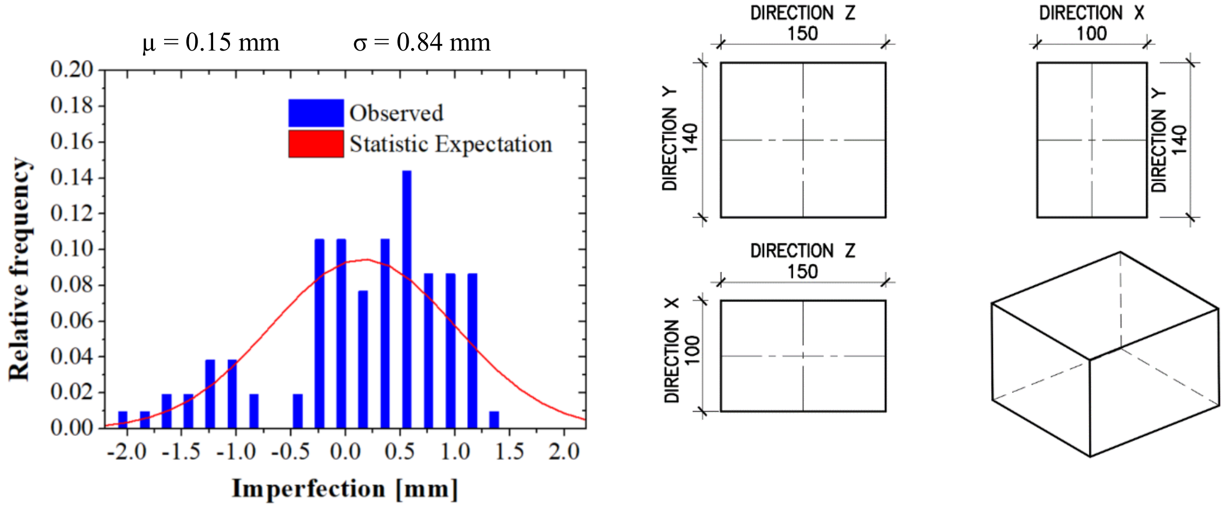

c) Parallel to pressing / Direction Z (150 mm)

d) Bricks prescribed dimension

Figure 3-4 – Brick shape imperfections for brick *C*: a) height; b) thickness; c) length (μ indicates the average of the deviation from the prescribed dimension and σ indicates the standard deviation of the deviation); d) Brick prescribed dimension

3.1.2 Compressive behaviour

Several compressive tests were carried out to determine the compressive strength of the material (f_c) at ambient and high temperatures (Table 3-2). Bricks *A* and *B* were used to extract the specimens for testing. The specimens were cylindrical and had 50 mm of diameter. The heights of the specimens are different, as a result of the different geometry of the bricks used to extract the specimens and their different extracting directions. The dimensions of the specimens were defined aiming to have the maximum height/diameter relation to be as closed as possible of the recommendations of RILEM (2001). Consequently, the specimens have different slenderness ratios (**Table 3-5**). The specimens were cored from the block units using a diamond drill. Afterwards, the specimens were cut to size using a diamond saw, grinded, and dried in an electric furnace at 105 ºC for 24 hours. The coring direction and the specimens' dimensions are detailed in **Figure 3-5**.

Table 3-2 – Bricks' compressive strength tests

Test series		Brick	Temperature	Coring direction	Specimens dimensions
S01		A	Ambient temperature	Pressing	ø 50 × 120 mm
S02		B	Ambient temperature	Pressing	ø 50 × 100 mm
S03		B	Ambient temperature	Perpendicular to pressing	ø 50 × 50 mm
S04	S04.600 S04.800 S04.1000	B	600ºC 800 ºC 1000 ºC	Pressing	ø 50 × 100 mm

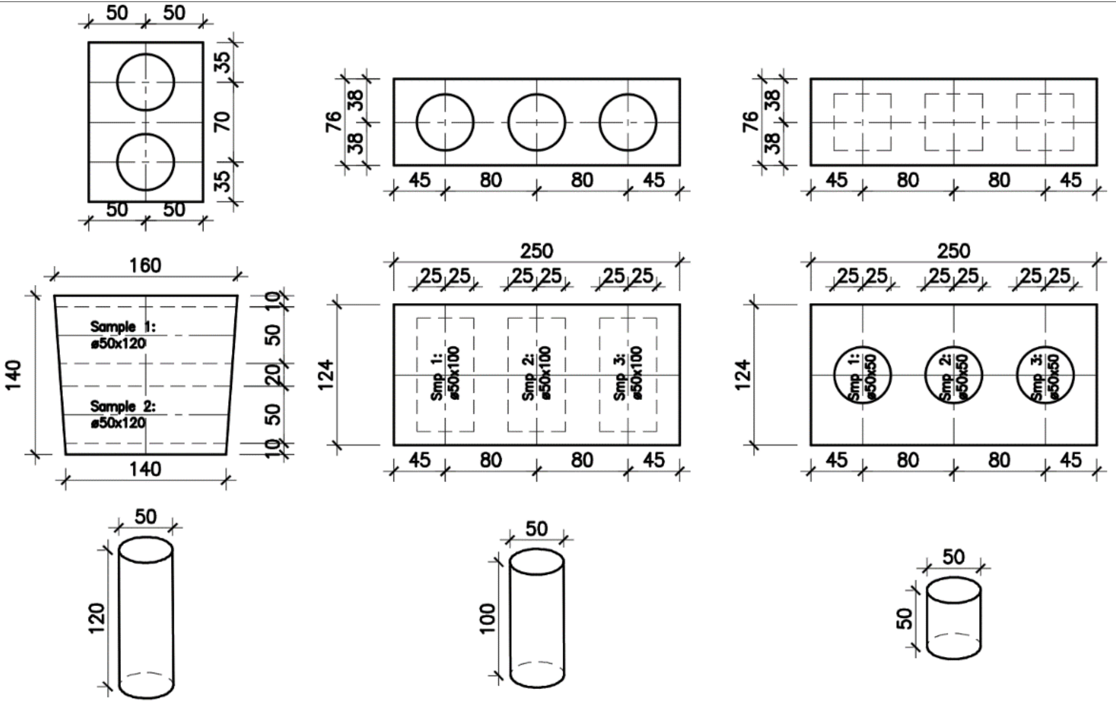

a) b) c)

Figure 3-5 – Specimens dimensions: a) Series S01, b) Series S02 and S04; c) Series S03

The experimental setup comprises: a) One universal testing machine Servosis MUE-402E (maximum capacity of 200kN); b) One electric tubular split furnace (used for the high temperature tests – series S04); c) One datalogger TML TDS-601 model for data acquisition (**Figure 3-6**a). For the high temperature tests, refractory steel load rods were used to apply to mechanical load (**Figure 3-6**b). Rockwool was used in to insulate the furnace openings. Although the samples had different aspect ratios, no correction coefficient was applied in the compressive strength of the specimens as there was a lack of literature references to do so.

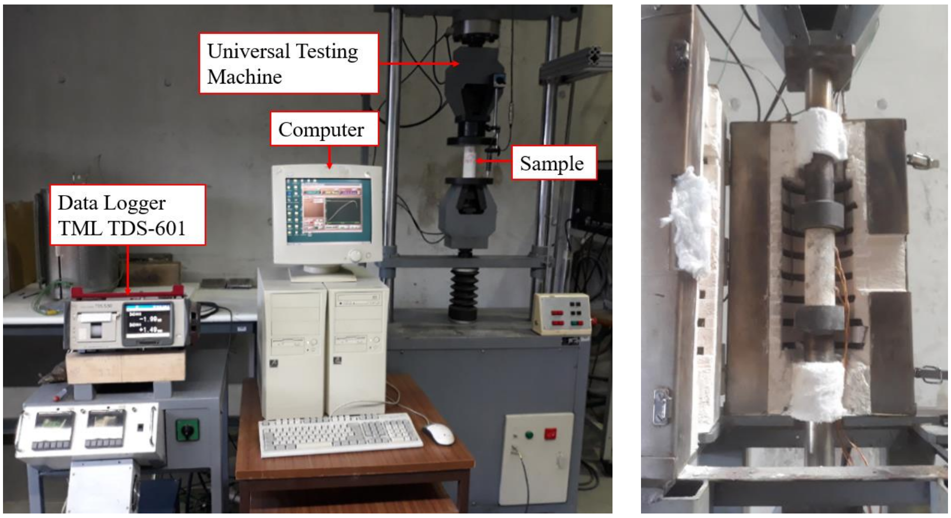

a) b)

Figure 3-6 – Overall view of the experimental setup: a) Ambient temperature tests, b) High temperature tests.

3.1.3 Test procedure

The EN 993-5:2018 - Methods of test for dense shaped refractory products - Determination of cold crushing strength (EN 993-5, 2018) is valid only to test the refractory bricks at ambient temperature, however, the load application rate recommended by this standard is relatively high (1 MPa/s), which may result in an overestimation of the cold crushing strength. Moreover, the standard recommends the use of force control in the tests, which does not allow the determination of the post-peak response of the specimen. Therefore, the test procedure was determined based on previous experimental campaigns available in the literature (Callister and Callister Jr, 2001; Ceylantekin and Aksel, 2012; Nath and Tripathi, 2015; Mukhopadhyay *et al*, 2016; Musante *et al*, 2012).

Series S01, S02 and S03 were tested at ambient temperature. The specimens were placed in the testing machine and tested under displacement control at the rate of 0.01%/s up to failure. Series S04 was tested at high temperatures (600ºC, 800ºC and 1.000ºC). The specimens were placed in the testing machine that applied, under force control, an initial pre-compression load of 2 kN. At his stage, the heating of the specimen was initiated at a rate of 5ºC/min (Callister and Callister Jr, 2001; Ceylantekin and Aksel, 2012; Nath and Tripathi, 2015; Mukhopadhyay *et al*, 2016; Musante *et al*, 2012). After reaching the target temperature, a dwell time of one hour was given in order to homogenize the temperature inside the specimen. After this dwell time, the compression test was carried out under displacement control at the same rate of 0.01%/s up to the failure of the specimen.

In order to confirm that the temperature was homogeneous, thermocouples were installed in different positions of the specimens in series 4. The thermocouple measurements indicated that at the time of the application of the mechanical load, the specimen was indeed subjected to homogeneous temperature (**Figure 3-7**). The position of the thermocouples was chosen based on RILEM (2001) standard recommendations.

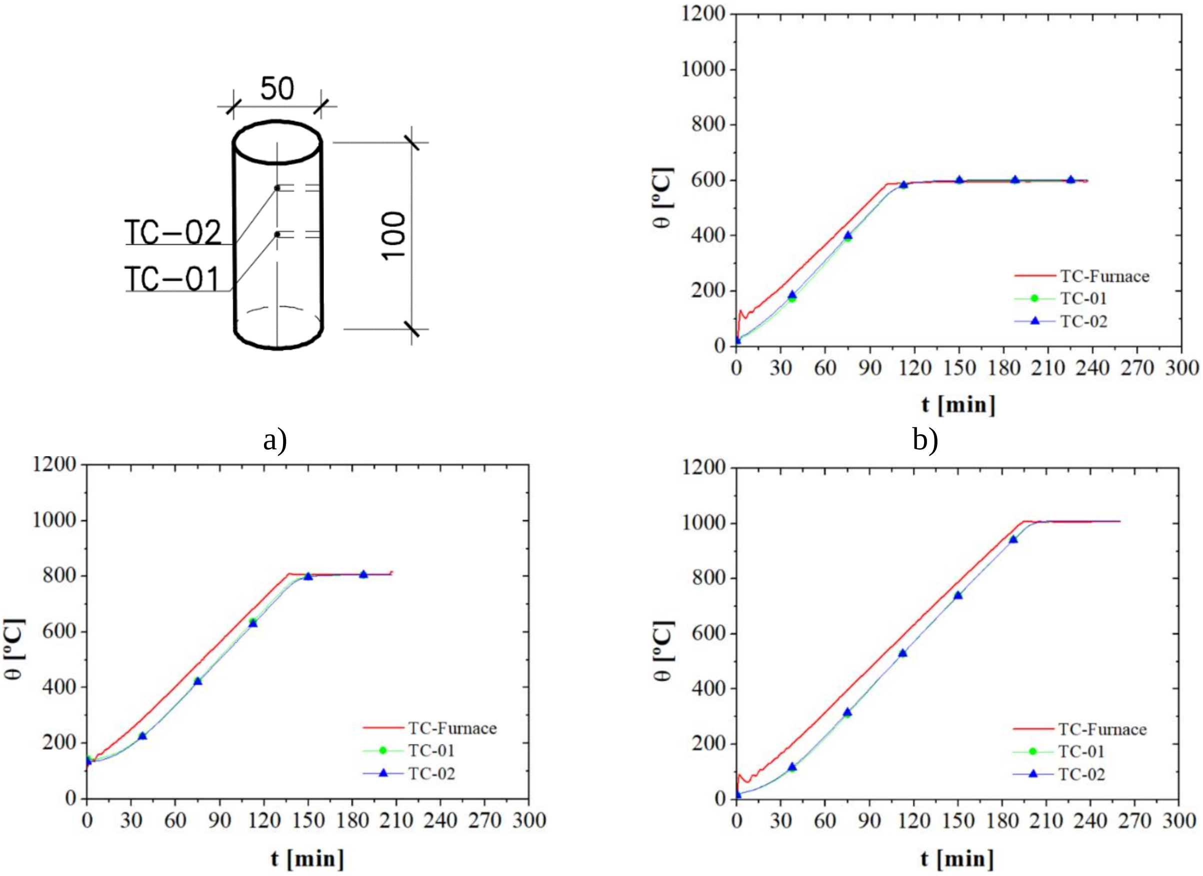

a) b) c) d)

Figure 3-7 – Temperature monitoring inside the specimen: a) Thermocouple’s location [mm]; b) S04.600; c) S04.800; d) S04.1000

3.1.4 Results and discussion

The overall results of the compression tests can be seen in **Table 3-3**. The average compressive strength ($f_{c\ avg}$) of brick *A* tested in the pressing direction (series S01) was 29.2 MPa. The average compressive strengths ($f_{c\ avg}$) of brick *B* tested in the pressing direction (series S02) and perpendicular to the pressing direction (series S03) were 34.4 MPa and 27.4 MPa, respectively. The specimens of series S04 were tested at different temperatures (as shown in **Table 3-2**): 600ºC, 800ºC and 1.000ºC. The average compressive strength ($f_{c\ avg}$) for these temperatures is 24.2MPa, 34.4 MPa and 27.0 MPa, respectively. In **Table 3-3**, σ indicates the standard deviation of the test results.

Table 3-3 – Overall results for the compressive strength tests

Test series	Direction	Temperature	Specimen	f_c [MPa]	$f_{c\ avg}$ [MPa]	σ (f_c) [MPa]
S01	Pressing	20ºC	S01.01	34.4	29.2	3.20
			S01.02	29.4		
			S01.03	26.2		
			S01.04	26.8		
S02	Pressing	20ºC	S02.01	35.6	32.4	3.65
			S02.02	34.4		
			S02.03	27.3		
S03	Perpendicular to Pressing	20ºC	S03.01	27.5	27.4	0.16
			S03.02	27.6		
			S.03.03	27.2		
S04	Pressing	600ºC	S04.600.01	25.9	24.2	2.38
			S04.600.02	25.9		
			S04.600.03	20.8		
	Pressing	800ºC	S04.800.01	35.8	34.4	1.69
			S04.800.02	35.3		
			S04.800.03	32.0		
	Pressing	1000ºC	S04.1000.01	24.2	27.0	4.08
			S04.1000.02	32.8		
			S04.1000.03	24.1		

Figure 3-8 presents the stress-strain curves for test series S01, S02 and S03. The anisotropic behaviour of the material is observed by comparing test series S02 and S03, although these two series have different aspect ratios for the specimens. Still, a significant difference in the compressive strength and in the stiffness was found. It is noted also that the peak strains (less than 0.1%) are relatively low when compared to other concrete-like civil engineering materials. As expected, the compressive strength of the brick is higher in the pressing direction. The scatter obtained on the results (an average coefficient of variation about 10%) is expected for refractory materials, as the setting method and positions of the

bricks in the kiln during firing may affect its mechanical properties (Heindl and Mong, 1936; Stuppfler and Dahlem, 2015; Dahlem *et al*, 2015; Czechowski *et al*, 2015).

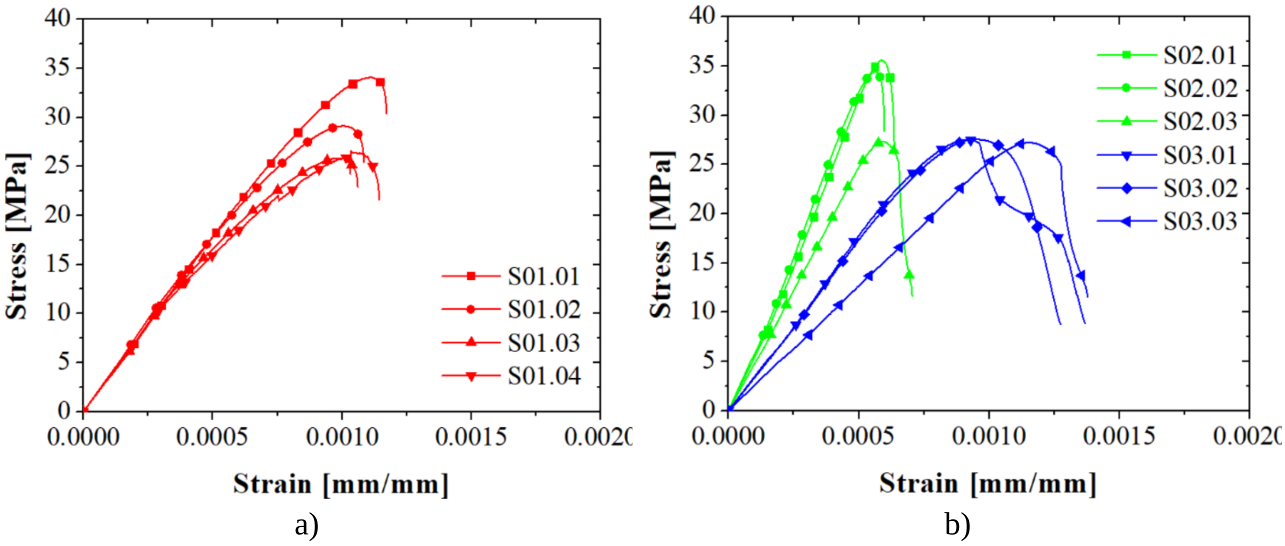

Figure 3-8 – Stress-strain curves: a) S01, b) S02 and S03

Considering only values in the pressing direction, it can be seen that the increase of temperature lowers the compressive strength initially, followed by an increase (at 800º C), and finally by a decrease (at 1000º C), as summarized in **Table 3-3**. The evolution of the compression strength versus temperature is presented in **Figure 3-9**. The reduction of f_c at 600ºC may have been caused by the development of microcracks in the structure of the material due to differential thermal expansion between the matrix and the grains (Kaczmarek *et al*, 2019). The increasing of f_c at 800 ºC is most likely caused by crack restoration (Kaczmarek *et al*, 2019). The slightly reduction of f_c at 1000 ºC is caused by the formation of viscous phases at the material (Kaczmarek *et al*, 2019) (**Figure 2-3**a).

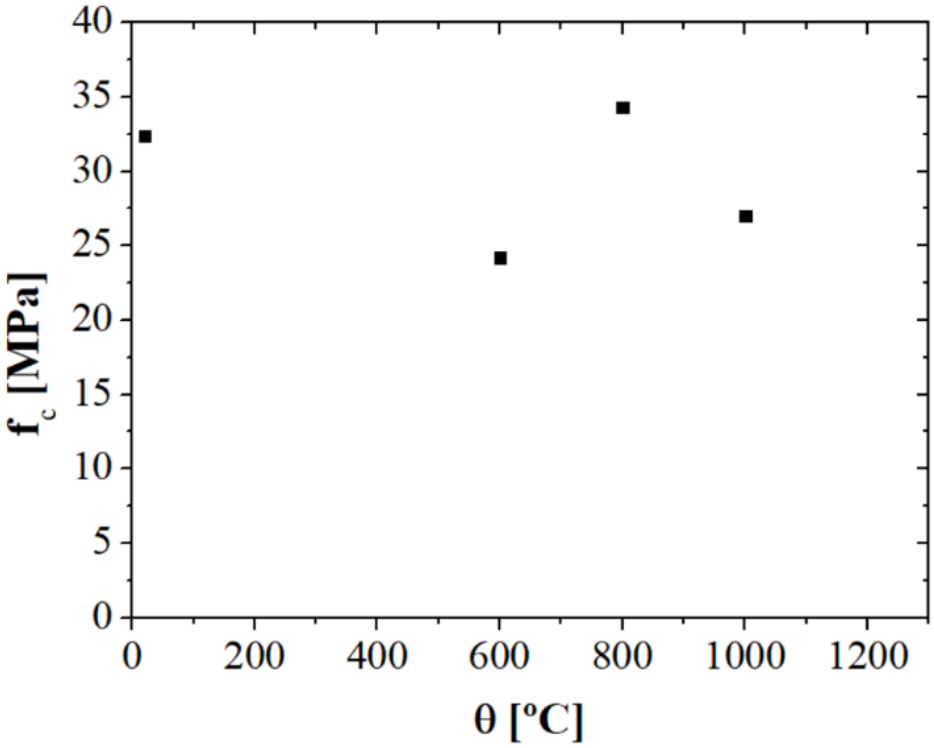

Figure 3-9 – Compression strength versus temperature: S02 and S04

Besides the maximum strength and the stress-strain relations, the failure modes were also analysed. **Figure 3-10** presents the specimens after failure for series S01 and S04. It is possible to identify a diagonal crack in the specimens, for both ambient temperature and high temperature, meaning that the failure mode was not influenced by the high temperatures of the test.

a)

b) c) d)

Figure 3-10 – Specimens after failure: a) S01; b) S04.600; c) S04.800; d) S04.1000

3.2 Joint normal behaviour

This section presents the characterization of the normal behaviour of the joint, based on experimental and numerical studies. It includes a classical joint closure test, measurement and analyses of the heterogeneity of the joints in a wallet using DIC, and numerical studies showing the influence of the bricks' imperfections.

3.2.1 Classical joint closure test

The joint closure test allows to assess the normal behaviour of the dry joints. In this test, two stacked bricks are compressed, and the displacements are recorded (Gasser *et al*, 2004; Andreev *et al*, 2012; Allaoui *et al*, 2018). The joint thickness may be obtained based on the force-displacement diagram. The adopted specimens consisted of a masonry prism composed of two stacked bricks with dry joint. The brick type *B* was used (**Figure 3-3**b). The bricks were cut using a circular diamond saw, and the final dimensions of the bricks composing the specimen were 124×124 mm by 76 mm in height. When building the specimen, the original face of the brick was used at the joint. The final dimensions of the prism were 124×124 mm by 152 mm in height. The joint closure tests were performed at ambient temperature. A multipurpose Servo Hydraulic Universal Testing Machine W+B Series LFV (maximum capacity of 600 kN) was used (**Figure 3-11**a). The displacements were measured with an Epsilon extensometer connected to the machine (**Figure 3-11**b).

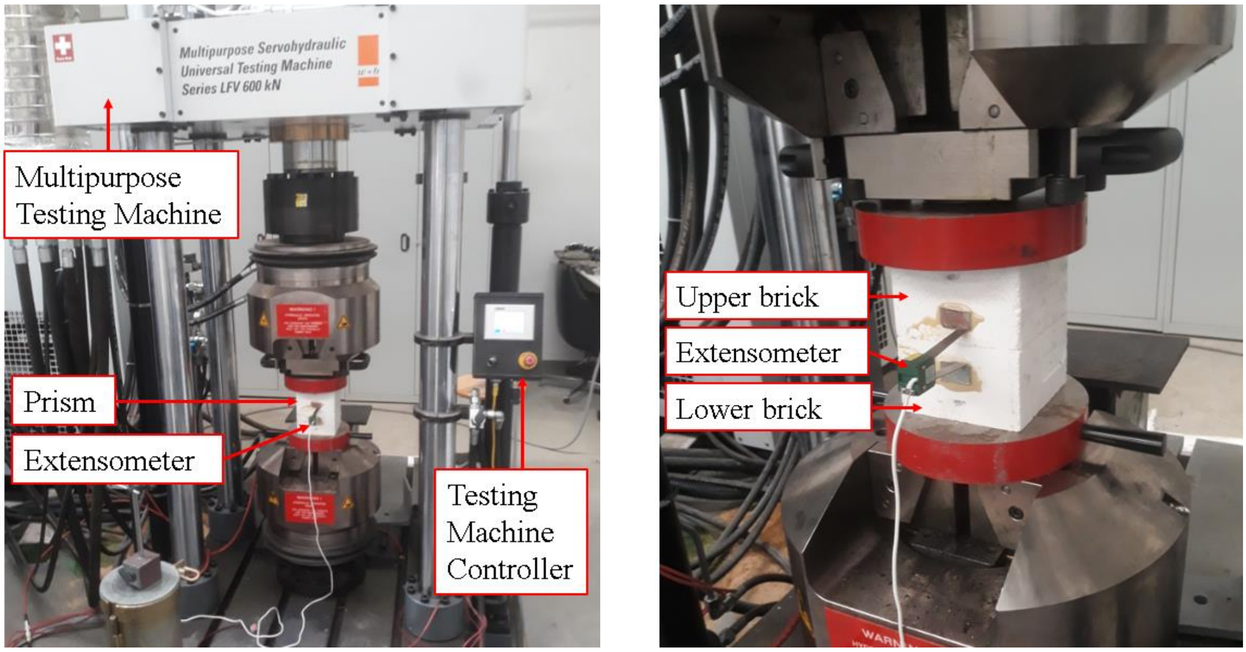

a) b)

Figure 3-11 – Joint closure test - Experimental setup: a) Overview, b) Details of prism and LVDT

A compressive load was applied under load control at the constant rate of 0.5 kN/s, up to 150 kN. At this load level, the average compressive stress was 9.76 MPa and a linear behaviour was expected at the bricks. The thickness of the joints was estimated based on the force-displacement curve obtained in the joint closure test, considering the intersection of the linear section of the curve, with the horizontal axis in the plot (Gasser *et al*, 2004). Three load cycles were applied to the specimen.

The result of the joint closure test is given in **Figure 3-12**. At the first cycle, it is possible to identify a behaviour, which is different from the behaviour of the subsequent cycles due to adjustment of the contact surface at the joint. The initial joint thickness was 0.022 mm. For the second and third load cycles, a more similar behaviour was observed, and the joint thickness reduced then to 0.007 mm. This reduction is caused by joint degradation due to crushing of initial non-flat surfaces of the bricks. This happens along the first load cycle, as observed by other researchers (Allaoui *et al*, 2018; Gasser *et al*, 2004; Andreev *et al*, 2012; Prietl, 2006; Prietl *et al*, 2006) and as shown in this joint closure test. The joint degradation increases the contact area between the bricks, leading to an increase of the initial stiffness of the prism.

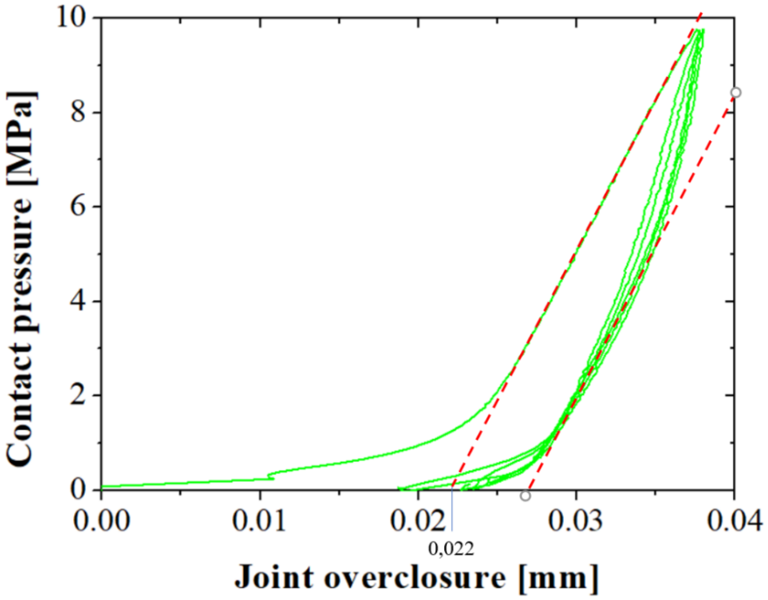

Figure 3-12 – Joint closure curve

3.2.2 Heterogeneity in joint behaviour

When the bricks are dry-stacked to form a masonry wallet, the imperfections of the bricks dimensions are not corrected by a mortar layer. In this situation it is not possible to ensure the levelling of the courses and some voids are created. Consequently, the bricks' imperfections have a significant impact on the load transfer through the masonry and the supporting conditions of each brick. In order to assess this phenomenon, one of the wallets tested under uniaxial compression (Chapter 4) was chosen for additional detailed analyses of its joint behaviour (**Figure 3-13**). Additional information regarding the test setup of the wallet can be seen in the next chapter. In this section, only the results regarding its joint behaviour are assessed.

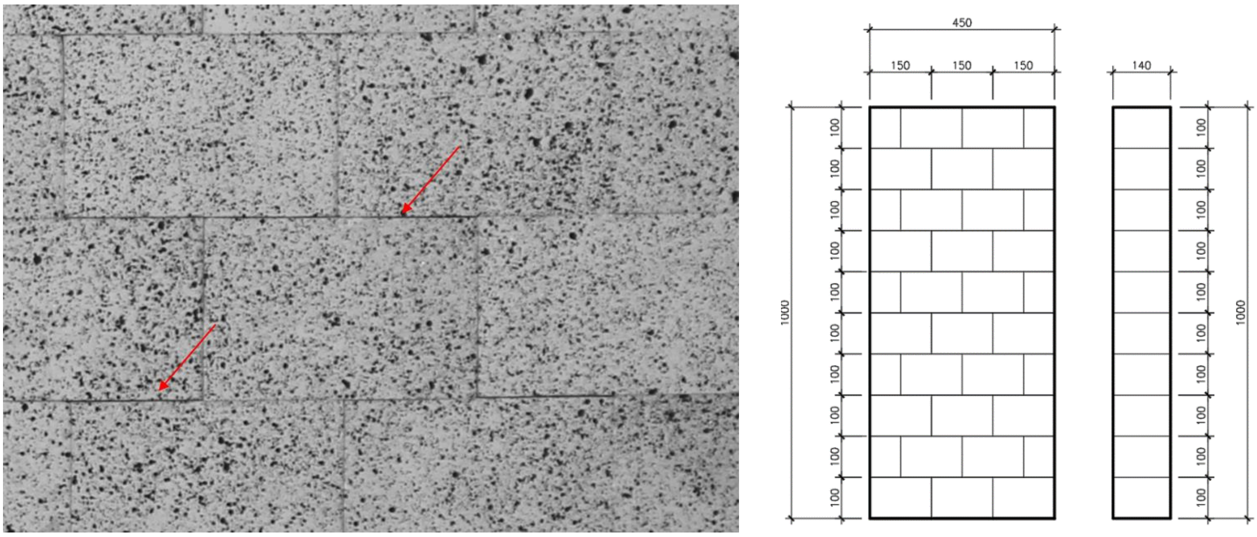

a) b)

Figure 3-13 – Specimen details: a) Bed joints imperfections in mortarless refractory masonry; b) Dimensions of the masonry wallet

Joint closure curves, at different points, were obtained using DIC (**Figure 3-14**a). **Figure 3-14**b presents the curves for different points in the wall and compares with the curve obtained in the classical joint closure test. It is possible to identify a significant scattering on the curves obtained by the DIC in different locations. This is a direct result of the different conditions on the support and load of each brick, caused by the bricks' shape imperfections. It is also noted that this behaviour is three-dimensional, even if only one face of the wall is measured with the DIC. The average of the DIC curves provides a significantly less stiff response than the curve obtained from the classical test, because the bricks in the masonry wallet are arranged in a more complex way, when compared with the precious prism, with a non-continuous vertical joint and several bricks in a course. Consequently, the shape imperfections of the bricks result in larger initial joint thicknesses and has a considerable influence on the joint behaviour.

It seems clear, from the obtained results, that the results from classical joint closure test need to be used carefully, as the initial joint thickness measured in a single joint may deviate significantly from the one present in masonry walls or panels.

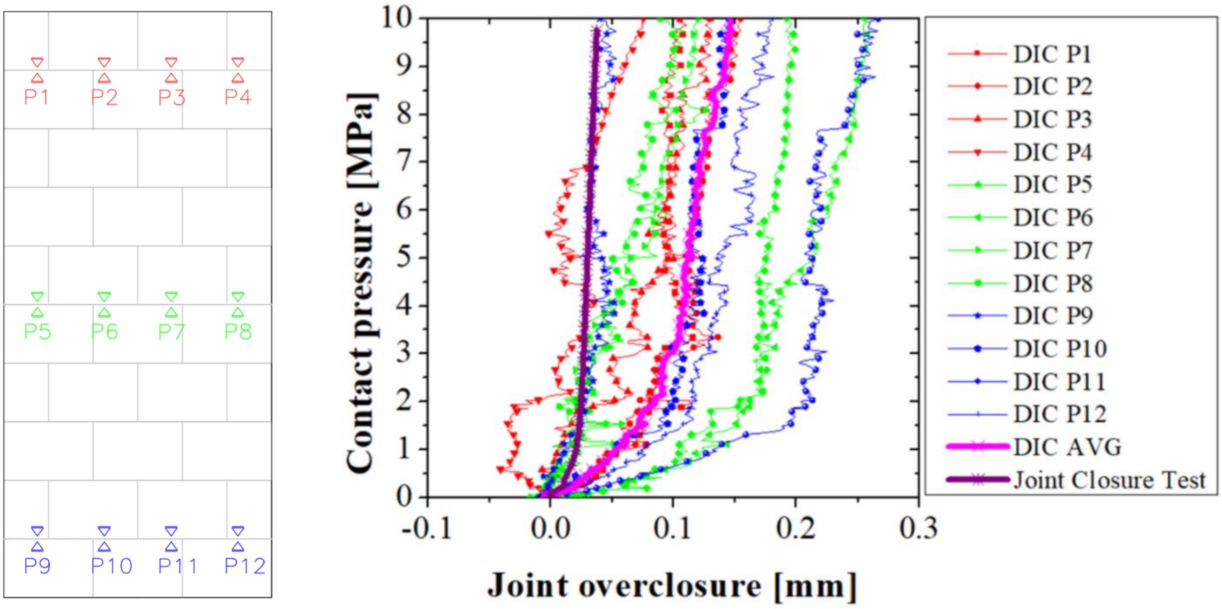

a) b)

Figure 3-14 – Heterogeneity in joint’s normal behaviour: a) Locations; b) Joint closure curves

3.2.3 Effects of brick’s height imperfections on its behaviour

In order to properly understand the influence of the bricks’ imperfection, several numerical models were developed considering different boundary conditions. This study is an extension of a previous work, where five different boundary conditions (see **Figure 2-16**) were studied (Ngapeya, 2018) and additional boundary conditions, with “banana shape” (see **Figure 2-14**d), are now considered. As stated, these load cases occur because the masonry blocks do not have constant height and there is no mortar layer between the courses to ensure levelling. For this purpose, a numerical model was developed to assess the bricks loadbearing capacity and to determine the crack pattern expected for the bricks.

3.2.4 Numerical model

The numerical analyses presented in this work were performed using the Finite Element (FE) software Abaqus. The Concrete Damage Plasticity (CDP) model was used. This model allows failure under compressive crushing and tensile cracking. It should be highlighted that additional details regarding the modelling approach, as well as the constitutive models used are given in Chapter 6. As these numerical analyses are simple and intend only to see specific topics, this section only focuses on the results, in order to avoid repetition throughout this document.

The Young’s modulus obtained in series S03 was used for this study. The density of the material was measured experimentally. The tensile strength (f_t) and fracture energy (G_f) were obtained by the wedge split test (Kaczmarek *et al*, 2019). **Table 3-4** presents the full mechanical properties adopted in the numerical model. The bricks *C* were used in this study. The brick was discretized with 8-node solid elements (C3D8R elements). The mesh is shown in **Figure 3-15**, comprising 20097 nodes and 17920 elements.

Table 3-4 – Parameters of the alumina spinel brick

Young´s modulus (E)	28500 MPa
Density	3130 kg/m^3
Dilatation angle (ψ)	20 ºC
Eccentricity (ε)	0.10
f_{b0}/f_{c0}	1.16
K_c	0.667
Viscosity parameter	0.02
f_c [MPa]	32.4
f_t [MPa]	4.3
G_f [J/m^2]	111.7

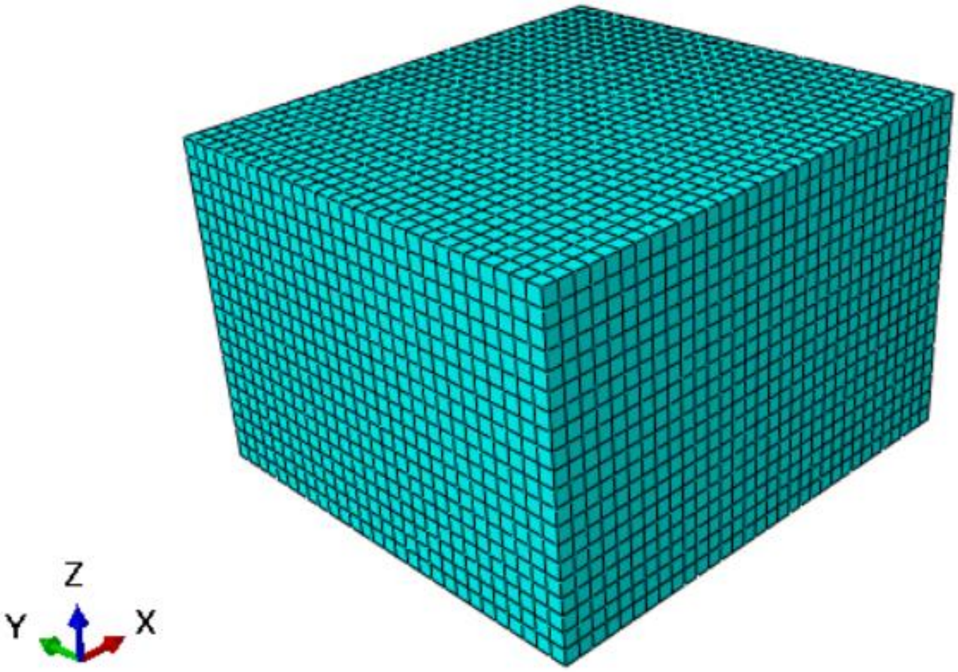

Figure 3-15 – Numerical model of the brick: Mesh details

3.2.5 Results and discussions

Table 3-5 presents the studied boundary conditions, including the applied loading and support conditions. The load percolation paths (minimum principal stresses) and the expected crack pattern (equivalent plastic strains) are presented.

In loading case 1, the brick is fully supported and loaded over the whole surface, therefore, it is able to reach 100% of its loadbearing capacity. For load case 2, the brick is loaded only in half of its top surface and due to the flow of forces the brick is able resist 51.2% of the full capacity. Loading case 3, as stated by Ngapeya *et al* (2018), is the worst scenario, with the stresses distributed only in the middle of the brick, and, due to shear, it can only withstand 10.8% of the full capacity. In loading case 4, the brick is supported and loaded at the same side, by only half of its length. Therefore, it can develop 41.8% of the full loadbearing capacity. In loading case 5, which it is similar to loading case 2, the brick is loaded in the whole top surface but supported only by half of its bottom surface, consequently it can develop up to 38.5% of its full capacity. In loading case 6, the brick is fully loaded, but supported only by the edges (banana shaped bricks). In this case, the brick can develop up to 67.9 % of its full capacity. In loading case 7, the brick also has a banana shape, and is loaded only in the central part and supported by the edges. In this case, the brick can withstand 32.8% of its compressive strength.

The compressive stress-strain curves of the different configurations are presented in Figure 3-16. The stress concentrations are evidenced by the reduction of the linear part of the curve. In loading case 1, the brick is fully supported and loaded, therefore, its apparent stiffness is the same of the material. In the other loading cases, the brick's apparent Young's moduli are significantly smaller when compared to the material. Consequently, the observed difference between the stiffness of the masonry panel and the stiffness of the individual brick, may be associated with an uneven stress distribution.

Figure 3-17 presents a comparison between the crack patterns numerically predicted and experimentally observed (obtained with the experimental campaign described in Chapter 4). A correlation between the crack patterns in the wall and the different simulations can be clearly observed.

Table 3-5 – Loading cases by brick's support and loading conditions

Loading Case	Structural system	Stress flow	Crack pattern
Loading Case 1 Loadbearing capacity: 100.0 %	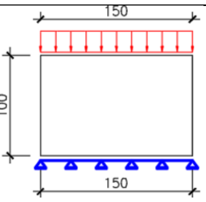	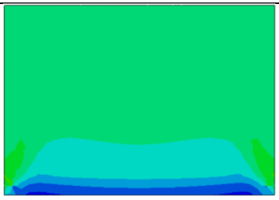	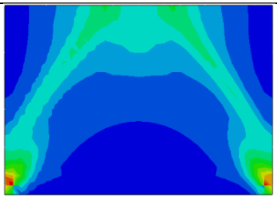
Loading Case 2 Loadbearing capacity: 51.2 %	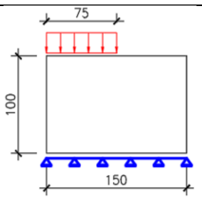	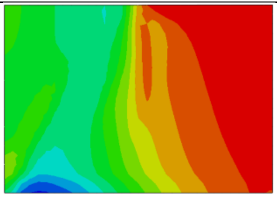	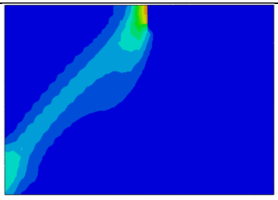
Loading Case 3 Loadbearing capacity: 10.8 %	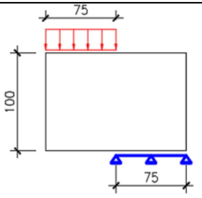	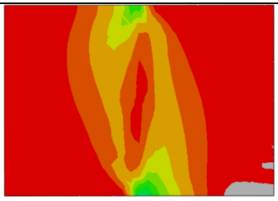	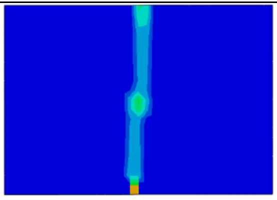
Loading Case 4 Loadbearing capacity: 41.8 %	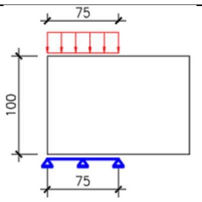	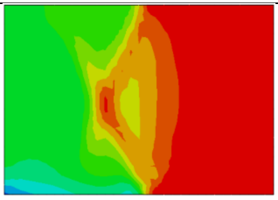	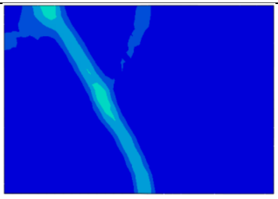
Loading Case 5 Loadbearing capacity: 38.5 %	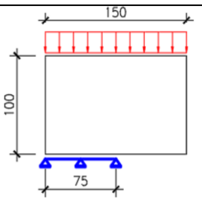	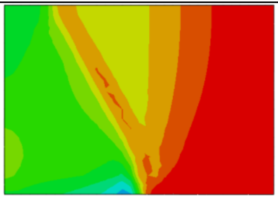	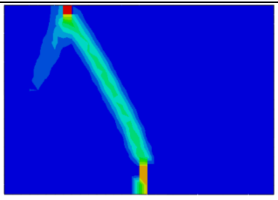
Loading Case 6 Loadbearing capacity: 67.9 %	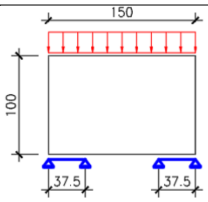	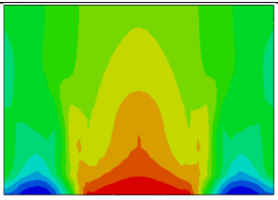	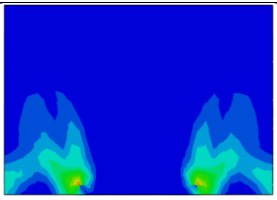
Loading Case 7 Loadbearing capacity: 32.8 %	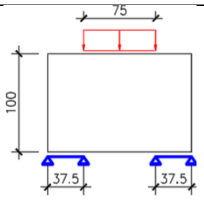	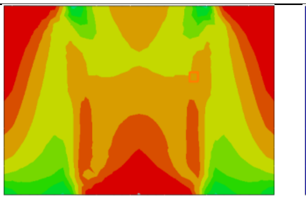	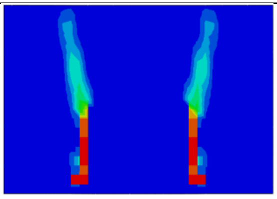

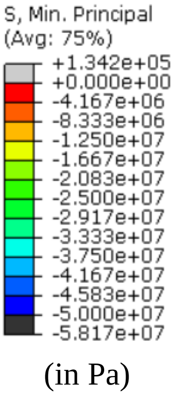

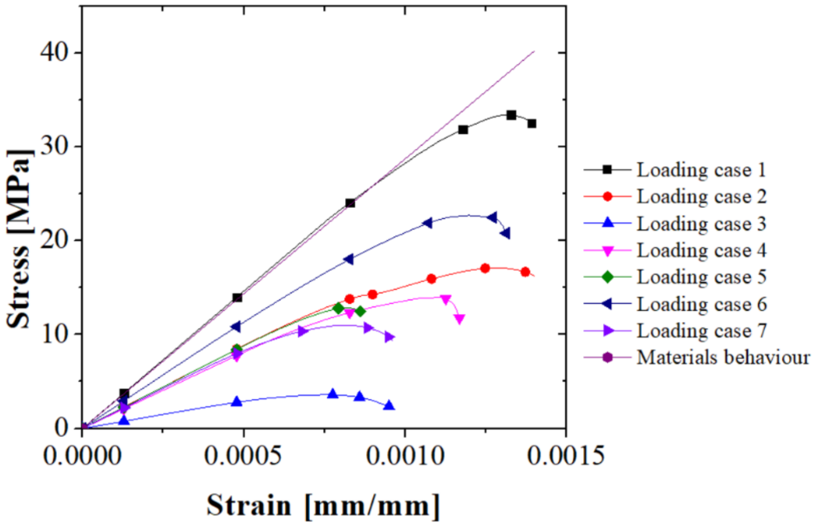

Figure 3-16 – Bricks stress-strain curves for loading cases 1 to 7

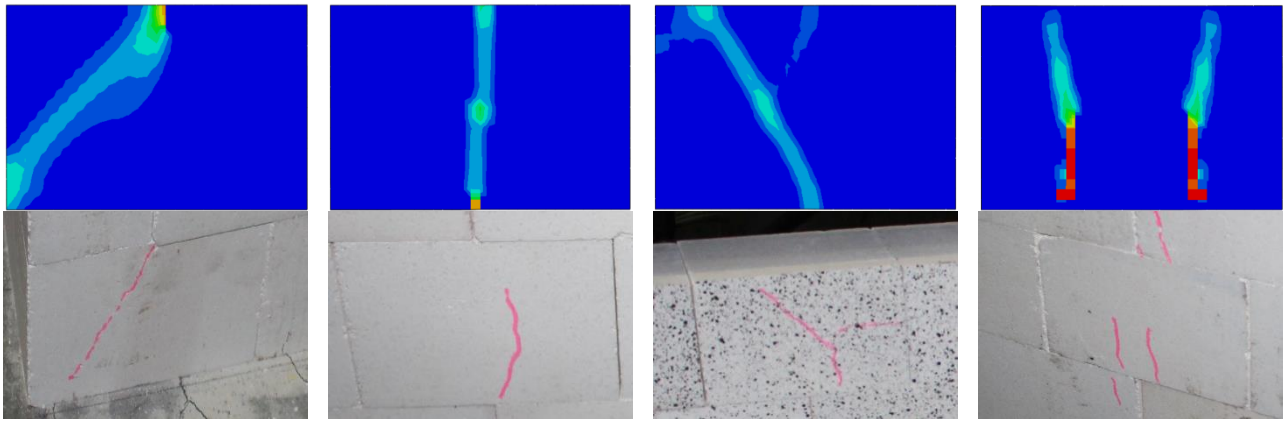
Loading case 2 Loading case 3 Loading case 4 Loading case 7

Figure 3-17 – Crack's pattern: Numerical predictions vs experimental results

3.2.6 Effects of brick's height imperfections on a masonry panel

Based on the results obtained previously and aiming at observing the influence of the bricks' imperfections on a full masonry panel, another numerical model was built. Here, besides the bricks also the joints are considered. The geometry of the model is shown in **Figure 3-18**. The bricks imperfections were randomly generated based on the statistical distribution shown in **Figure 3-18**a. The dry joints were modelled as surface-to-surface contact interactions, the pressure-overclosure relations used to represent the different joints thickness considered are presented in **Figure 3-19**a, these curves aim to account the differences in brick's height. The final mesh was generated automatically by Abaqus software and was rather refined, with 18900 elements and 26800 nodes (**Figure 3-18**b).

Different analyses were performed, considering three temperatures (ambient temperature, 1300ºC and 1500 ºC) and two load levels (3MPa and 5MPa). The load levels were chosen based on the available literature of the creep parameters. For the models at ambient temperature, the CDP model was used, with the parameters indicated in **Table 3-4**. For the simulations at high temperatures, a viscoplastic solution was chosen, considering creep effects. The Norton-Bayle creep law was used, and the creep parameters were obtained from Samadi *et al* (2020), the creep curves are shown in **Figure 2-9**. The load was applied at 0.5 MPa/min and 0.3 MPa/min for the load levels of 5 MPa and 3 MPa, respectively, consequently the loading stage lasts 10 minutes. After the loading stage, 20 minutes of simulation were considered to observe the evolution of the viscoplastic strains. Thus, the total time considered for the analyses was 30 minutes.

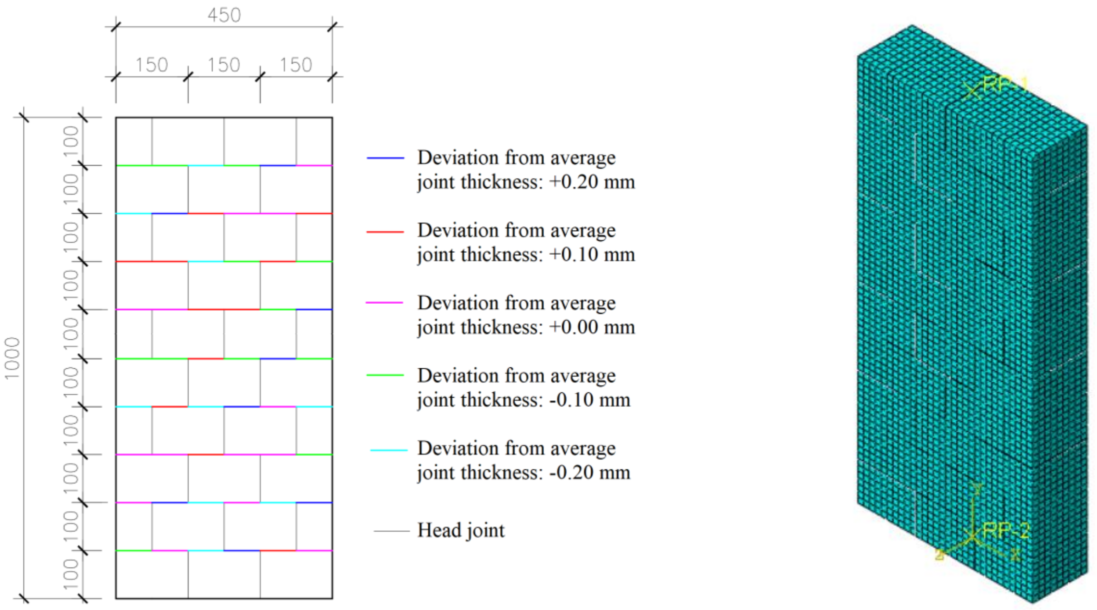

a) b)

Figure 3-18 – Specimens: a) dimensions and joint thickness; b) Numerical model

3.2.7 Results and discussions

The numerical model was validated against experimental results of compressive tests performed in masonry wallets (see Chapter 4), as shown in **Figure 3-19**b. The numerical result is in good agreement with the experimental tests. The stresses developed in the specimen are presented in **Figure 3-20** and **Figure 3-21** for the loading levels of 3 MPa and 5 MPa, respectively. The stresses were plot for 3 min, 5 min, 10 min and 30 min. The loading level for each period is also indicated. For the simulations performed at ambient temperature, it is possible to identify significant stress concentrations in the wall caused by the geometrical imperfections. Based on the vertical stress distribution it is possible to identify the load percolation path. As observed by Ngapeya *et al* (2018), the failure of some bricks may be reached in spite the fact that the loading applied on the wall is far from the ultimate loading capacity of the brick.

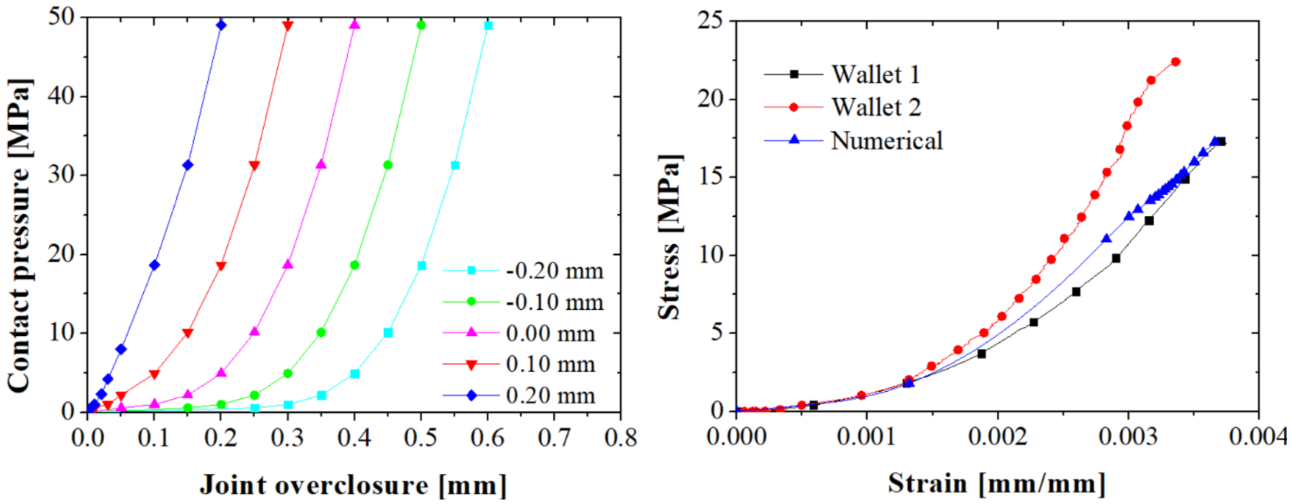

a) b)

Figure 3-19 – Joint behaviour: a) Joints pressure-overclosure relations; b) Validation of the numerical model.

The simulations performed at high temperatures are subjected to creep. The viscoplastic strains occur with higher intensity in the areas where the stresses are higher, i.e., it is more significant along the loading path percolation. Due to this effect, the creep strains reduce the stress concentrations in the wall. The reduction is higher for the temperature of 1500 ºC, as the creep strain rate increases with the temperature. The increasing of the load level from 3 MPa to 5 MPa, had also an impact on reducing the stress concentrations, as the strain rate increased with the loading level. Therefore, due to creep and the viscoplastic strains developing, the masonry joints close led to a homogeneous stress distribution in the wall.

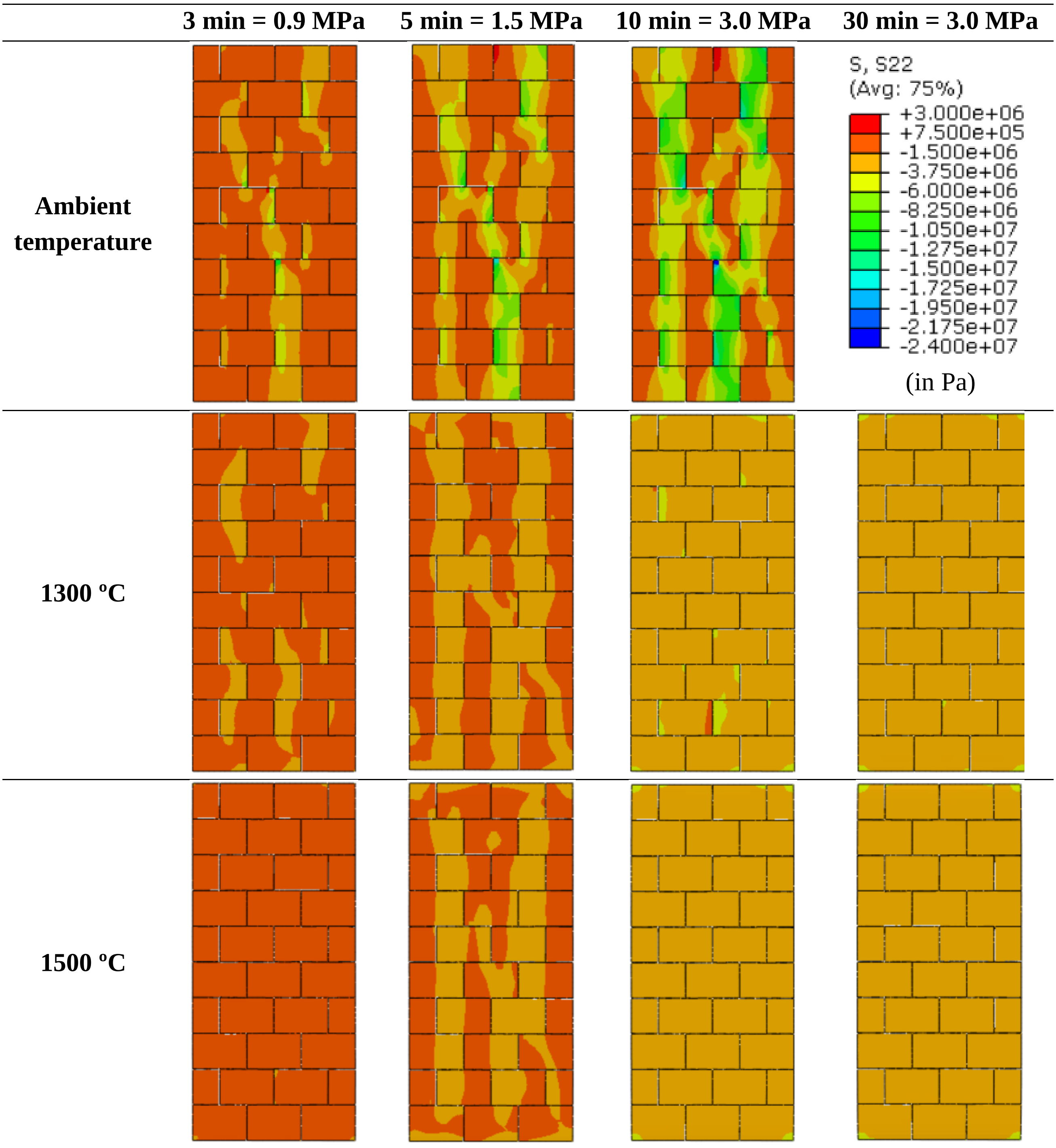

Figure 3-20 – Effects of brick's imperfections in height on the wall's behaviour at ambient temperature, 1300 ºC and 1500 ºC – Loading level of 3 MPa

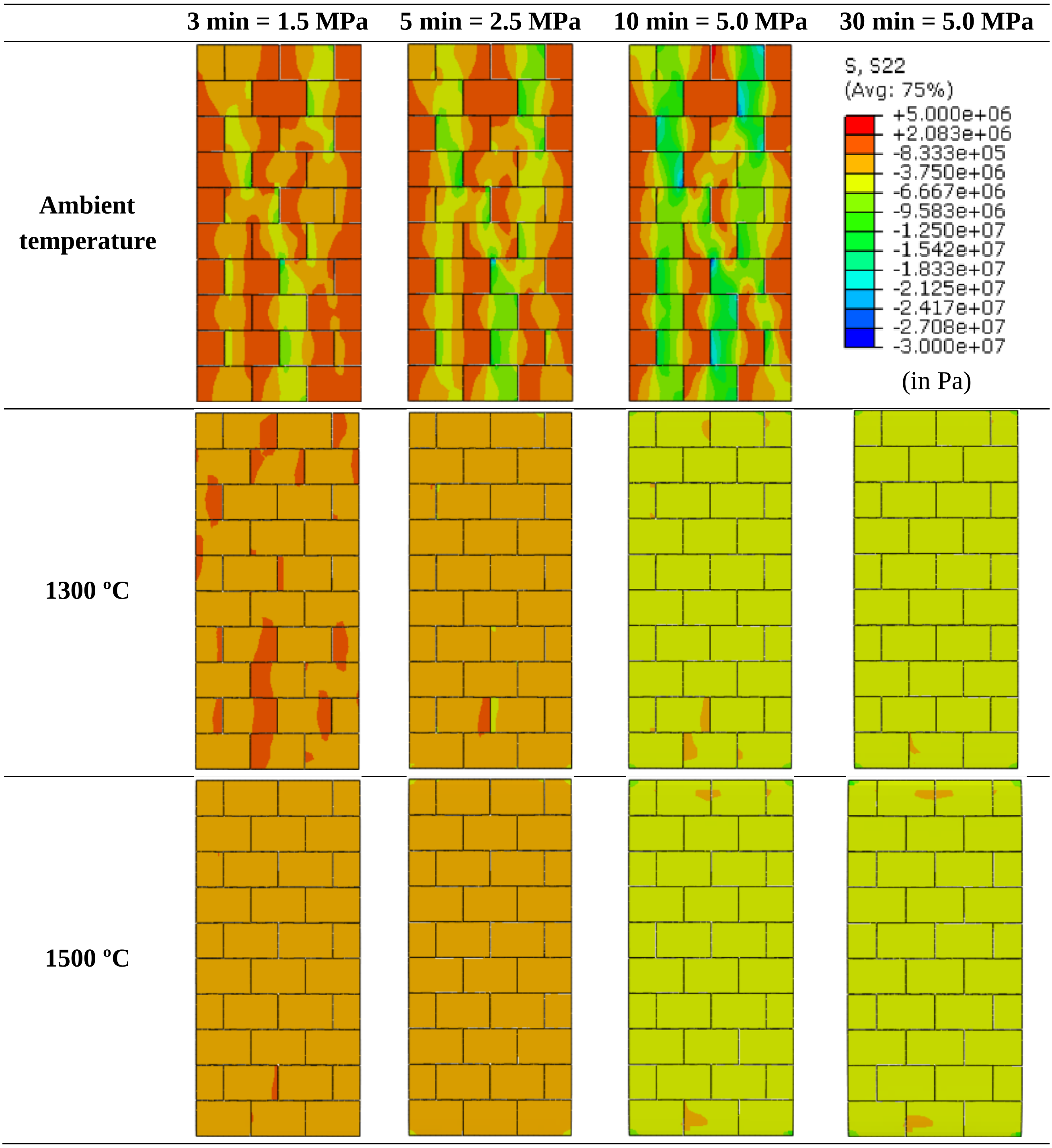

Figure 3-21 – Effects of the imperfections in height on the wall’s behaviour at ambient temperature, 1300 ºC and 1500 ºC - Loading level of 5 MPa

3.2.8 Comparison between bed and head joint behaviour

Aiming to evaluate the differences between the behaviour of the bed and head joints under biaxial conditions, an inverse identification of the joint properties was performed, based on the experimental results provided by Prietl (Prietl, 2006; Prietl *et al*, 2006). This author developed a dedicated device to test refractory wallets under biaxial compression (**Figure 3-22**) and performed tests at ambient and high temperatures.

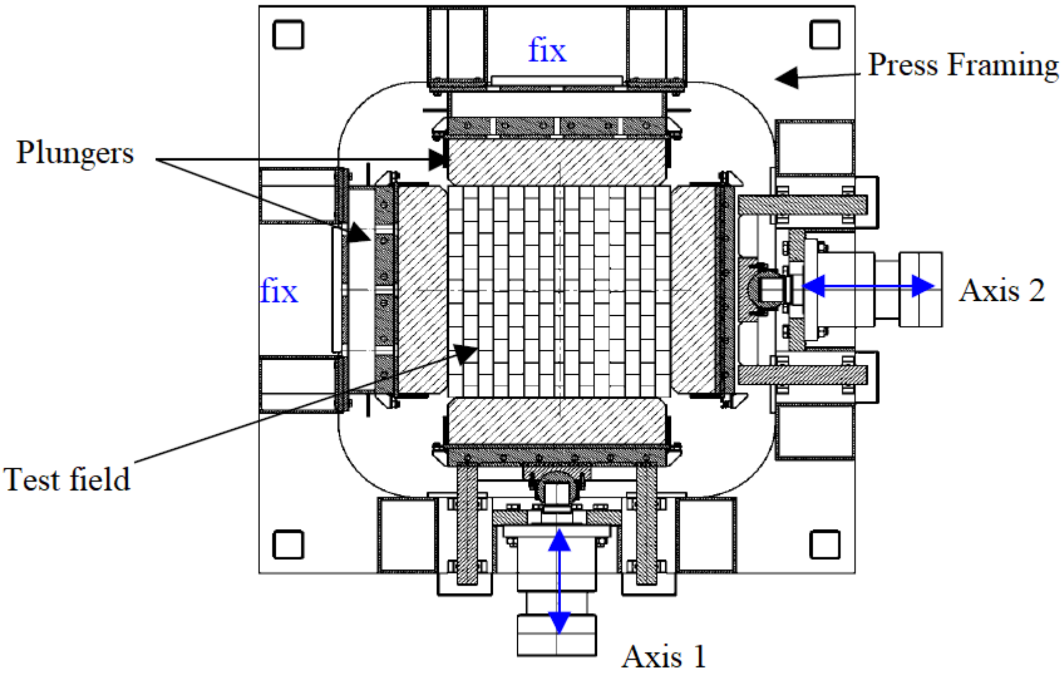

Figure 3-22 – Biaxial press: Experimental setup (Prietl, 2006)

3.2.8.1 Numerical model

The numerical model was based on the experimental setup adopted by Prietl (2006). A detailed micro-modelling strategy was adopted, in which the bricks are represented by continuous elements and the dry joint interfaces are represented by surface-to-surface contacts. The masonry wall was discretized with 8-node solid elements (C3D8R elements), the final mesh was generated automatically by Abaqus software and was rather refined, with 121708 elements and 231844 nodes (**Figure 3-23**). The Concrete Damage Plasticity (CDP) model was used to represent the magnesia-chromite bricks. **Table 3-6** presents the mechanical properties adopted in the numerical model for the magnesia chromite bricks.

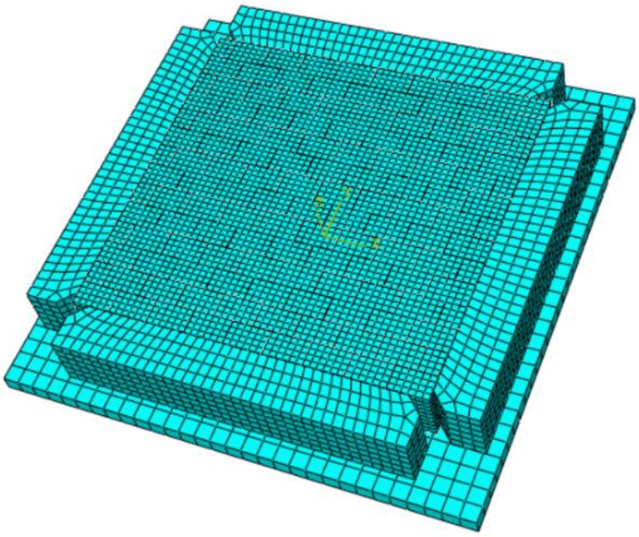

Figure 3-23 – Numerical model: mesh

Table 3-6 – Mechanical properties of the magnesia chromite bricks (Nguyen *et al*, 2009)

f_c [MPa]	105.0
f_t [MPa]	7.76
G_f [J/m^2]	131.1

3.2.8.2 Results and discussions

The inverse identification of the joint parameters was performed using the experimental results provided by Prietl (Prietl, 2006; Prietl *et al*, 2006). The inverse identification procedure consists in testing different joint pressure-overclosure curves until a satisfactory agreement with the experimental results is reached. The validation of the numerical is shown in Figure 3-24a. The joint closure curves for bed and head joints obtained are shown in Figure 3-24b. The head joints present a stiffer behaviour when compared to the bed joints. This is mostly likely because the head joints are formed by one brick in contact with another brick, while the bed joints are formed by one brick in contact with two other bricks. Consequently, in the latter case, the imperfections of multiple bricks aligned in a masonry course affect more strongly the joint behaviour and results in a joint with a higher compressibility and a lower stiffness.

Figure 3-25 shows the displacement distribution for different loading levels. The displacements in the direction perpendicular to the bed joints are higher, as the number of joints in this direction is higher and these joints present higher compressibility. Moreover, it was possible to see that a significant part of the displacements is related to joint closure process, as high displacements are obtained for small loading levels (**Figure 3-25** a and b), as confirmed by the experimental results.

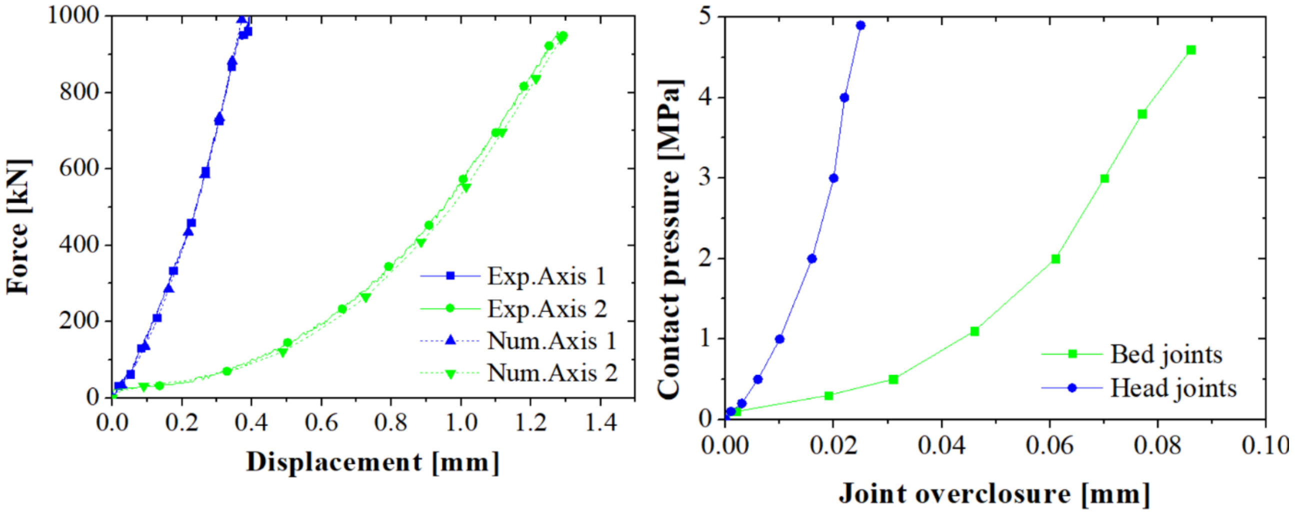

a) b)

Figure 3-24 – Results for biaxial compression: a) Force-displacement diagram (experimental and numerical); b) Joint closure relations for head and bed joints

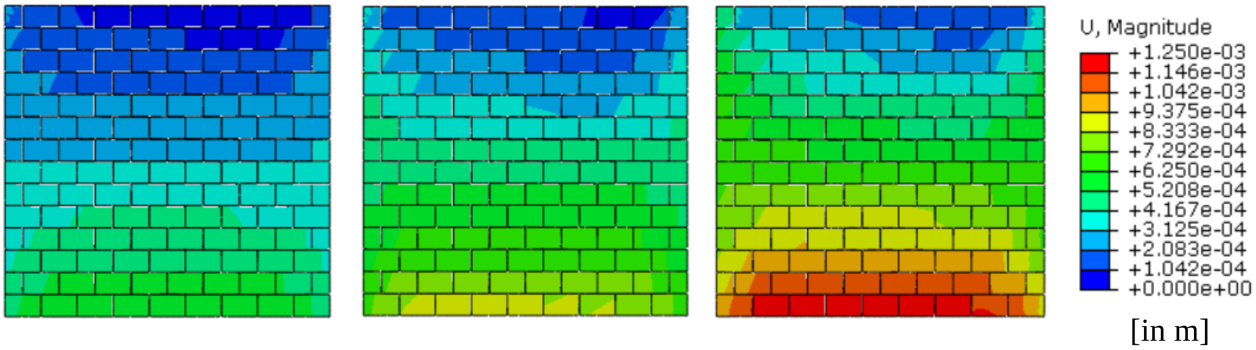

a) b) c)

Figure 3-25 – Displacement fields at ambient temperature for different loading levels: a) 25%, b) 50%, c) 100%

3.3 Joint tangential behaviour

The shear behaviour of joints in masonry is ruled by the Coulomb friction law (Gasser *et al*, 2004; Nguyen *et al*, 2009). The part 3 of EN 1052-3 (2002) is widely used to determine the initial shear strength at ambient temperature for joints with mortar. The triplet shear tests may be also used to characterize dry joints. However, it is a challenge to perform this test at high temperatures, as it requires the application of loads in two perpendicular directions. The Slant Shear test was successfully used to characterize the brick/mortar interface at ambient and high temperatures (Brulin *et al,* 2020), however, the slant shear test cannot be used in the case of dry joints.

When dealing with mortarless masonry, only the friction coefficient (or friction angle) needs to be identified. A simple test is the use of an inclined plane, with increasing rotation, which makes possible to measure the initial angle of sliding (Gasser *et al*, 2004). This test can be easily adapted to be performed at high temperatures. A dedicated device was developed in this research to evaluate the friction angle of dry joints at ambient and high temperatures.

The experimental characterization of the tangential behaviour of dry joints comprised fifteen tests performed at ambient and high temperatures divided in four series (**Table 3-7**). Series ST.RT had six specimens and was tested at room temperature. The series ST.300, ST.600 and ST.900 had three specimens each and were tested ad 300 ºC, 600 ºC and 900 ºC, respectively.

Table 3-7 – Test series – Slip Test

Series	Specimen	Testing temperature
ST.RT	ST.RT.01.01 ST.RT.01.02 ST.RT.01. 03 ST.RT.02. 01 ST.RT.02. 02 ST.RT.02. 03	Ambient temperature
ST.300	ST.300.01 ST.300.02 ST.300.03	300 ºC
ST.600	ST.600.01 ST.600.02 ST.600.03	600 ºC
ST.900	ST.900.01 ST.900.02 ST.900.03	900 ºC

3.3.1 Test setup

In the test setup a tilting beam was positioned inside an electrical furnace with a pinned support. A hydraulic jack, connected to the beam by a load rod, was used to increase the inclination of the beam. Two stacked bricks were positioned on the device, the bottom brick was constrained by steel plates, but the upper brick was allowed to move (Figure 3-26). When the hydraulic jack goes upward, it increases the inclination of the beam, from horizontal position up to the friction angle of the joint (Figure 3-26b).

A picture of the experimental setup is presented in **Figure 3-27**. A W+B servo controlled hydraulic unit was used to control the hydraulic jack. The data was acquired using a TML TDS-601 Datalogger. In order to avoid overheating of the inclinable beam and hydraulic jack, ceramic wool was used to protect the steel components from high temperatures. Moreover, a cooling device was used to cool the load rod, avoiding excessive temperatures in the hydraulic jack.

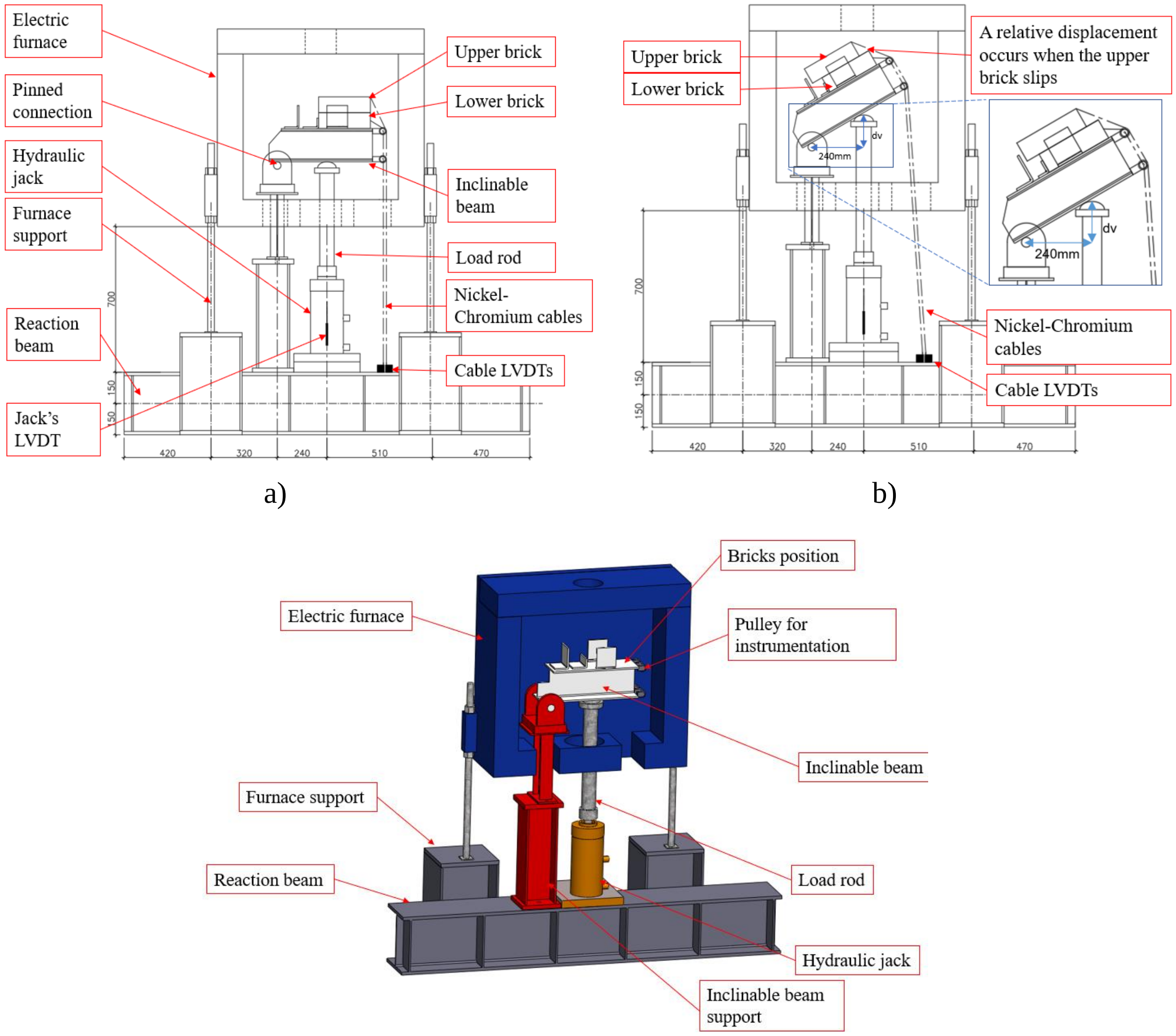

a)

b)

c)

Figure 3-26 – Slip test scheme: a) before slipping, b) after slipping; c) 3D model

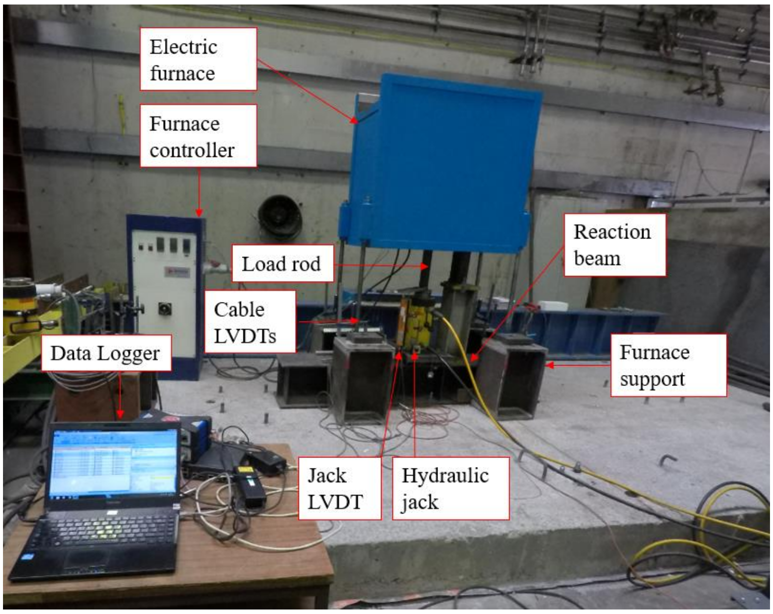

Figure 3-27 – General view of the slip test experimental set-up

Two cable LVDTs were used to measure the displacement of the bottom brick and one cable LVDT was used to monitor the displacement of the upper brick. The LVDTs were connected to the bricks using Nickel-Chromium cables in order to avoid the influence of their thermal elongation (**Figure 3-28**). When the upper brick slips, a differential displacement between these LVDTs is registered. A rod LVDT was used to measure the displacement of the hydraulic jack and another one was used to feed the servo controller unit. The details of the LVDTs are presented in **Figure 3-29**.

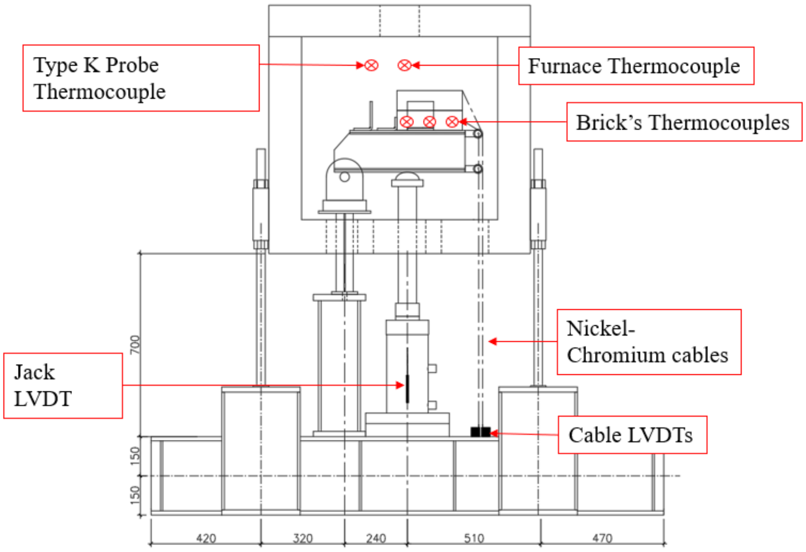

Figure 3-28 – Slip test instrumentation: LVDTs and thermocouples

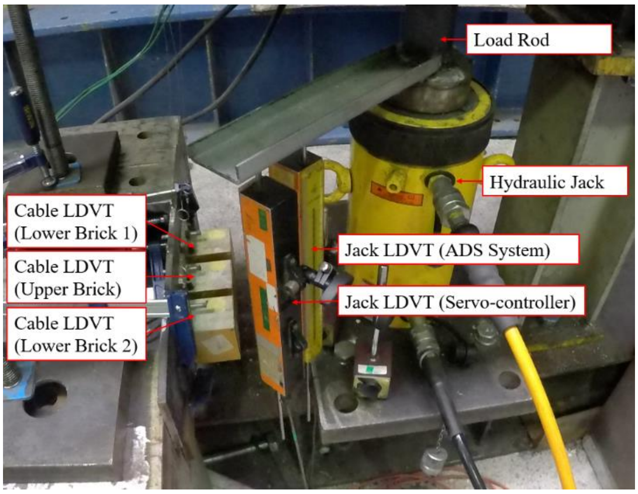

Figure 3-29 – Slip test instrumentation: LVDTs – Details

The friction angle (*ø*) between the bricks may be calculated by the arctangent of the vertical displacement measured at the jack (d_v) divided by the offset between the axis of the jack and the axis of the hinge (**Figure 3-26**b), as shown in **Eq. 5:**

$$\varnothing = atan\,(d_v / 240mm) \tag{5}$$

The furnace had built-in type K thermocouples for controlling the temperatures, but an additional type K probe thermocouple was used to measure the temperatures inside of the furnace during the test. Additionally, three type K wire thermocouples were used to measure the temperatures inside the brick (**Figure 3-30**).

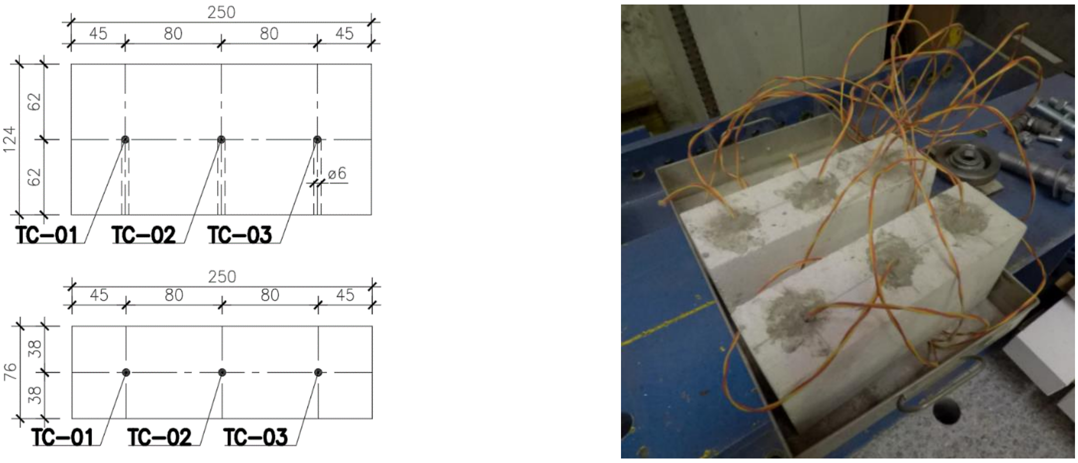

a) b)

Figure 3-30 –Thermocouples embedded in the bricks: a) Position; b) Specimens

The specimens consisted of two stacked bricks of type *B* (250×124×76 mm), therefore the final dimensions of the prism were 250×124×152 mm (Oliveira *et al*, 2019). The prism can be seen in **Figure 3-31**.

Figure 3-31 – Prism composed by two stacked bricks inside the furnace chamber

In order to confirm that the temperature was homogenized within the specimen, the bottom brick had thermocouples **Figure 3-32** shows the position of the thermocouples installed in the specimens and the development of the temperature in the specimens. At the time of the application of the mechanical load the specimen was under homogeneous temperature.

The experimental procedure had the following steps: *i*) The bricks were placed at the inclinable beam and the instrumentation (LVDT and thermocouples) was installed; *ii*) The furnace was set to heat at 10ºC/min; *iii*) When the temperature test was reached, a dwell time of 90 minutes was applied; *iv*) The hydraulic jack was set to move upward at a rate of 0.5 mm/s, up to the maximum of 170 mm; *v*) When the upper brick slips, a difference of the readings of LVT01 and LVT02 is observed, at this moment the friction angle is reached; *vi*) The friction angle is calculated based on the displacement of the hydraulic jack and the offset between the hinge axis and the hydraulic jack axis, as shown in Eq. 5.

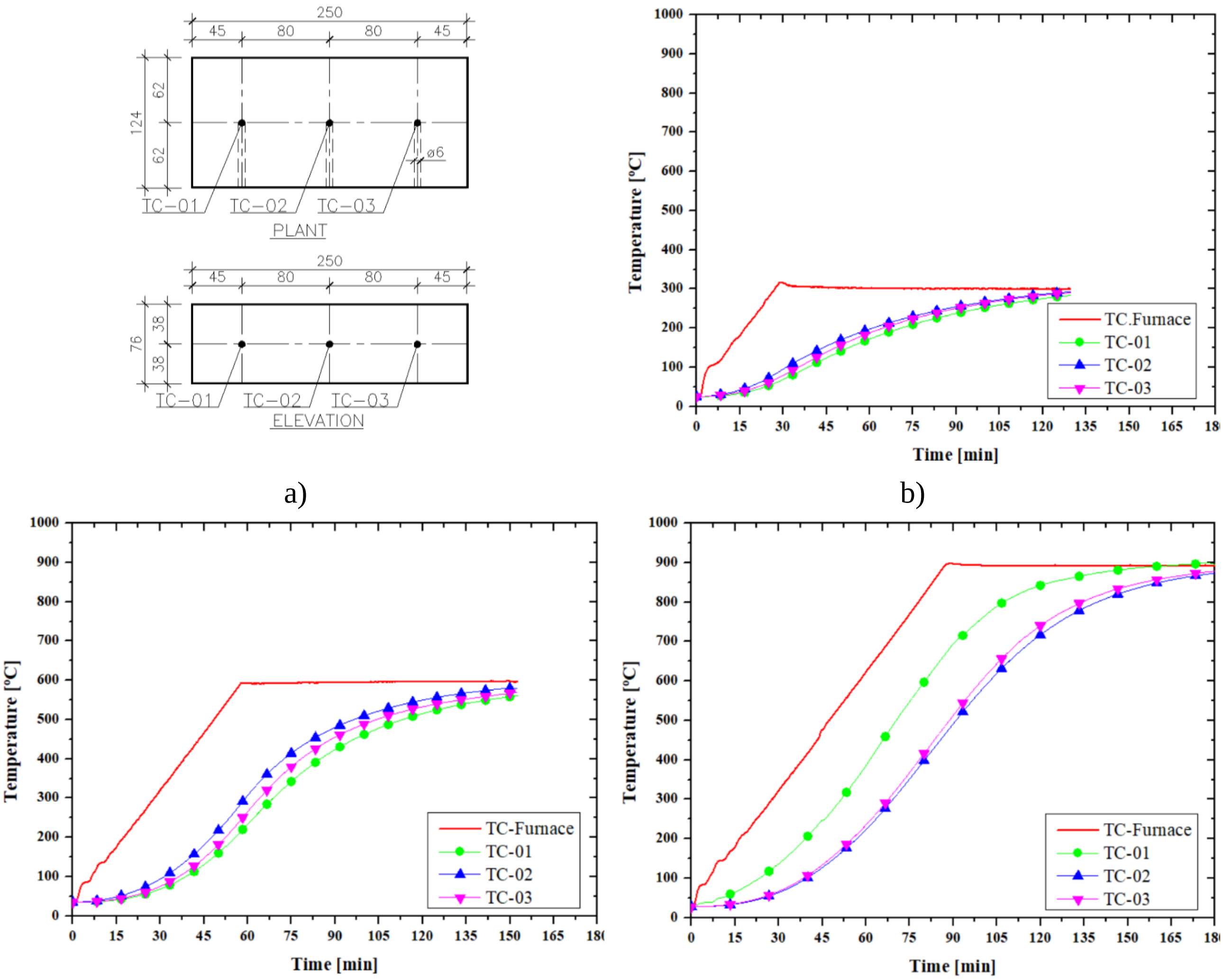

a) b)

c) d)

Figure 3-32 – Temperatures of the slip-test: a) Thermocouple position, b) Temperatures of specimen ST.300.01; c) Temperatures of specimen ST.600.01; d) Temperatures of specimen ST.900.01

3.3.2 Results and discussion

Figure 3-33 shows the displacement curves for the different temperatures. The curves of the graphs are from the first specimen among the tests carried. Six specimens for ambient temperature and three specimens for each temperature were tested. These displacements were measured in the hydraulic jack (jack's LVDT) and the brick (cable LVDT).

The slip test results for ambient temperature, 300ºC, 600ºC and 900ºC are presented in Table 3-8. The friction angle (*ø*), friction coefficient (*μ*) and the standard deviations are also presented. The average friction angle at ambient temperature is 30.9º. The friction angle at 300ºC was 26.5º that is below the value at ambient temperature. However, a small increase is observed when comparing with the value at 300ºC, being 27.0º for 600ºC and 27.9º for 900ºC (**Figure 3-34**). The reduction of the friction coefficient when compared to the ambient temperature results was 14.2%, 12.6% and 9.7% for the temperatures of 300ºC, 600ºC and 900ºC, respectively. A small standard deviation was found for all test series.

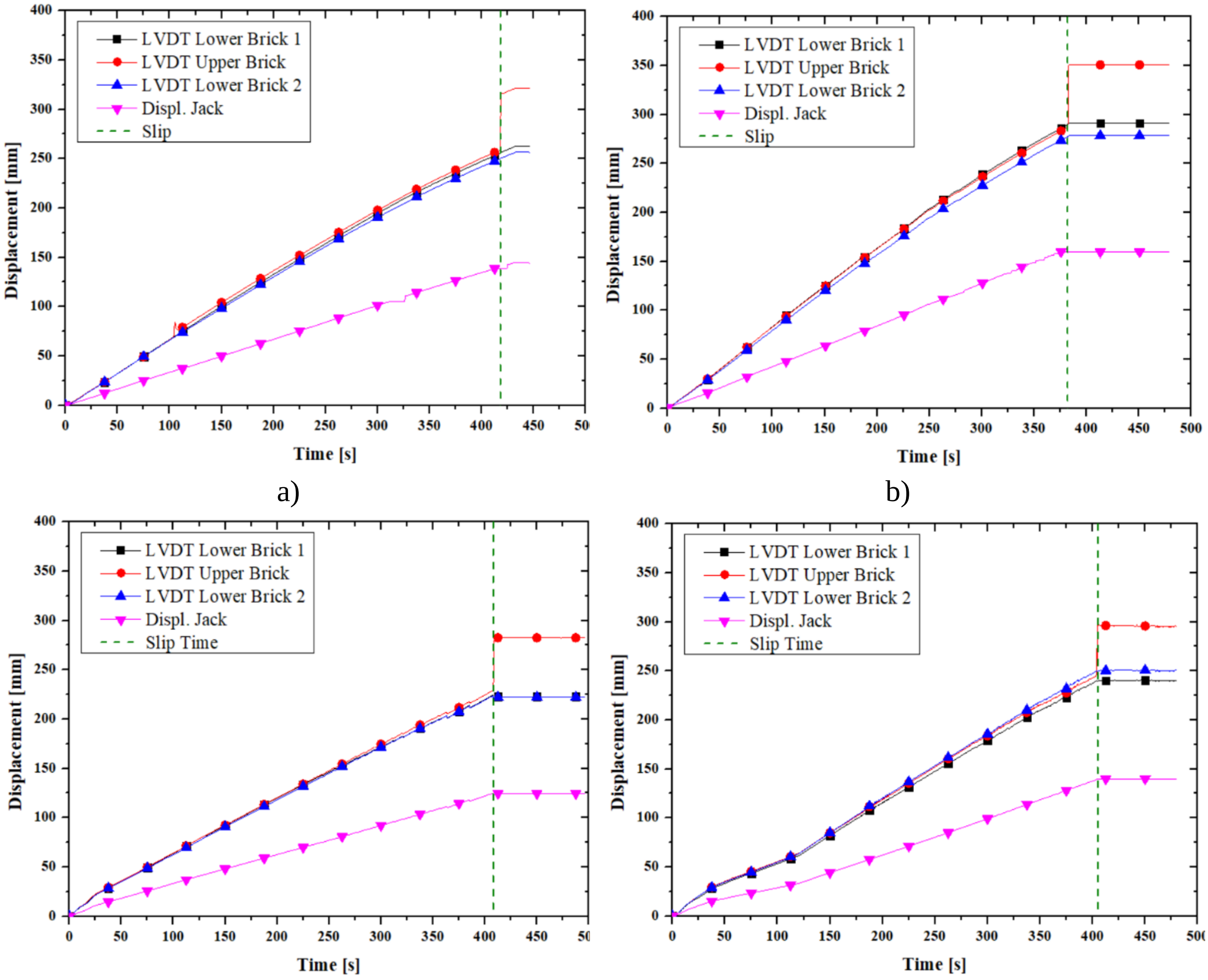

a) b) c) d)

Figure 3-33 – Displacements: a) ambient temperature; b) 300ºC; c) 600 ºC; d) 900 ºC

The configuration of the specimens before and after the tests are shown in **Figure 3-35**. The slipping of the bricks occurred aligned as expected, the bricks did not touch the lateral steel pieces used to protect the resistances of the furnace.

Table 3-8 – Results of the slip tests at ambient and high temperatures

Test series	Temperature	Specimen	Hydraulic jack displacement	Horizontal offset	$\o$	μ	$\o_{avg}$	$\sigma(\o)$	μ_{avg}	$\sigma(\mu)$
			[mm]	[mm]	[°]	[-]	[°]	[°]	[-]	[-]
ST.RT	20 °C	ST.RT.01A	138.9	240.0	30.06	0.58	30.9	0.78	0.598	0.02
		ST.RT.01B	143.6	240.0	30.89	0.60				
		ST.RT.01C	147.8	240.0	31.63	0.62				
		ST.RT.02A	139.1	240.0	30.10	0.58				
		ST.RT.02B	146.6	240.0	31.42	0.61				
		ST.RT.02C	135.5	240.0	29.45	0.56				
ST.300	300 °C	ST.300.01	119.1	240.0	26.39	0.50	26.5	0.49	0.498	0.01
		ST.300.02	122.8	240.0	27.10	0.51				
		ST.300.03	116.6	240.0	25.91	0.49				
ST.600	600 °C	ST.600.01	124.8	240.0	27.47	0.52	27.0	0.55	0.510	0.01
		ST.600.02	118.4	240.0	26.26	0.49				
		ST.600.03	124.2	240.0	27.36	0.52				
ST.900	900°C	ST.900.01	133.4	240.0	29.07	0.56	27.9	1.17	0.530	0.03
		ST.900.02	129.4	240.0	28.33	0.54				
		ST.900.03	118.6	240.0	26.30	0.49				

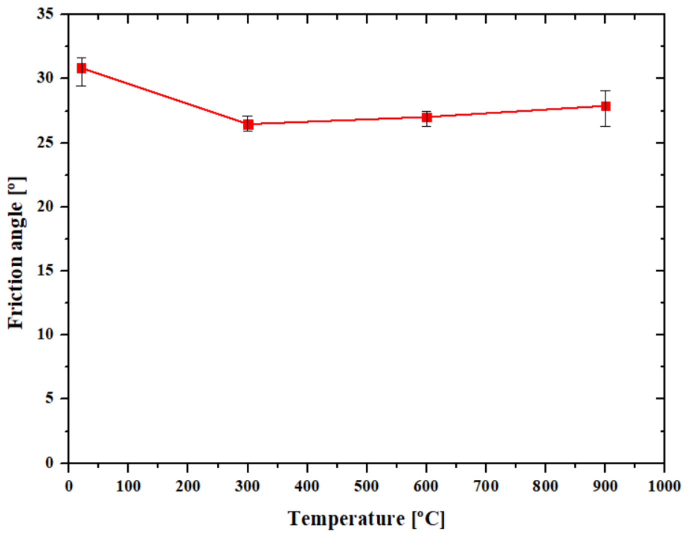

Figure 3-34 – Evolution of the friction angle with the temperature

a) b)

Figure 3-35 – Slip test specimens: a) Beginning of the test; b) After slipping

3.4 Final remarks

This chapter presented the characterization of the masonry units and joints. The compressive strength at ambient and high temperatures of the bricks were assessed. A statistical analysis of the distribution of the brick shape imperfections was carried out. Experimental and numerical studies were performed for analysing the normal behaviour of dry joints: a classical joint closure test was presented, the bed joint closing states were measured for a masonry wallet using DIC, the effects of brick imperfections in height on the loadbearing capacity of the brick and of the wall at ambient and high temperatures were determined and a comparison between the bed and head joints behaviour was presented. The joint tangential behaviour was analysed, and a tailored test device was developed for evaluating the friction coefficient between the bricks at ambient and high temperatures.

Refractory bricks exhibited anisotropic behaviour and mould dependent characteristics. The tested specimens presented different compressive strength (f_c), compressive strain at the peak stress (ε_{c1}), ultimate compressive strain (ε_{cu}) and Young's modulus (E). These differences were found for different shapes of the bricks and for different directions in the same brick. The anisotropic behaviour of the material and the mould dependent mechanical parameters are caused by the pressing and the firing procedure.

The brick shape imperfections followed a Gaussian distribution. The imperfections were found to be smaller (from -1.1 mm up to +0.8 mm) and with a smaller standard deviation ($\sigma = 0.41$ mm) in the directions perpendicular to pressing. In the direction of pressing, higher imperfections (from - 2.4 mm up to +1.4 mm) and a higher standard deviation ($\sigma = 0.84$ mm) were observed. In the pressing direction, the dimensions of the brick were influenced by the pressing procedure and by the amount of material injected in the moulds, whereas in the perpendicular direction mostly the firing process played a role.

A classical joint closure test was performed in two stacked bricks and compared to joint closure measurements on a refractory wallet measured by DIC. It was observed that the heterogeneity on the joint closure was higher in the masonry wallet. In the latter case, the geometric imperfections in a full course influence the contact conditions of the bricks, resulting in joints with higher heterogeneity and compressibility.

A numerical study was presented evaluating the effects of bricks’ height imperfections on the loadbearing capacity of the brick itself. The five original loading cases were expanded to seven loading cases aiming to consider “banana shaped” bricks. The load bearing capacity and the expected crack pattern were determined for each loading case. The crack paths predicted numerically were able to replicate the cracks observed in experimental tests of dry-stacked masonry wallets.

The influence of the bricks’ height imperfections on the behaviour of masonry walls was studied numerically. Two loading levels (3 MPa and 5 MPa) and three temperatures (ambient temperature, 1300 ºC and 1500 ºC) were considered. The brick imperfections were randomly considered in the wall following the statistical distribution obtained in the present research. For the ambient temperature models, the imperfections resulted in stress concentrations and in a non-homogeneous flow of forces through the wall, as observed by Ngapeya *et al* (2018). For the high temperature models, the viscoplastic effects led to reductions in stress concentrations. It was observed that higher temperatures and higher loading levels results in a more homogeneous stress distribution, as the creep strain rate is increased.

An inverse identification of the bed and head joints pressure-overclosure curves was performed based on the experimental results provided by Prietl (2006). It was observed that the head joints present a stiffer behaviour when compared to the bed joints and smaller compressibility, most likely because they are formed by one brick in contact with one brick, while the bed joints reflect the irregularity of the multiple bricks. Consequently, in the latter case the imperfections have larger influence on the joint behaviour, resulting in a thicker joint.

A newly test setup for evaluating the friction coefficient between bricks in dry joints was developed and presented. The equipment was used to evaluate the friction coefficient of the alumina spinel bricks at ambient temperature, 300 ºC, 600 ºC and 900 ºC. A reduction of the friction coefficient was found when subjected to high temperatures.

4 EXPERIMENTAL TESTS ON REFRACTORY MASONRY WALLS UNDER UNIAXIAL COMPRESSION

During service conditions, dry-stacked masonry used in the refractory linings of industrial vessels are submitted to high compressive loads, creep, abrasion, corrosion and thermal shock. The stability of these linings is essential to ensure the safety and efficiency of the industrial process. However, very few experimental studies have been conducted on the behaviour of dry-stacked refractory masonry at ambient and high temperatures at large scale. There is a need for more research to obtain an accurate understanding of the behaviour of these masonry structures, as highly nonlinear behaviour, cracks due to bricks' height imperfections and brittle failure has been observed. The effects of brick's height imperfections (Ngapeya *et al*, 2018) and surface contact unevenness (Zahra and Dhanasekar, 2018) in dry-stacked masonry has been investigated, as well as the joint closure behaviour in refractory (Gasser *et al*, 2004; Nguyen *et al*, 2009; Andreev *et al*, 2012; Allaoui *et al*, 2018). Nevertheless, only a few references can be found in the literature with regards to sub-system scale (wallets) (Prietl, 2006; Prietl *et al*, 2006).

A key issue on the mechanical behaviour of dry-stacked masonry is the joint closure mechanism. Due to bricks' height imperfections and the unevenness surface contact, the presence of dry joints reduces the global stiffness of the linings, leading to a reduction on the stresses generated during heating (Andreev *et al*, 2012; Allaoui *et al*, 2018). Consequently, the joint closure curve has a large impact on the structural behaviour of the linings. Nevertheless, the joint behaviour changes with the dimensions of the bricks, the fabrication tolerances and the aspect ratio of the masonry (Ngapeya *et al*, 2018).

This chapter intends to present a test setup that was previously used to test concrete masonry wallets at high temperatures (Lopes *et al*, 2017; Oliveira *et al*, 2021). Due to the higher mechanical resistance of the tested material, the structural capacity of the reaction frame was improved, the columns and beams were replaced by profiles with a larger cross-section. A hydraulic actuator (3000 kN) and a load cell (5000 kN) with higher capacity were used. Moreover, DIC technique (Dupre *et al*, 2018; Belrhiti *et al*, 2017) was used to map the in-plane displacement fields.

The objective of this work was to study the behaviour of dry-stacked refractory masonry walls at ambient and high temperatures under uniaxial compression loads. Five test series have been studied. Two series at ambient temperature and three series at high temperatures. The experimental program comprised fourteen specimens(Table 4-1):

- Test series S01.AT.LBC: carried out at ambient temperature (AT) with the objective of evaluating the loadbearing capacity (LBC) of the wall.
- Test series S02.AT.CIC: carried out at ambient temperature (AT) aiming to assess the behaviour of the dry-stacked masonry under cyclic loads (CIC).

- Test series S03.HT.LL8: carried out at high temperatures (HT) aiming to evaluate the thermomechanical performance of the masonry under constant load level of 8 MPa (LL8). The mechanical load was applied and then the specimen was heated according to the standard ISO 834-1 (1999).
- Test series S04.HT.RTE: tested at high temperatures (HT) aiming to assess the behaviour of masonry under restrained thermal elongation (RTE). First, a mechanical load of 5 MPa was applied to the specimen, the hydraulic jack is blocked at its current position and the specimen was heated with the same heating rate of test series S03.HT.LL8.
- Test series S05.HT.LL10: carried out at high temperatures (HT) aiming to evaluate the thermomechanical behaviour of the masonry wall with higher slenderness ratio under a 10 MPa load level (LL10). The mechanical load was applied and then the specimen was heated with the same heating rate of S03.HT.LL8 and S04.HT.RTE.

Table 4-1 – Test series for the uniaxial tests

Series	Specimen	Temperature of the test	Thermal restraining	Type of control	Load level
S01.AT.LBC	S01.AT.LBC.01	Ambient temperature	None	Displacement	Up to failure
	S01.AT.LBC.02				
	S01.AT.LBC.03				
S02.AT.CIC	S02.AT.CIC.01			Displacement	Cyclic loading 1, 2, 5 and 8 MPa
	S02.AT.CIC.02				
	S02.AT.CIC.03				
S03.HT.LL8	S03.HT.LL8.01	High temperatures	Constant loading and no thermal restraining	Load	8 MPa
	S03.HT.LL8.02				
	S03.HT.LL8.03				
S04.HT.RTE	S04.HT.RTE.01		Thermal restraining	Displacement	Pre-load: 5 MPa + Effects of restrained thermal elongation
	S04.HT.RTE.02				
	S04.HT.RTE.03				
S05.HT.LL10	S05.HT.LL10.01		Constant loading and no thermal restraining	Load	10 MPa
	S05.HT.LL10.02				

4.1 Test setup

The experimental tests were carried out at the Laboratory of Testing Materials of the University of Coimbra, in Portugal. The test setup has been used before (Lopes *et al*, 2017; Oliveira *et al*, 2021) and was improved for this experimental campaign. The schematic view of the test set-up is shown in **Figure 4-1**.

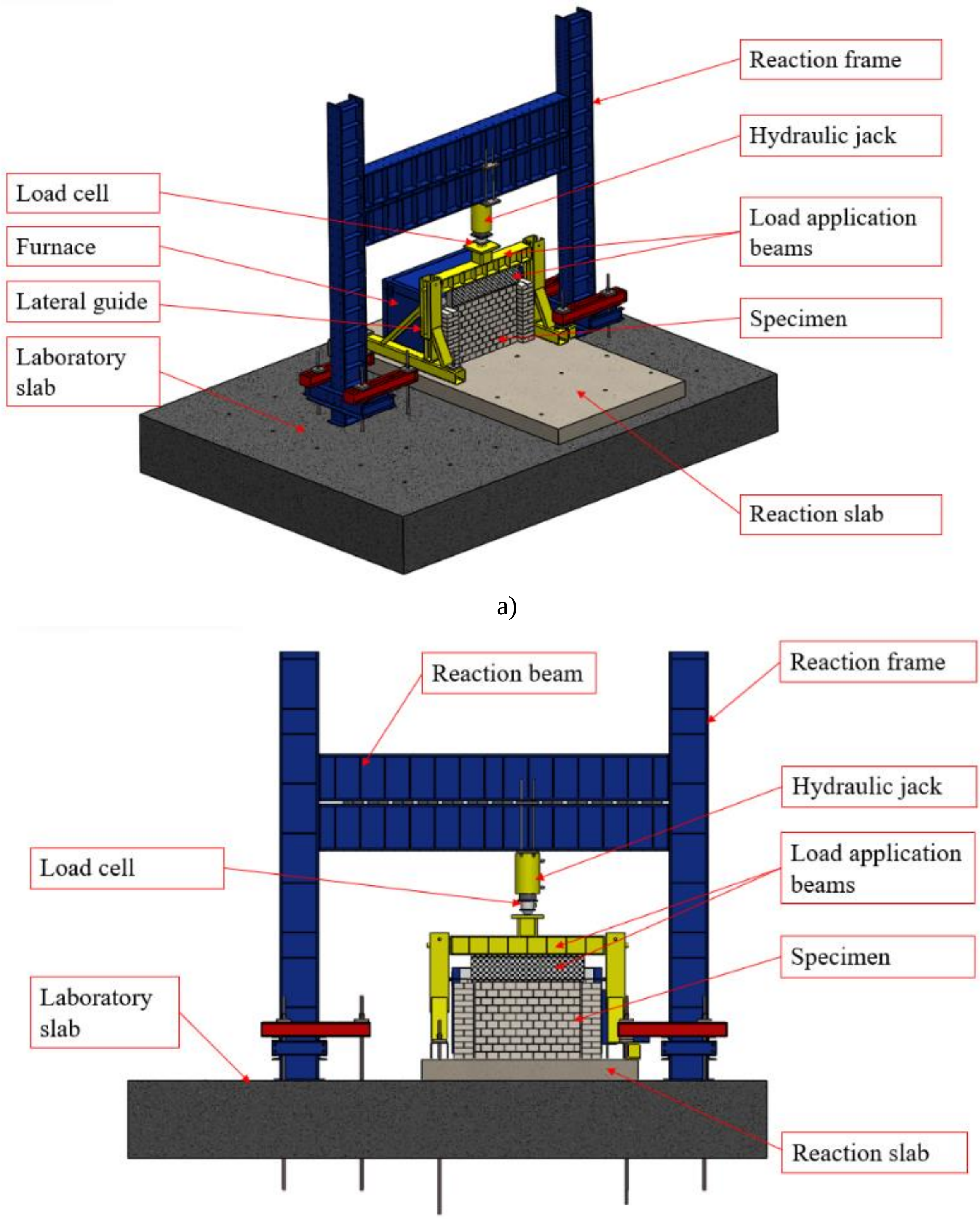

a)

b)

Figure 4-1 – Test set-up: a) Isometric view; b) Front view

The test set-up consisted of one reaction frame composed by two HEB500 columns and two overlapping HEB600 beams (4500 mm span). The hydraulic jack had the capacity of 3000 kN and the load cell used to measure the applied load had the capacity of 5000 kN. For the experiments performed at high temperatures one modular electric furnace (45 kVA) was used to heat the specimens. The hydraulic jack applied the load in the plane of the wall by two load beams. The top one was a HEB240 steel beam with web stiffeners and the bottom one was a composite beam (tubular steel section filled with concrete). The verticality of the load application was ensured by two lateral steel frames working as guides. The hydraulic jack was controlled by a servo hydraulic central unit W+B NSPA700/DIG2000. Aiming to limit the heat loses, two masonry columns were built at the edges of the specimens, the gap between the masonry wallet and columns (15 mm) was filled with rockwool, therefore, there was no mechanical restraint at the sides of the specimen.

The reaction frame was bolted to the laboratory slab by eight steel anchors (ø40 mm). The specimens were built in the reaction slab over a 10 mm grout layer. Rockwool was used for the thermal insulation of the reaction slab and to fill the gap between the specimens and the lateral masonry columns. The pictures of the experimental set-up are presented in **Figure 4-2** and **Figure 4-3** for the tests at ambient and high temperatures, respectively.

a) b)

Figure 4-2 – Test set-up at ambient temperatures: a) Front view; b) Back view

a) b) c) d) e) f)

Figure 4-3 – Test set-up at high temperatures: a) General overview of the test setup; b) Back view; c) Specimen in position for testing; d) End of the test; e) Resistances of the furnace; f) Bottom insulation

The load cell used to measure the loading applied to the specimen was placed between the hydraulic jack's head and the loading beams (**Figure 4-4**). The connection between the hydraulic jack and the load beams was pinned.

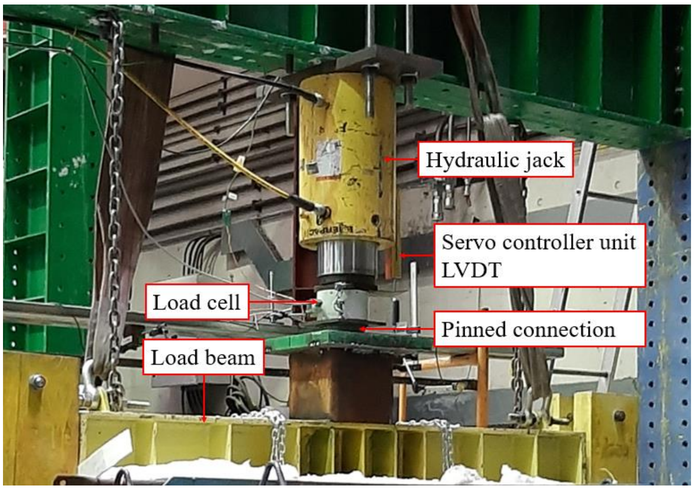

Figure 4-4 – Hydraulic jack and load cell details

The servo hydraulic central unit W+B NSPA700/DIG2000 and the data acquisition system are presented in **Figure 4-5**.

Figure 4-5 – Servo control central unit and data acquisition system

Three LVDTs placed at the top of the steel loading beam were used to measure the in-plane displacements (LVDT-IP). The distance between the LVDTs was 150 mm for test series S01.AT.LBC and 600 mm for the others test series. The positioning of the three in-line LVDTs allowed to identify possible rigid body rotations in the load application beam.

Three laser LVDTs were used to measure the out-of-plane displacements (LVDT-OoP) in the specimens of test series S01.AT.LBC and five LVDTs were used for the other series. Due to the temperatures developed in the specimens, non-contact LVDTs were chosen (Panasonic HL-G1 series). The positioning of the LVDTs is detailed in Figure 4-6.

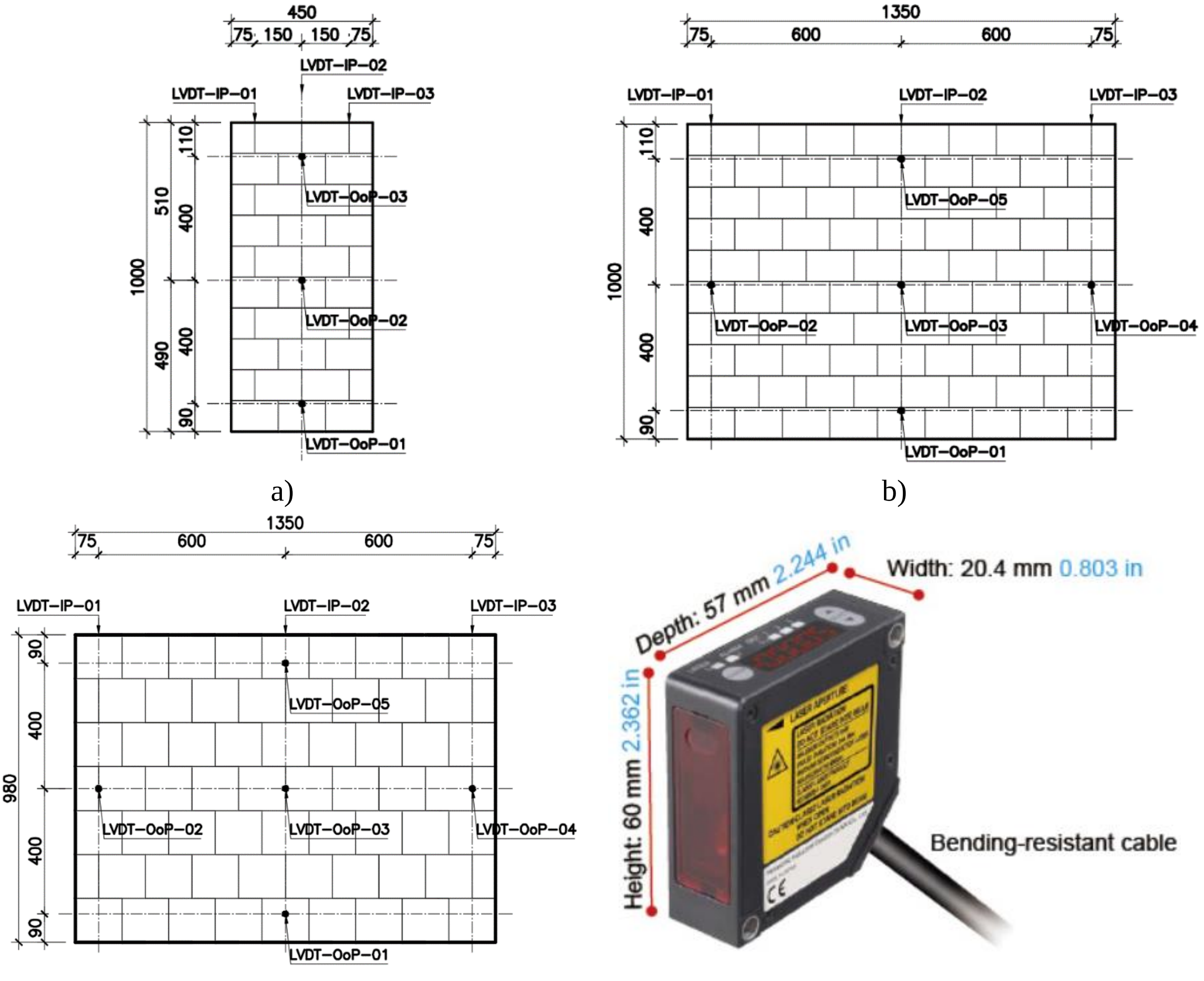

a) b)

c) d)

Figure 4-6 – LVDTs instrumentation: a) Series S01.AT.LBC; b) Series S02.AT.CIC, S03.HT.LL8 and S04.HT.RTE; c) Series S05.HT.LL10; d) Detail of the laser LVDT

Digital image correlation (DIC), a contactless measurement technique, was used to measure the in-plane displacements fields. This technique was developed in the beginning of the 1980’s and improved over the time (Besnard *et al*, 2006). The basic principle is to compare two images that represent different states of the specimen, a reference and a deformed condition. The technique assumes that the grey level distribution follows the material strains and remains homogenous in the subset (Dupre *et al*, 2018; Belrhiti *et al*, 2017). An 18 MPx (5184×3486) camera was used for image acquisition and three LED reflectors were used to provide suitable lighting conditions. The image processing was performed using subsets of 100×100 pixels. The speckle patter application had the following steps: *i*) the bricks were laid on a horizontal plane; *ii*) the speckle pattern was applied by means of an aerograph; *iii*) a dwell time of 48 hours was considered for drying. The speckle pattern application, its details and the DIC system are shown in Figure 4-7.

a) b)

c) d)

Figure 4-7 – DIC: a) Speckle pattern preparation; b) Details of the speckle pattern; c) DIC set-up; d) Camera

The thermal instrumentation comprised eighteen type K wire thermocouples (TC) embedded in the bricks (10 mm depth). Nine installed in the hot face (TC-HF) and nine in the cold face (TC-CF), as detailed in Figure 4-8. The holes used to install the TCs (ø6 mm) were made in the bricks using diamond crown drills. Subsequently, the thermocouples were placed in position and grouted. Additionally, one type K probe thermocouple was used to feed the furnace controller and one type K probe thermocouple was used to record the temperature in the furnace. The type K thermocouples are composed by Nickel-Chromium / Nickel-Alumel alloys and can operate between -270 ºC and 1260ºC.

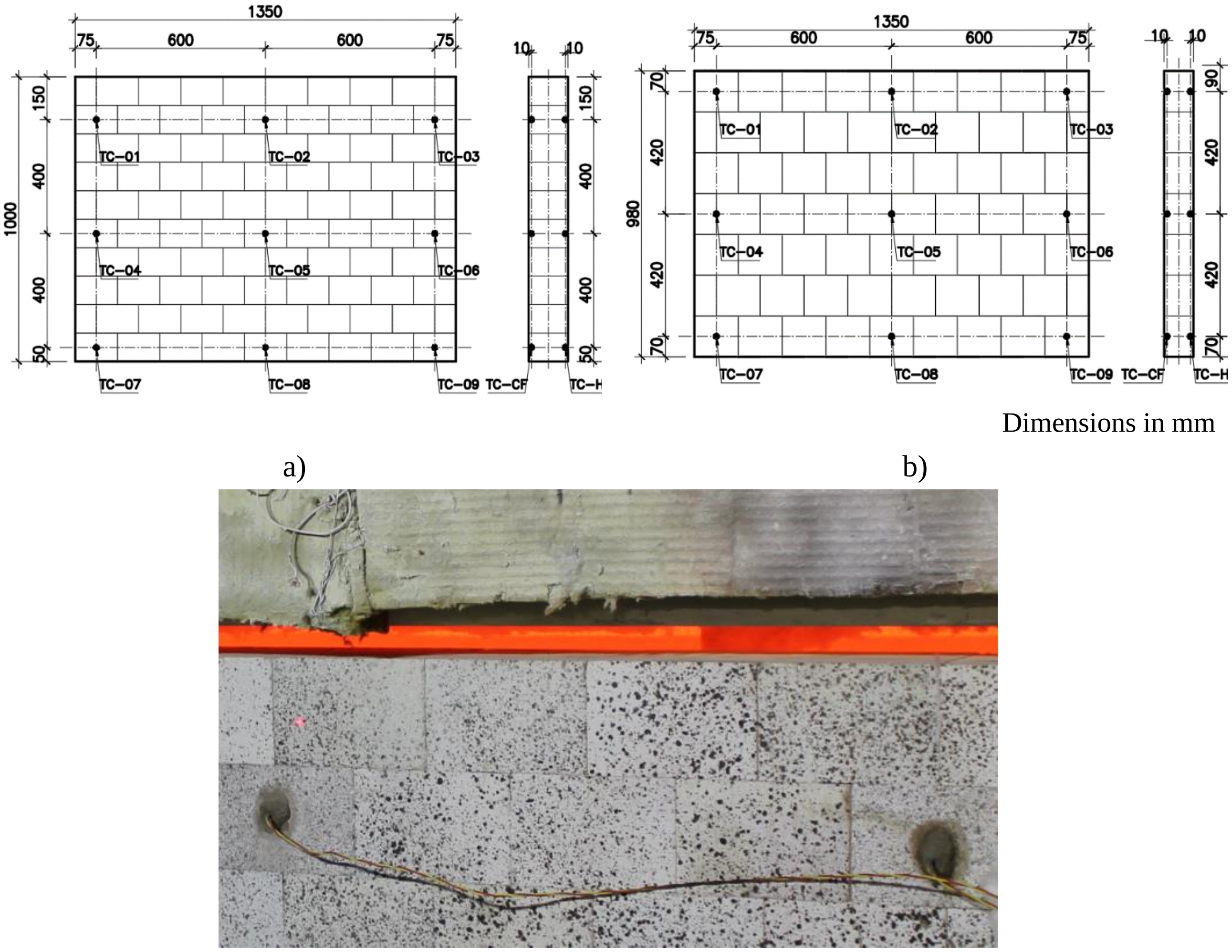

Dimensions in mm

a)

b)

c)

Figure 4-8 – Thermal instrumentation: a) Test series S03 and S04; b) Test series S05; c) Detail of thermocouples embedded in the bricks

4.2 Specimens and test procedure

The specimens consisted of dry-stacked masonry walls made of high-alumina bricks. The properties of the material and the dimensions of the bricks were described in Section 3.1. In order to fully characterize the masonry thermomechanical behaviour, three different configurations were used in the tests. **Figure 4-9** presents the general arrangement of the specimens.

The choice of the thickness for test series S01 to S04 (140 mm) was based on the usual thickness of the working lining of steel ladles. For test series S05, a smaller thickness (100 mm) was used aiming to increase the slenderness of the wall. The length of the wall for test series S01 (450 mm) was chosen based on the structural capacity of the loading frame and the maximum capacity of the hydraulic jack, as this series aims to assess the loadbearing capacity of the wall. The length of the specimens used in test series S02 to S05 (1350 mm) was chosen based on the dimensions of the opening of the electric furnace used.

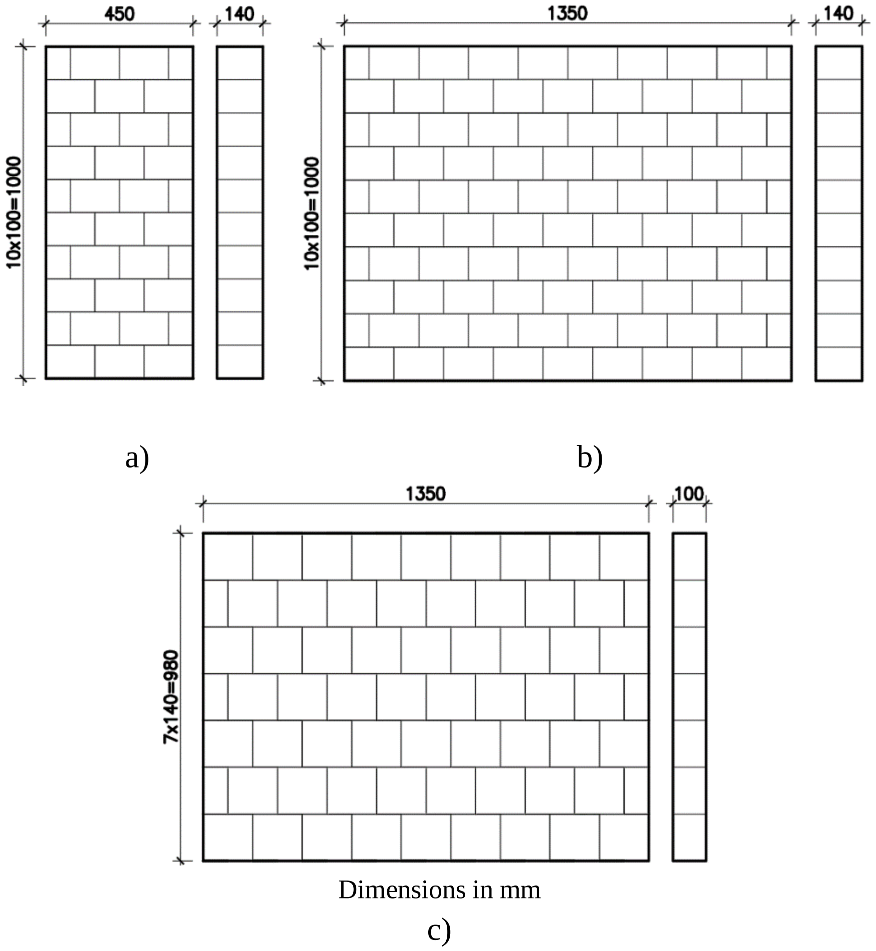

a) b)

c)

Figure 4-9 – Uniaxial specimen dimensions: a) Test series S01.AT.LBC; b) Test series S02.AT.CIC, S03.HT.LL8 and S04.HT.RTE; c) Test series S05.HT.LL10

The following test procedures were used in the different test series:

- **Test series S01.AT.LBC:** The objective of test series S01.AT.LBC was to assess the loadbearing capacity of the refractory masonry walls. The test procedure in series S01.AT.LBC had the following steps: *i*) the masonry specimens were built in the testing system; *ii*) the loading beams were placed on the top of the specimens using a crane; *iii*) the instrumentation was installed; *iv*) the loadbearing capacity test was performed under displacement control at a rate of 0.01 mm/s up to failure of the specimen.

- **Test series S02.AT.CIC:** The objective of test series S02.AT.CIC was to assess the behaviour of refractory masonry under cyclic loading. Steps *i*, *ii* and *iii* of this test procedure were similar to the ones presented for test series S01.AT.LBC. Then: *iv*) the test was performed under displacement control at a rate of 0.01 mm/s; v) the wall was submitted to four loading and unloading cycles with increasing load, to the following stress levels: 1, 2, 5 and 8 MPa. The specimens were not tested up to the failure.

- **Test series S03.HT.LL8:** Series S03.HT.LL8 was tested at high temperatures. Steps *i*, *ii* and *iii* of the test procedure were similar to the ones presented for series S01.AT.LBC. Then: *iv*) the specimen was loaded under displacement control at a rate of 0.01 mm/s up to 8 MPa at ambient temperature, *v*) the control procedure was changed to load control and set to keep the current load; *vi*) the furnace was turned on and the specimen was heated according to the standard fire curve ISO 834-1 (1999); *vii*) the wall was monitored for five hours: the temperatures, applied load, in-plane and out-of-plane displacements were recorded. The specimens were not tested up to the failure due to limitations on the maximum operating time of the furnace.

- **Test series S04.HT.RTE:** The objective of series S04.HT.RTE was to assess the mechanical behaviour of refractory masonry walls subjected to restrained thermal elongation. Steps *i*, *ii* and *iii* of the test procedure were similar to the ones presented for series S01.AT.LBC. Then: *iv*) the specimen was loaded under displacement control at the rate of 0.01 mm/s up to 5 MPa; *v*) the hydraulic jack was fixed at its current position; *vi*) the furnace was turned on and the specimen was heated according to the standard fire curve ISO 834-1 (1999); *vii*) the wall was monitored for five hours: the temperatures, applied load, in-plane and out-of-plane displacements were recorded. The specimens were not tested up to the failure due to limitations on the maximum operating time of the furnace.

- **Test series S05.HT.LL10**: The objective of series S05.HT.LL10 was to assess the mechanical behaviour of refractory masonry walls subject to constant load (10 MPa) under increasing temperature. Steps *i*, *ii* and *iii* of the test procedure were similar to the ones presented for series S01.AT.LBC. Then: *iv*) the specimen was loaded under displacement control at a rate of 0.01

mm/s up to 10 MPa at ambient temperature, *v*) the control procedure was changed to load control and set to keep the current load; *vi*) the furnace was turned on and the specimen was heated according to the standard fire curve ISO 834-1 (1999); *vii*) the wall was monitored for five hours: the temperatures, applied load, in-plane and out-of-plane displacements were recorded. Failure occurred to the combined stress level, thermal bowing and temperature increase.

4.3 Results and discussion

The experimental results are presented and discussed in this section. For each test series, results in terms of displacements, strains, forces, stresses, temperatures are presented and discussed. Wherever possible, comparisons with literature results are made. The experimental results allowed to identify the effects of the stress concentrations caused by brick's height imperfections in the mechanical behaviour of the bricks and in the loadbearing capacity of the specimens, the evolution of the wall's stiffness with the load application, the developed crack patterns and the mechanical behaviour of the specimens at ambient and high temperatures.

4.3.1 Test series S01.AT.LBC

Test series S01.AT.LBC aimed to evaluate the loadbearing capacity of the specimen. The evolution of the in-plane and out-of-plane displacements measured in the tests are being presented in **Figure 4-10** and **Figure 4-11**, respectively. A small scattering on the in-plane displacements was observed, as expected for masonry walls. The differences in the readings of LVDT-IP-1 and LVDT-IP-3 indicated a slight rotation of the load application beam. The positive displacement rate at LVDT-IP-1 of specimen S01.AT.LBC.02 (**Figure 4-10**b) and the LVDT-IP-3 of specimen S01.AT.LBC.03 (**Figure 4-10**c) also evidenced this rotation. Small out-of-plane displacements were observed during the tests for all specimens (**Figure 4-11**), which indicates a good overall quality of the wall construction and ensures the verticality of the applied load.

The evolution of the forces applied to the specimen and the evolution of the average in-plane displacements are being presented in **Figure 4-12**. The maximum force was 1100 kN (17.5 MPa), 851 kN (13.5 MPa) and 1417 kN (22.5 MPa) for the tested specimens, respectively. The maximum average in-plane displacement by the end of the test was 4.71 mm ($\varepsilon = 0.0005$), 5.11 mm ($\varepsilon = 0.0005$) and 6.12 mm ($\varepsilon = 0.0006$), respectively.

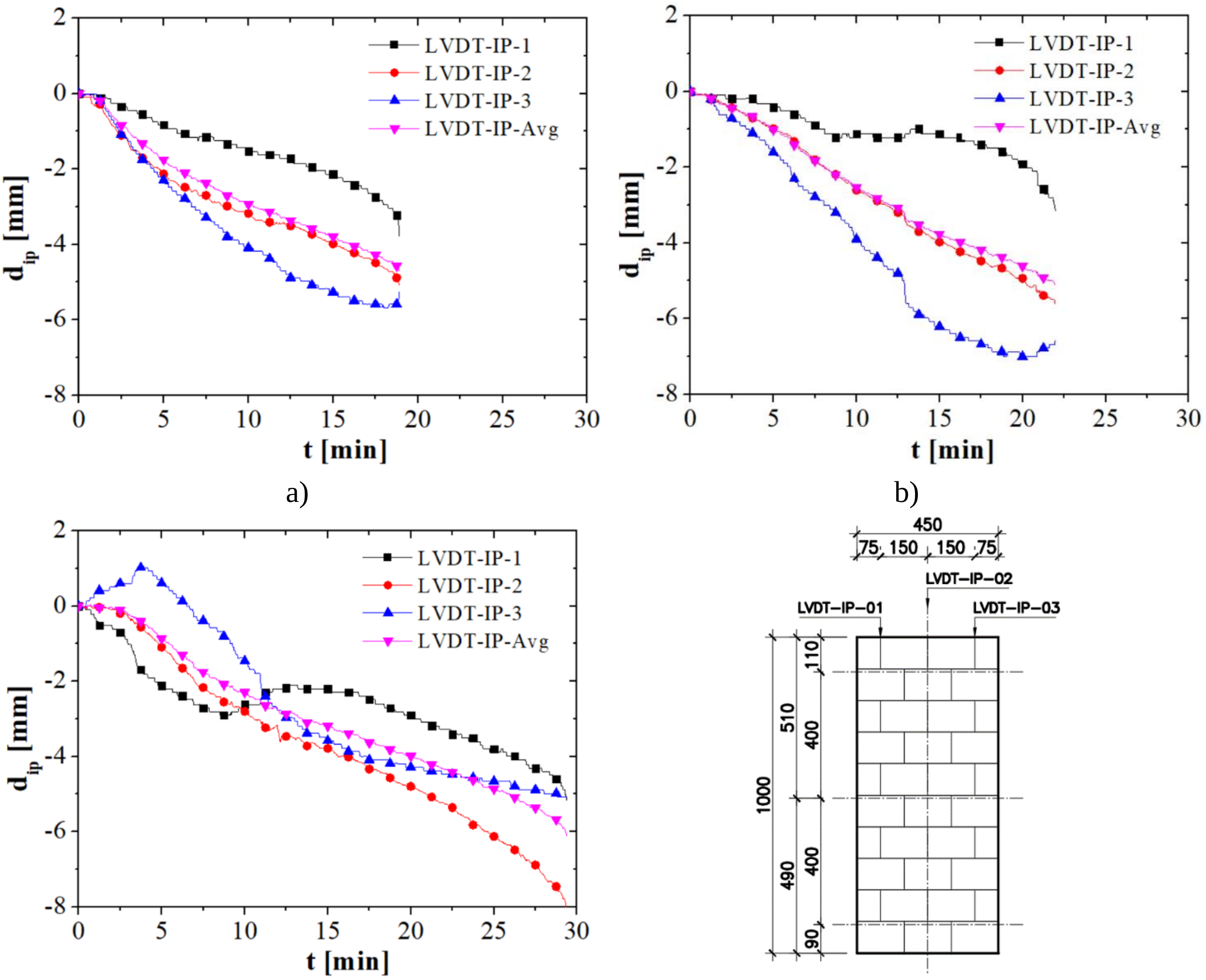

a) b)

c) d)

Figure 4-10 – Test series S01.AT.LBC – In-plane displacements: a) S01.AT.LBC.01; b) S01.AT.LBC.02; c) S01.AT.LBC.03; d) LVDTs location

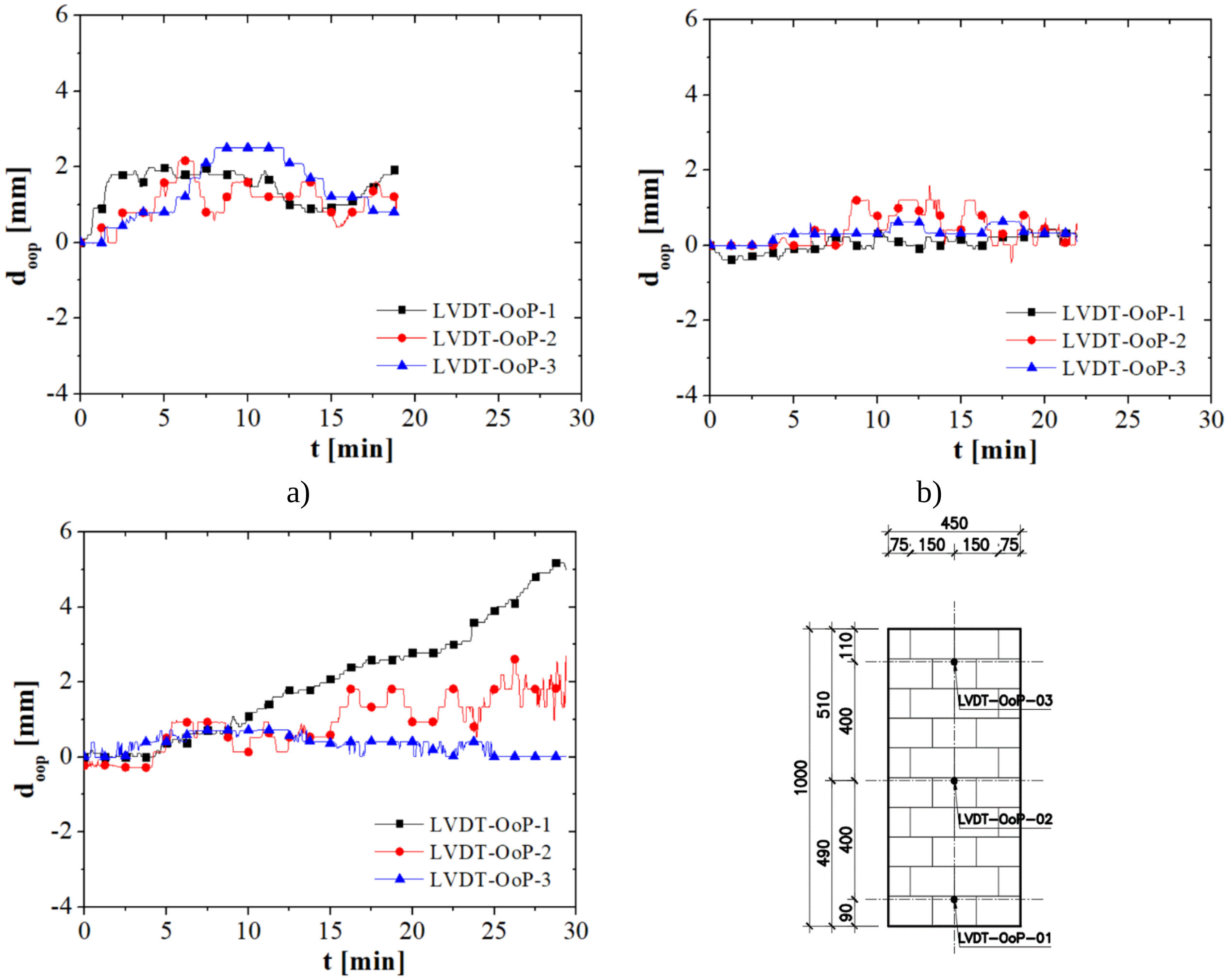

a) b) c) d)

Figure 4-11 – Test series S01.AT.LBC – Out-of-plane displacements: a) S01.AT.LBC.01; b) S01.AT.LBC.02; c) S01.AT.LBC.03; d) LVDTs location

The stress-strain curves of test series S01.AT.LBC are presented in **Figure 4-13**. Three different stages were observed: *i*) joint closure; *ii*) linear behaviour; *iii*) plastic behaviour and failure. During stage *i*, the stiffness of the wall increased from almost zero up to 6.2 GPa. In this stage crushing of brick's initial non-plane surfaces occurs (Allaoui *et al*, 2018; Gasser *et al*, 2004; Andreev *et al*, 2012). The joint closure curve is strongly heterogeneous along the joints as it is influenced by the bricks shape imperfections, bricks surface roughness and construction faults (Allaoui *et al*, 2018; Gasser *et al*, 2004; Andreev *et al*, 2012; Zahra and Dhanasekar, 2018; Ngapeya *et al*, 2018).

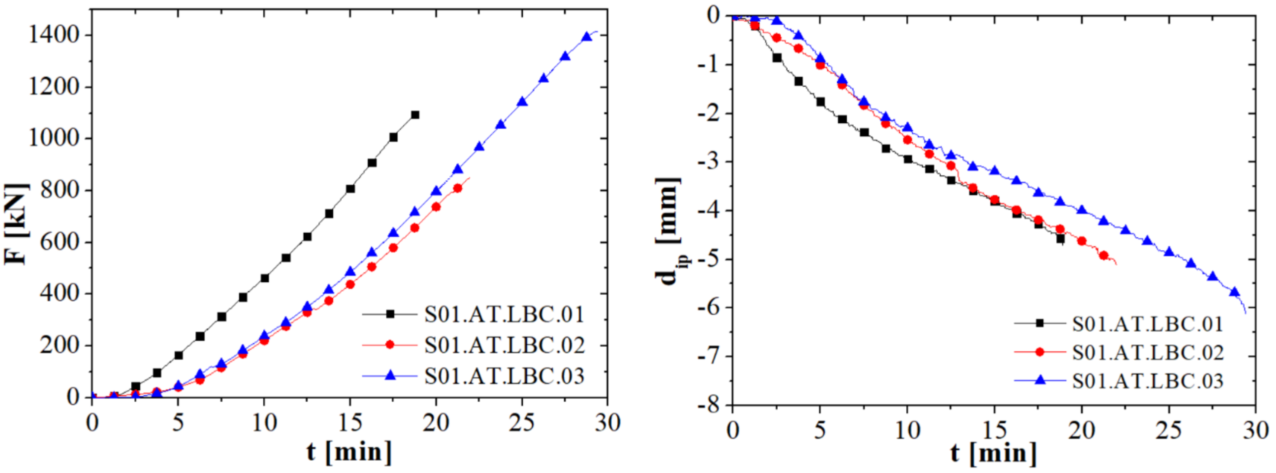

a) b)

Figure 4-12 – Test series S01.AT.LBC: a) Force vs time; b) Average in-plane-displacement versus time

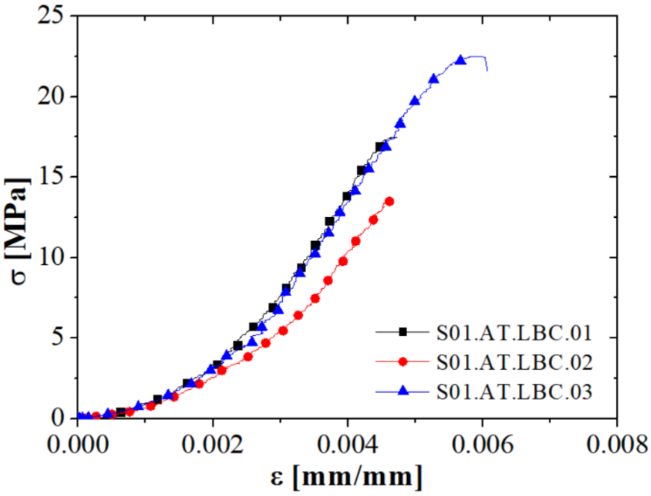

Figure 4-13 – Test series S01.AT.LBC – Stress-strain curves

During stage *ii*, a linear behaviour was observed in the stress-strain curves, however the stiffness of the wall was significantly smaller than the Young's modulus of the brick, indicating a non-homogeneous stress distribution in the wall, most likely caused by the bricks' shape imperfections. Ngapeya *et al* (2018) reported a similar behaviour where the non-homogeneous stress distributions along the wall led to a reduction of its structural capacity. The non-homogeneous stress distribution in the wall was also evidenced by the DIC analysis. Figure 4-14 presents the measured in-plane displacement fields for specimens S01.AT.LBC.02 and S01.AT.LBC.03.

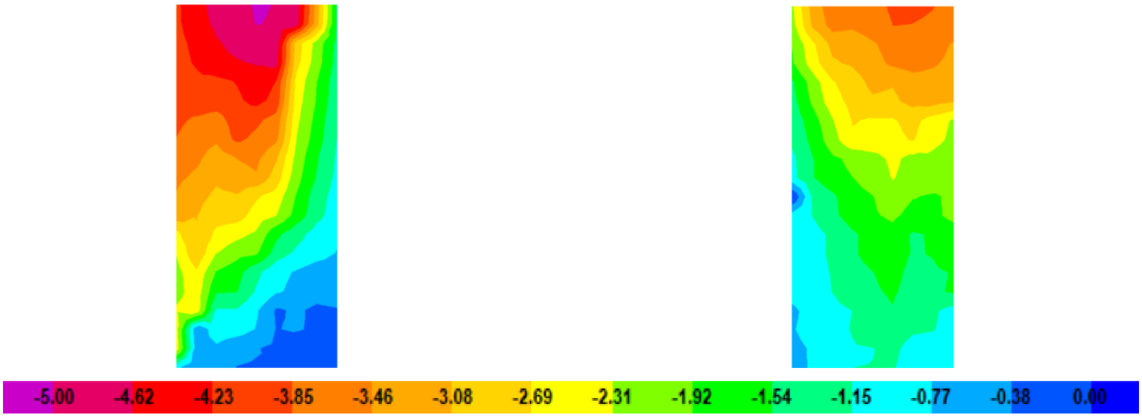

a) b)

Figure 4-14 – Test series S01.AT.LBC – In-plane displacement fields: a) S01.AT.LBC.02; b) S01.AT. LBC.03 (in mm)

During stage *iii*, a slight decrease of the wall’s stiffness was observed, which is typical on masonry due to the development of cracks in the material. These cracks are mostly thin and distributed in the specimen. A very brittle failure was observed in all specimens. The compressive strength for specimens S01.AT. LBC.01, S01.AT. LBC.02 and S01.AT. LBC.03 was 17.5 MPa, 13.5 MPa and 22.5 MPa, respectively. Specimen S01.AT.LBC.02, presented a low compressive strength due to an uneven load distribution in the specimen, caused by a relatively large shape imperfection, as observed in the DIC analysis (Figure 4-14a). The average compressive strength was 17.8 MPa (20.0 MPa if specimen S01.AT.LBC.02 is disregarded). The failure sequence is presented in Figure 4-15. **Figure 4-16** presents the picture taken by the DIC camera during the failure of specimen S01.HT.LBC.02.

a) b) c)

Figure 4-15 – Test series S01.HT.LBC – Images of testing sequence: a) Before testing; b) Failure; c) After testing

Figure 4-16 – Test series S01.HT.LBC.02 – Specimen failure

4.3.2 Test series S02.AT.CIC

Test series S02.AT.CIC aimed to evaluate the behaviour of refractory masonry under cyclic load. The evolution of the in-plane and out-of-plane displacements measured in the tests are being presented in **Figure 4-17** and **Figure 4-18**, respectively. As expected, a small scattering on the in-plane displacements was observed. As in the previous series, small out-of-plane displacements were observed during the tests (**Figure 4-18**), which indicates a good overall quality of the wall construction and ensures the verticality of the applied load.

Figure 4-19 presents the stress-strain curves obtained experimentally for test series S02.AT.CIC. Based on the stress-strain curve, it is possible to observe an increasing residual strain after each loading cycle. This residual strain was caused by the crushing of initially non-flat brick's surfaces in contact at the bed joints. The evolution of the residual strain with the applied load is shown in Figure 4-20a. The crushing of brick's surfaces happened during the loading cycles of the tests and resulted in the increase of the contact area between the bricks. Consequently, it increased the stiffness of the wall. As an example, the evolution of the stiffness of the specimen S02.AT.CIC.02 with the load cycles is presented in Figure 4-20b. The values shown in the graph are the maximum stiffness measured for each cycle. The values measured during the loading and unloading stages are presented in blue and red, respectively. The numbers in the subscript stand for the load cycle and the letters L and U stand for loading and unloading stages, respectively. The stiffness of the wall (13.0 GPa in the last unloading cycle) was significantly lower than the one of the material (28.8 GPa), indicating stress concentrations in the specimen.

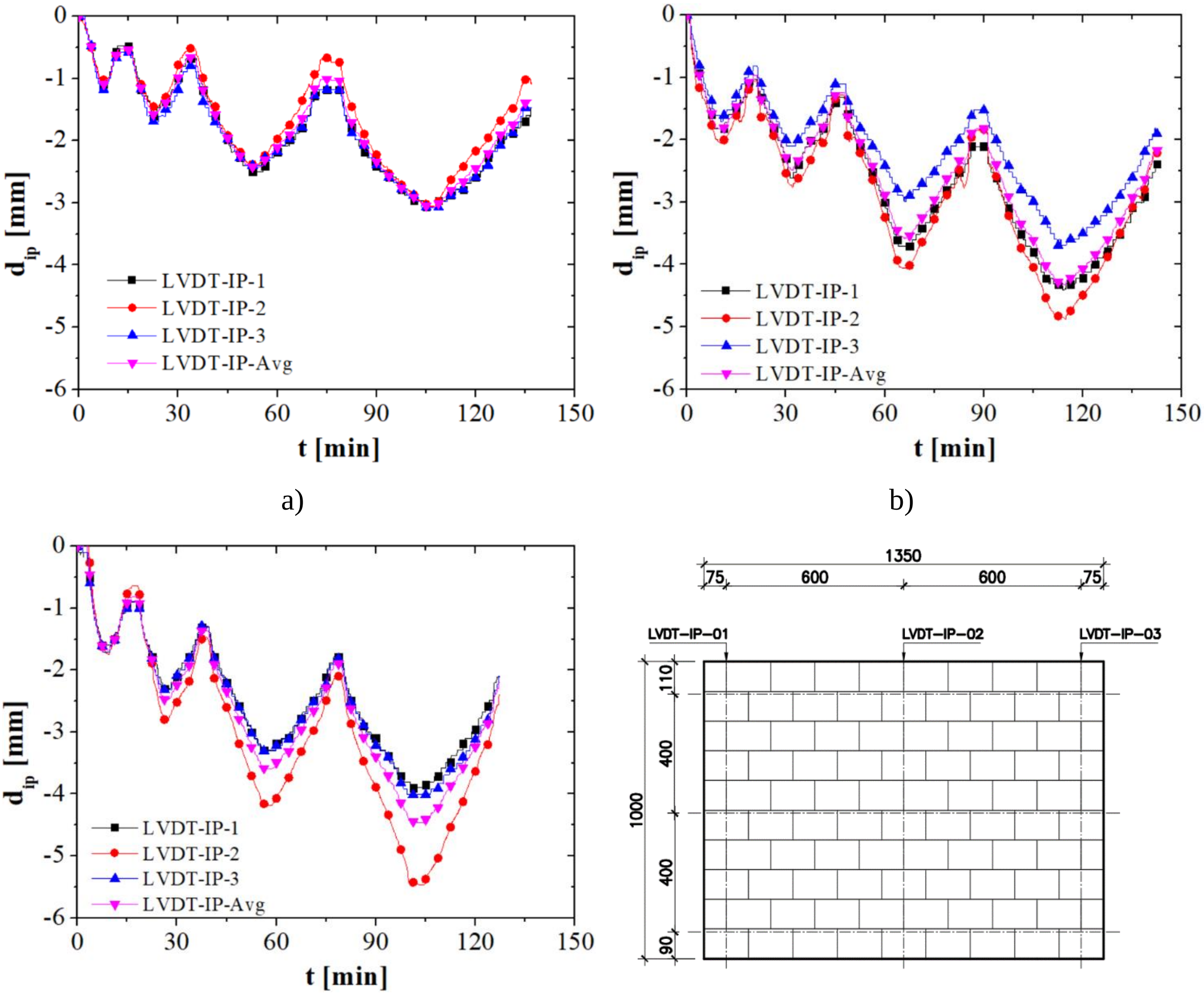

a)

b)

c)

d)

Figure 4-17 – Test series S02.AT.CIC – In-plane displacements: a) S02.AT.CIC.01; b) S02.AT.CIC.02; c) S02.AT.CIC.03; d) LVDTs location

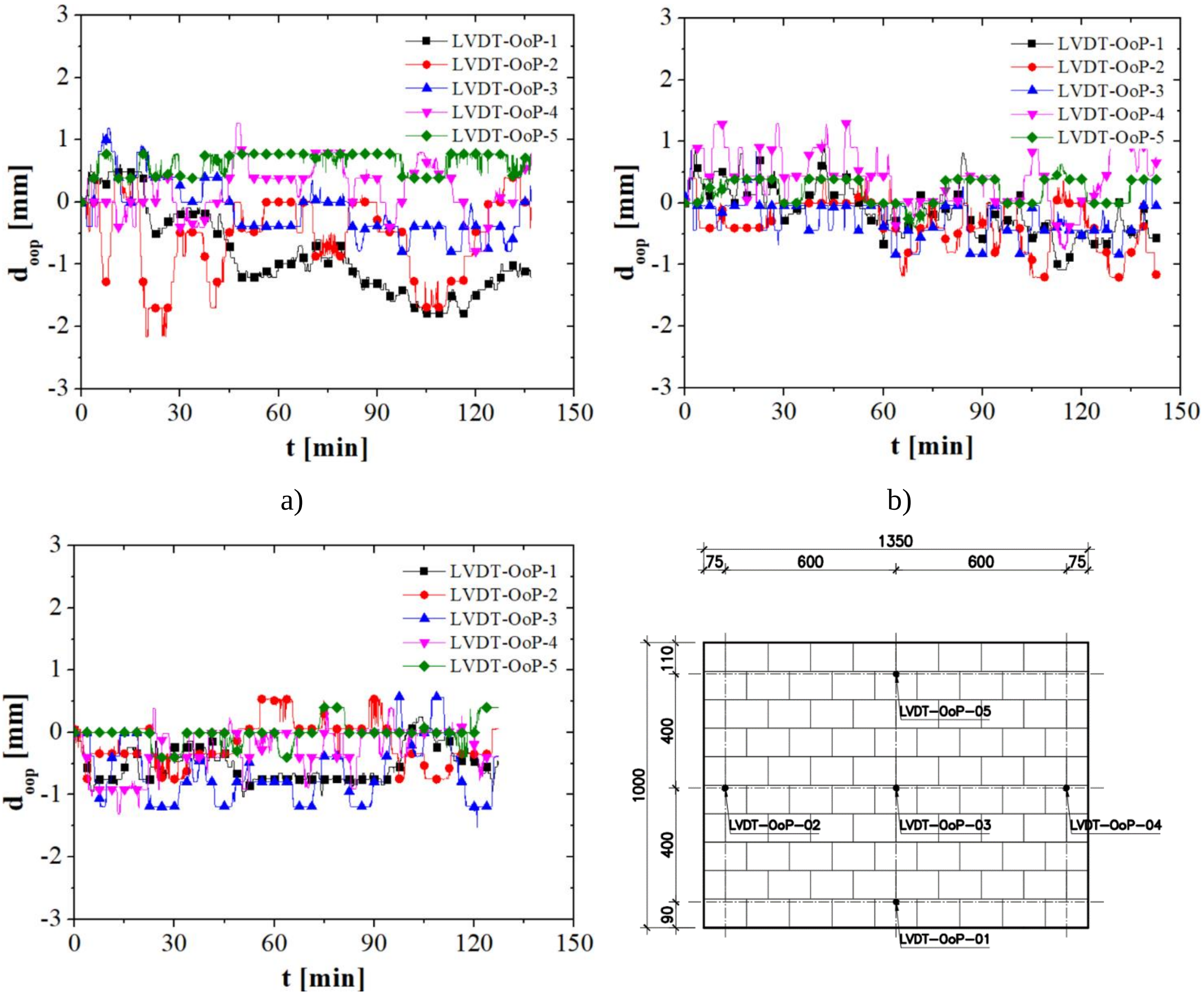

a) b)

c) d)

Figure 4-18 – Test series S02.AT.CIC – Out-of-plane displacements: a) S02.AT.CIC.01; b) S02.AT.CIC.02; c) S02.AT.CIC.03; d) LVDTs location

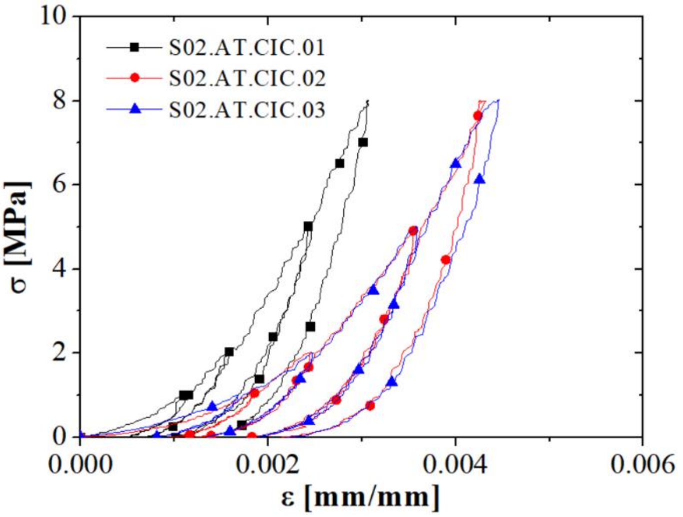

Figure 4-19 – Test series S02.AT.CIC – stress-strain curves

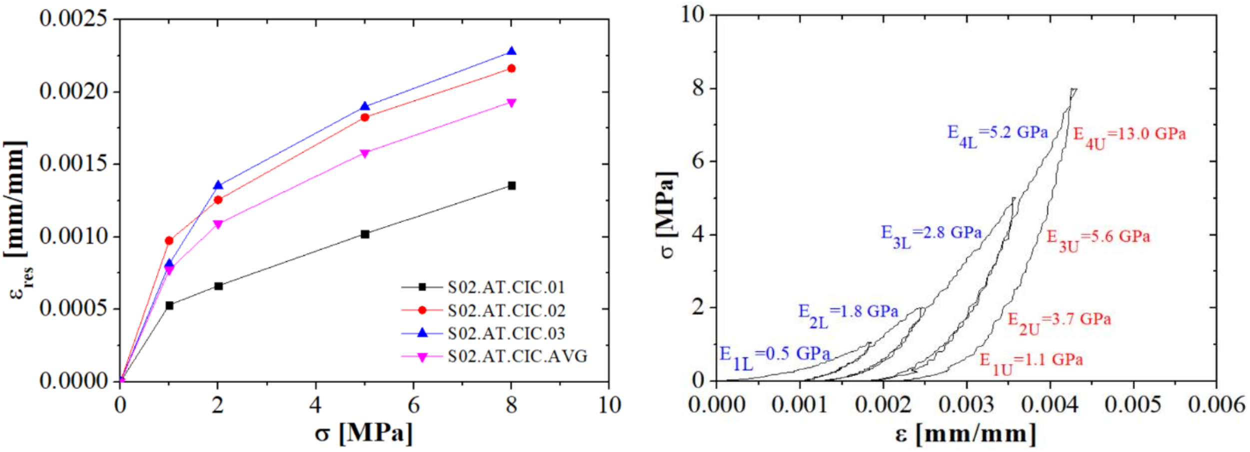

a)

Figure 4-20 – Test series S02.AT.CIC – Joint crushing process: a) Evolution of residual strain with load level; b) Evolution of wall's stiffness after joint crushing

The bricks' shape imperfections are the main contributor for the unevenness stress distribution obtained along the wall (Ngapeya *et al*, 2018), as observed in the test series S01.AT.LBC. Figure 4-21 presents the in-plane displacement fields measured by DIC for specimen S02.AT.CIC.02. The flow of in-plane forces can be easily identified: the regions with higher displacements indicates the presence of two pressure bulbs in the wall. It is also observed that the residual displacements are higher in the areas of the pressure bulbs. The bricks' shape imperfections in dry-stacked masonry led to stress concentrations in the wall. Consequently, it was possible to observe cracks even for the relatively low load levels applied (8 MPa), as shown in Figure 4-22. The cracks were mostly located in the middle of the bricks (cross joints) and were caused by the non-uniform loading and support conditions of the blocks.

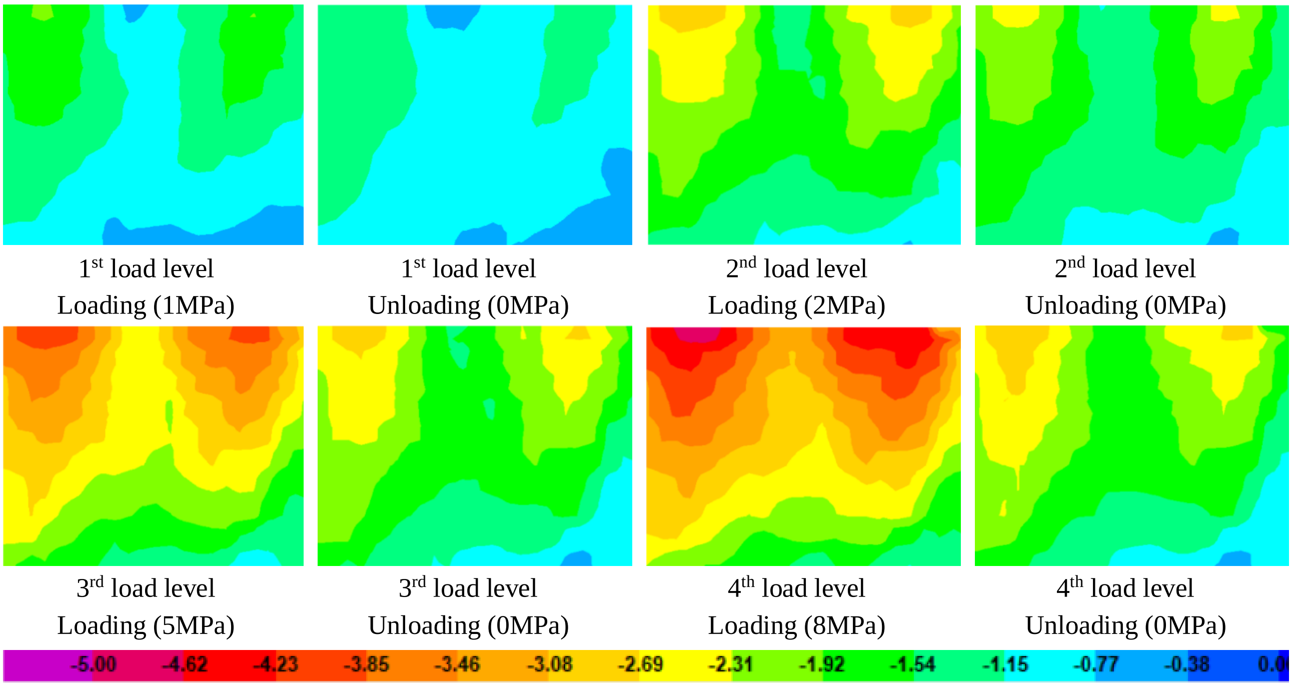
1st load level Loading (1MPa)

1st load level Unloading (0MPa)

2nd load level Loading (2MPa)

2nd load level Unloading (0MPa)

3rd load level Loading (5MPa)

3rd load level Unloading (0MPa)

4th load level Loading (8MPa)

4th load level Unloading (0MPa)

Figure 4-21 –In plane displacement fields measured by DIC for test series S02.AT.CIC.02 [in mm]

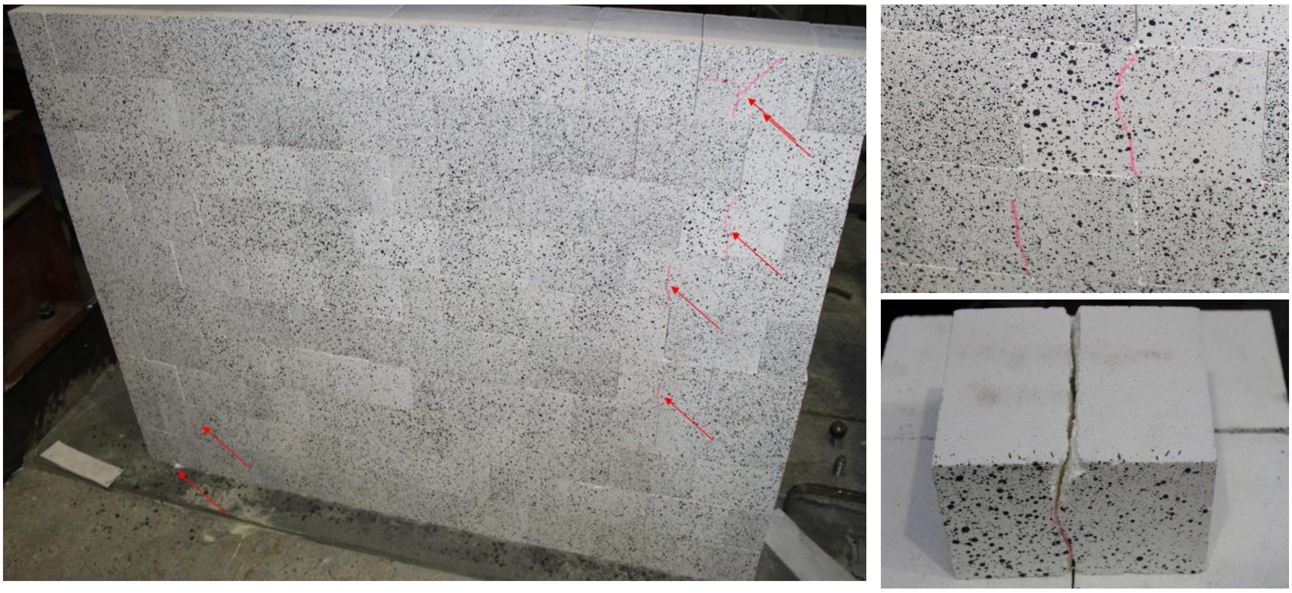

Figure 4-22 – Test series S02.AT.CIC: Cracks patterns observed by the end of the test.

4.3.3 Test series S03.HT.LL8

The temperatures measured by the thermocouples within the specimens of test series S03.HT.LL8 are presented in **Figure 4-23**. The standard fire curve ISO 834-1 (1999) and the temperature measured inside the furnace are presented in red. The purple dashed line indicates the beginning of the heating process. In this figure “HF” and “CF” stands for the thermocouples of the hot and cold face, respectively. The position of the thermocouples in the wall can be seen in **Figure 4-23**e.

Due to the high thermal capacitance of the specimen, the furnace was not able to follow the programmed curve. The temperatures in the hot face started to increase rapidly when the thermal load is applied. Due to the relatively low thermal conductivity of the refractory materials (**Figure 2-5**a), the temperatures on the cold face took some time to start increasing.

The temperatures in the first course of the bricks (bottom of the wall), measured by TC-07, TC-08 and TC-09, were lower than the average temperatures of the wall. This was caused in part by the furnace’s internal arrangement of the resistances, making this area less exposed to radiation (**Figure 4-3**e), due to heat losses through the reaction slab (**Figure 4-3**f), and due to the air convective currents inside the furnace.

In general, a relatively homogeneous temperature distribution was found in the wall within a range of ±15%. The difference between the average and the maximum and minimum temperatures measured were also slightly influenced by the depth at which the thermocouples were embedded and by heat losses at the edges of the specimens.

The accurate measurement of the temperature fields within the specimen along the test is important as it has a significant impact on the thermomechanical behaviour of the specimens. The temperature gradient through the thickness of the wall led to thermal bowing on the specimen. Consequently, significant out-of-plane displacements were observed during the heating stage of the tests.

The in-plane displacements measured by the LVDTs and the average of these values are being presented in **Figure 4-24**. The out-of-plane displacements are given in **Figure 4-25**. Small out-of-plane displacements are observed during the load stage. The out-of-plane displacements increase during the heating stage, due to the thermal bowing of the wall.

The average of the measured in-plane displacements is presented in Figure 4-26a. At the beginning of the test, from 0 to 20 minutes, the pre-compression stress of 8 MPa was applied, and negative displacements were observed, as a result of the joint closure and brick´s deformation. The maximum displacements after load application were -3.12 mm (ε = -0.0031), -3.76 mm (ε = -0.0038) and -3.49 mm (ε = -0.0035) for specimens S03.HT.LL8.01, S03.HT.LL8.02 and S03.HT.LL8.03, respectively.

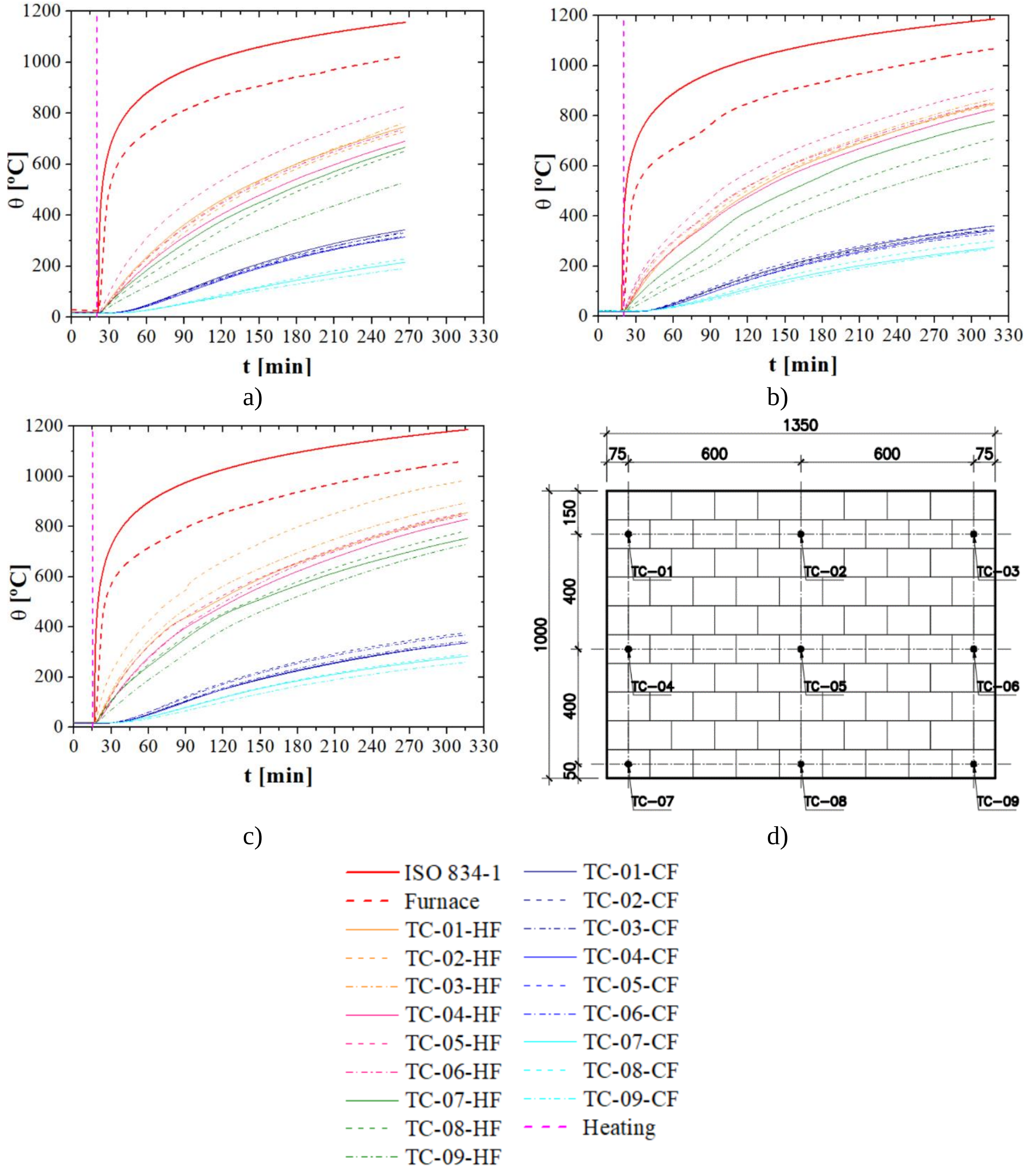

a) b)

c) d)

e)

Figure 4-23 – Test series S03.HT.LL8 – Temperature evolution: a) S03.HT.LL8.01; b) S03.HT.LL8.02; c) S03.HT.LL8.03; d) Legend; e) Thermocouple’s location

At 20 minutes after the beginning of the test, the furnace was turned on and the temperatures at the hot face started to increase. After 45 to 60 minutes of the beginning of the test, the effects of the thermal elongation started to rise, and the wall presented a positive strain rate. The thermal elongation surpassed the displacements caused by the mechanical loading after 244 min, 249 min and 252 min of the beginning of the test, for specimens S03.HT.LL8.01, S03.HT.LL8.02 and S03.HT.LL8.03, respectively. Test S03.HT.LL8.01 was stopped after 265 minutes, with a positive displacement of 0.24 mm (ε = 0.0002). Tests S03.HT.LL8.02 and S03.HT.LL8.03 were stopped after 300 minutes, with maximum displacements of 0.61 mm (ε = 0.0006) and 0.80 mm (ε = 0.0008), respectively.

The force measured by the load cell positioned at the top of the steel loading beam is given in Figure 4-26b. It is possible to observe that the load level remained constant during the performed tests. The load of 1512 kN results in the stress level of 8 MPa in the wall.

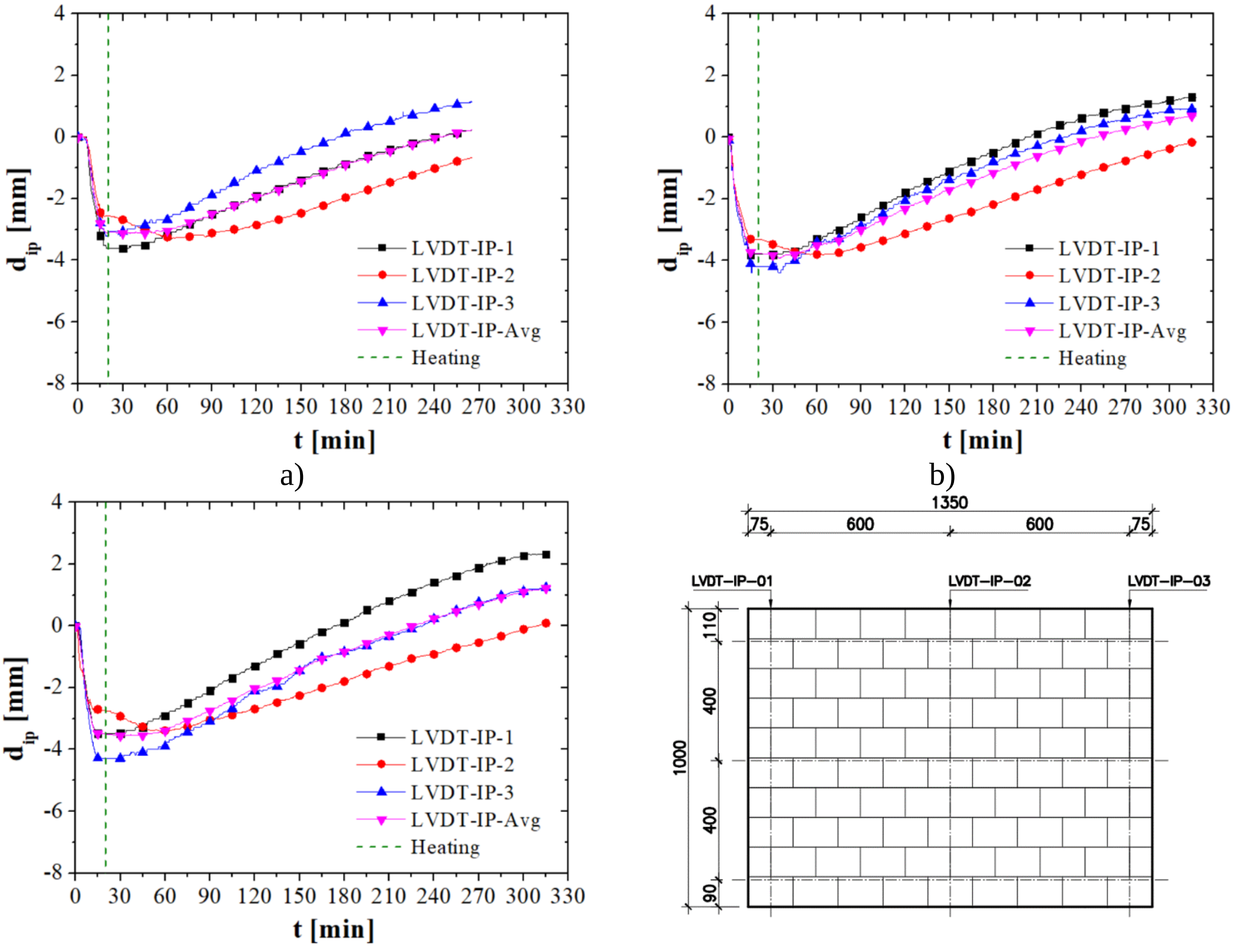

a) b) c) d)

Figure 4-24 – Test series S03.HT.LL8 – In-plane displacements: a) S03.HT.LL8.01; b) S03.HT.LL8.02; c) S03.HT.LL8.03; d) LVDTs location

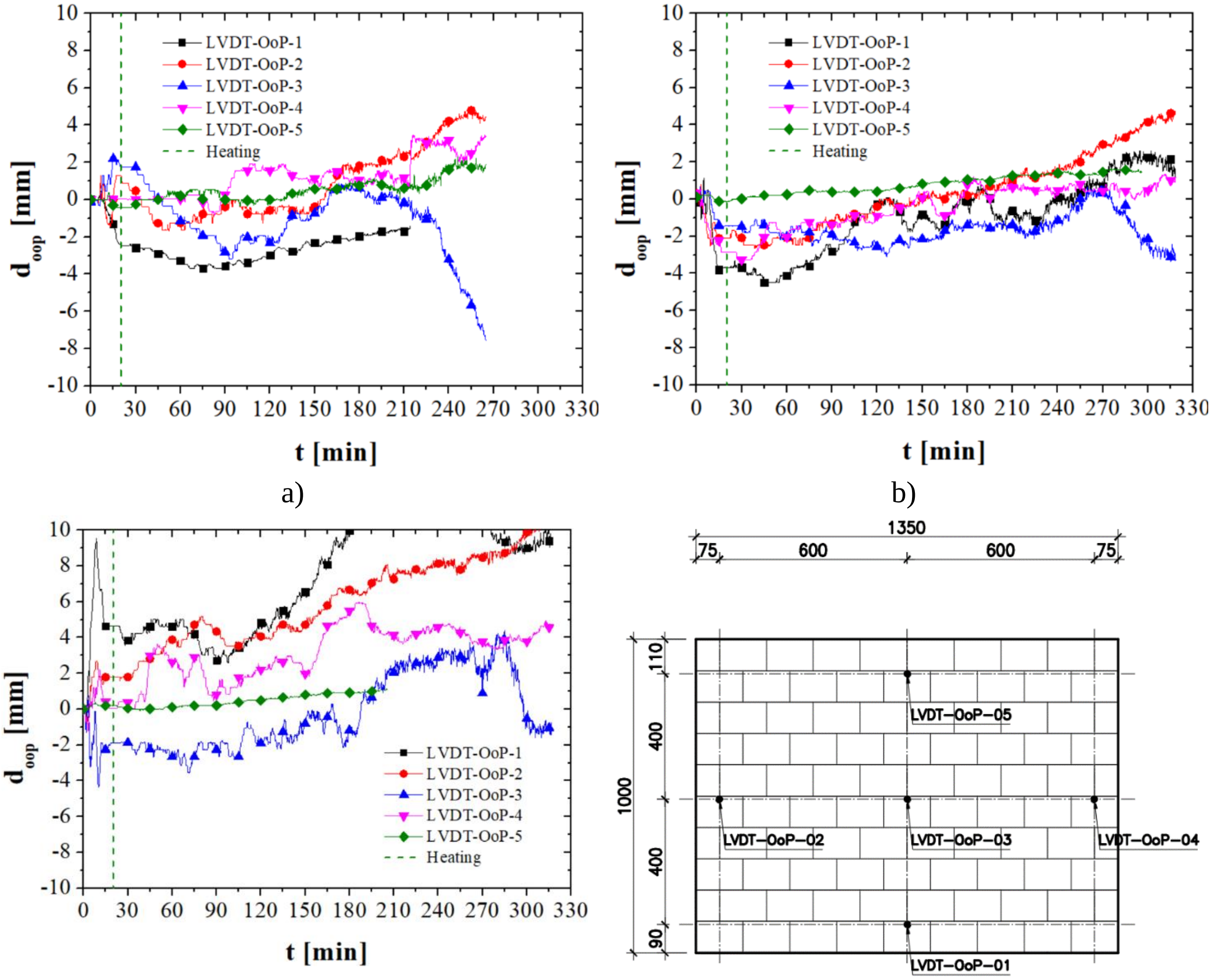

a) b) c) d)

Figure 4-25 – Test series S03.HT.LL8 – Out-of-plane displacements: a) S03.HT.LL8.01; b) S03.HT.LL8.02; c) S03.HT.LL8.03; d) LVDTs location

Despite the relatively low load level in the wall, some cracks were observed in the specimen upon completion of the test. Figure 4-27 shows the cracks observed in the interface between the load application beam and the wall's top surface. These cracks were caused by a high stress state reached in this region, as the mechanical load restrains the elongation of the specimen. **Figure 4-28** shows the vertical cracks observed in the middle of the bricks (indicated by the red arrows), caused by the unevenness stress distribution, as discussed in series S02.AT.CIC. The cracks of the bricks, resulted in rigid body motion of the adjacent bricks, leading to head joint opening (indicated by the green arrows).

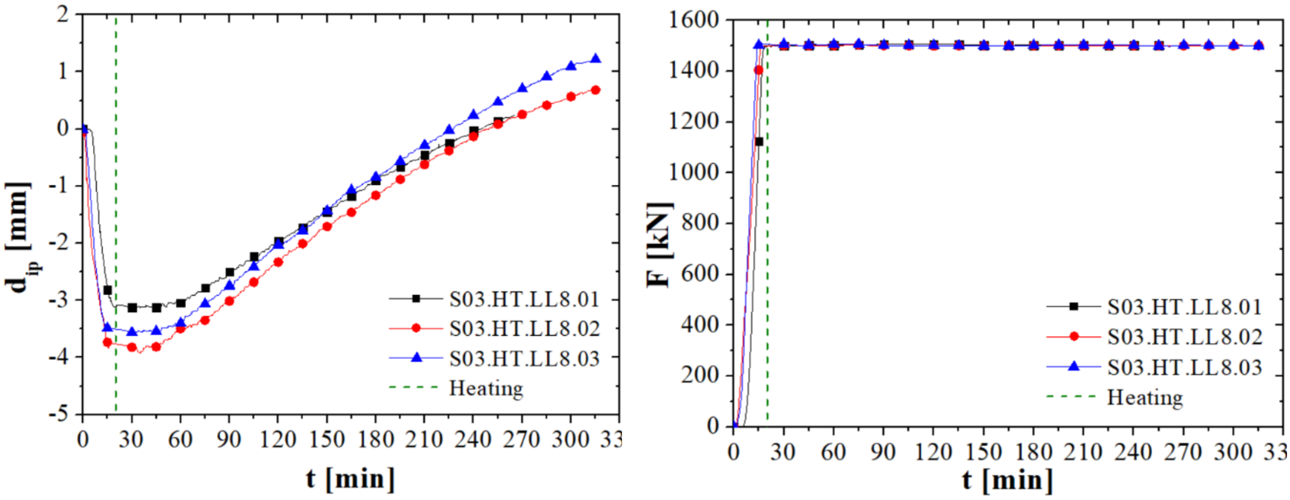

a) b)

Figure 4-26 – Test series S03.HT.LL8: a) Average in-plane displacements; b) Average forces

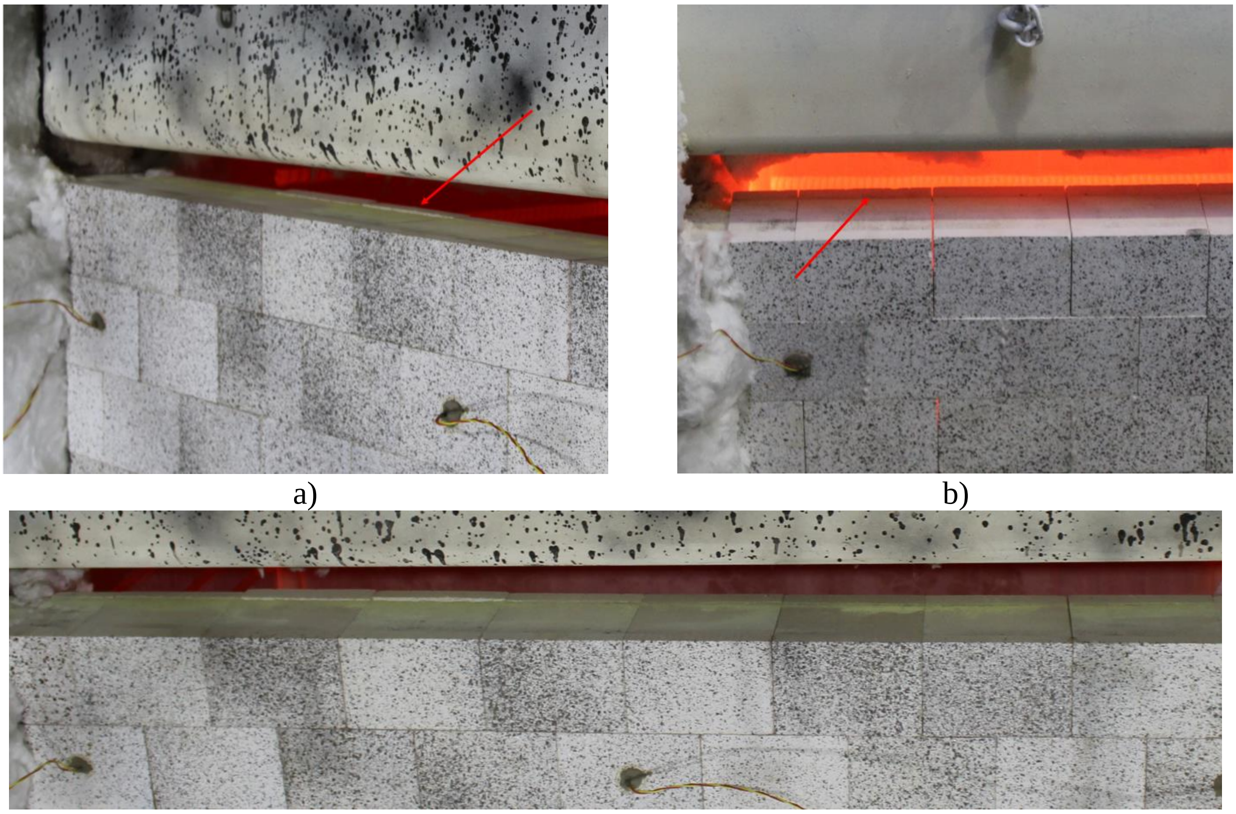

a) b) c)

Figure 4-27 – Test series S03 – Damage in the wall upon completion of the test - Cracks in the interface between load application beam and wall: a) S03.HT.LL8.01, b) S03.HT.LL8.02; c) S03.HT.LL8.01

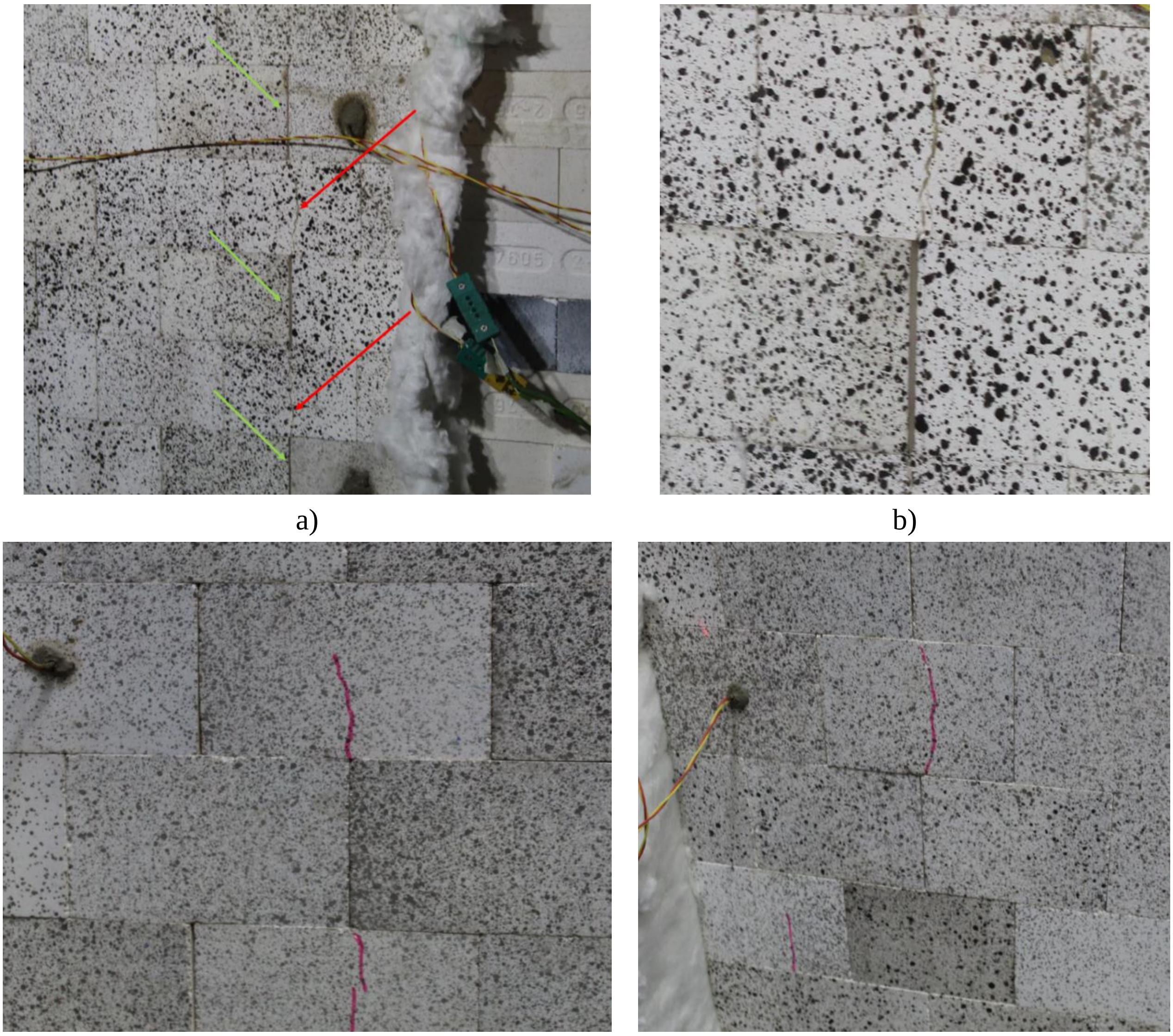

a) b)

c) d)

Figure 4-28 – Test series S03 – Damage in the wall upon completion of the test: a) Vertical cracks in bricks and joint openings; b) Crack details; c) Cracks details; d) Cracks details

4.3.4 Test series S04.HT.RTE

The temperatures measured by the thermocouples within the specimens of test series S03.HT.LL8 are presented in Figure 4-29. The standard fire curve ISO 834-1 (1999) and the temperature measured inside the furnace are presented in red. The purple dashed line indicated the beginning of the heating process. In this figure "HF" and "CF" stands for the thermocouples of the hot and cold face, respectively. The position of the thermocouples in the wall can be seen in Figure 4-29e.

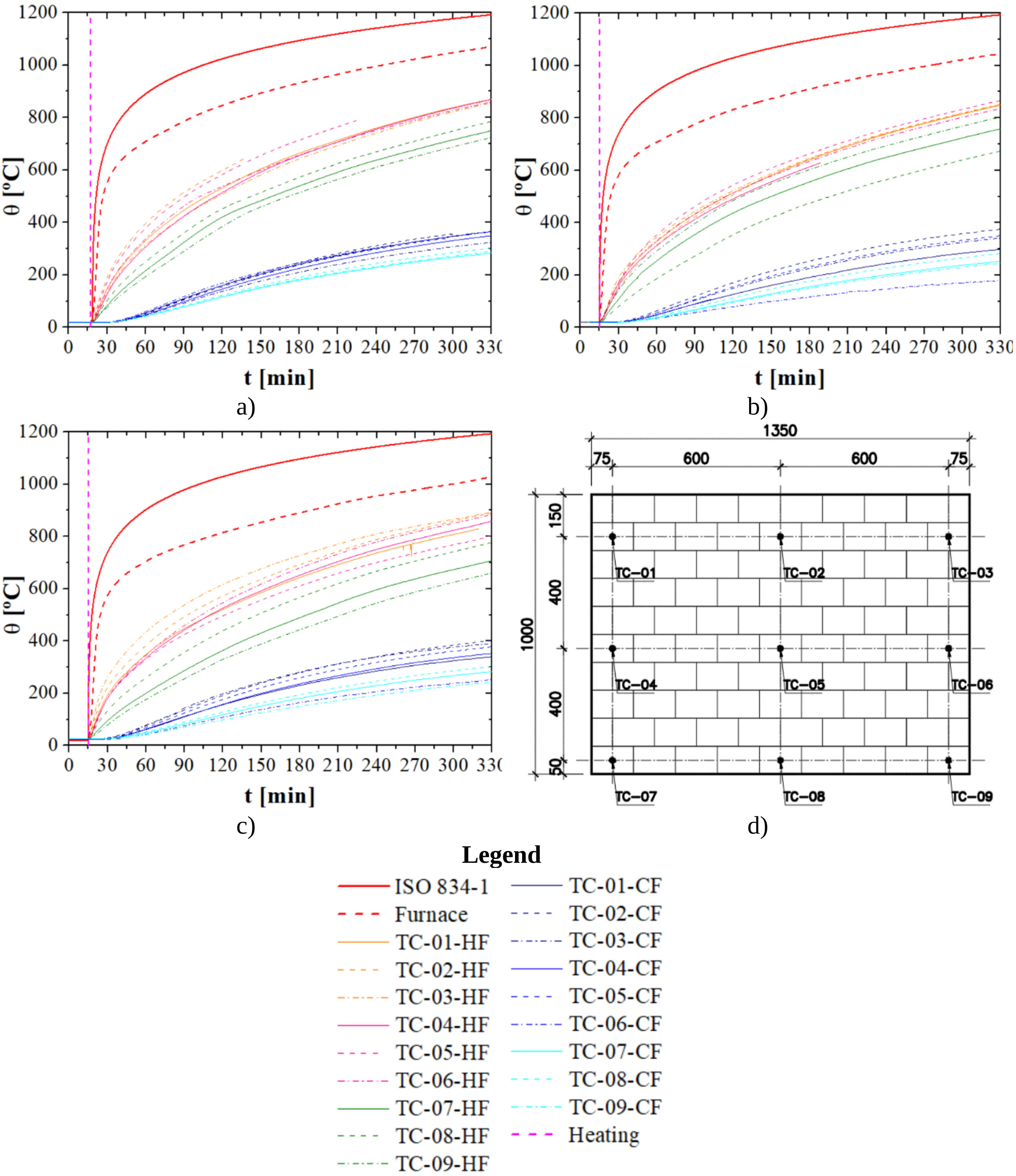

a)

b)

c)

d)

e)

Figure 4-29 – Test series S04.HT.RTE – Temperature evolution: a) S04.HT.RTE.01; b) S04.HT.RTE.02; c) S04.HT.RTE.03; d) Thermocouple location; e) Legend

As in the previous test series, the high thermal capacitance of the specimen did not allow the furnace to follow the programmed curve. The temperatures in the hot face started to increase rapidly at the beginning of the heating. Due to the relatively low thermal conductivity of the refractory materials, the temperatures on the cold face took some time to start increasing. Once again, the temperatures in the first course of the bricks (bottom of the wall) were lower than the average temperatures of the wall, as explained in section 4.3.3. In some cases (*e.g.* TC-02-HF and TC-05-HF of specimen S04.HT.RTE.02), the detachment of the thermocouple was observed. In these cases, the thermocouple and the grout layer used to fix it disconnected from the hole made in the brick and felt. Consequently, the measurements of these thermocouples were removed from the graphs after the moment of the detachment.

The in-plane displacements measured by the LVDTs and the average of these values are being presented in **Figure 4-30**. The LVDT-IP-2 of test S04.HT.RTE.02 did not work properly, therefore, for this test, only the LVDT-IP-1 and LVDT-IP-3 were used to calculate the average displacement. The equipment was replaced for the following tests.

The out-of-plane displacements are given in **Figure 4-31**. Relatively small out-of-plane displacements were obtained during the load application at ambient temperature. When the heating started, it was possible to identify a significant increasing in the out-of-plane displacements, caused by the thermal bowing due to the thermal gradient through the thickness of the wall.

The average in-plane displacements are presented in **Figure 4-32**a. At the beginning of the test, from 0 to 20 minutes, the mechanical load of 5 MPa (945 kN) was applied, and a negative displacement was observed, as a result of the joint closure and brick´s behaviour. The maximum displacements after load application were -2.53 mm (ε = -0.0025), -3.22 mm (ε = -0.0032) and -4.15 mm (ε = -0.0042) for test specimens S04.HT.RTE.01, S04.HT.RTE.02 and S04.HT.RTE.03, respectively.

After 20 minutes, the furnace was turned on and the heating started, consequently the temperature increased, and the effects of thermal elongation led to a positive strain rate. The thermal elongation surpassed the displacements caused by the mechanical load after 173 min, 206 min and 261, for the test specimens S04.HT.RTE.01, S04.HT.RTE.02 and S04.HT.RTE.03, respectively. All tests were stopped after 320 minutes. At this moment, the maximum displacements observed were 2.31 mm (ε = 0.0023), 1.74mm (ε = 0.0017) and 0.75 mm (ε = 0.0008) for test specimens S04.HT.RTE.01, S04.HT.RTE.02 and S04.HT.RTE.03, respectively.

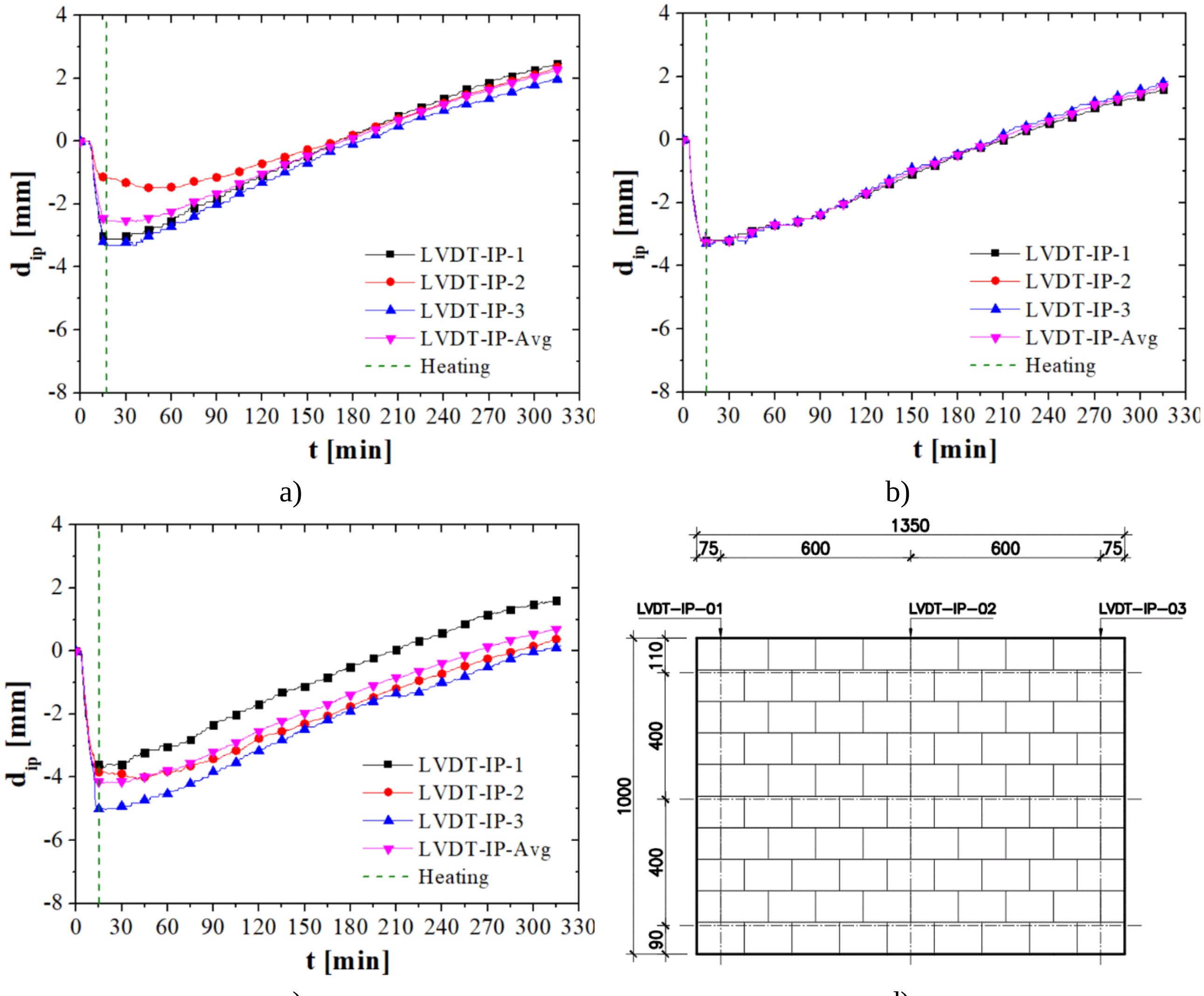

a) b)

c) d)

Figure 4-30 – Test series S04.HT.RTE – In-plane displacements: a) S04.HT.RTE.01; b) S04.HT.RTE.02; c) S04.HT.RTE.03; d) LVDTs position

Figure 4-32b presents the evolution of the forces developed in the specimen. From 0 to 20 minutes, a pre-load of 5 MPa was applied. Then, the position of the hydraulic jack was blocked, and the thermal load was applied. As expected, the thermal elongation led to an increasing compressive force in the wall. By the end of the test, the measured stresses for test series S04.HT.RTE.01, S04.HT.RTE.02 and S04.HT.RTE.03 were 6.47 MPa (1222kN), 6.22 MPa (1185 kN) and 6.08 MPa (1149 kN), respectively.

During the heating stage of series S04.HT.RTE the hydraulic jack movement was blocked, in fact the LVDT used to feed the servo-controller unit of the jack did not presented measurements during the heating stage. However, the reaction frame (composed by two HEB500 columns and two HEB600 beams) worked as a spring with axial stiffness K_B (see **Figure 4-32**c). The increasing of the vertical load in the wall caused by the restrained thermal elongation led to displacements in the reaction frame and consequently to strains in the wall.

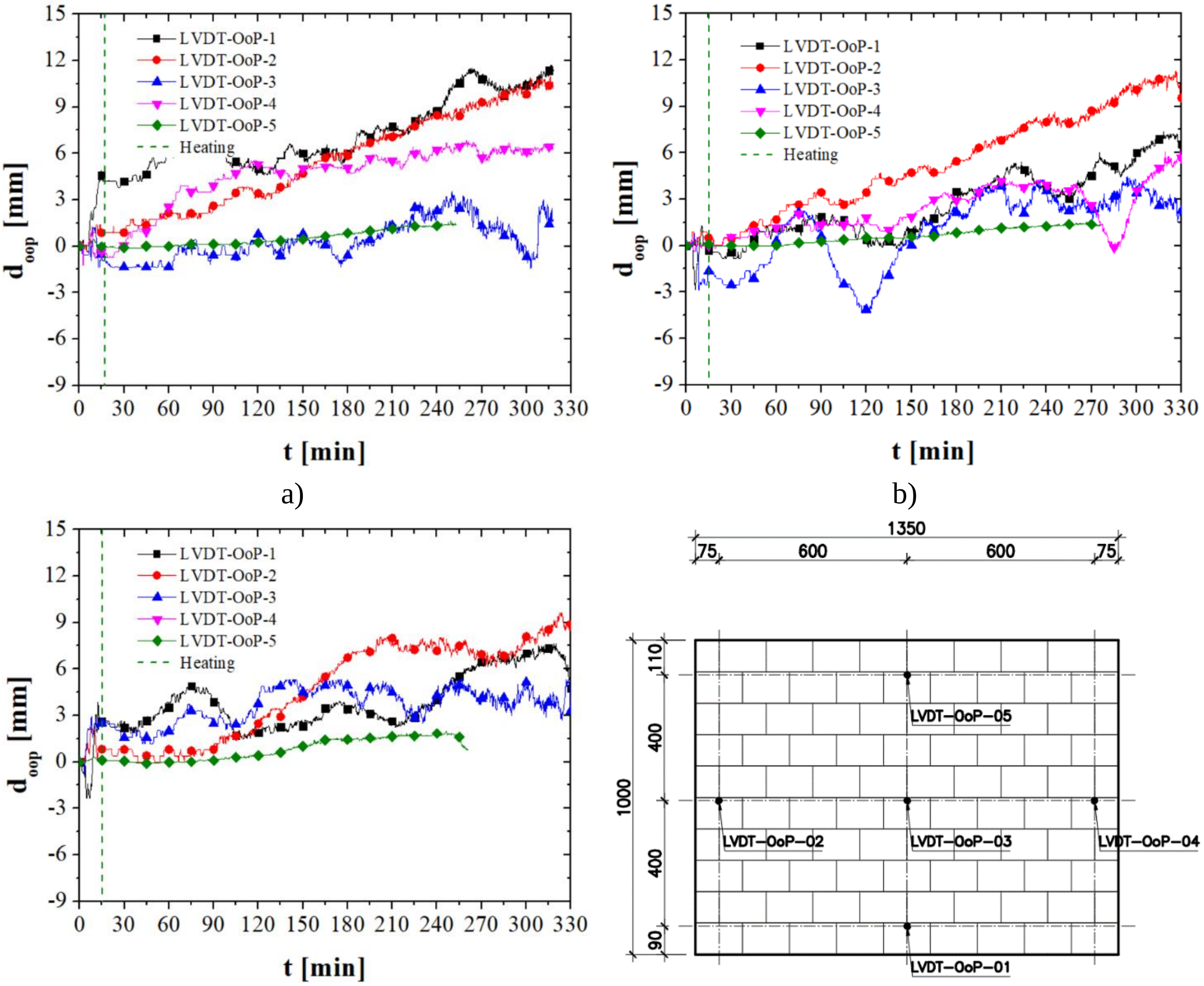

a) b) c) d)

Figure 4-31 – Test series S04.HT.RTE – Out-of-plane displacements: a) S04.HT.RTE.01; b) S04.HT.RTE.02; c) S04.HT.RTE.03; d) LVDTs position

Despite the relatively low load level in the wall, again some cracks were observed between the load application beam and the wall's top surface (similar to Figure 4-27). Figure 4-33 presents vertical cracks observed in the middle of the bricks (indicated by the red arrows), caused by an unevenness stress distribution, as discussed in test series S02.AT.CIC and S03.HT.LL8. Rigid body motions caused by the cracks in the bricks were also observed, leading to head joint opening (indicated by the green arrows).

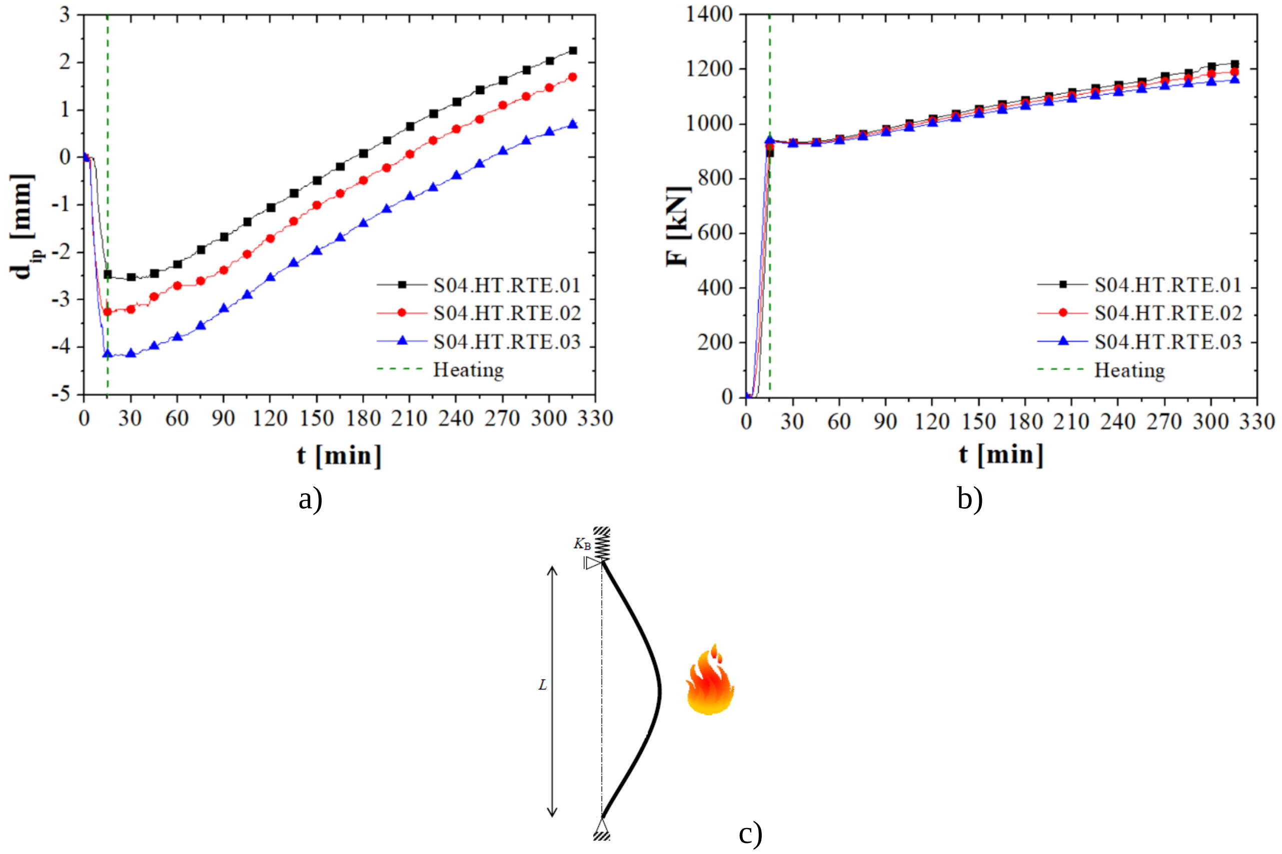

a)

b)

c)

Figure 4-32 – Test series S04.HT.RTE: a) Average in-plane displacements; b) Forces; c) Structural schematics

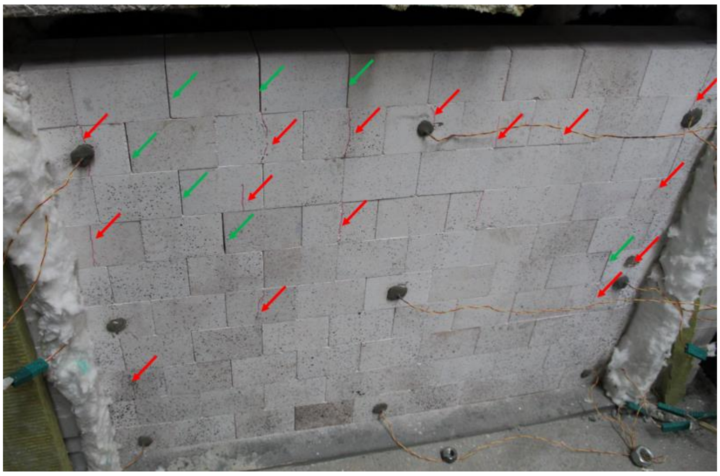

Figure 4-33 – Test series S04.HT.RTE – Failures in the wall: Vertical cracks in bricks and joints openings (S04.HT.RTE.02)

Figure 4-34 presents the cracks observed in specimen S04.HT.RTE.01 after the end of the test. The observed cracks were located at the cross-joints and where caused by the brick shape imperfections. These imperfections result in a non-homogeneous stress distribution in the wall, as discussed in Chapter 3. The stresses concentrations were also responsible for the crushing observed in **Figure 4-34**b.

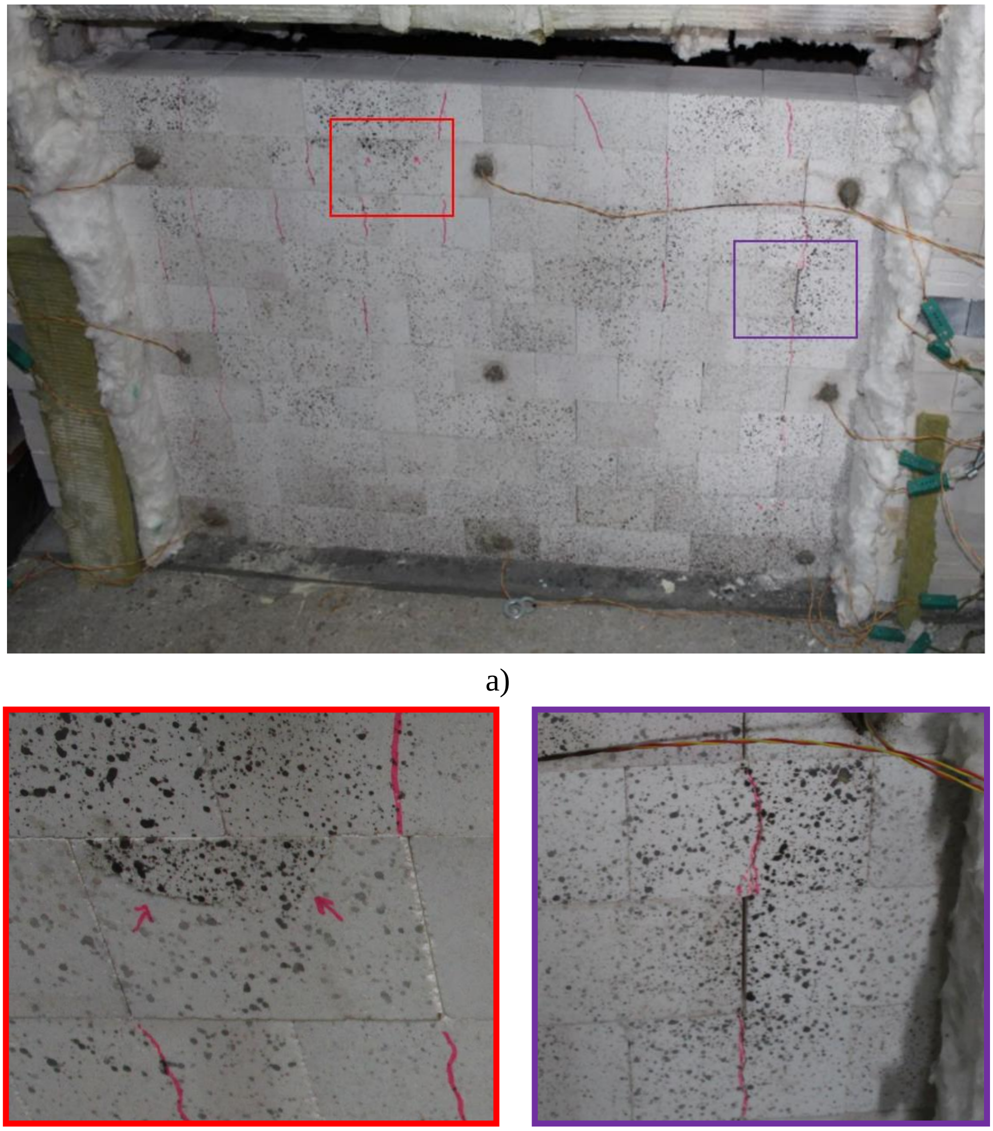
a)

b)

c)

Figure 4-34 – Test series S04.HT.RTE – Overview of vertical cracks in specimen S04.HT.RTE.01; b) Brick crushing due to stress concentrations at the cross joints; c) Brick cracks and joint opening

4.3.5 Test series S05.HT.LL10

The measured temperatures are presented in Figure 4-35. The position of the thermocouples is also shown. The temperatures in specimen S05.HT.LL10.02 were slightly higher than in the specimen S05.HT.LL10.01, since insulation was placed in the cold face of the wall. The objective was to heat the specimen as much as possible.

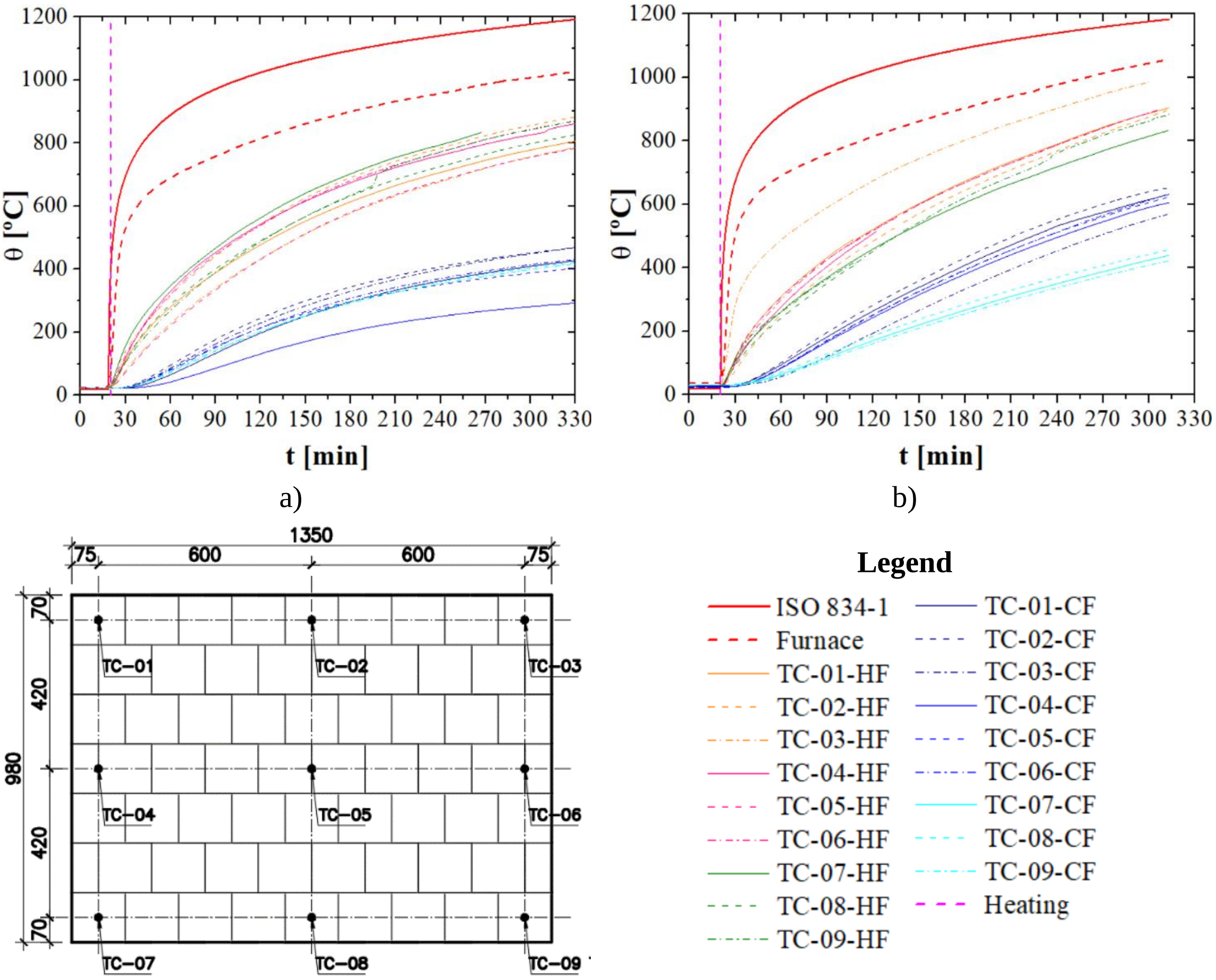

a) b)

c) d)

Figure 4-35 – Test series S05.HT.LL10 – Temperature evolution: a) S05.HT.LL10.01; b) S05.HT.LL10.02; c) Thermocouple location; d) Legend

The in-plane displacements measured by the LVDTs and the average of these values are presented in Figure 4-36. The average displacement of both tests after load application were similar, however in the case of test S05.HT.LL10.02 the failure of the specimen was observed, as shown in Figure 4-36b. The specimen S05.HT.LL10.01 did not reach failure, however, it was possible to observe a reduction of stiffness after 300 minutes of testing (Figure 4-36a).

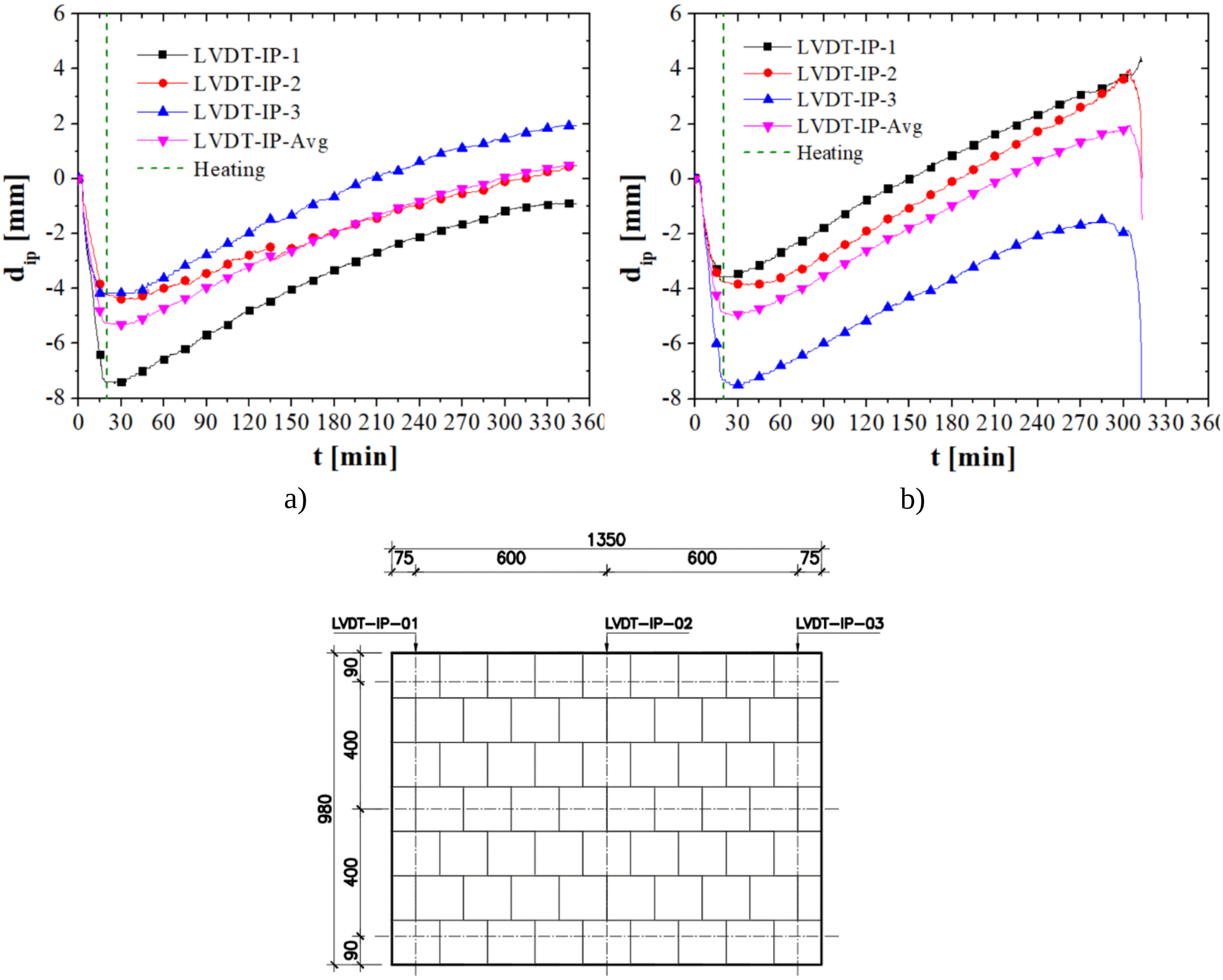

a) b)

c)

Figure 4-36 – Test series S05.HT.LL10 – In-plane displacements: a) S05.HT.LL10.01; b) S05.HT.LL10; c) LVDTs location

The out-of-plane displacements are given in **Figure 4-37**. The smaller thickness of the wall (100 mm), when compared to the specimens of test series S02.AT.CIC, S03.HT.LL8 and S04.HT.RTE (140 mm), resulted in a higher slenderness ratio of the wall and consequently higher out-of-plane displacement during the loading stage. During the heating stage, the out-of-plane displacements increased significantly.

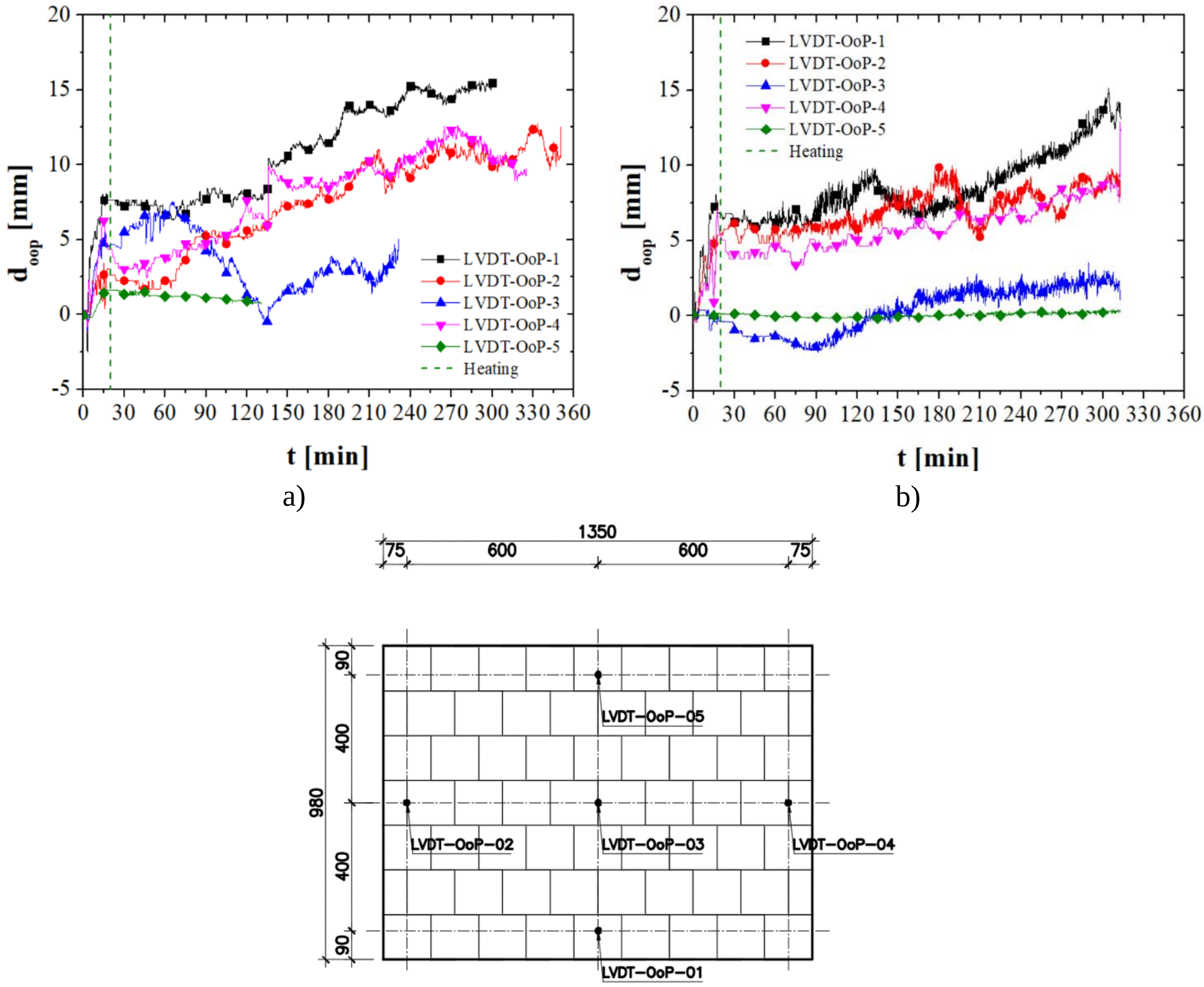

a)

b)

c)

Figure 4-37 – Test series S05.HT.LL10 – Out-of-plane displacements: a) S05.HT.LL10.01; b) S05.HT.LL10; c) LVDTs location

The average of the in-plane displacements is presented in **Figure 4-38**a. At the beginning of the test, from 0 to 20 minutes, the load was applied, and a negative displacement was again observed. The displacements after load application were -5.25 mm (ε = -0.0053) and -4.86 (ε = -0.0049) mm for specimens S05.HT.LL10.01 and S05.HT.LL10.02, respectively. When the furnace was turned on (at 20 minutes) the temperatures at the hot face started to increase, consequently the thermal elongation started, and the wall presented a positive strain rate. The thermal elongation surpassed the displacements caused by the mechanical load after 296 min and 214 min for specimens S05.HT.LL10.01 and S05.HT.LL10.02, respectively.

Figure 4-38b presents the measured load during the test. A small pressure drop was observed in the hydraulic jack for specimen S05.HT.LL10.01, most likely caused by cracks in the bricks. However, the servo-controller unit corrected it immediately, increasing the pressure in the hydraulic jack and returning the applied force to the target. The brittle failure of the specimen S05.HT.LL10.02 resulted in a quick reduction of the force measured by the load cell positioned at the top of the steel loading beam.

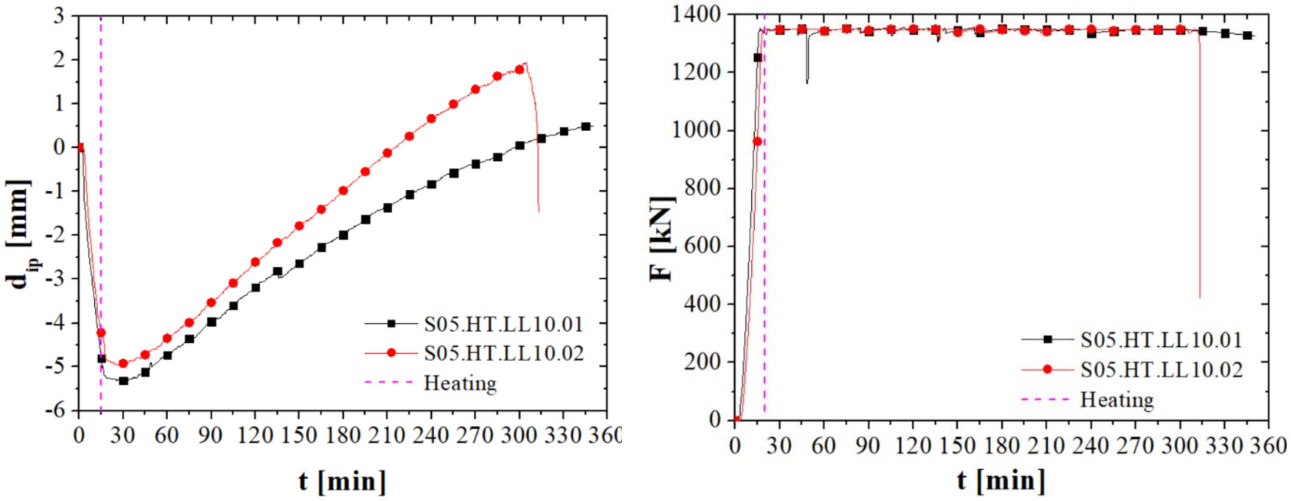

a) b)

Figure 4-38 – Test series S05.HT.LL10: a) Average in-plane displacements; b) Forces

The test for specimen S05.HT.LL10.01 was finished after 360 minutes. At this moment, a positive displacement of 0.49 mm (ε = 0.0005) was registered. The failure of this specimen was not observed in the test. Nevertheless, some cracks and crushing were observed in the specimen, as shown in **Figure 4-39**a. The temperatures in specimen S05.HT.LL10.02 increased slightly faster in comparison with the other specimen due to the thermal insulation installed in front of the wall. As shown in **Figure 4-39**a, the strain rate of S05.HT.LL10.02 was higher as the thermal elongation is more significant.

The thermal gradient in the wall led to significant thermal bowing, defined as an out-of-plane displacement of the specimen. The thermal bowing caused an eccentricity in the vertical load and led to sudden failure of the wall, as seen in **Figure 4-40**.

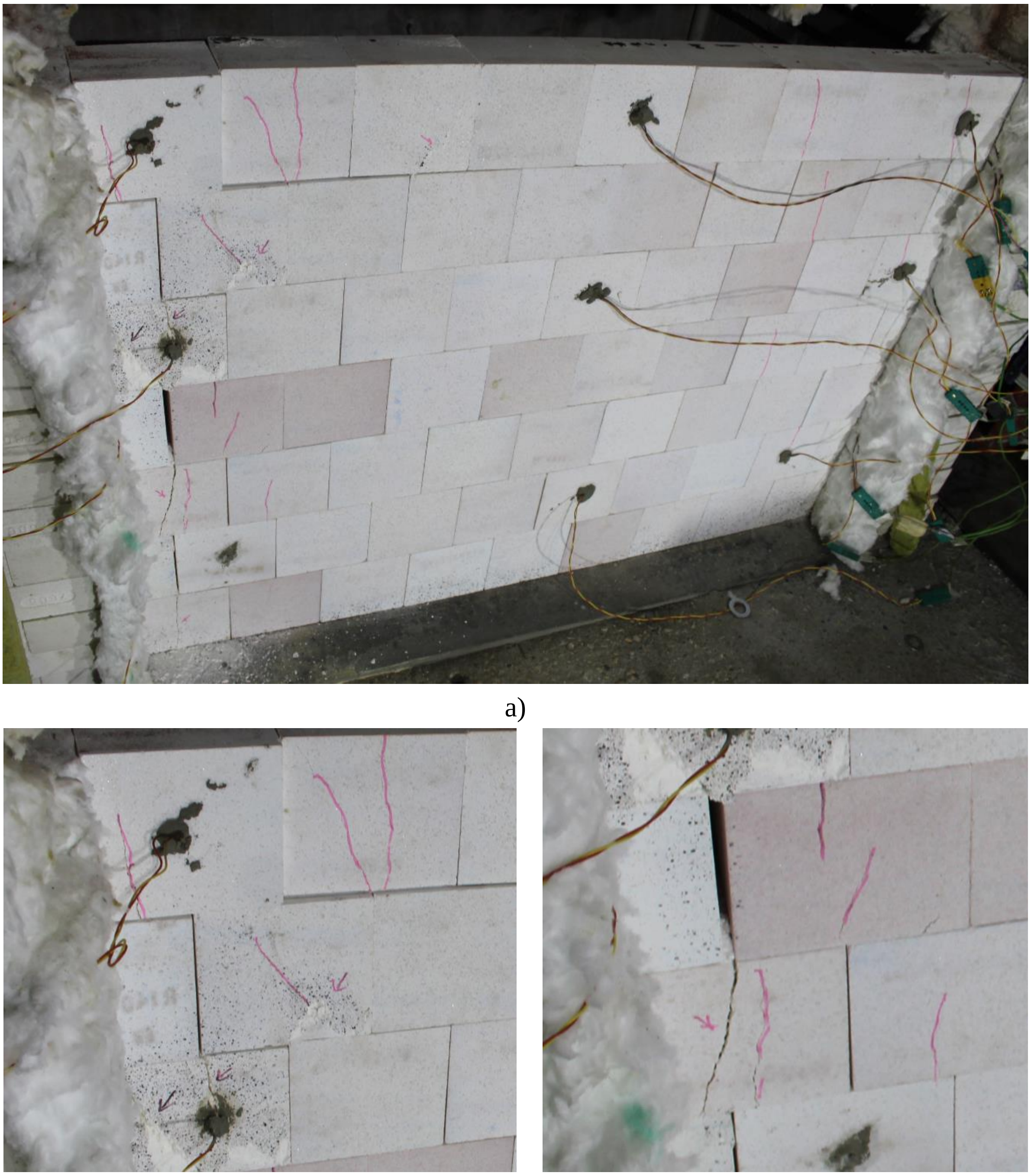

a)

b) c)

Figure 4-39 – Test series S05.HT.LL10 – Vertical cracks in bricks and joint openings in specimen S05.HT.LL10.01: a) Crack's location; b) Details of the top left side; c) Details of the bottom left side

a) b)

c) d)

Figure 4-40 – Test series S05.HT.LL10 – Failure of specimen S05.HT.LL10.02: a) Overview; b) Top view; c) Details of bricks’ failure from the left side of the wall; d) Details of bricks’ failure from the right side of the wall

4.4 Final remarks

As reported in the literature review, refractory materials have a highly heterogeneous behaviour resulting in a high scattering on their properties, which was observed in the experimental results. This scatter was found in the experimental results, including the in-plane stiffness, the load-bearing capacity, the temperature distribution, the evolution of the reaction forces and the in-plane and out-of-plane displacements, as shown in Section 4.3. The heterogeneous behaviour of the refractories shall be considered in the design of the linings, increasing the safety factors of the structures or using the most unfavourable values for the analysis.

Test series S01.AT.LBC aimed to assess the loadbearing capacity of the specimens. The experimental results showed three different stages of the stress-strain curves: *i*) joint closing state; *ii*) linear behaviour; and *iii*) plastic behaviour and failure. In the first stage, the stress-strain curve had a parabolic shape, the contact area between the bricks increased with the applied load and consequently the in-plane stiffness of the wallet increased as well. The second stage was evidenced by a linear behaviour on the stress-strain curve, the increasing of the contact area between the bricks and the stiffness increasing of the wallet was no longer significant. In the third stage the plastic effects started to rise, the cracks in the specimen led to a reduction on the wall's stiffness and a brittle failure was observed. The effects of the brick's height imperfections on the uneven stress distribution in the specimen and on the load percolation path was discussed in detail in Section 4.3.1.

Test series S02.AT.CIC aimed to evaluate the behaviour of the walls under cyclic loading. Four load cycles with increasing load level were applied to the specimen. The crushing of initial non-plane bricks' surfaces caused by the mechanical loading were observed and evidenced by the residual strains obtained after each load cycle. The residual strains increased with the load level. The crushing of non-plane bricks surfaces increased the contact area between the bricks, and consequently the wall's in-Chapter 3. Despite the small load level applied to the specimen, some cracks were found in the bricks, caused by the non-uniformity on the load and support conditions of the bricks.

Test series S03.HT.LL8, S04.HT.RTE and S05.HT.LL10 were tested at high temperatures. The temperature evolution in S03.HT.LL8 and S04.HT.RTE were similar, as the specimens of these series had the same geometry. A small scattering on the temperature measurements in the furnace was obtained, most likely caused by different insulation conditions of the experimental setup, however it has no significant impact on the test results. Additionally, some scatter was obtained in the readings of the thermocouples embedded in the bricks. The position of the thermocouples may change during the grouting procedure; therefore, they might end up being installed at slightly different depths. The differences in depth of the thermocouples and the differences in the thermal boundary conditions and exposure to the furnace's resistances in different parts of the wall were responsible for these scattering. Nevertheless, a relatively homogenous temperature distribution was found in the wall. Due to the high thermal capacity of the specimens, the furnace was not able to follow the standard fire curve (ISO 834-1, 1999).

In test series S03.HT.LL8, the specimens were tested under a constant load level of 8 MPa. The mechanical load was applied at ambient temperature and a negative displacement was observed, due to joint closure and bricks’ stiffness. When the furnace was turned on a positive strain rate was observed. The effects of the thermal elongation surpassed the effects of the mechanical loading after 248 minutes on average. A small scattering on the displacements was found during the test. Despite the small load level applied to this test series, cracks were observed in the wall by the end of the tests, caused by the unevenness of loading and support conditions of the bricks. Head joints opening were also observed.

Test series S04.HT.RTE was tested with restrained thermal elongation. A mechanical load of 5MPa was applied at ambient temperature, the hydraulic jack movement was blocked and the furnace was turned on. The restrained thermal elongation led to a reaction force that increased the stress level on the specimens. By the end of the tests, an average increase of 1.25 MPa was observed in the load. The cracks and head joint opening observed in S03.HT.LL8 were also obtained. A relatively small scattering was found in the displacement and reaction forces’ evolution. In test series S05.HT.LL10 the specimens with higher slenderness ratio were tested under a load level of 10 MPa and the wall failure at high temperatures was observed. The thermal bowing of the specimen, caused by the temperature gradient across the thickness of the wall, resulted in eccentricity in the load application and led to failure in specimen S05.HT.LL10.02

Due to limitations in the uniaxial experimental setup, it was not possible to achieve the service temperatures of the industrial linings in the experimental campaign. The service temperatures of the working lining of steel ladles are around 1650 ºC. The maximum temperature measured in the specimens were around 900 ºC. Moreover, the refractory layers are usually submitted to biaxial compression in service. The next chapter addresses these issues.

5 EXPERIMENTAL TESTS ON REFRACTORY MASONRY WALLS UNDER BIAXIAL COMPRESSION

The previous chapter presented the experimental characterization of the refractory masonry under uniaxial compression at ambient and high temperatures (up to 900 ºC). Nevertheless, the refractory linings are usually submitted to higher temperatures (up to 1650 ºC) and biaxial compression in service. In the available literature there are results of biaxial compression tests (Prietl, 2006) up to 1200 ºC, still far from the service temperature.

The experimental campaign presented in this chapter is a step forward in the research carried out by Prietl (2006) on refractory wallets under biaxial compression. Several improvements were performed in the experimental setup: *i*) the heating elements were replaced to reach temperatures up to 1500ºC; *ii*) the insulation of the device was redesigned to reduce the heat losses; *iii*) the DIC technique was used in the tests at ambient temperature to map the strain fields in the specimens.

The objective of this work was to study the behaviour of dry-stacked refractory wallets at ambient and high temperatures (up to 1500ºC) under uniaxial and biaxial compression loads. Six different test series are being studied. At ambient temperature, the series S06.AT.LBJ and S07.AT.LHJ aimed to assess the mechanical behaviour of masonry wallets subjected to loading in the directions of the bed and head joints, respectively. The series S08.AT.LBI aimed to assess the behaviour of the wallet at ambient temperature under biaxial load. At high temperatures, the series S09.HT.CBJ and S10.HT.CBI aimed to assess the creep behaviour of the specimen in the direction of the bed joints and under biaxial loads, respectively. The series S11.HT.RBI aimed to evaluated the behaviour of the specimen under biaxial relaxation. The experimental results are being used for validation of the numerical models presented in Chapter 6.

5.1 Experimental programme

The experimental programme comprised several tests performed at ambient and high temperatures divided in six series (Table 4-1):

- Series S06.AT. LBJ: carried out at ambient temperature (AT) with the objective of evaluating the mechanical behaviour of the wallet loaded at the bed joints (LBJ).
- Series S07.AT.LBJ: carried out at ambient temperature (AT) aiming to assess the behaviour of the dry-stacked masonry loaded at the head joints (LHJ).
- Series S08.AT. LBI: carried out at ambient temperature (AT) with the objective of evaluating the mechanical behaviour of the wallet loaded in biaxial conditions (LBI).
- Series S09.HT.CBJ: carried out at high temperatures (HT) aiming to evaluate the creep (C) behaviour of the wallet under loading in the bed joints (BJ)

- Series S10.HT.CBI: carried out at high temperatures (HT) aiming to evaluate the creep (C) behaviour of the wallet under loading in biaxial conditions (BI)
- Series S11.HT.RBI: carried out at high temperatures (HT) aiming to evaluate the relaxation (R) behaviour of the wallet under loading in biaxial conditions (BI)

Table 5-1 – Test series for the biaxial tests

Series	Test Number	Temperature of the test	Load conditions	Type of control	Maximum load
S06.AT. LBJ	S06.AT. LBJ.01	Ambient temperature	Bed directions: Loaded Head direction: Constrained	Displacement	6 MPa
	S06.AT. LBJ.02				
S07.AT. LHJ	S07.AT. LHJ.01		Bed directions: Constrained Head direction: Loaded	Displacement	6 MPa
	S07.AT. LHJ.02				
S08.AT.LBI	S08.AT.LBI.01		Bed directions: Loaded Head direction: Loaded	Displacement	6 MPa
	S08.AT.LBI.02				
S09.HT.CBJ	S09.HT.CBJ.01	High temperatures	Bed directions: Loaded Head direction: Constrained	Load	6 MPa
	S09.HT.CBJ.02				4 MPa
S10.HT.CBI	S10.HT.CBI.01		Bed directions: Loaded Head direction: Loaded	Load	4 MPa
	S10.HT.CBI.02				
S11.HT.RBI	S11.HT.RBI.01		Bed directions: Loaded Head direction: Loaded	Displacement	1st cycle: 4MPa 2nd cycle: 6MPa
	S11.HT.RBI.02				

5.2 Test setup

These experimental tests were carried out at the Technology Centre Leoben (TCL) of RHI-Magnesita, in Austria. This test setup has been used before (Prietl, 2006) and it was improved for this experimental campaign. The schematic view of the test set-up is presented in Figure 4-1.

The test set-up consisted of a monolithic reaction frame in which the hydraulic jacks, LVDTs and heating system were connected. Two perpendicular hydraulic jacks with the capacity of 1000 kN were used, a Rexroth controller unit was used to control them. The applied forces were measured by two pressure gauges per cylinder. A 48-channel data acquisition system was used to record the data from the experiments. The biaxial press is shown in **Figure 5-2**.

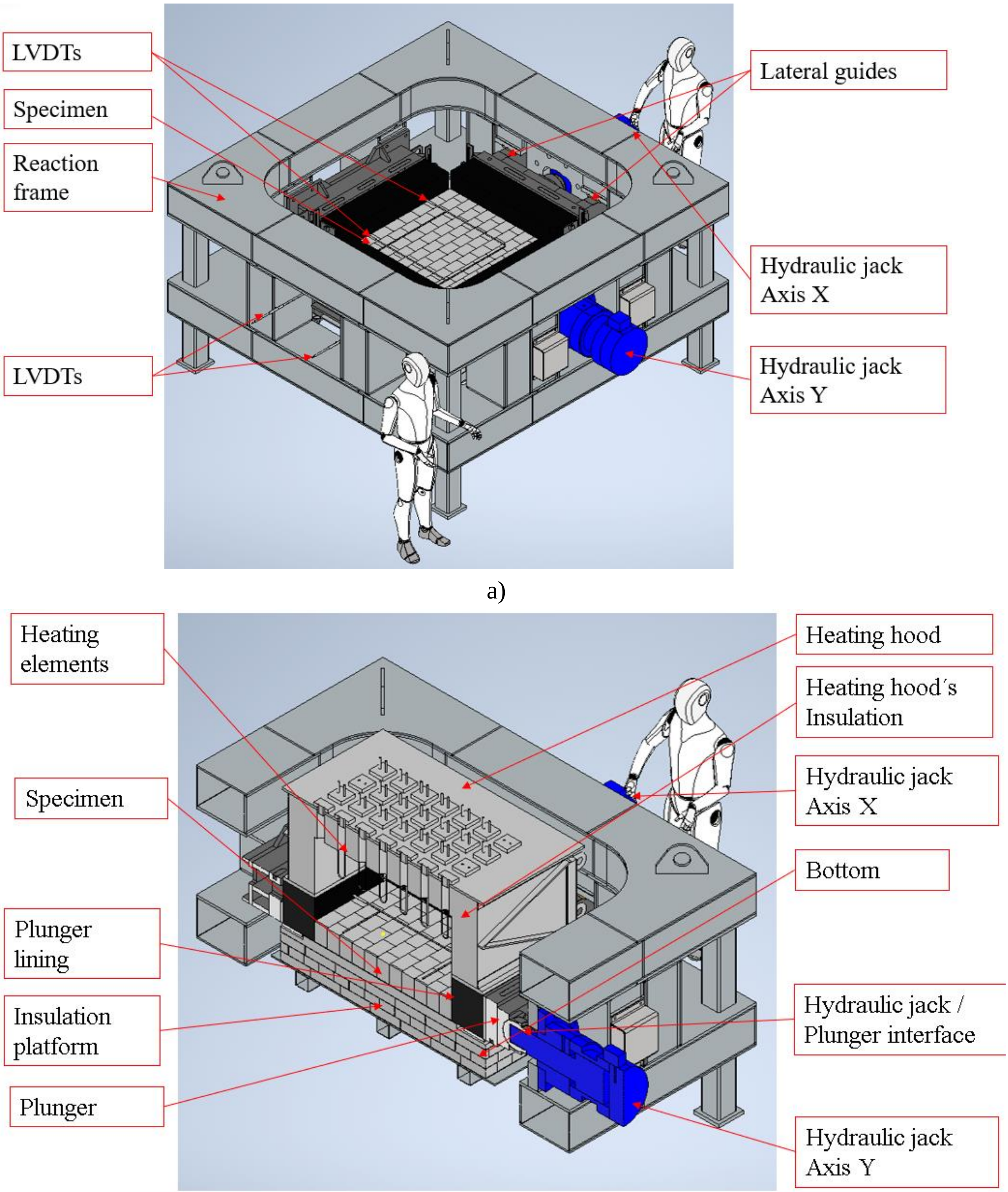

a)

b)

Figure 5-1 – Test set-up: a) Isometric view; b) Section view

a)

b) c) d)

Figure 5-2 – Test set-up: a) Isometric view; b) Hydraulic jacks; c) Pressure gauges; d) Data acquisition system

The specimens were placed on the top of an insulated platform, as shown in **Figure 5-1**b. The platform was responsible for holding the specimen and guarantee thermal insulation. It was composed by a 10 mm steel shell reinforced by square tubes (**Figure 5-1**b). Scaffolding feet were used to allow the proper levelling. The platform was lined with four refractory insulation layers (**Figure 5-3**a, b and c). Ceramic wool was used to fill the gaps and guarantee proper insulation **Figure 5-3**d). The last insulation layer had smaller dimensions, in order to allow the movement of the hydraulic jack. The gaps were closed using ceramic wool. The details of the bottom are being presented in **Figure 5-3**.

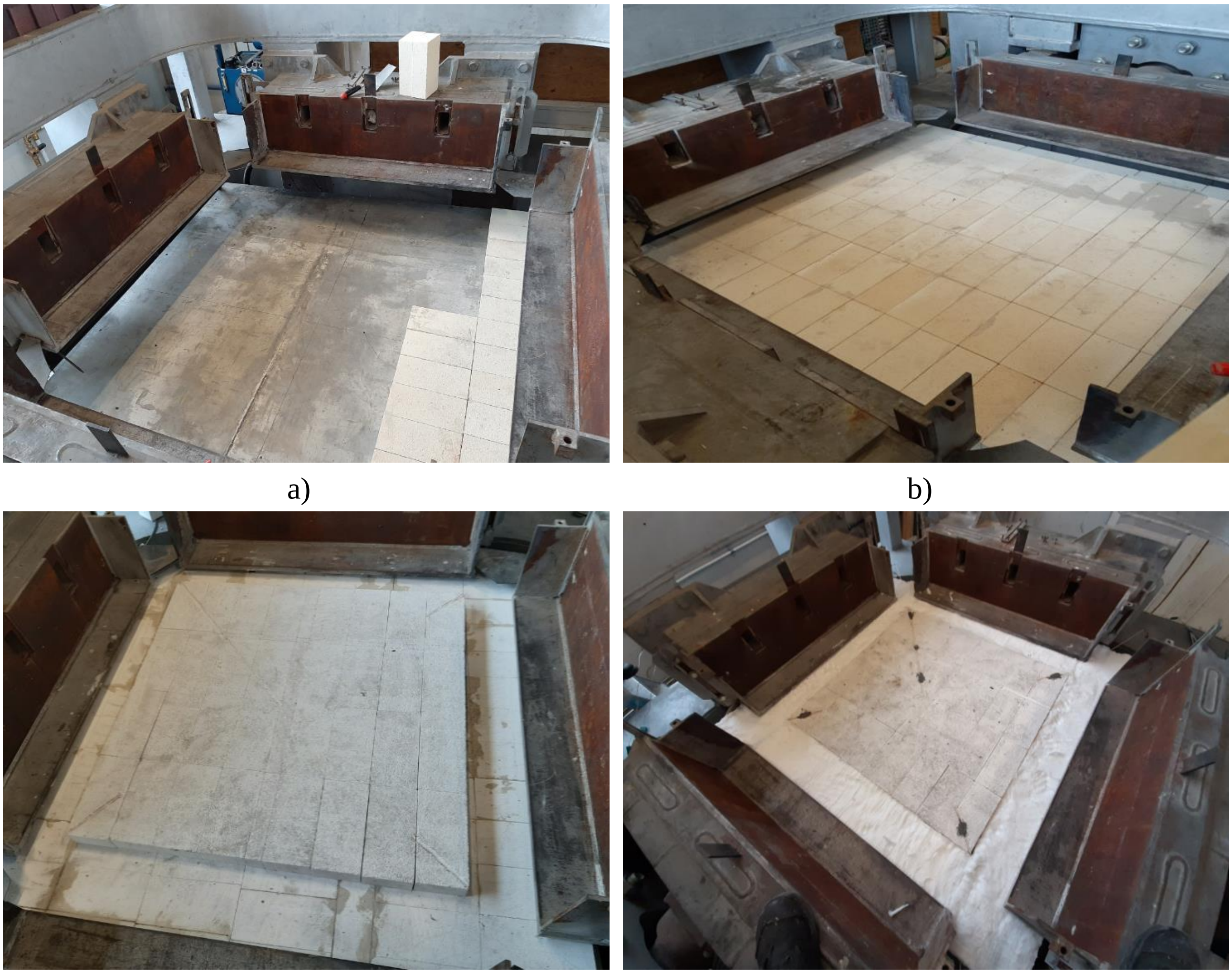

a) b)

c) d)

Figure 5-3 – Assembly of the insulation platform: a) Steel shell and first insulation layer; b) Third insulation layer; c) Last insulation layer; d) Last insulation layer with thermocouples and rockwool

The mechanical load is applied to the specimen by the plungers. The machine is equipped with two fixed plungers and two movable plungers, as shown in **Figure 5-4**. The plungers are composed by a water-cooled steel part and by a refractory lining. The steel part was responsible for guarantying the loadbearing capacity and the refractory linings was responsible for withstanding the higher temperatures. The fixed plungers had three opening each one, where the instrumentation (thermocouples and LVDTS) was placed.

The fixed plungers were rigidly connected to the machine frame by using structural bolts. The moveable plungers were connected to the hydraulic jacks by pinned connectors that allow the rotation of the plunger. Two lateral guides in each moveable plunger were responsible for avoiding rotations in the axial direction of the jacks. Therefore, the only rotation allowed by the experimental system was the vertical (out-of-plane) direction.

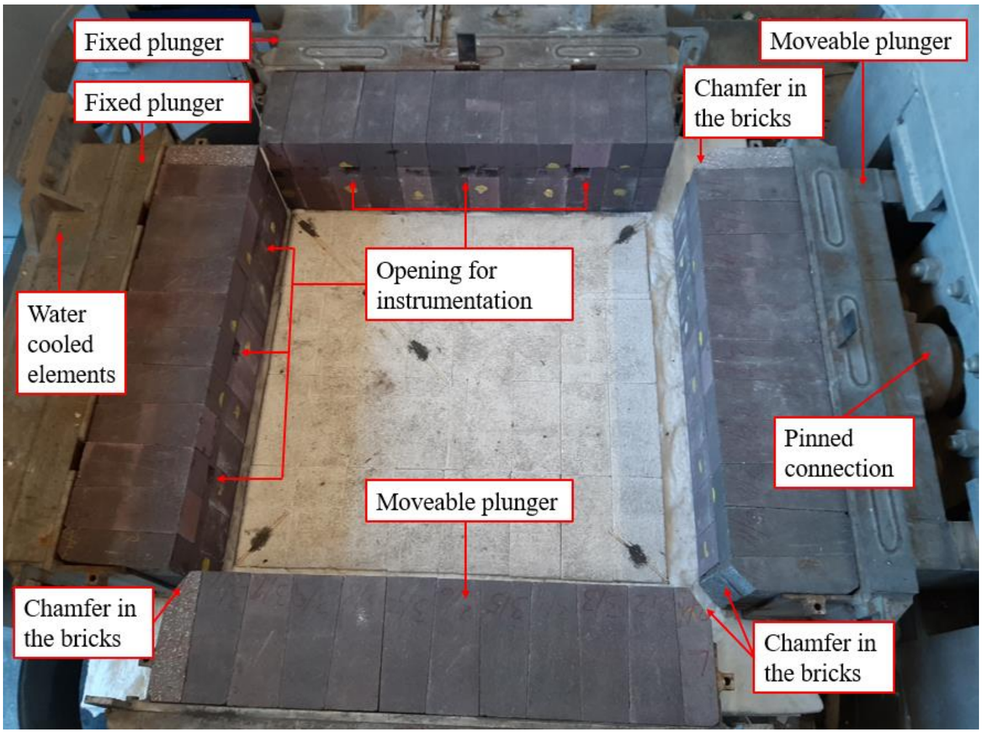

Figure 5-4 – Plungers – General arrangement

The plungers' linings was made by dry-stacked magnesia-chromite bricks. The main raw material of these bricks were chrome ore and fused magnesia chromite, as shown in **Table 5-2**. The brick has an elevated cold crushing strength (80 MPa), high resistance to creep in compression and a high refractoriness under load ($T_{0.5}$ = 1700 °C). The plunger linings had 250 mm in thickness, 300 mm in height and 1100 mm in length. The bricks were dry-stacked on the steel part of the plungers (**Figure**

5-5a). The details of the bricks and the plunger final arrangements are shown in **Figure 5-5**b and **Figure 5-5**c, respectively.

Table 5-2 – Chemical composition of the plungers' bricks

Chemical analysis: Fired substance (1025 °C) according to ISO 12677 (2011)					
MgO	**Cr_2O_3**	**Al_2O_3**	**Fe_2O_3**	**CaO**	**SiO_2**
56.5 %	25.0 %	6.0 %	10.0 %	0.6 %	1.3 %

To avoid the contact of the plunger linings during the movement of the hydraulic jacks, 40x40 mm chamfers have been done in the edges of the linings, as detailed in **Figure 5-5**d. A drawback of this system is the non-uniformity in the loading of the brick positioned at the edge of the specimen.

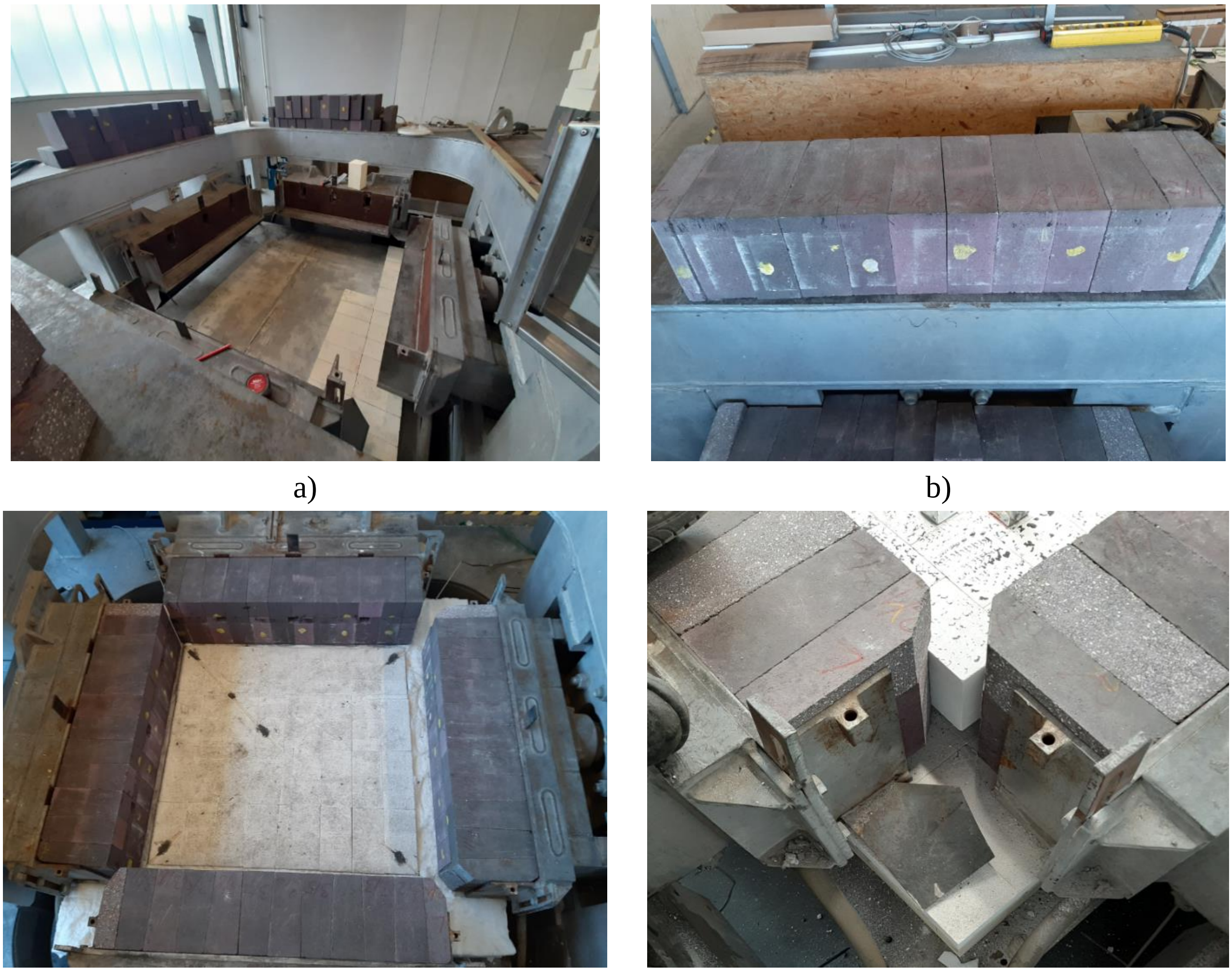

a) b)

c) d)

Figure 5-5 – Plunger lining details: a) Plungers without the linings; b) Bricks of plungers' lining; c) Plungers with linings; d) Details in the lining to allow the plungers' movements

The heating chamber was composed by an external steel shell insulated with ceramic wool (200 mm thickness). The heating elements chosen were the Kanthal Super 1900, thirty-six heating elements were used in the first tests, latter this number was reduced to thirty aiming to increase the power of the system. The total estimated power of the furnace was 59 kVA at 1500 °C. The details of the heating chamber are given in **Figure 5-6**. A 100 kVA transformer with a secondary voltage of 95 V was used to feed the resistances. Two type S thermocouples were used to measure the temperature inside the heating chamber.

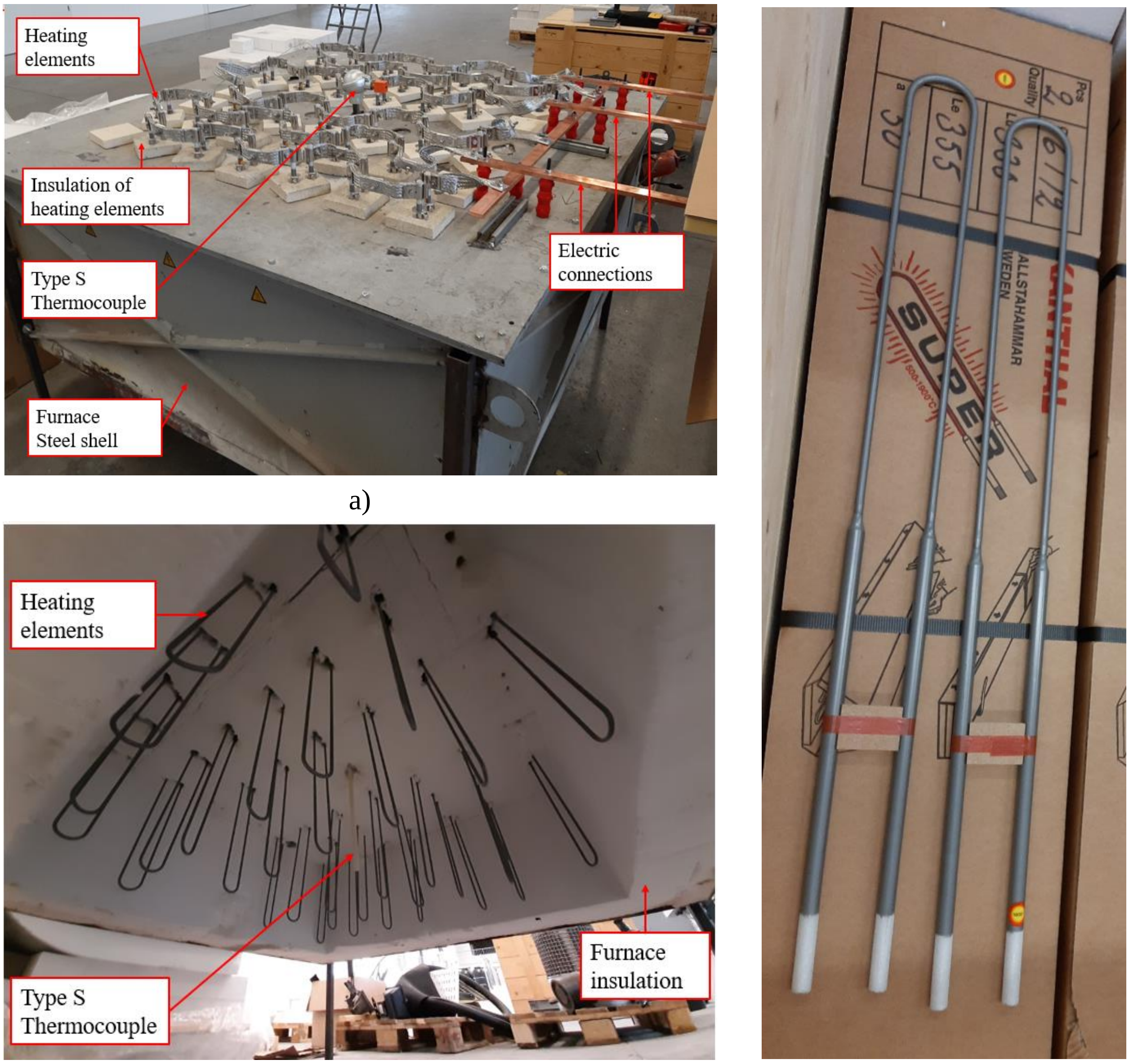

a)

b)

c)

Figure 5-6 – Heating chamber: a) Overview; b) Bottom view; c) Heating elements details

The correct insulation of the biaxial press is key aspect to limit heat losses and reach the desired temperature. Ceramic wool blankets were used to insulate the bottom of the press, the edges of the linings, the interface between the furnace and the plungers and the exposed face of the plunger bricks (Figure 5-7). The ceramic wool was composed by SiO_2, CaO and MgO and the had the density of 128 kgf/m^3. Different thicknesses (19, 25 and 50 mm) were used aiming to achieve the best insulation conditions.

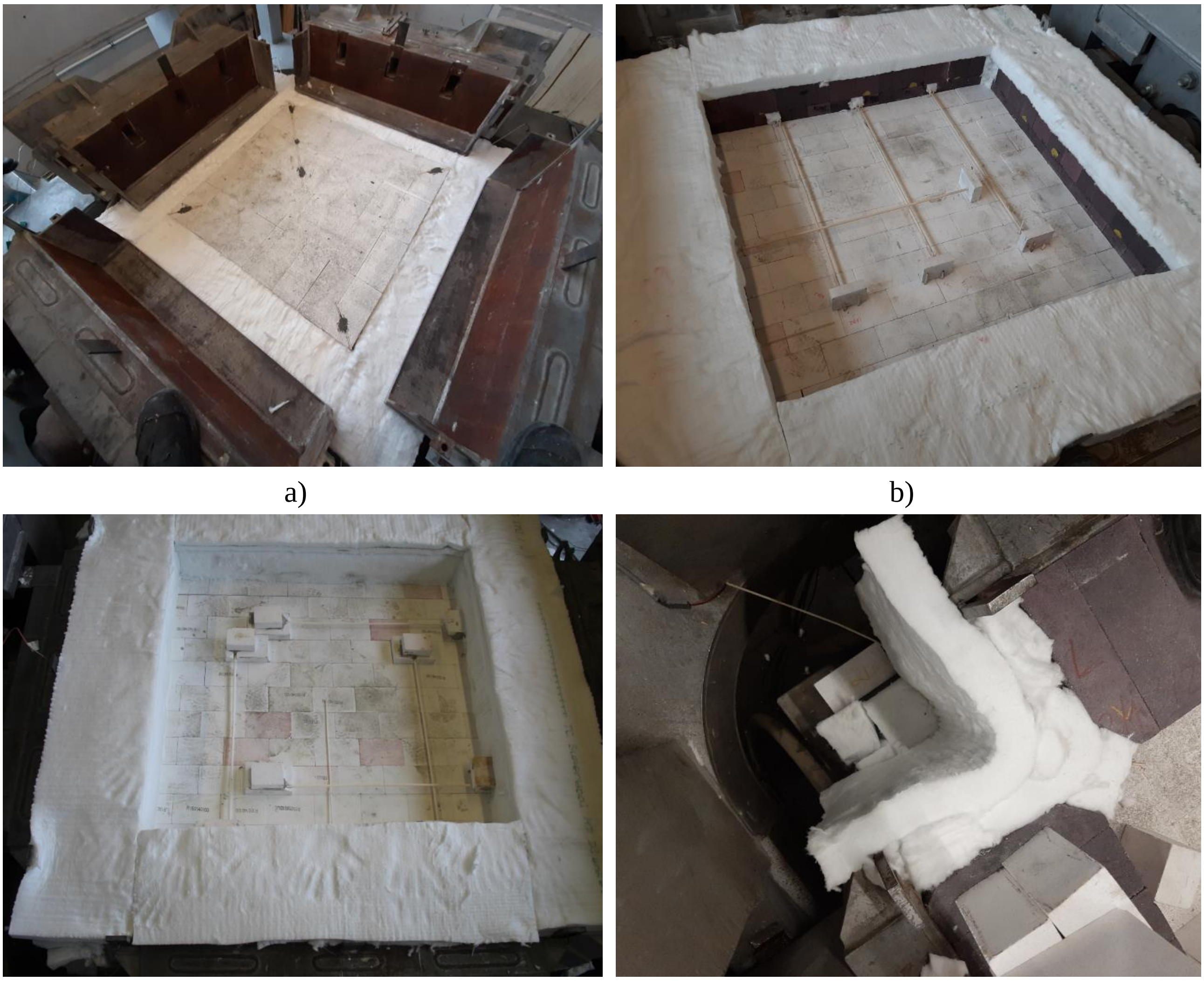

a) b)

c) d)

Figure 5-7 – Insulation details: a) Bottom; b) Plunger interface with the heating chamber; c) Exposed face of the plungers; d) Details of plunger chamfers

A water-cooling system was used to control the temperatures in the plungers. Only the metallic part of the plungers was cooled (**Figure 5-8** a). The system was composed by two pipelines, one used for input of the cold water and the other used for output of the hot water. The input and output hydraulic connections of the plungers were equipped with type K thermocouples to measure the water's temperature. A mechanical valve was used to control the water flow.

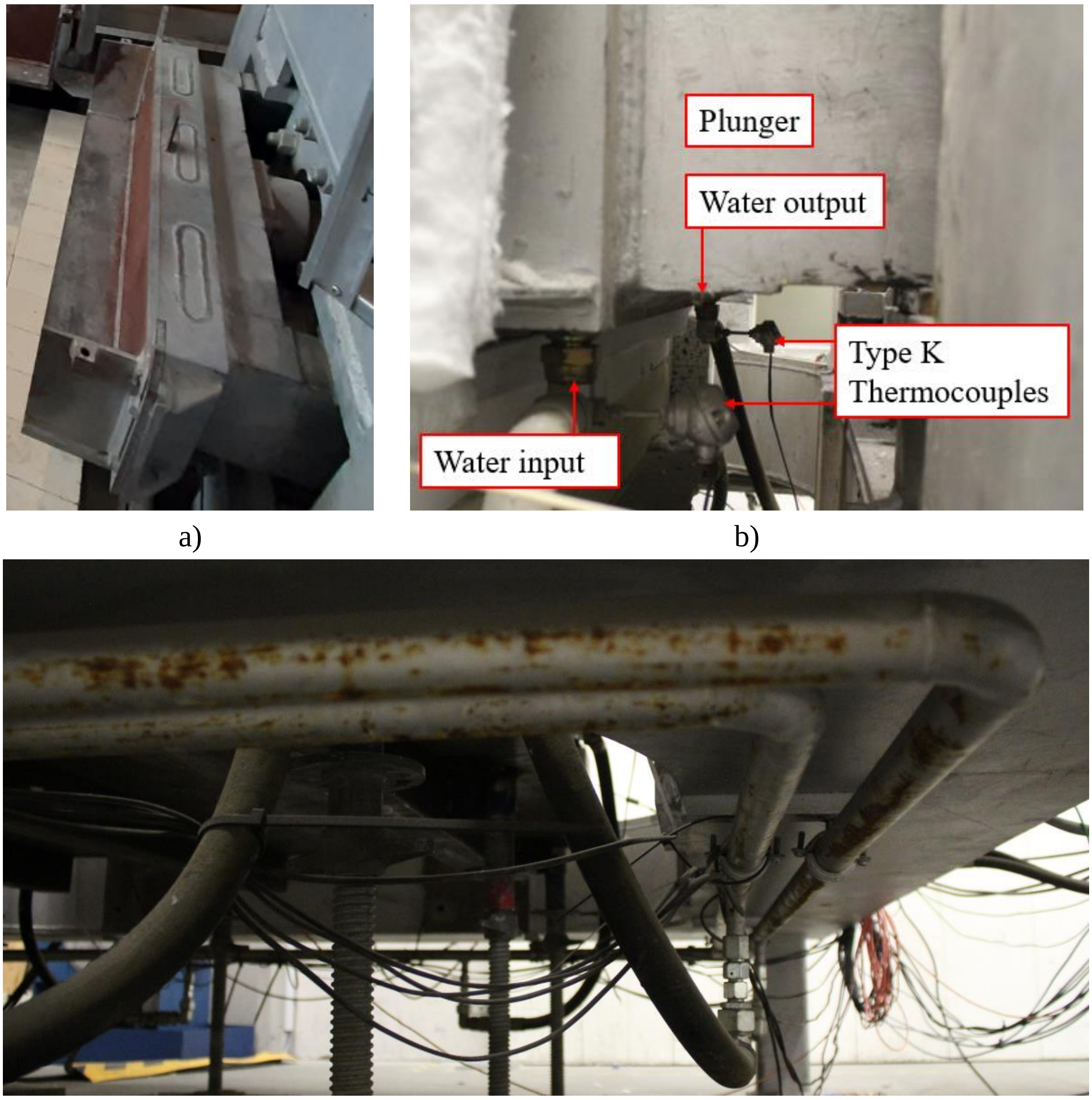

a) b)

c)

Figure 5-8 – Water cooling details: a) Cooled part of plungers; b) Thermocouples of the system; c) Pipes

5.3 Specimens and instrumentation

The specimens consisted of dry-stacked masonry walls made of the same bricks used in the uniaxial experimental campaign presented in Chapter 4. The properties of the material and the dimensions of the bricks were described in section 3.1. In order to fully characterize the masonry thermomechanical behaviour, three different configurations were used in the tests. **Figure 4-9** presents the general arrangement of the specimens. The tested specimens had eleven courses of bricks, each course had seven bricks and one-half brick.

The thickness of the wallet (140 mm) was based on the usual thickness of the working linings of the steel ladles, as shown in Chapter 4. The in-plane dimensions of the wall (1100×1125 mm) were based in the inner dimension of the test field of the biaxial press.

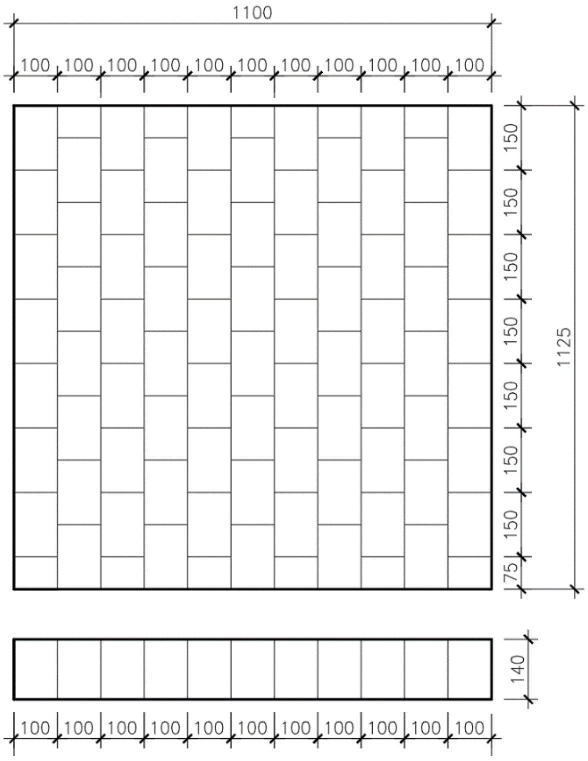

Figure 5-9 – Biaxial specimens dimensions

The displacements were measured using inductive LVDTs WA-50 of HBM made. The measurement range of the equipment is 50 mm. For the tests performed at ambient temperature, the LVDTs were fixed at the tip of an corundum tube (ø15 × ø11 × 400mm), the other tip was fixed in the bricks using two steel angle section (**Figure 5-10**). A second corundum tube (ø8 × ø5 × 1225 mm) was placed concentrically to the external tube and fixed in the specimen by using another steel piece and a screw.

This system allowed the measurement of the relative displacements between the points in which the corundum tubes were fixed.

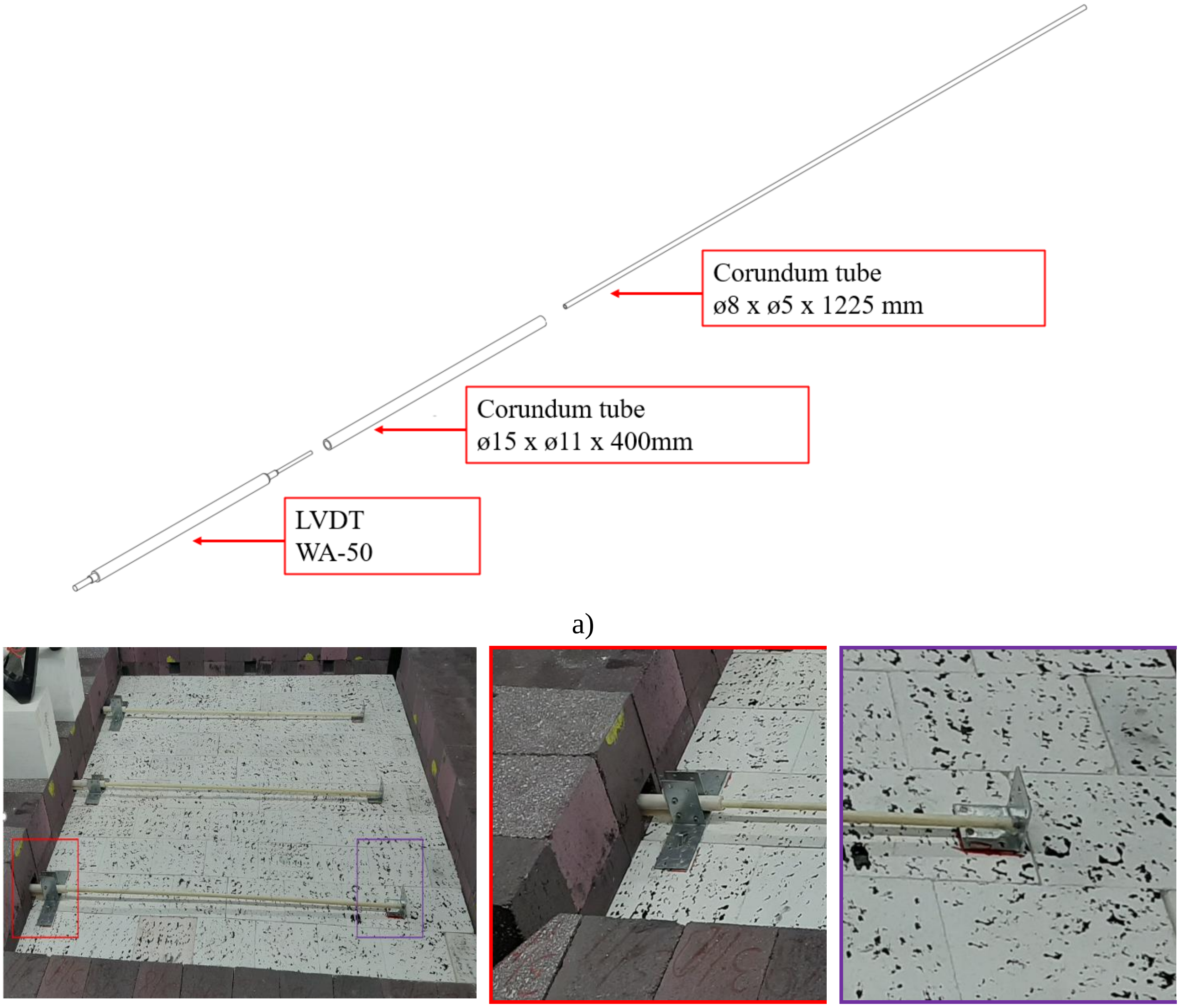

a)

b) c) d)

Figure 5-10 – LVDTs used in the ambient temperature test: a) General arrangement; b) Overview; c) Detail A of fixation; d) Detail B of fixation

The location of the LVDTs for test series S06.AT.LBJ, S07.AT.LHJ and S08.AT.LBI are given in **Figure 5-11**, **Figure 5-12** and **Figure 5-13**, respectively.

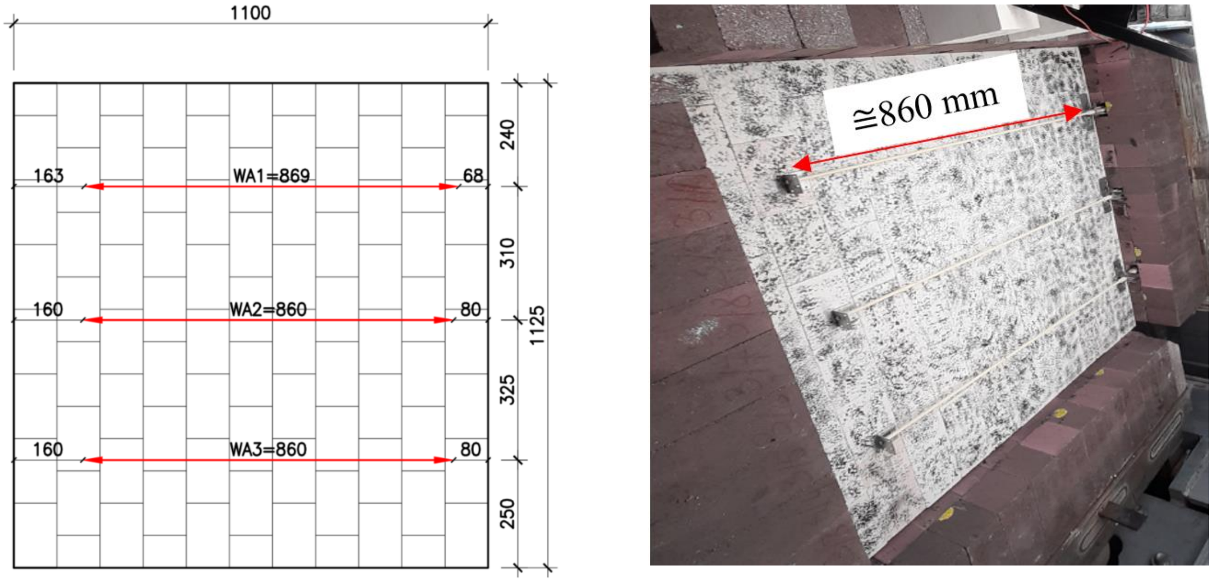

a) b)

Figure 5-11 – LVDTs used at test series S06.AT.LBJ: a) Location; b) Overview

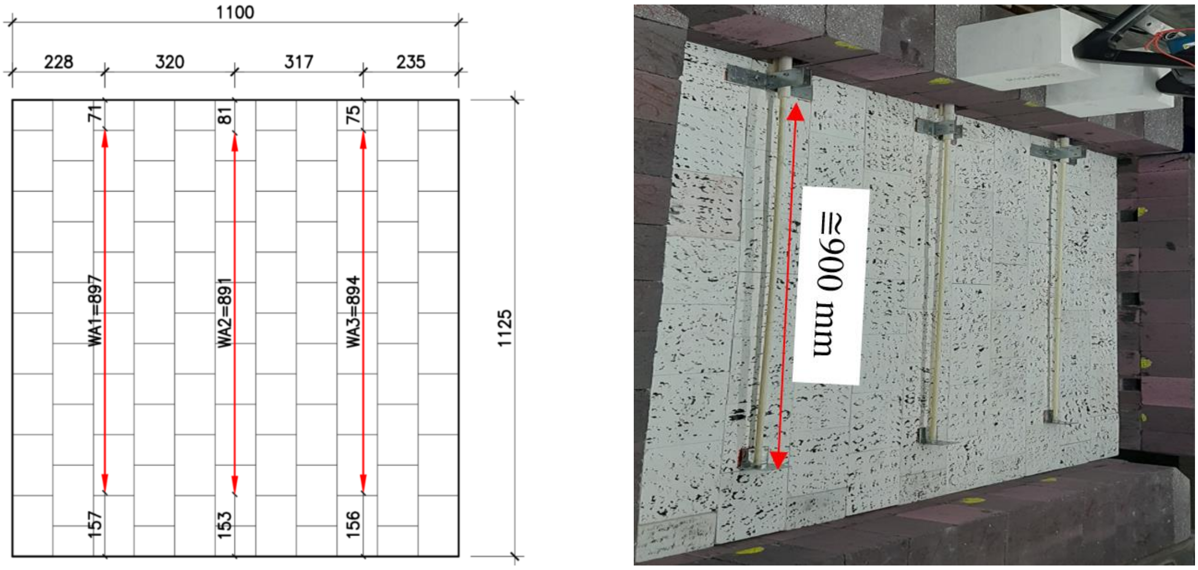

a) b)

Figure 5-12 – LVDTs used at test series S07.AT.LHJ: a) Location; b) Overview

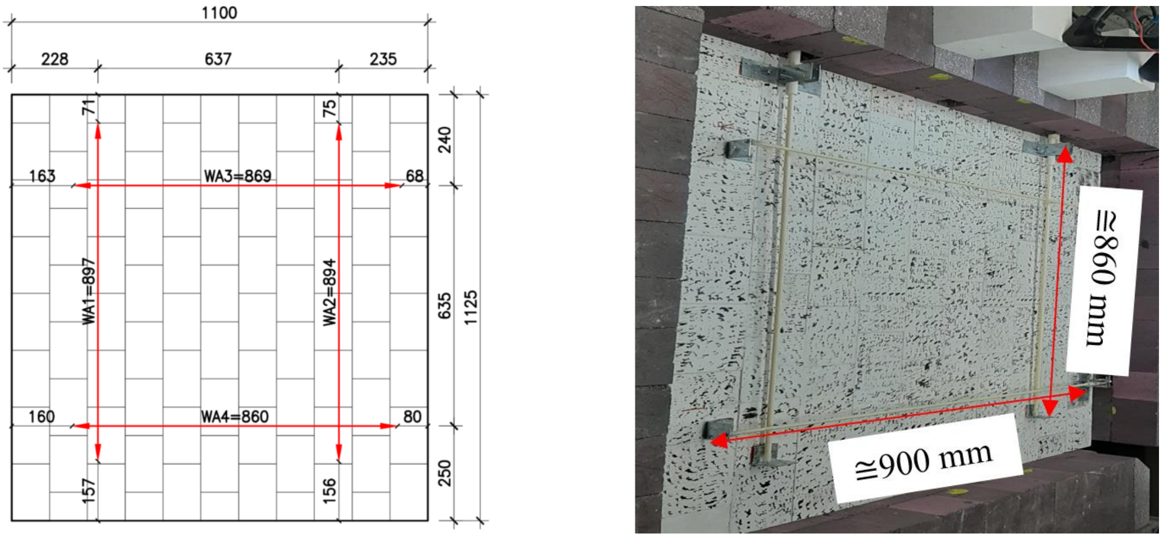

a) b)

Figure 5-13 – LVDTs used at test series S08.AT.LBI: a) Location; b) Overview

The LVDTs system used in the high temperature tests followed the same concept of the one used in the ambient temperature tests but with some extra components (**Figure 5-14**). The LVDT (2) was fixed to a metallic tube (1) by two screws (3). In the other tip of the metallic tube (1) a corundum tube (4) was fixed, the corundum tube (4) was also fixed in the specimen. A second corundum tube (5) was placed concentrically to these tubes (1 and 4) and fixed to the specimen. A third corundum tube (6) with a type B thermocouple was placed inside tube (5). A metallic piece (7) was used to fix the tubes 5 and 6 to the LVDT (1). The components of the LVDT system are detailed in **Figure 5-15**.

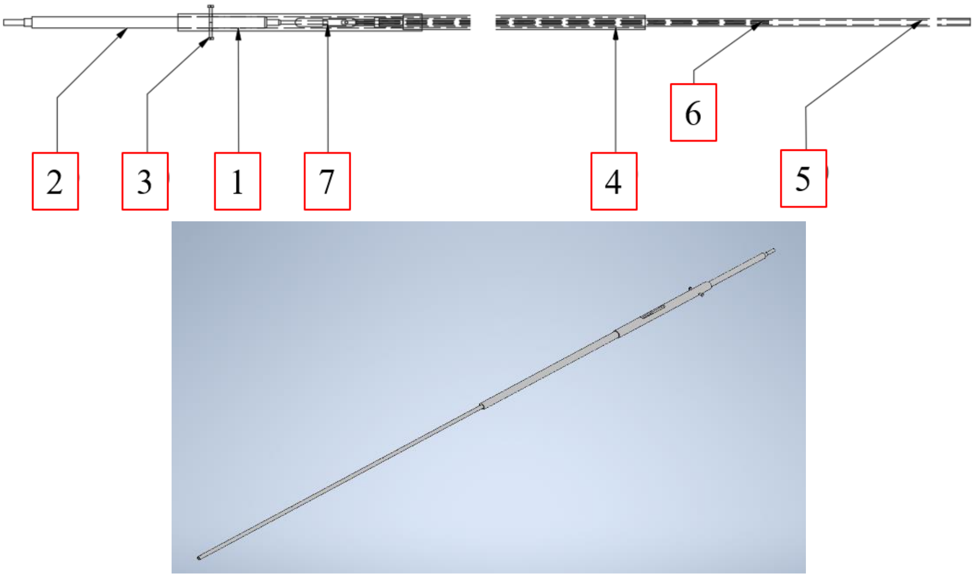

Figure 5-14 –LVDTs system

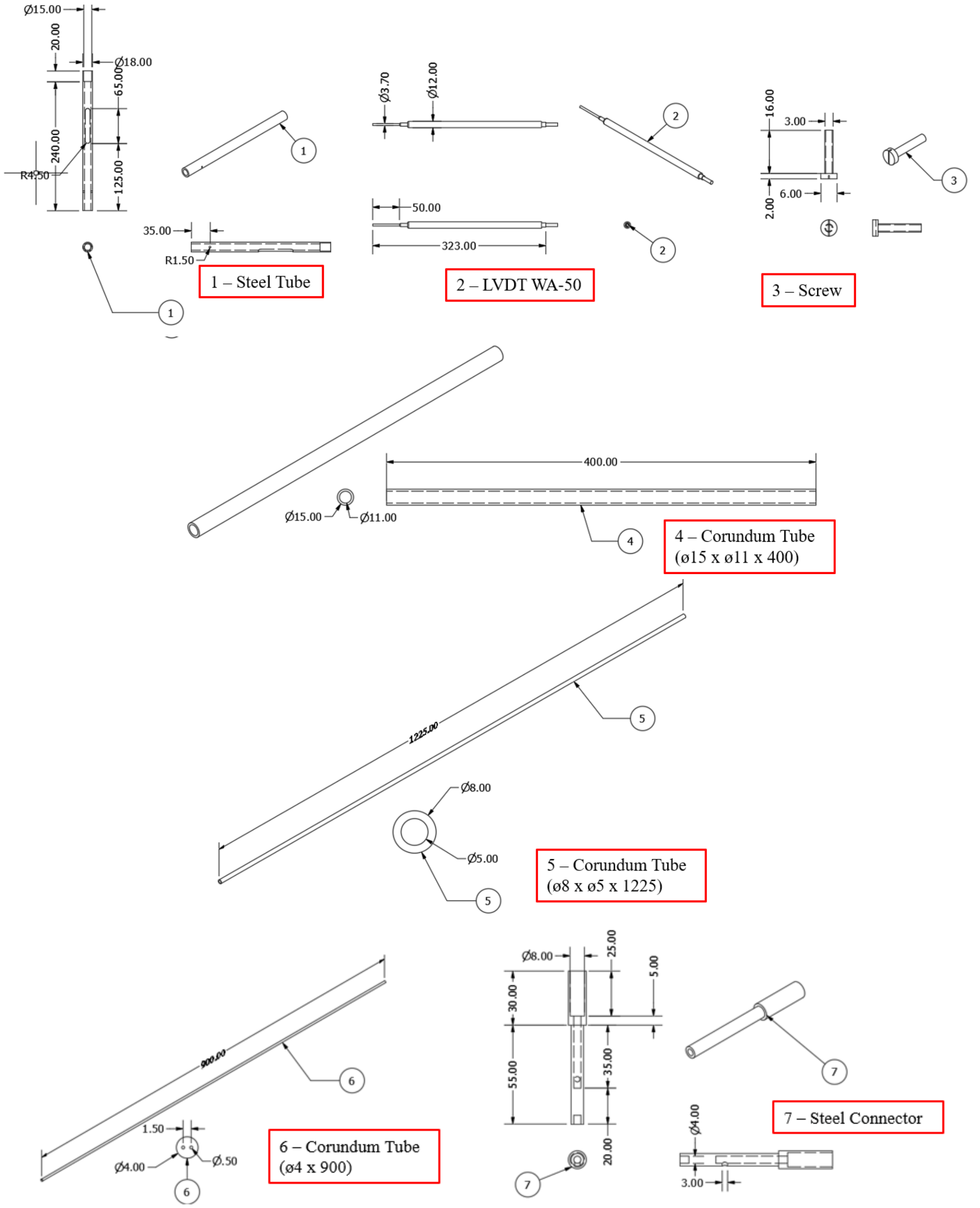

Figure 5-15 – Components of the LVDTs system

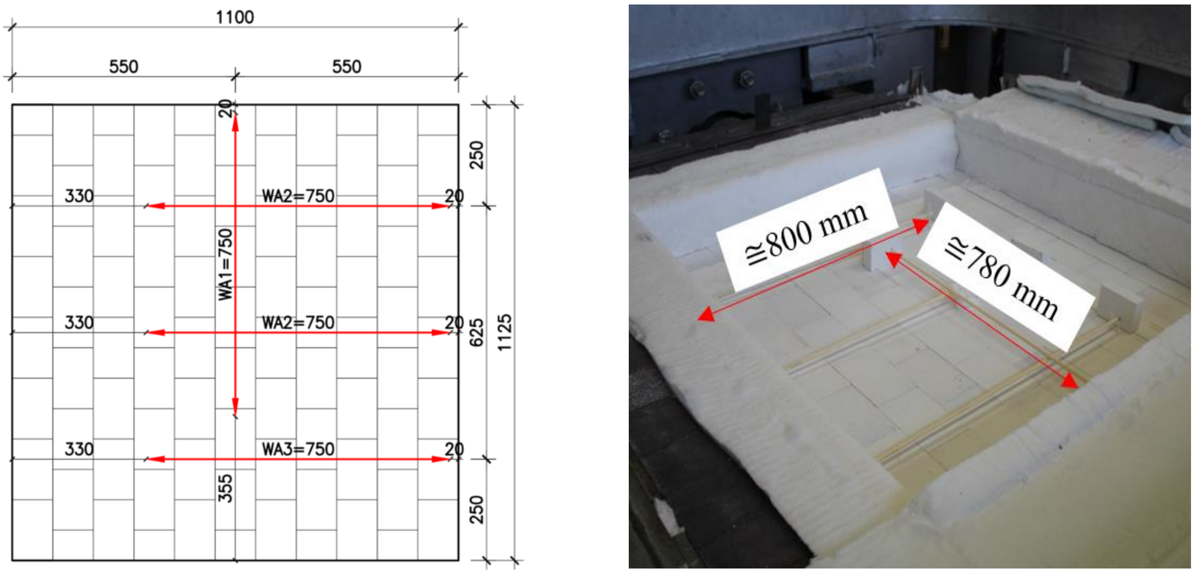

a) b)

Figure 5-16 – LVDTs used at test series S09.HT.CBJ: a) Location; b) Overview

a) b)

Figure 5-17 – LVDTs used at test series S10.HT.CBI and S11.HT.RBI: a) Location; b) Overview

The DIC technique (Dupre *et al*, 2018; Belrhiti *et al*, 2017; Besnard *et al*, 2006) was also used to measure the in-plane displacements fields in the tests performed at ambient temperature. In spite of the recent developments in the use of DIC at high temperatures (Teixeira *et al*, 2019; Kaczmarek *et al*, 2019), the absence of windows in the furnace did not allow the use of the technique for the other tests.

An 18 MPx (5184×3486) camera was used for image acquisition and three LED reflectors were used to provide enough light. The used configuration allowed to plot the in-plane displacements and strain field obtained during the tests. The image processing was performed using subsets of 120×120 pixels. The speckle patter application had the following steps: *i*) the bricks were laid on a horizontal plane; *ii*) the speckle pattern was applied by means of a paintbrush; *iii*) a dwell time of 24 hours was considered for drying. The speckle pattern application, its details and the DIC system are shown in Figure 4-7.

a) b)

Figure 5-18 – Digital Image Correlation: a) DIC set-up; b) DIC details

The thermal instrumentation comprised five type B thermocouples installed at the cold face of the wall, five type B thermocouples installed in the hot face and two type S thermocouple in the heating chamber. The thermocouples wires (ø 0.5 mm) were placed inside alumina tubes to avoid undesired contact of the wires and for mechanical protection.

The type B thermocouples are composed by Platinum-Rhodium (30%) / Platinum-Rhodium (6%) alloys and are able to operate from 0ºC to 1700ºC. The Type S are made with Platinum-Rhodium (10%) / Platinum and are able to operate from 0ºC to 1600ºC.

The type S thermocouples installed in the middle of the heating chamber were also placed inside an alumina tube, as shown in **Figure 5-19**. One thermocouple was used to feed the furnace controller and the other one was connected to the data acquisition system. The thermocouples of the cold face were placed in the upper face of the last insulation layer, in contact with the cold face of the specimen. The location of the thermocouples is given in **Figure 5-20**.

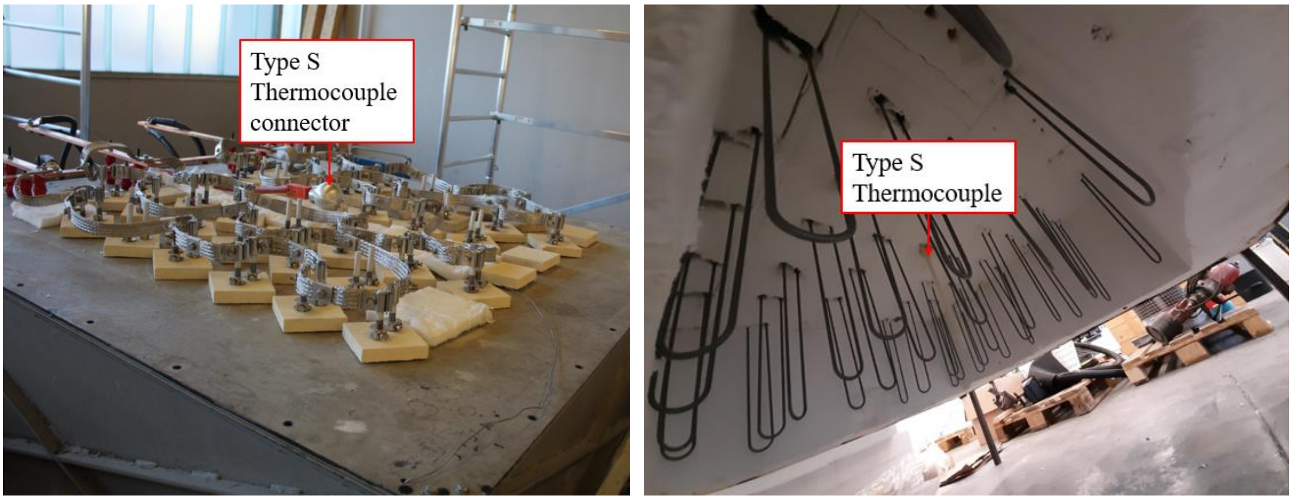

a) b)

Figure 5-19 – Heating chamber thermocouple: a) External view; b) Internal view

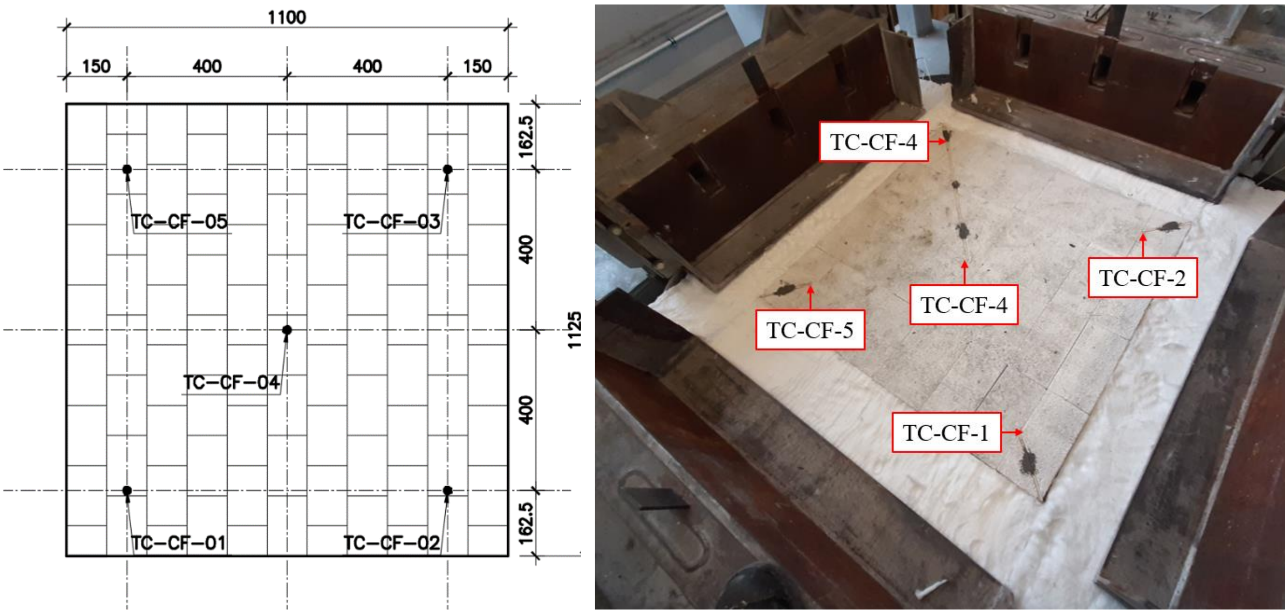

a) b)

Figure 5-20 – Thermocouples of cold face: a) Location; b) Details

The LVDT instrumentation of test series S09.HT.CBJ was different from the one used for test series S10.HT.CBI and S11.HT.RBI. The thermocouples of the hot face were installed inside the LVDT tubes, therefore, their positions were also different. The location of the thermocouples used in test series S09.HT.CBJ is given in **Figure 5-21** presents the details of the thermal instrumentation of S10.HT.CBI and S11.HT.RBI.

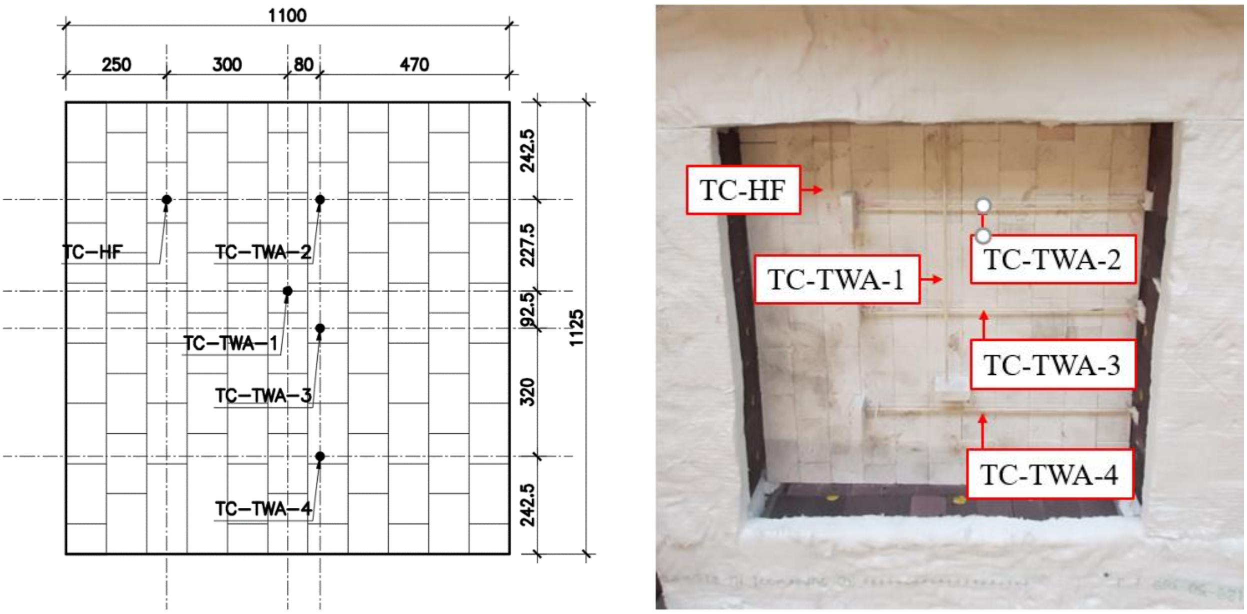

a) b)

Figure 5-21 – Thermocouples of hot face – S09.HT.CBJ: a) Location; b) Thermocouple distribution

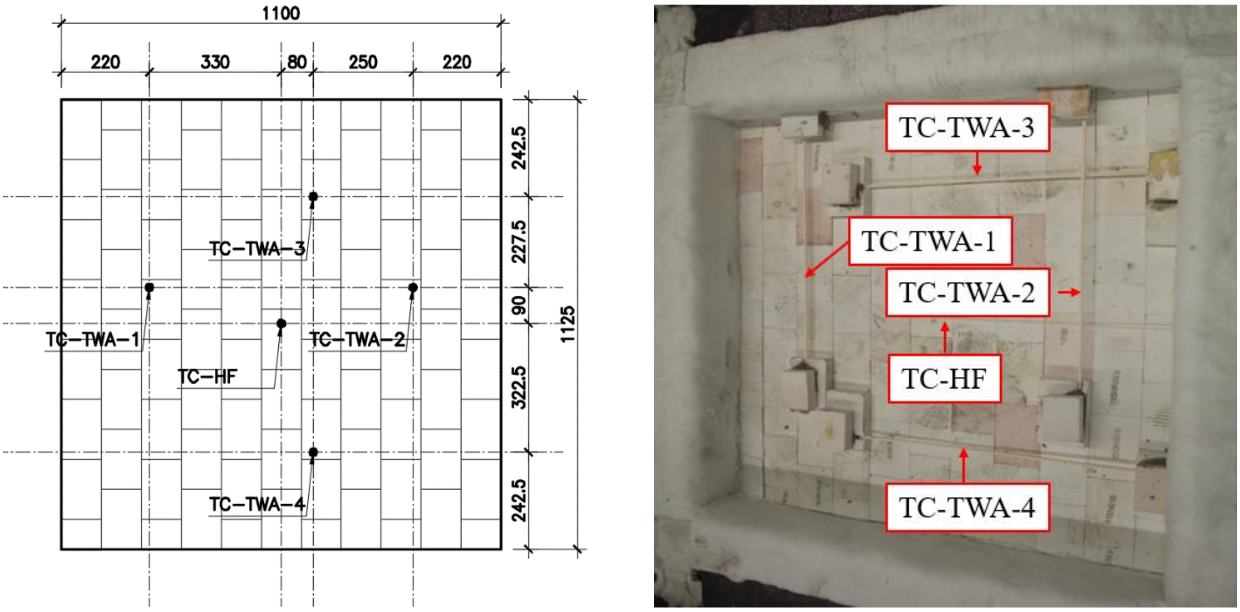

a) b)

Figure 5-22 – Thermocouples of hot face – S10.HT.CBI and S11.HT.RBI: a) Location; b) Thermocouple distribution

5.4 Test procedure

The following test procedures were used in the different test series:

- **Test series S06.AT.LBJ:** The objective of test series S06.AT.LBJ was to assess the loadbearing capacity of the refractory masonry walls loaded in the bed direction with a mechanical constraint in the head direction. The test procedure in series S01.AT.LBC had the following steps: *i*) the masonry specimens were built in the testing field; *ii*) the instrumentation was installed; *iii*) a pre-compressive load of 20 kN was applied; *iv*) the specimen was loaded in the direction of the bed joints under displacement control at a rate of 0.02 mm/s up to the maximum load of 6 MPa; *v*) when the maximum load was reached, the specimen was unloaded at the same strain rate. *vi*) The steps *iv* and *v* were repeated twice.
- **Test series S07.AT.LHJ:** The objective of test series S07.AT.LHJ was to assess the loadbearing capacity of the refractory masonry walls loaded in the head direction with a mechanical constraint in the bed direction. The test procedure was the same of S06.AT.LBJ, however, the load direction was the head joints and the displacement rate was 0.007 mm/s.
- **Test series S08.AT.LBI:** Series S08.AT.LBI aimed to assess the mechanical behaviour of masonry wallets at ambient temperature loaded under biaxial conditions. Steps *i*, *ii* and *iii* of the test procedure were similar to the ones presented for series S06.AT.LBJ. *iv*) the specimen was loaded in both directions under displacement control at a rate of 0.007 mm/s up to the maximum load of 6 MPa. *v*) when the maximum load was reached in both directions, the specimen was unloaded and two additional load cycles were applied.
- **Test series S09.HT.CBJ:** The objective of series S09.HT.CBJ was to assess the creep behaviour of refractory masonry walls subjected to uniaxial creep. Steps *i*, *ii* and *iii* of the test procedure were similar to the ones presented for series S01.AT.LBC. Then: *iv*) the furnace was placed in position; *v*) the specimen was heated; *vi*) a dwell time of 18.0 hours was considered; *vii*) the mechanical load was applied in direction X under displacement control at a rate of 0.007 mm/s. *viii*) The hydraulic jacks were set to force control to keep the current force; *ix*) The specimen was monitored for 18.0 hours, the temperatures and displacements were recorded; *x*) the specimen was unloaded and two more load cycles were performed.
- **Test series S10.HT.CBI:** The objective of series S10.HT.CBI was to assess the creep behaviour of refractory masonry walls subjected to biaxial creep. Steps *i* to *v* of the test procedure were similar to the ones presented for series S09.HT.CBJ. Then: *iv*) the furnace was placed in position; v) the specimen was heated; *vi*) a dwell time of 18.0 hours was considered; *vii*) the mechanical load was applied in directions X and Y under displacement control at a rate of 0.007 mm/s. *viii*) The hydraulic jacks were set to force control to keep the current force; *ix*)

The specimen was monitored for 16.0 hours; *x*) the specimen was unloaded and two more load cycles were performed.

- **Test series S11.HT.RBI:** The objective of series S11.HT.RBI was to assess the relaxation behaviour of refractory masonry walls subjected to biaxial loading. Steps *i* to *v* of the test procedure were similar to the ones presented for series S09.HT.CBJ. Then: *iv*) the furnace was placed in position; v) the specimen was heated; *vi*) a dwell time of 18.0 hours was considered; *vii*) the mechanical load of 4 MPa was applied in directions X and Y under displacement control at a rate of 0.007 mm/s. *viii*) The hydraulic jacks were set to keep the same position; *ix*) The specimen was monitored during the relaxation process; *x*) the specimen was unloaded; *xi*) The steps *vii* to *x* are repeated once with the load level of 6 MPa.

The heating procedure comprised the following steps: *i*) from ambient temperature to 500ºC in ten minutes; *ii*) from 500 ºC to 1500ºC in ten hours; *iii*) dwell time of 18 hours at 1500 ºC.

5.5 Results and discussion

The experimental results are presented and discussed in this section. For each test series, results in terms of displacements, strains, forces, stresses, temperatures are presented and discussed. Wherever possible, comparisons with literature results are made. The experimental results allowed to assess the mechanical behaviour of the system. The effects of the stress concentrations caused by brick's height imperfections and its effects on the loadbearing capacity of the specimens, the evolution of the wall's stiffness with the load application, the developed crack patterns and the mechanical behaviour of the specimens at ambient and high temperatures.

5.5.1 Test series S06.AT.LBJ

Test series S06.AT.LBJ aimed to evaluate the mechanical behaviour of masonry wallets loaded in bed joints with lateral restraints in the direction of the head joints. The evolution of the in-plane displacements measured in the tests are presented in **Figure 5-23**. The LVDTs used to measure the in-plane displacements (WA-2, WA-3 and WA-4) and the average of their values (WA-Avg) are presented. As expected for masonry walls and as observed in the previous tests, a small scattering on the in-plane displacements was observed.

The maximum strain obtained for test series S02.AT.LBJ.01 and S02.AT.LBJ.02 was 0.0024 and 0.0022, respectively. No significant increasing on the maximum strains were observed for the second and third load cycles when compared to the first load cycle.

As observed in test series S02.AT.CIC, residual strains are obtained after the first loading cycle. The average residual strain after the first load cycle for test series S06.AT.LBJ.01 and S06.AT.LBJ.01 was

0.0015 and 0.0012, respectively. The increasing of the residual strains after the second and third load cycles were not significant.

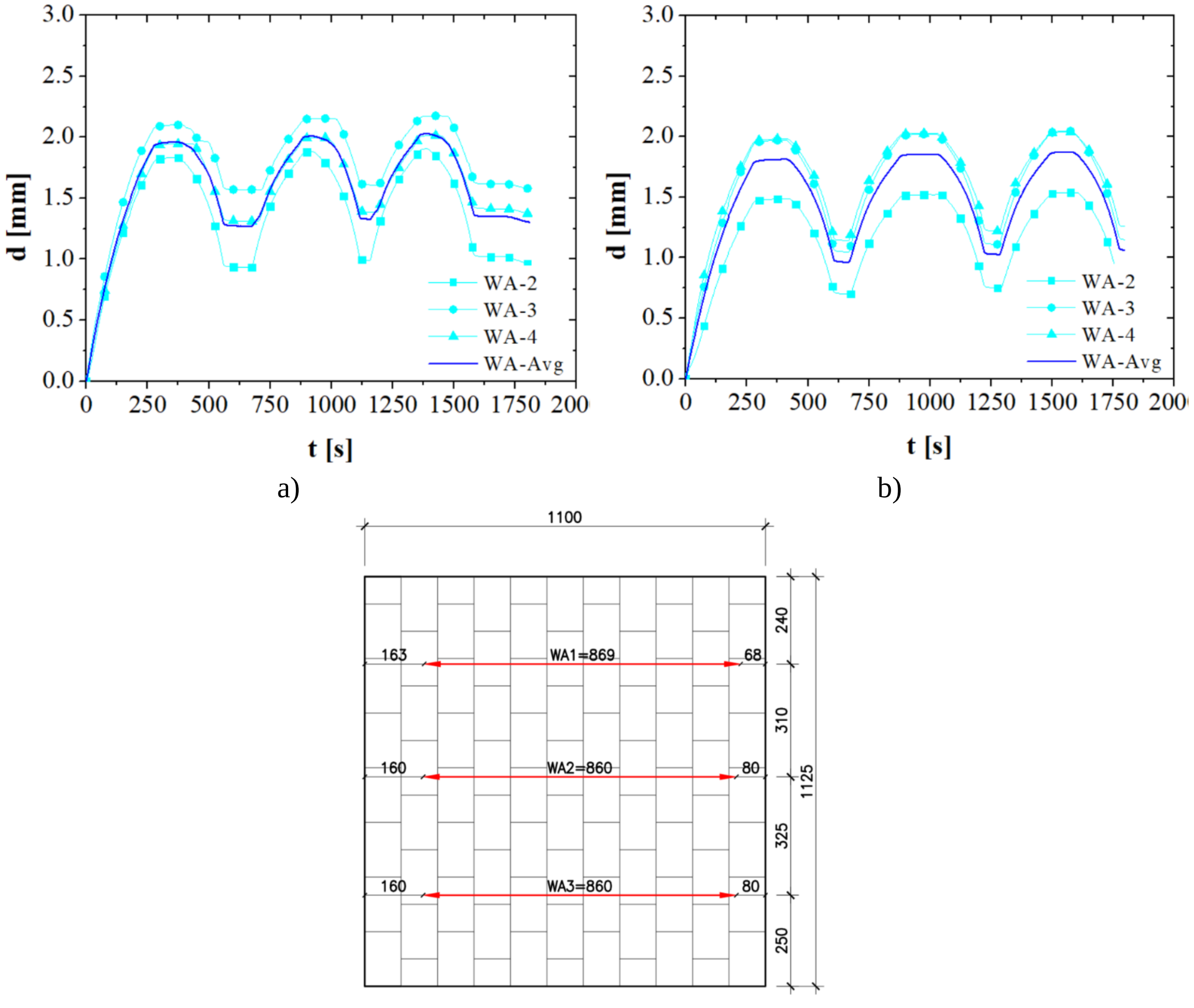

a)

b)

c)

Figure 5-23 – Test series S06.AT.LBJ – In-plane displacements: a) S06.AT.LBJ.01; b) S06.AT.LBJ.02; c) LVDTs' location

The measured forces and stresses during the test are shown in **Figure 5-24** and **Figure 5-25**, respectively. The lateral restraint provided by the blocked plunger prevented elongation of the wall in the direction perpendicular to the loading (due the Poisson's effect), consequently, a reaction force was observed in the head joint direction. In test series S06.AT.LBJ.01 and S06.AT.LBJ.02 the maximum reaction forces were 103.6 kN (0.67 MPa) and 101.3 kN (0.66 MPa), respectively.

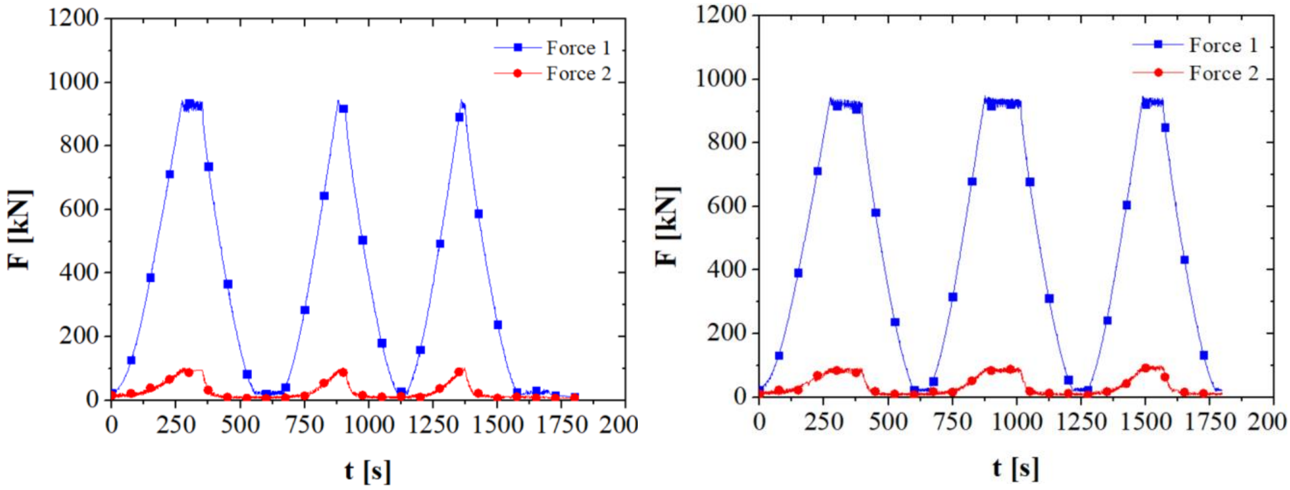

a) b)

Figure 5-24 – Test series S06.AT.LBJ – Forces: a) S06.AT.LBJ.01; b) S06.AT.LBJ.02

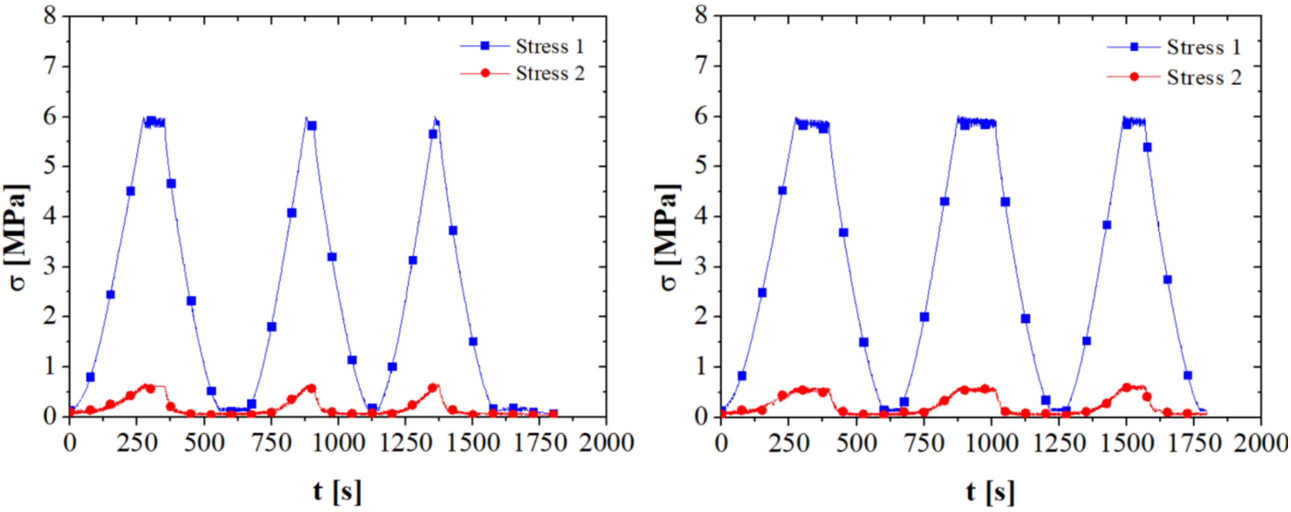

a) b)

Figure 5-25 – Test series S06.AT.LBJ – Stresses: a) S06.AT.LBJ.01; b) S06.AT.LBJ.02

The stress-strain curves obtained in test series S06.AT.LBJ are presented in **Figure 5-26**. A small scattering was observed between the tests results. As noticed in test series S02.AT.CIC, an increasing of the stiffness is observed after the loading stage, caused by the increasing of the contact area between the bricks.

In test series S06.AT.LBJ, a sudden drop of stresses at the beginning of the unloading stage was observed. It was caused by the methodology used to measure the forces. The forces were calculated based on the pressure gages of the hydraulics, as the experimental setup does not allow the use a load cell due to limited space. When the hydraulic jack starts to move in the backward direction this phenomenon was observed.

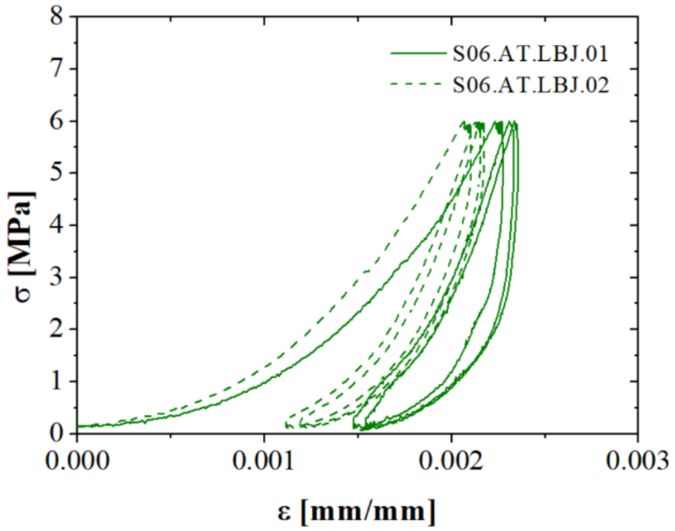

Figure 5-26 – Test series S06.AT.LBJ – Stress-strain curves

As observed in test series S02.AT.CIC, a few cracks were detected in the specimen in spite of the small load level applied (6 MPa). The cracks were mostly located at the cross-joints and were caused by the non-uniform loading and support conditions of the blocks, as discussed in Chapter 3 and as observed in the experiments presented in Chapter 4.

Figure 5-27 – Test series S06.AT.LBJ – Cracks observed in the specimen S06.AT.LBJ.01

5.5.2 Test series S07.AT.LHJ

The test series S06.AT.LBJ evaluated the structural response of masonry wallets loaded in the direction of the bed joints. This test series, S07.AT.LHJ, aims to evaluate the mechanical behaviour of masonry wallets loaded in head joints direction with lateral restraints in the direction of the bed joints. The evolution of the in-plane displacements measured in the tests are presented in **Figure 5-28**. The LVDTs used to measure the in-plane displacements (WA-1, WA-2 and WA-3) and the average of their values (WA-Avg) are presented. As observed in the previous case, a small scattering on the in-plane displacements was noticed.

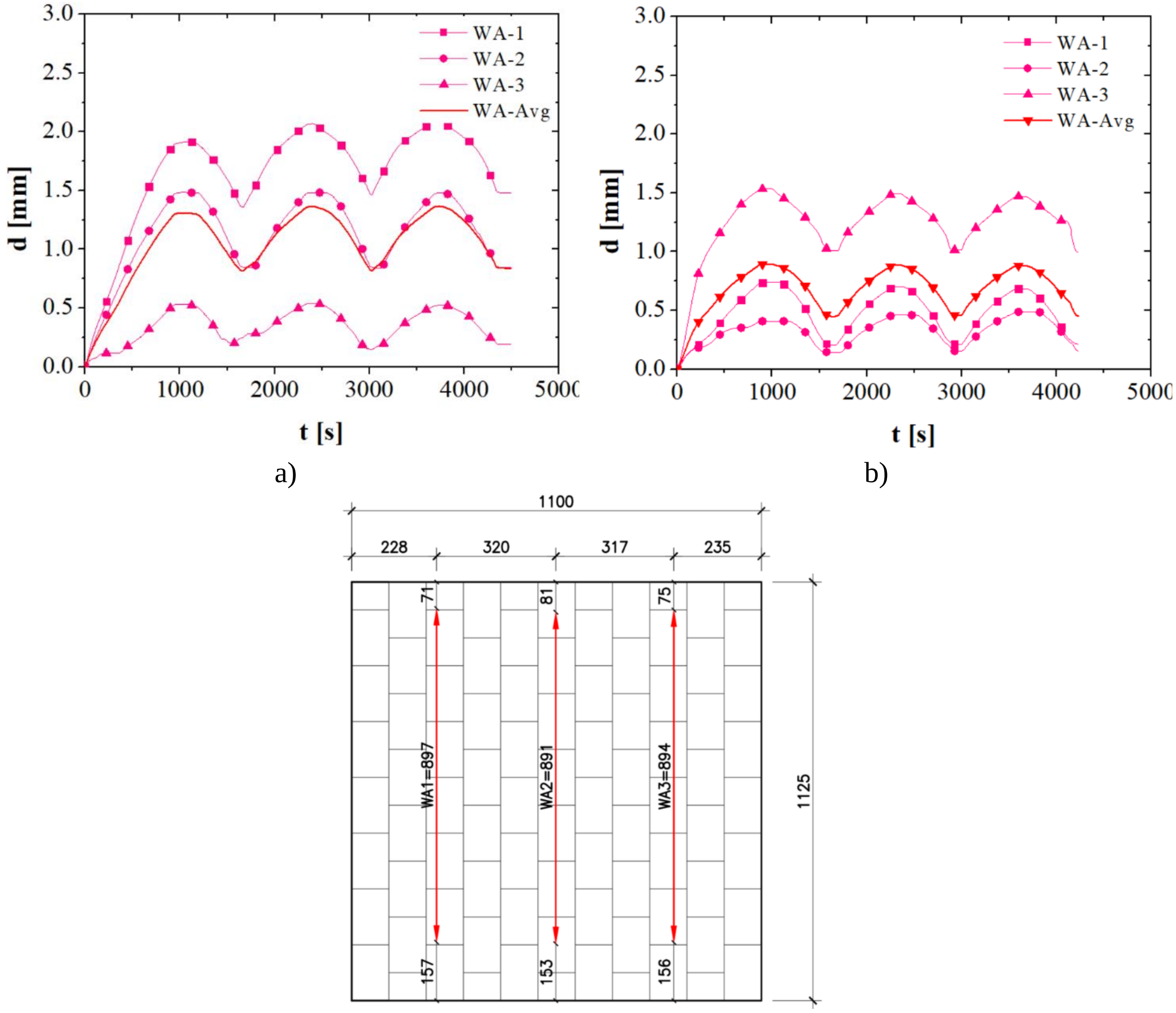

a)

b)

c)

Figure 5-28 – Test series S07.AT.LHJ – In-plane displacements: a) S07.AT.LHJ.01; b) S07.AT.LHJ.02; LVDTs' location

The maximum strain obtained for test series S07.AT.LHJ.01 and S07.AT.LHJ.02 was 0.0015 and 0.0010, respectively. As observed in test series S06.AT.LBJ, no significant increasing on the maximum strains were observed for the second and third load cycles when compared to the first cycle.

The residual strains caused by the crushing of initial non-plane surfaces of the bricks were also observed in this test series. The average residual strain after the first load cycle for test series S07.AT.LHJ.01 and S07.AT.LHJ.01 were 0.0010 and 0.0005, respectively. As observed in test series S06.AT.LBJ, the increasing of the residual strain after the second and third load cycles was not significant.

The measured forces and stresses during the test are shown in **Figure 5-29** and **Figure 5-30**, respectively. The lateral restraint provided by the blocked plunger prevents the elongation of the wall in the direction perpendicular to the loading (Poisson's effect), therefore, a reaction force was observed in the head joint direction. In test series S07.AT.LHJ.01 and S07.AT.LHJ.02 the maximum reaction forces were 149.8 kN (0.95 MPa) and 115.8 kN (0.74 MPa), respectively. Due to the higher stiffness of the wall in the direction of the head joints, the reaction forces were slightly higher than the ones obtained in test series S06.AT.LBJ.

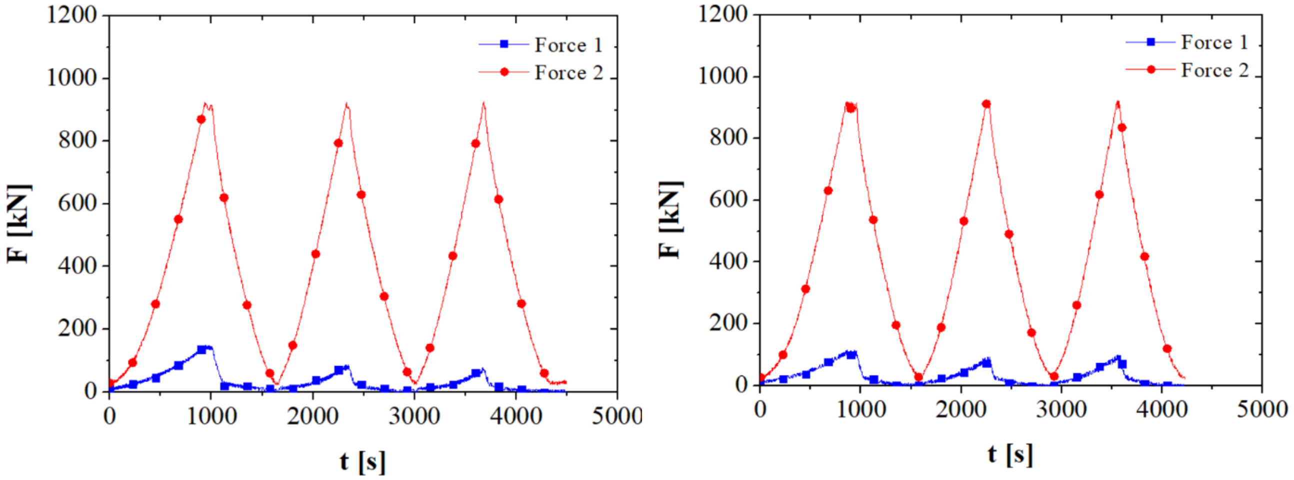

a) b)

Figure 5-29 – Test series S07.AT.LHJ – Forces: a) S07.AT.LHJ.01; b) S07.AT.LHJ.02

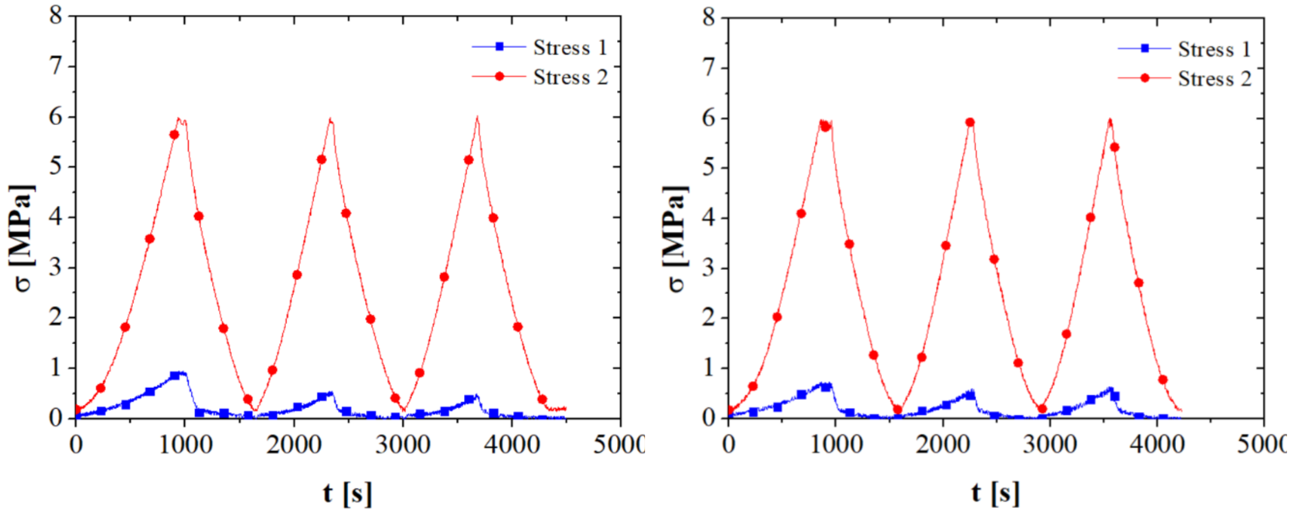

a) b)

Figure 5-30 – Test series S07.AT.LHJ – Stresses: a) S07.AT.LHJ.01; b) S07.AT.LHJ.02

The stress-strain curves obtained in test series S07.AT.LHJ are presented in **Figure 5-31**. A higher scattering on the results were observed when compared to test series S06.AT.LBJ. As noticed in test series S02.AT.CIC and S06.AT.LBJ, an increasing of the wall stiffness is observed after the loading stage. The sudden drop of stresses at the beginning of the unloading stage was previously discussed and it is also observed in this test series.

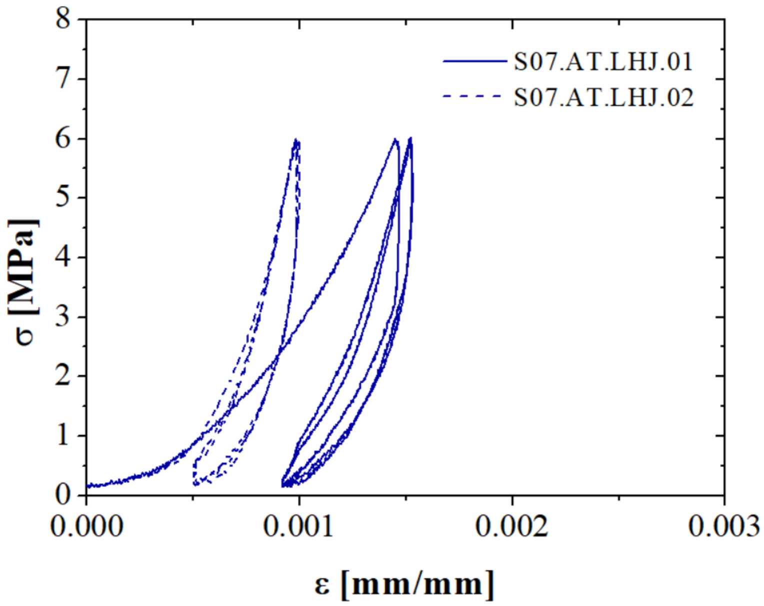

Figure 5-31 – Test series S07.AT.LHJ – Stress-strain curves

In spite of the small load level applied to the specimen (6 MPa), some cracks were observed in the head joints, as shown in **Figure 5-32**a. The crushing of edges of the bricks was also identified (**Figure 5-32**b and c), mostly likely caused by stresses' concentration due to bricks' shape imperfections. A few cracks were observed at the cross joints (**Figure 5-32**d), caused by the reaction force in the direction perpendicular to the loading.

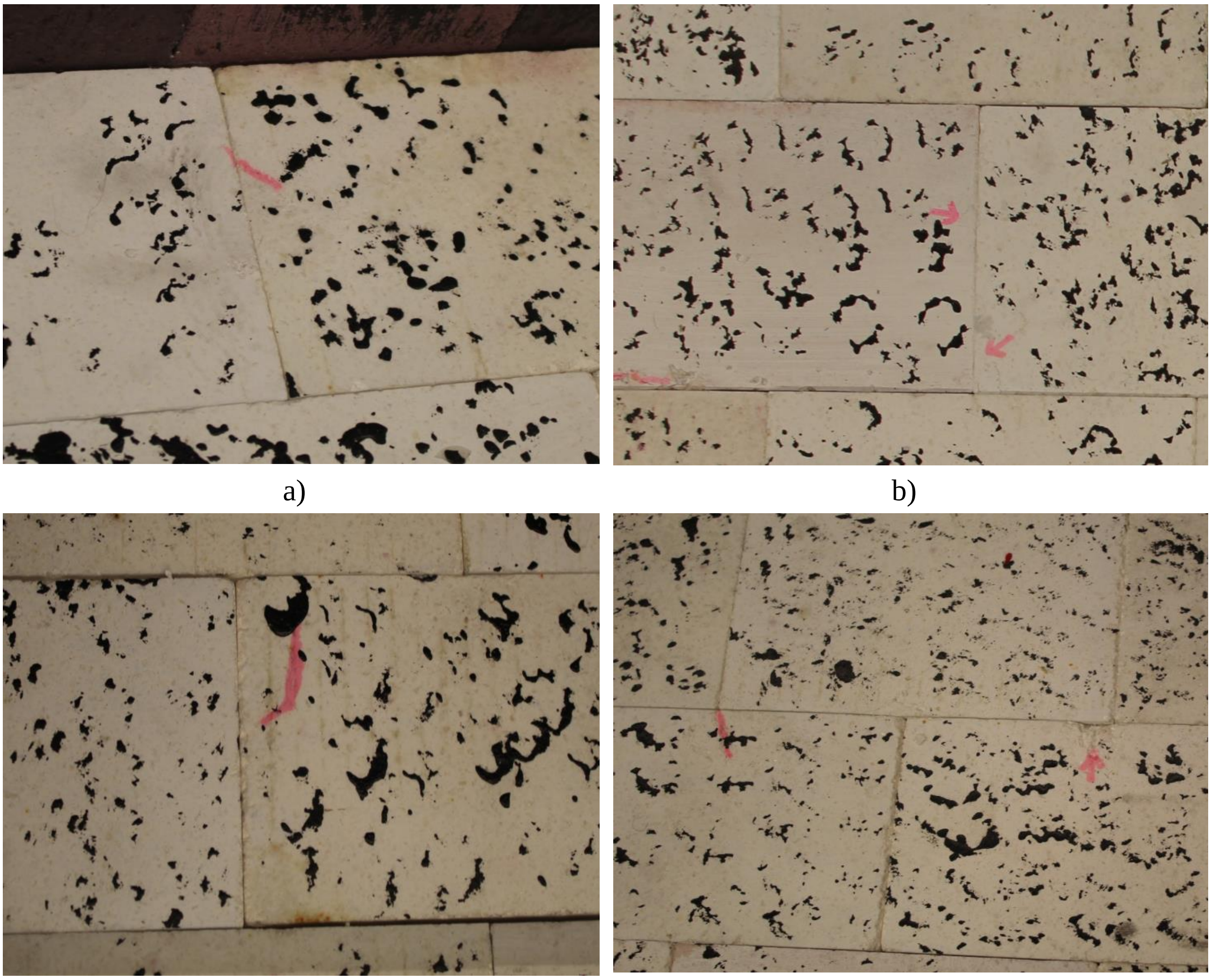

a) b)

c) d)

Figure 5-32 – Test series S07.AT.LHJ – Cracks observed in the specimen S07.AT.LHJ.01

5.5.3 Test series S08.AT.LBI

The previous two test series S06.AT.LBJ and S07.AT.LHJ evaluated the structural response of masonry wallets loaded with uniaxial compression. This test series, S08.AT.LBI, aims to evaluate the mechanical behaviour of masonry wallets loaded in biaxial conditions at ambient temperature. The evolution of the in-plane displacements measured in the tests are presented in **Figure 5-33**. The LVDTs used to measure the in-plane displacements (WA-1 to WA-4) and the average of their values in each direction (WA-Avg-X and AW-Avg-Y) are presented.

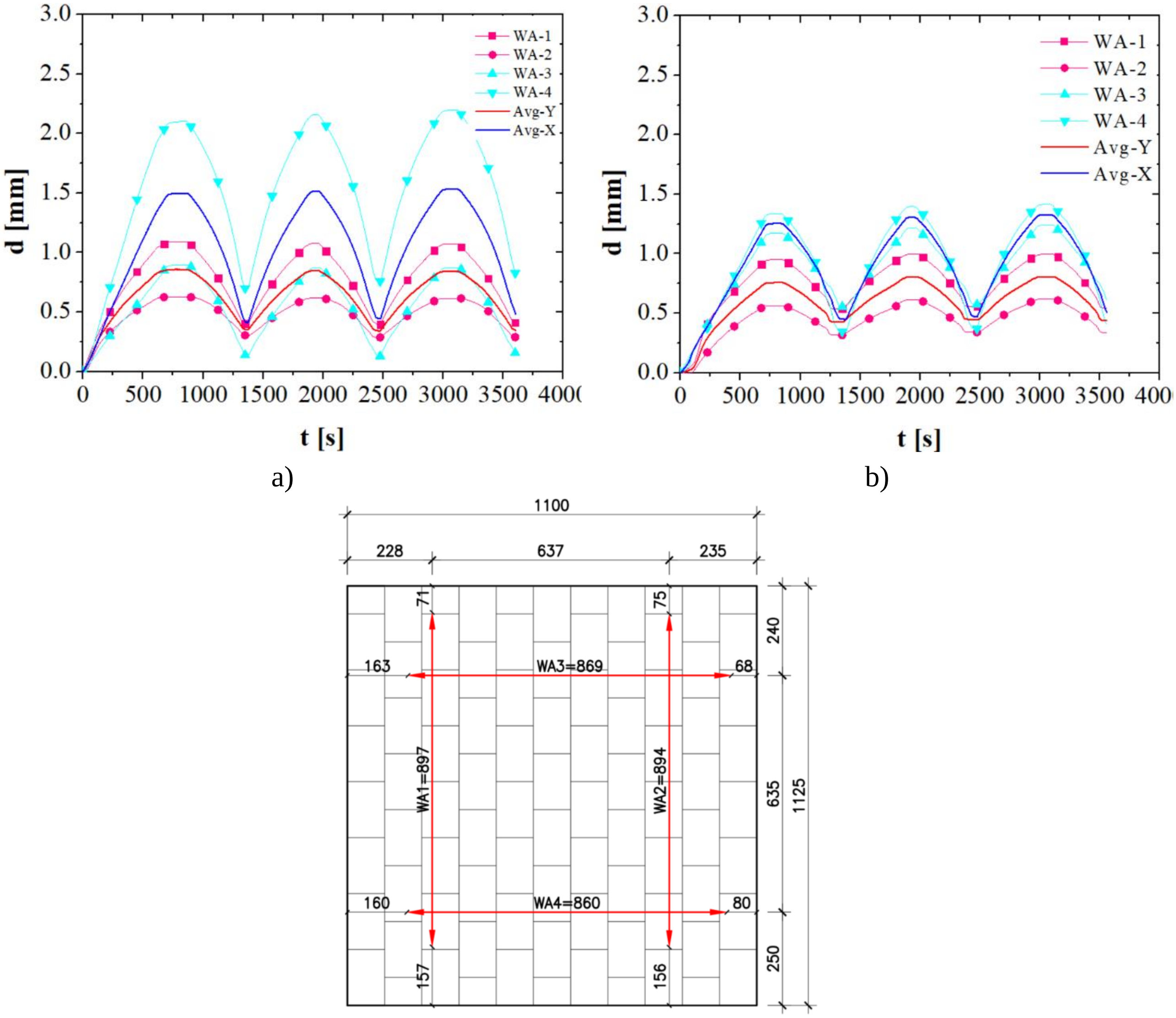

a)

b)

c)

Figure 5-33 – Test series S08.AT.LBI – In-plane displacements: a) S08.AT.LBI.01; b) S08.AT.LBI.02; c) LVDTs' location

The friction between the plungers and the wall is more significant in biaxial conditions. Therefore, smaller displacements were observed in the results of test series S08.AT.LBI. The comparison of the maximum and residual strains obtained in S06.AT.LBJ, S07.AT.LHJ and S08.AT.LBI is presented in **Table 5-3**. A significant reduction in the strains were observed for direction X and Y, moreover, the reduction in the residual strains after the first loading cycling was also obtained. Moreover, the joints present a stiffer behaviour under biaxial loading conditions.

Table 5-3 – Comparison of the maximum and residual strains in test series S06.AT.LBJ, S07.AT.LHJ and S08.AT.LBI

Test series	Specimen	ε_{max} X	ε_{max} Y	ε_{res} X	ε_{res} Y	$\varepsilon_{max,avg}$ X	$\varepsilon_{max,avg}$ T	$\varepsilon_{res,avg}$ X	$\varepsilon_{res,avg}$ Y
S06.AT.LBJ	01	0.0024	-	0.0015	-	0.0023	-	0.0014	-
	02	0.0022	-	0.0012	-				
S07.AT.LHJ	01	-	0.0015	-	0.0010	-	0.0013	-	0.0008
	02	-	0.0010	-	0.0005				
S08.AT.LBI	01	0.0016	0.0010	0.0005	0.0004	0.0015 (-34.7%)	0.0009 (-30.7%)	0.0005 (-64.3%)	0.0005 (-37.5%)
	02	0.0014	0.0008	0.0005	0.0005				

The measured forces and stresses during the test are presented in **Figure 5-34** and **Figure 5-35**, respectively. It was possible to observe that the loading and loading occurred simultaneously in both directions.

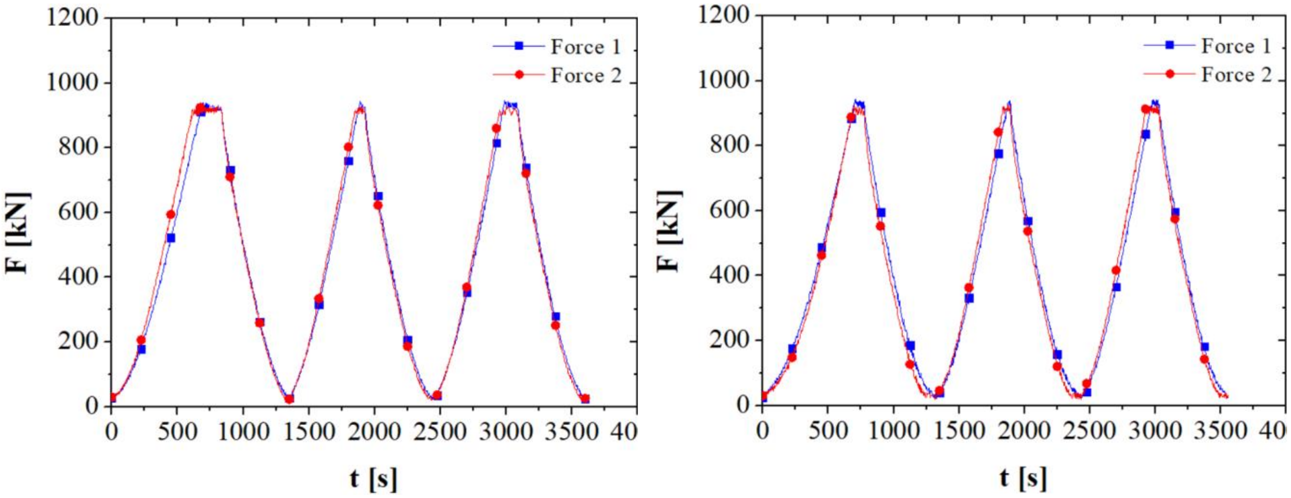

a) b)

Figure 5-34 – Test series S08.AT.LBI – Forces: a) S08.AT.LBI.01; b) S08.AT.LBI.02

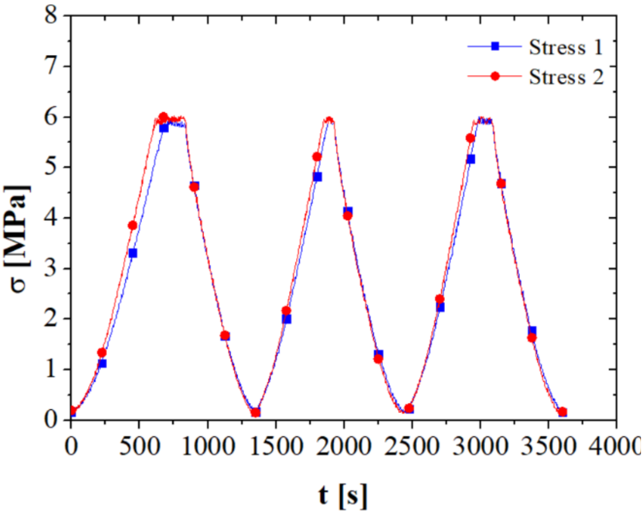

a) b)

Figure 5-35 – Test series S08.AT.LBI – Stresses: a) S08.AT.LBI.01; b) S08.AT.LBI.02

The stress-strain curves obtained in test series S08.AT.LBI are presented in **Figure 5-36**. The friction between the plungers and the specimen resulted in smaller strains and consequently an apparent higher stiffness in this test series. A small scattering on the results was observed. A sudden drop of stresses at the beginning of the unloading stage was previously discussed and it was also observed in this test series.

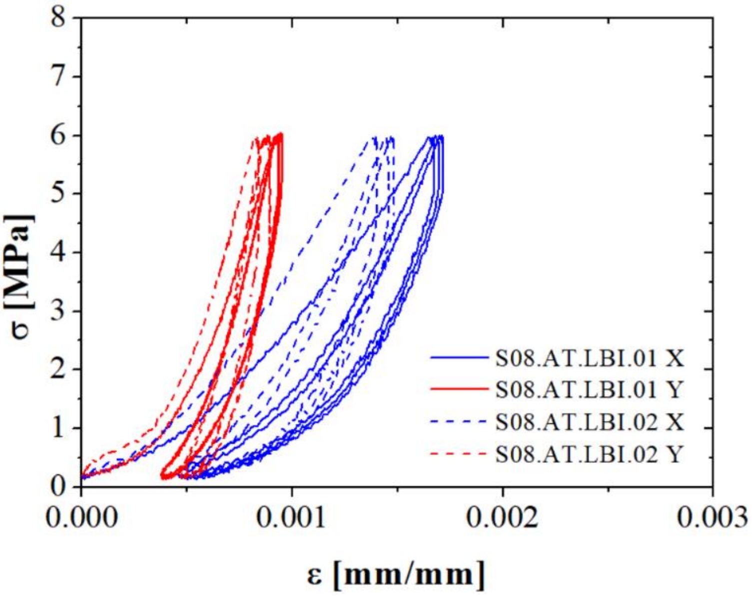

Figure 5-36 – Test series S08.AT.LBI – Stress-strain curves

The cracks observed in the specimen was similar to the ones already discusses in the previous sections. **Figure 5-37** shows the cracks observed in the bed joints and the crushing in the edges of the bricks at the head joints.

a) b)

Figure 5-37 – Test series S08.AT.LBI – Cracks observed in the specimen: a) Cracks at cross joints; b) Crushing at head joint

Figure 5-38 presents a comparison of the stress-strain curves obtained at the biaxial tests at ambient temperature.

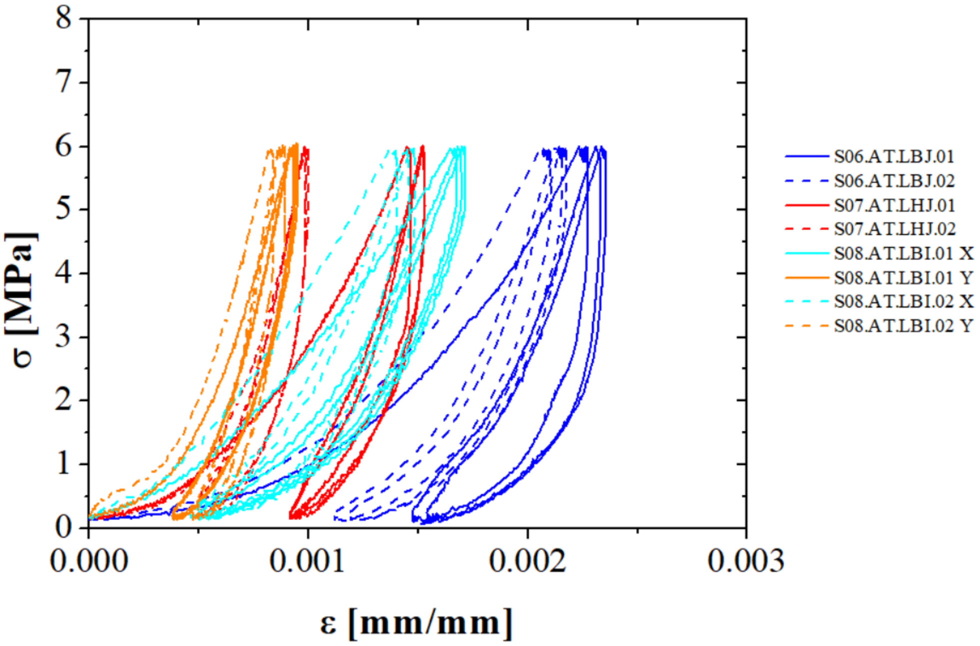

Figure 5-38 – Comparison of stress-strain curves obtained for test series S06.AT.LBJ, S07.AT.LHJ and S08.AT.LBI

5.5.4 Preliminary test at 1200 °C

A preliminary test was performed to calibrate the heating system of the machine. In this test, several changes were performed in the electrical connections: secondary voltage of the transformer and connections configuration (star and delta). This first test did not reach the desired temperature (1500 ºC), as the heating system did not have the required power, it was possible to achieve only 1200 ºC. The heating system was improved for the other tests.

The results of the preliminary test at 1200 ºC is given in this section. The temperatures measured by the thermocouples embedded in the bricks are presented in **Figure 5-39**. The temperatures recorded at the beginning of the test were around 180 ºC because the furnaces were previously turned on for testing. The temperature of the furnaces was not recorded for this test.

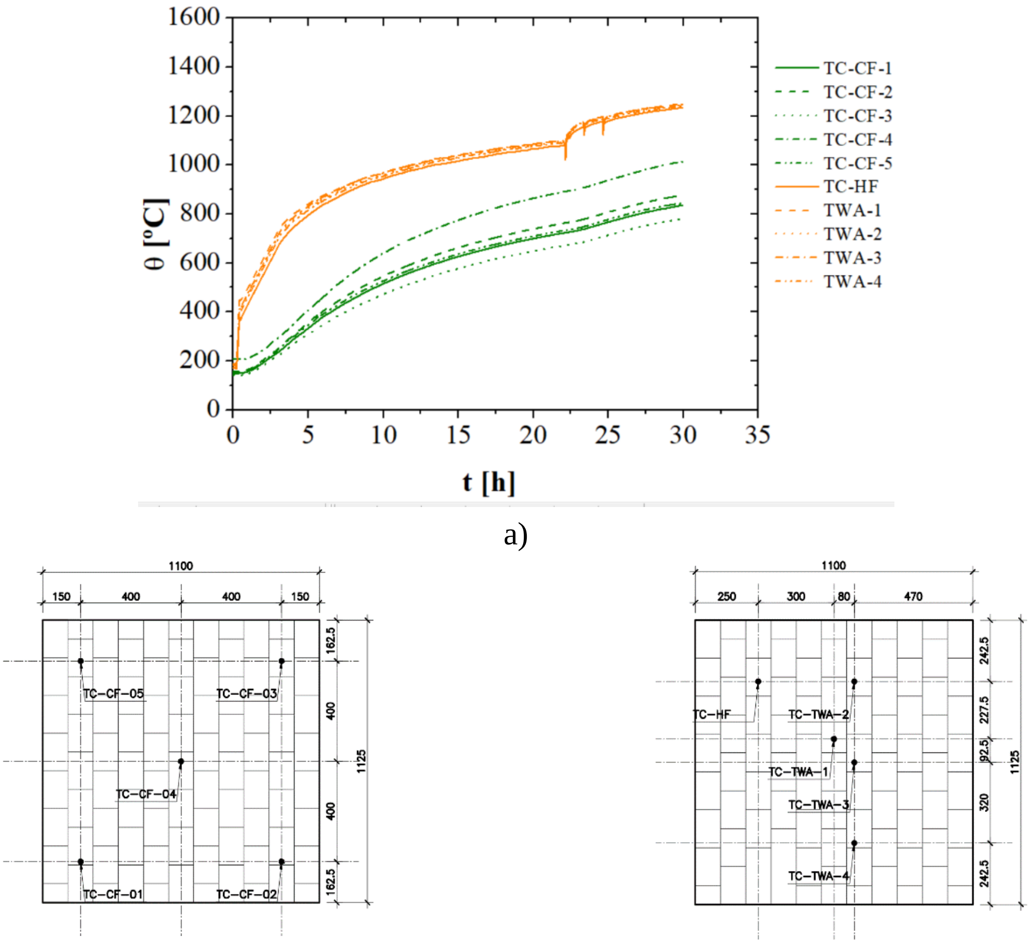

a)

b)

c)

Figure 5-39 – Test series S09.HT.CBJ – Preliminary test: a) Temperatures; b) Thermocouples of the cold face; c) Thermocouples of the hot face

The preliminary test was performed as a uniaxial creep test in the direction of the bed joints. The evolution of the in-plane displacements and strains are presented in **Figure 5-40**. The LVDTs used to measure the in-plane displacements (WA-2 and WA-3) and the average of their values (WA-Avg) are being presented. The LVDT WA-4 did not work properly during this test, therefore, it was ignored. A small scattering was observed between the measurements of LVDTs WA-2 and WA-3. It is possible to identify the creep strains during the holding stage (between 0.30 and 1.25 h).

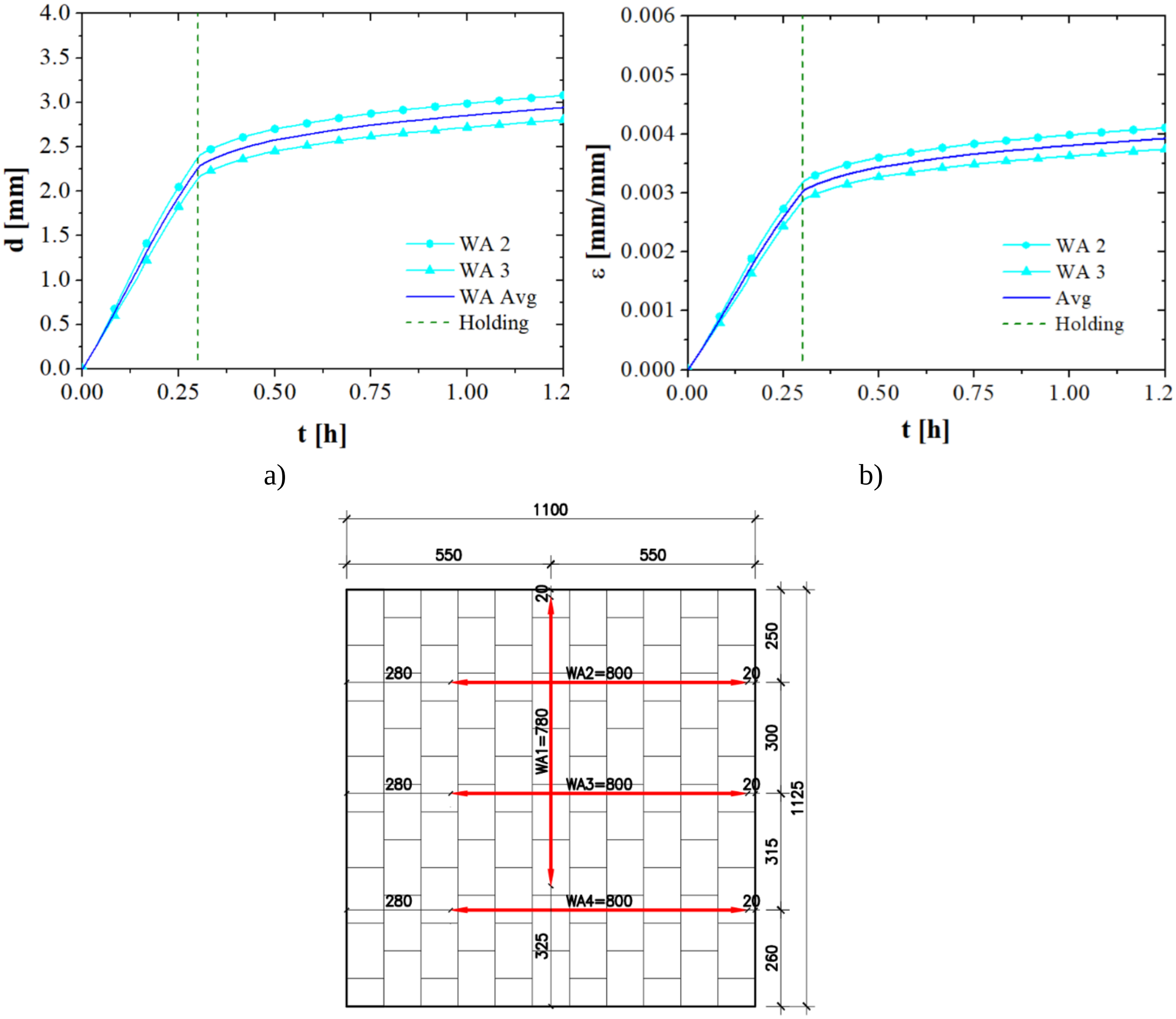

a) b)

c)

Figure 5-40 – Test series S09.HT.CBJ – Preliminary test: a) In-plane displacements; b) Strains

The measured forces and stresses during the test are shown in **Figure 5-41**. The lateral restraint provided by the blocked plunger prevents the Poisson's effect, therefore, a reaction force is observed in the head joint direction. The maximum reaction force was 67.2 kN (0.44 MPa). This value is smaller than the reaction forces obtained in test series S06.AT.LBJ (103.6 kN and 101.3 kN), as the creep and the high temperature reduced the stiffness of the specimen.

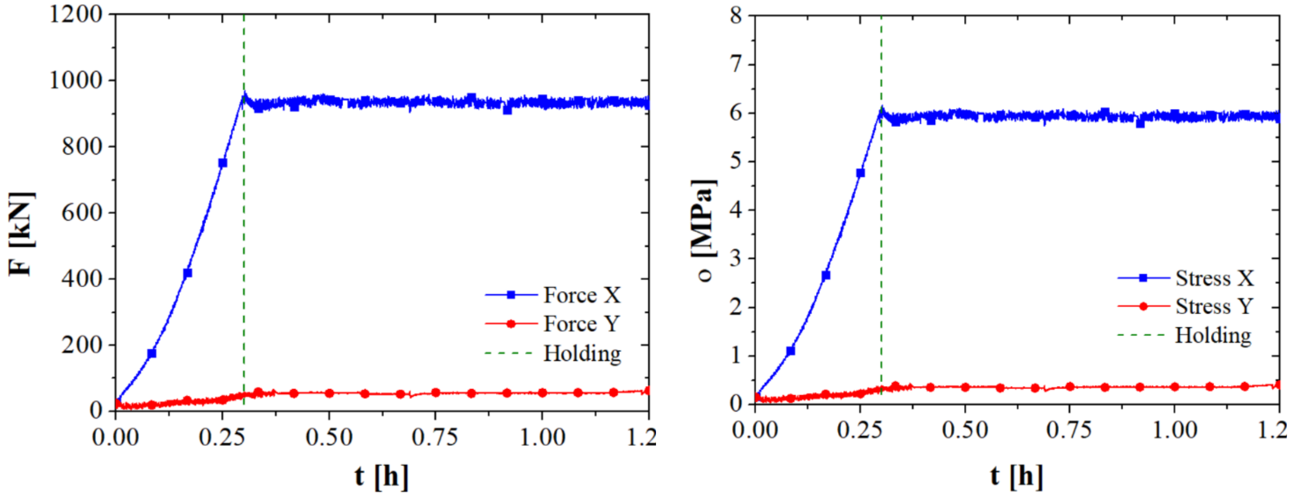

a) b)

Figure 5-41 – Test series S09.HT.CBJ – Preliminary test: a) Forces; b) Stresses

The stress-strain curves obtained in the preliminary test is presented in **Figure 5-42**. During the loading stage the average strain is 0.0030, which comprises the elastic strain in the bricks, the strains due to crack closure and crushing of initial non-plane surfaces and creep strain. This strain is 25% higher than the average obtained in test series S06.AT.LBJ (ε = 0.0024). During the holding stage, the total strain increases from 0.0030 to 0.0038, mostly caused by creep.

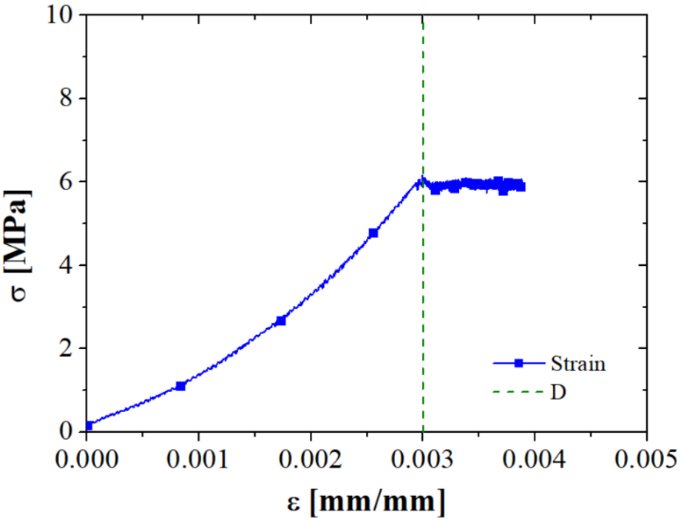

Figure 5-42 – Test series S09.HT.CBJ Preliminary – Stress-strain curves

5.5.5 Test series S09.HT.CBJ

The previous tests (S06.AT.LBJ, S07.AT.LHJ and S08.AT.LBI) have evaluated the structural response of refractory masonry under diversified loading conditions at ambient temperature. This test series, S09.HT.CBJ, aims to characterize the behaviour of refractory masonry under uniaxial compression at high temperature. The temperatures measured by the thermocouples embedded in the bricks are presented in **Figure 5-43**. The curves presented in red are the target heating and the temperature measured in the furnace ones, respectively.

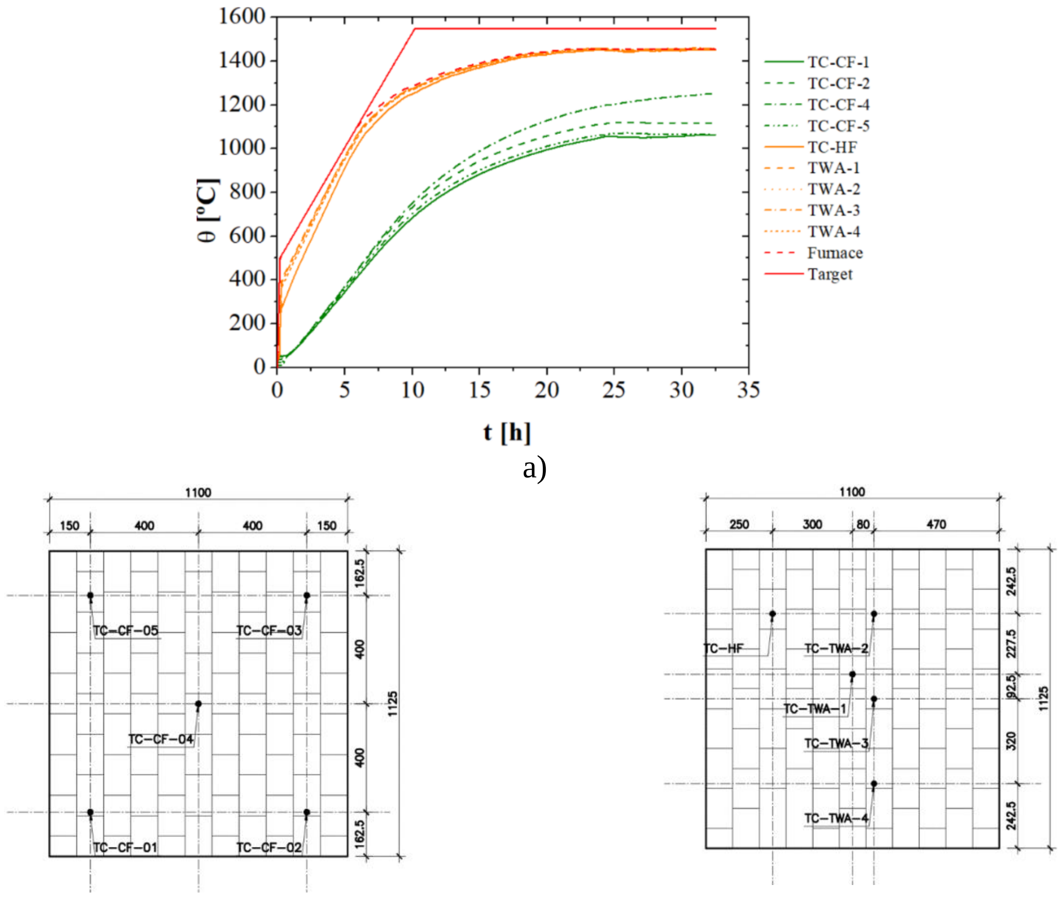

a)

b) c)

Figure 5-43 – Test series S09.HT.CBJ: a) Temperatures; b) Thermocouples of the cold face; c) Thermocouples of the hot face

Due to the high thermal capacitance of the test system (specimen and furnace), the furnace was not able to follow the programmed curve. The temperatures in the hot face started to increase rapidly when the thermal load is applied. Due to the relatively low thermal conductivity of refractory materials (**Figure 2-5**a), the temperatures on the cold face took some time to start increasing.

The temperatures in the thermocouples of the hot face (TWA-1 to TWA-4 and TC-HF) were directly exposed to the furnace radiation. Therefore, the thermocouples measured at this face are in good agreement with the furnace temperature. The temperatures in the thermocouples installed in the middle of the cold face (TC-CF-4) are slightly higher than the other thermocouples of the cold face due to heat loses in the borders of the specimen.

The evolution of the in-plane displacements and strains of specimen S09.HT.CBJ.01 are presented in **Figure 5-44**. This specimen was tested only for 3.5 hours. The LVDTs used to measure the in-plane displacements (WA-2, WA-3 and WA-4) and the average of their values (WA-Avg) are being presented. As expected for masonry walls and as observed in the previous tests, a small scattering on the in-plane displacements was observed. The average strain obtained when the maximum load was achieved at 0.73 h and the holding stage started was 0.0095. This value is significantly higher the maximum strain obtained in test series S06.AT.LBJ (ε = 0.0024) and in the preliminary test at 1200 ºC (ε = 0.0030), as the creep rate is higher for the temperature range of test S09.HT.CBJ. After 3 hours, by the end of the holding stage, the average strain was 0.0143. Analysing **Figure 5-44**b, it is possible to observe the primary and secondary creep in the specimen.

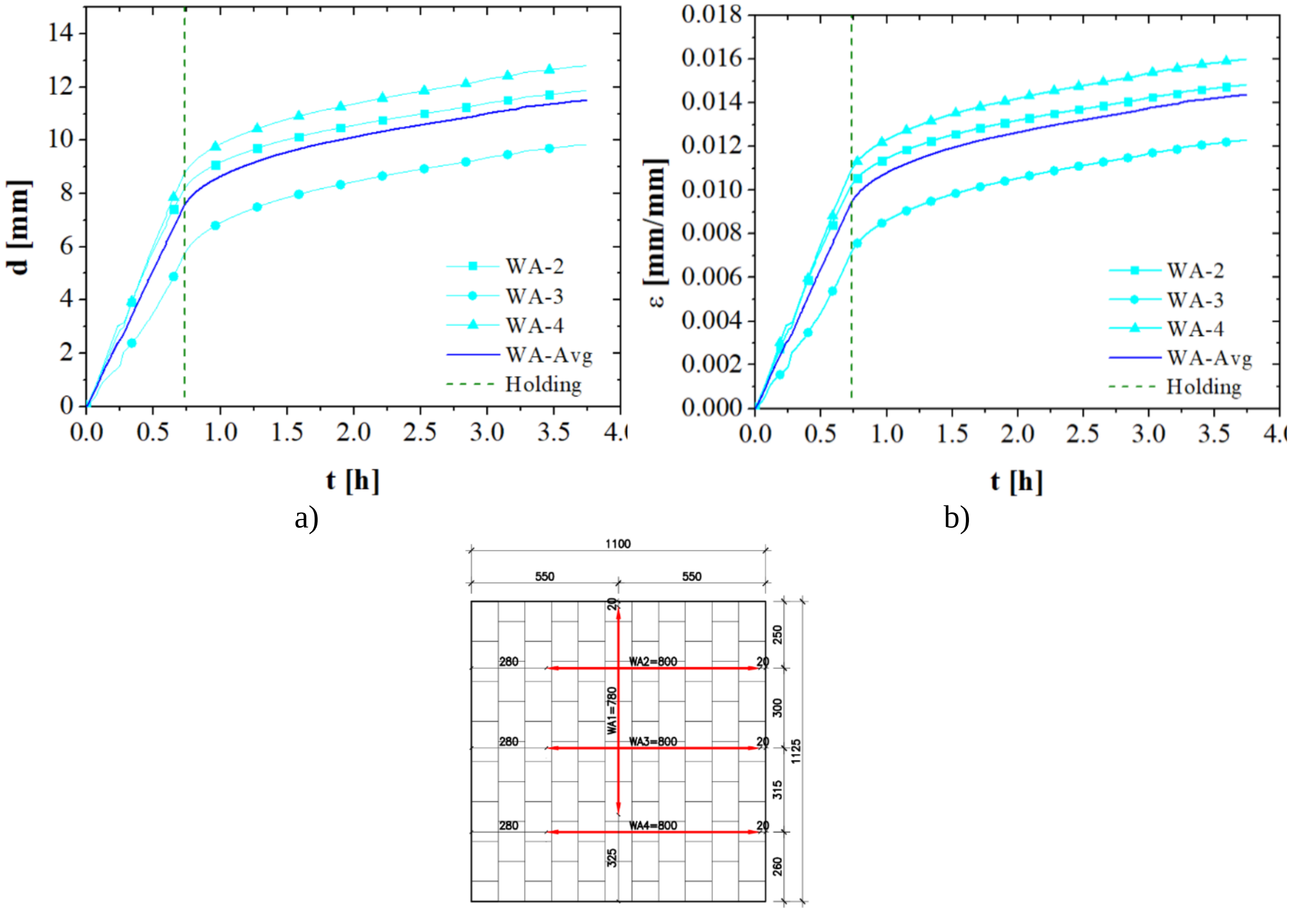

a)

b)

c)

Figure 5-44 – Test series S09.HT.CBJ.01: a) In-plane displacements; b) Strains; c) Position of the LVDTs

The evolution of the in-plane displacements and strains of specimen S09.HT.CBJ.02 are presented in **Figure 5-45**. The average strain obtained when the maximum load was achieved at 0.90h and the holding stage started was 0.0060. After 3 hours, the average strain was 0.0106. Analysing **Figure 5-45**b, it is possible to observe the first and secondary creep in the specimen.

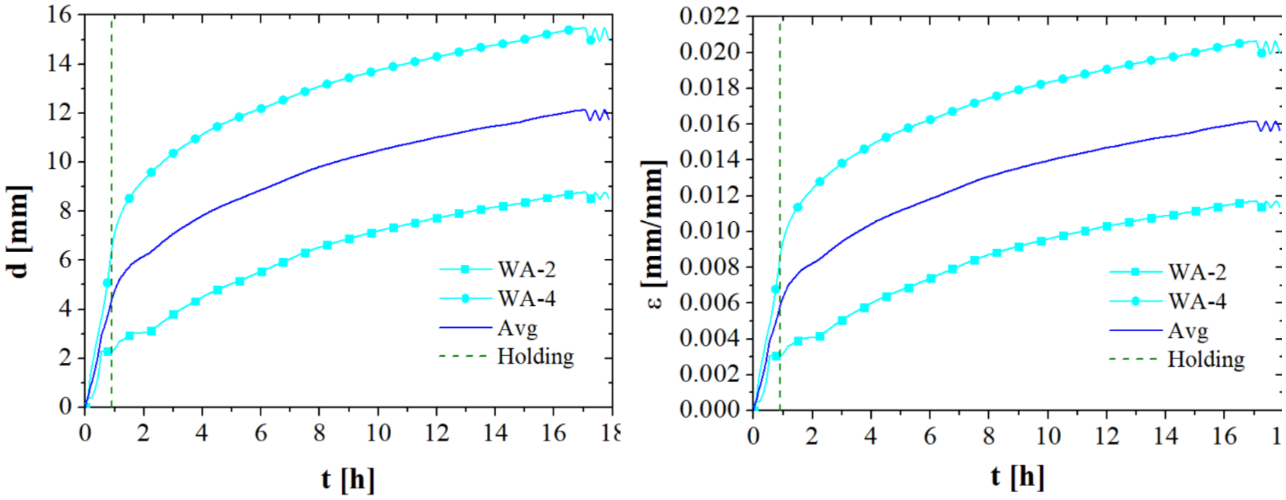

a) b)

Figure 5-45 – Test series S09.HT.CBJ.02: a) In-plane displacements; b) Strains

The measured forces and stresses during the test are shown in **Figure 5-46**. The lateral restraint provided by the blocked plunger prevents the Poisson's effect, therefore, a reaction force is observed in the head joint direction. The maximum reaction force was 83.6 kN (0.54 MPa) and 62.1 kN (0.4 MPa) for specimens S09.HT.CBJ.01 and S09.HT.CBJ.02, respectively. These values are smaller than the reaction forces obtained in test series S06.AT.LBJ (103.6 kN and 101.3 kN), as the creep and the high temperature reduce the stiffness of the specimen.

The stress-strain curves obtained in test series S09.HT.CBJ are presented in **Figure 5-47**. The behaviour of specimens S09.HT.CBJ.01 and S09.HT.CBJ.02 are compared in **Figure 5-48**. By the end of the loading stage the average strains are 0.0095 and 0.0078 for specimens S09.HT.CBJ.01 and S09.HT.CBJ.02, respectively. Three hours after the beginning of the holding stage the measured strains are 0.0144 and 0.0095, respectively.

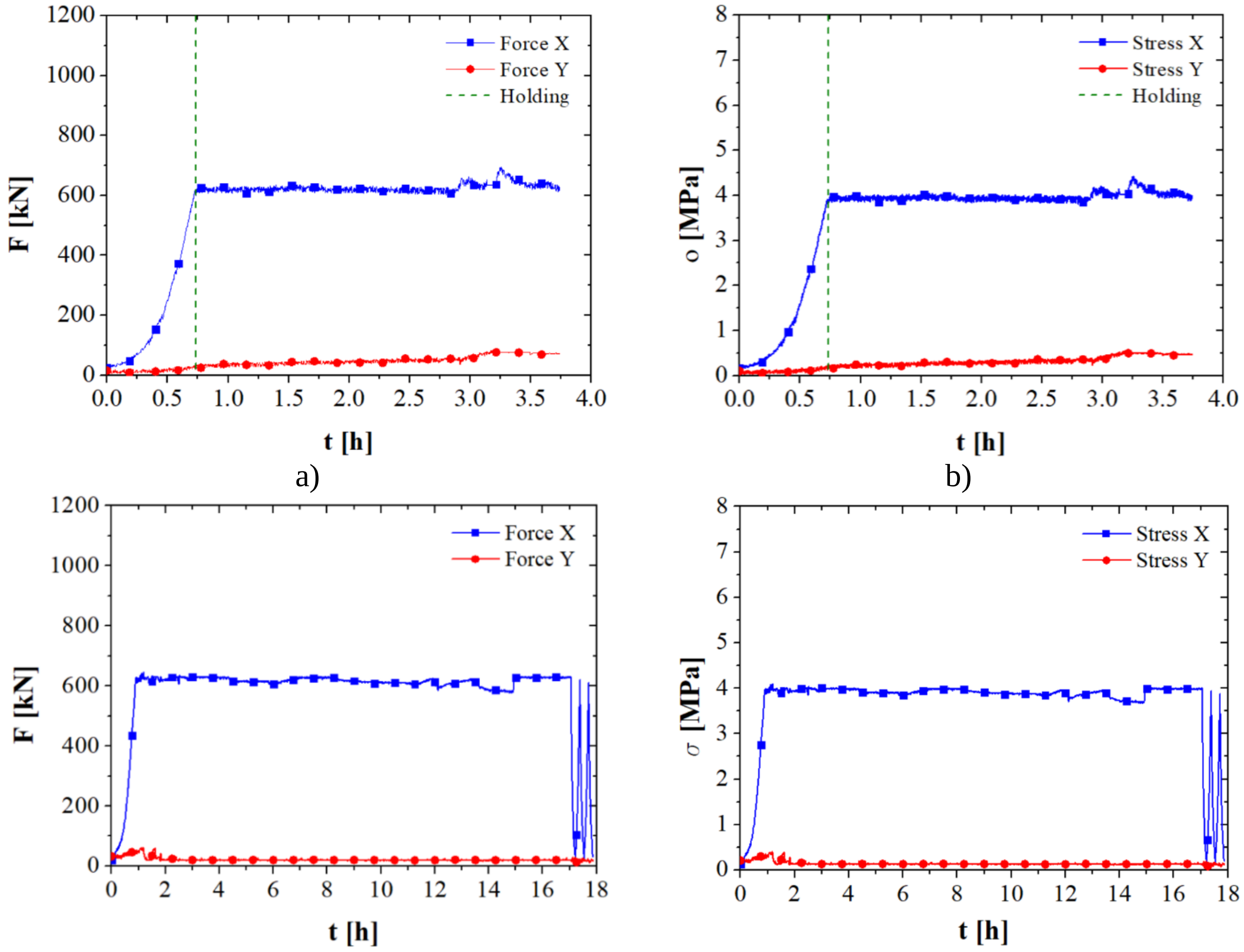

a) b) c) d)

Figure 5-46 – Test series S09.HT.CBJ – a) Forces S09.HT.CBJ.01; b) Stresses S09.HT.CBJ.02; c) Forces S09.HT.CBJ.02; d) Stresses S09.HT.CBJ.02

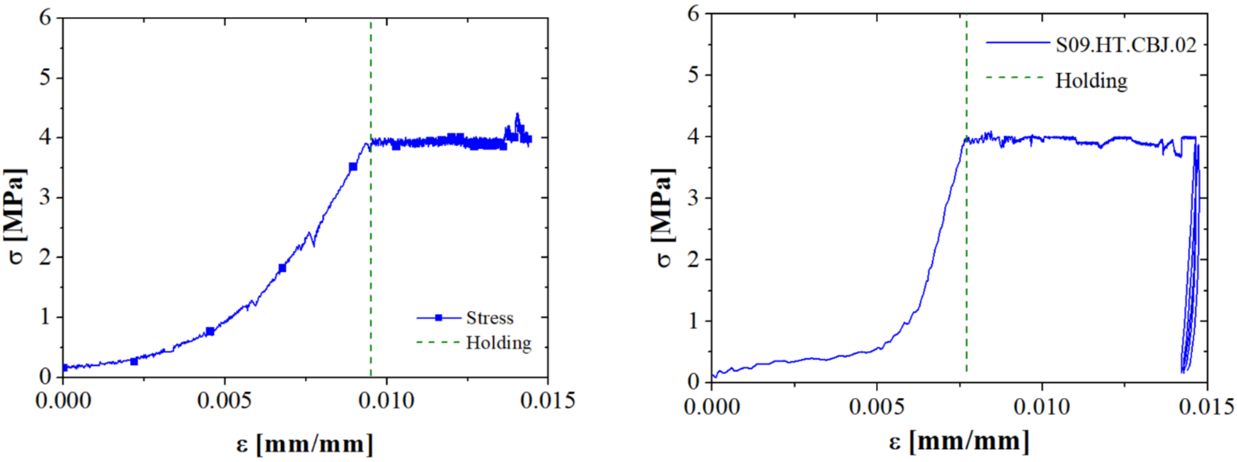

a) b)

Figure 5-47 – Test series S09.HT.CBJ – Stress-strain curves: a) S09.HT.CBJ.01; b) S09.HT.CBJ.02

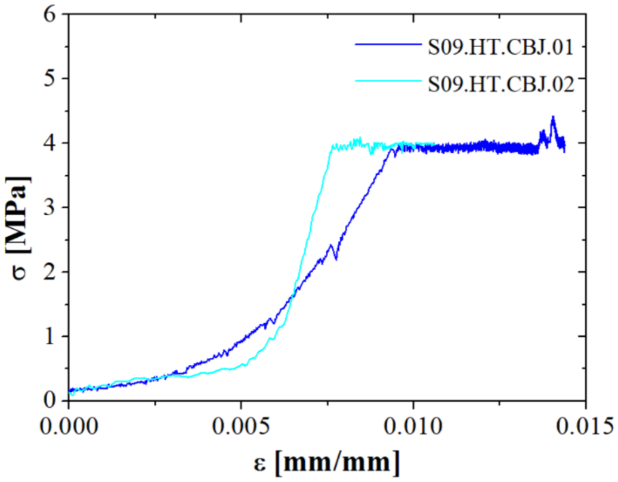

Figure 5-48 – Test series S09.HT.CBJ – Comparison of the stress-strain curves for the first 3.5 h of testing

The cracks at the cross joints caused by the bricks' height imperfections presented in the previous test series were also observed in this test series. At high temperatures (1480 ºC at the hot face), the creep effects are dominant. Therefore, the part of the brick submitted to higher compressive stresses presented higher creep strains, as observed in the comparison of **Figure 5-49**. The difference in the bricks' dimensions after the tests and the crack in the middle of the brick evidence that the left part of the brick had a higher creep strain.

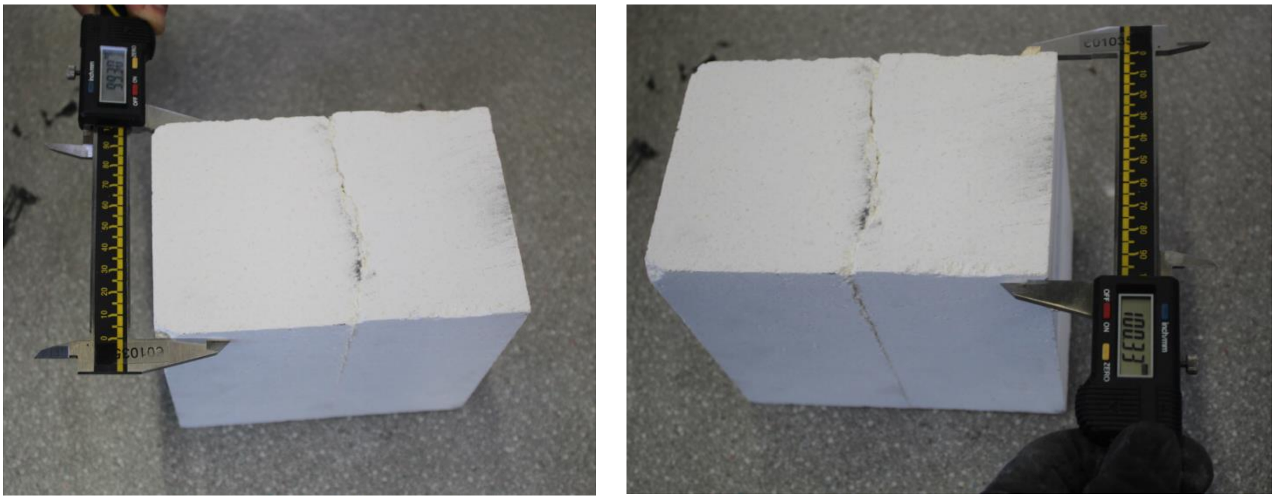
a) b)

Figure 5-49 – Test series S09.HT.CBJ – Different creep strains due to brick's height imperfections

The temperature curve defined for the heating of the specimens was relatively high. Industrial linings are usually heated up for a heating rate from 25ºC/h to 50ºC/h. The used curve comprised a heating from ambient temperature to 500ºC in 10 minutes, due to limitations in the experimental setup, as discussed previously in section 5.4. After the initial slope, from 500ºC to 1550ºC, a heating rate of 150 ºC/h was used. Some cracks were observed in a plane at a depth of 50 mm from the hot face, as shown in **Figure 5-50**. These cracks were mostly likely caused by the high heating rate used.

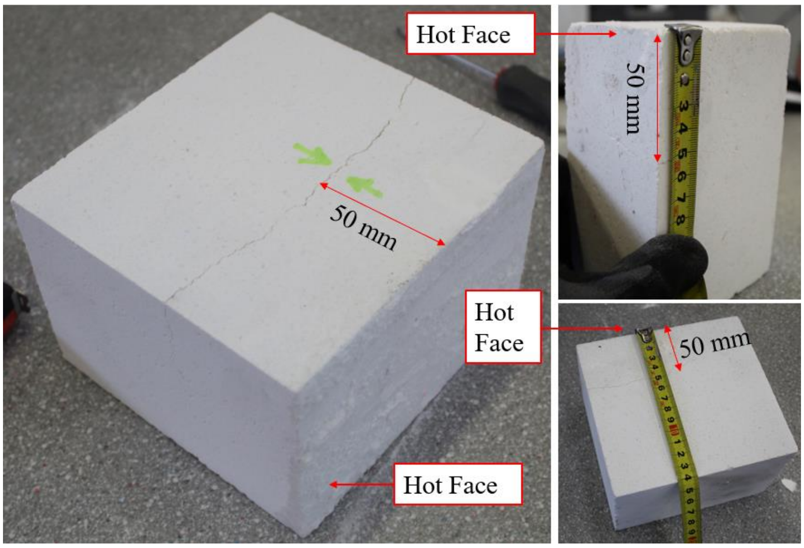

Figure 5-50 – Test series S09.HT.CBJ – Cracks 50 mm away from the hot face

The rockwool used for insulation melt during the test. The molten material got in touch with the specimen, and it was possible to identify some corrosion caused by the reaction between the alumina spinel brick and the rockwool, as shown in **Figure 5-51**. Nevertheless, only surface damage was observed.

Figure 5-51 – Test series S09.HT.CBJ – Reaction between alumina-spinel bricks and rockwool insulation

To allow the movement of the plungers, some chamfers were done in the bricks of the linings, as shown in **Figure 5-5**d. Therefore, the brick positioned in the edge of the wall was not being totally loaded. A creep failure was observed in this unit as shown in **Figure 5-52**.

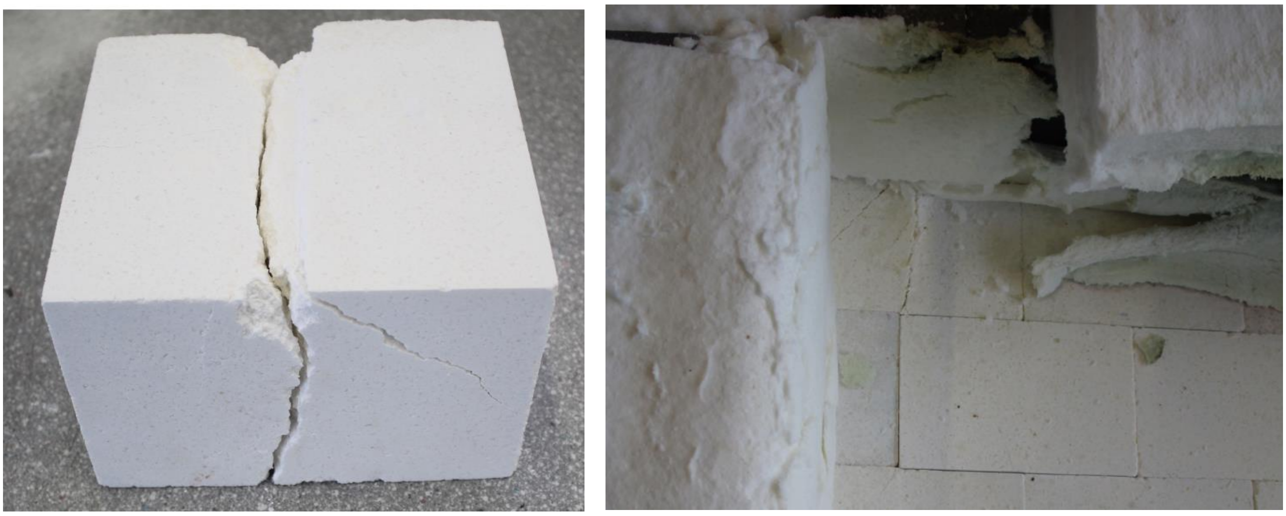

a) b)

Figure 5-52 – Test series S09.HT.CBJ – Creep failure at the brick adjacent to the plunger chamfers: a) details of the failure; b) Location of the brick

5.5.6 Test series S10.HT.CBI

The previous test series S09.HT.CBJ aimed to evaluate the response of refractory masonry under uniaxial compression at high temperature. This test series, S10.HT.CBI, aims to assess their structural response under biaxial loading. The temperatures measured by the thermocouples embedded in the bricks are presented in **Figure 5-53**a. The curves presented in red are the target heating and the temperature measured in the furnace ones, respectively. The position of the thermocouples is given in **Figure 5-53**b and **Figure 5-53**c.

The average temperatures recorded at the hot face during the test was 1482 ºC. A small variation was observed in the hot due to heat loses caused by the movement of the plungers, nevertheless it was not significant. The thermocouple of the cold face TC-CF-4 was in the middle of the specimen, therefore, it was less prone to heat loses, when compared to the thermocouples of the edge of the wall. The temperature in TC-CF-4 at the beginning of the test was 1266 ºC, by the end of the test, the thermocouple was registering 1299 ºC. The average temperature of TC-CF-1, TC-CF-2 and TC-CF-5 was 1123 ºC.

The evolution of the in-plane displacements and strains are being presented in **Figure 5-54**. The LVDTs used to measure the in-plane displacements in direction Y (WA-1 and WA-2) and direction X (WA-3 and WA-4) and the average of their values in each direction (Avg-X and Avg-Y) are shown.

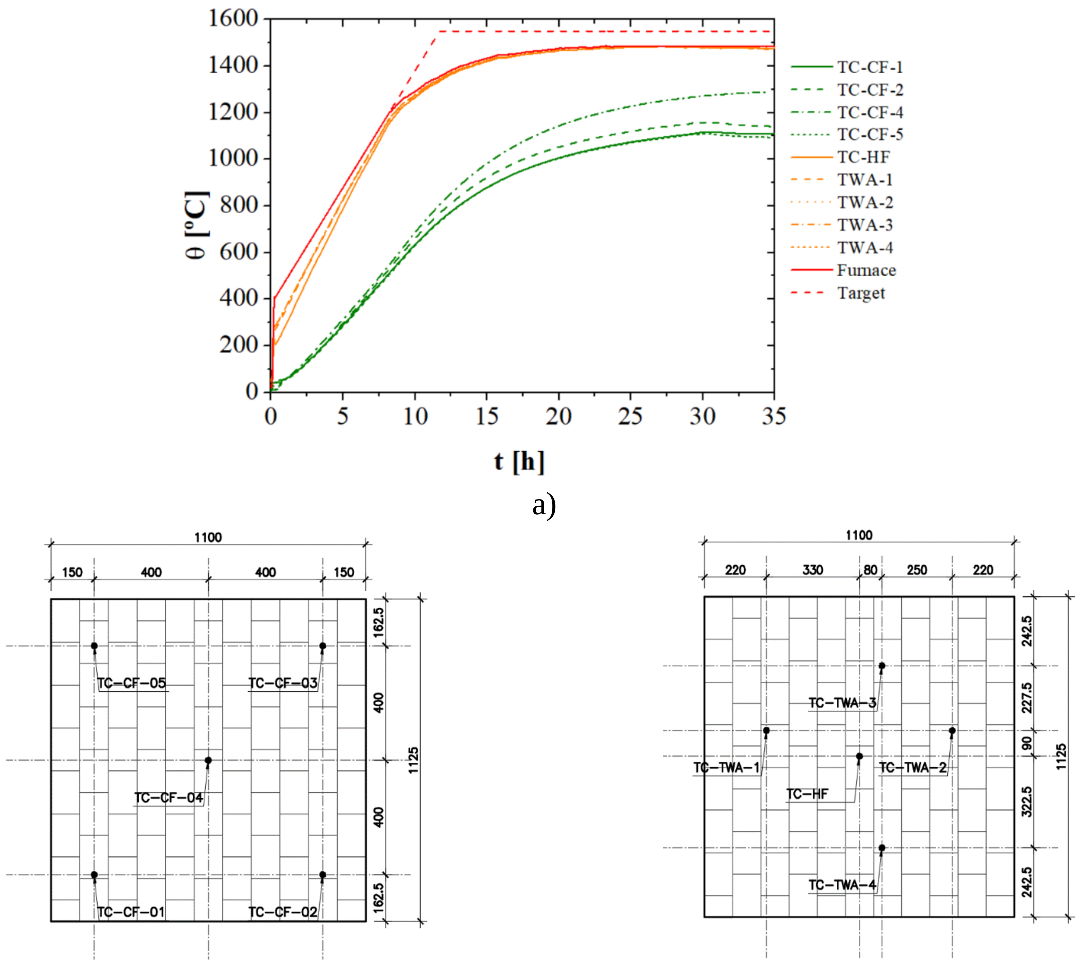

a)

b) c)

Figure 5-53 – Test series S10.HT.CBI: a) Temperatures; b) Thermocouples of the cold face; c) Thermocouples of the hot face

The measured forces and stresses during the test are presented in **Figure 5-55**. Some drops were observed in the forces of direction X, caused by a problem in the controller of the jack. Nevertheless, the noise did not affect the results of the test.

The stress-strain curves obtained in test series S10.HT.CBI are presented in **Figure 5-56**. During the loading stage the average strain was 0.0044 and 0.0032 in direction X and Y, respectively. The measured strain comprises the elastic strain in the bricks, the strains due to crack closure and crushing of the initial non-plane surfaces and creep strain. During the holding stage, the total strain increased to 0.0066 and 0.0053 in direction X and Y, respectively. The increasing in the strains was mostly caused by creep, as discussed in S09.HT.CBJ.

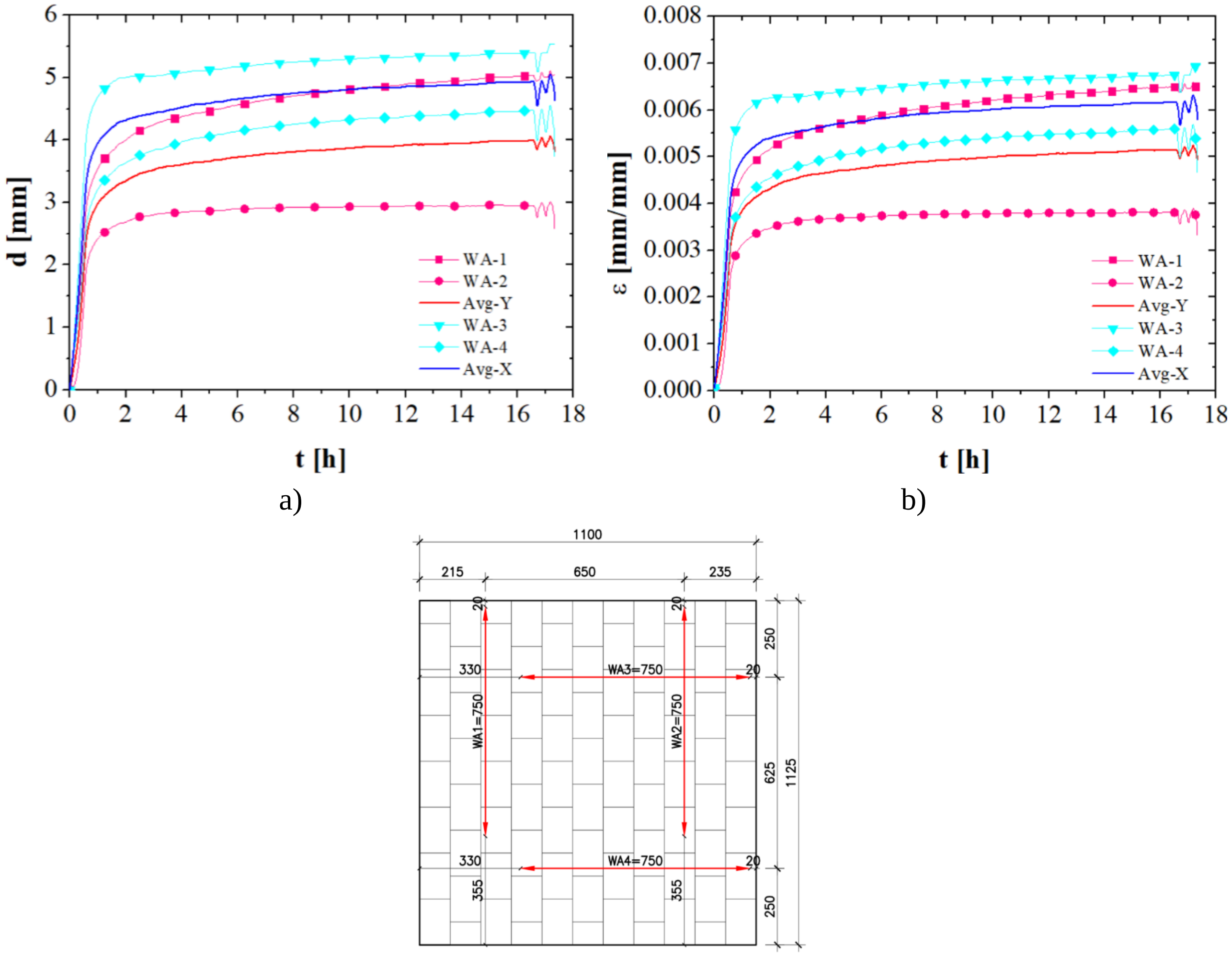

a)

b)

c)

Figure 5-54 – Test specimen S10.HT.CBI.01 – a) In-plane displacements; b) Strains; c) LVDTs location

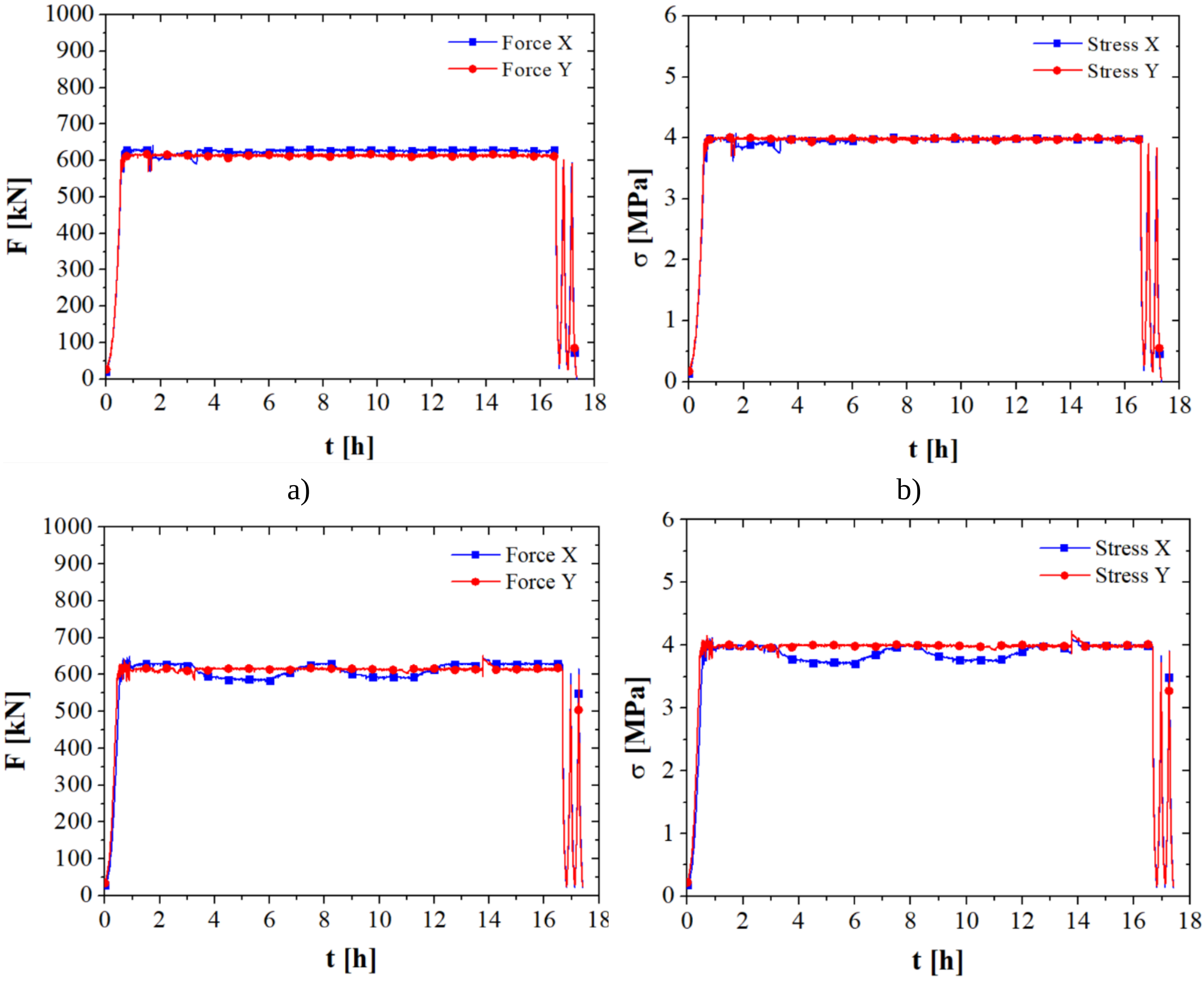

a) b) c) d)

Figure 5-55 – Test series S10.HT.CBI – a) Forces S10.HT.CBI.01; b) Stresses S10.HT.CBI.01; c) Forces S10.HT.CBI.02; d) Stresses S10.HT.CBI.02

The typical cracks noticed in the middle of the bricks presented in the previous test series were also observed. At high temperatures this crack was associated to large creep strains, as shown in **Figure 5-57**. The difference in the brick dimensions after the tests and the crack in the middle of the brick evidence that the right part of the brick had a higher creep strain. As noticed in test series S08.AT.LHJ and S09.AT.LBI, some crushing areas were observed at the head joints (**Figure 5-58**a). Several bricks were “glued” together in the interfaces of the head joints, as shown (**Figure 5-58**b).

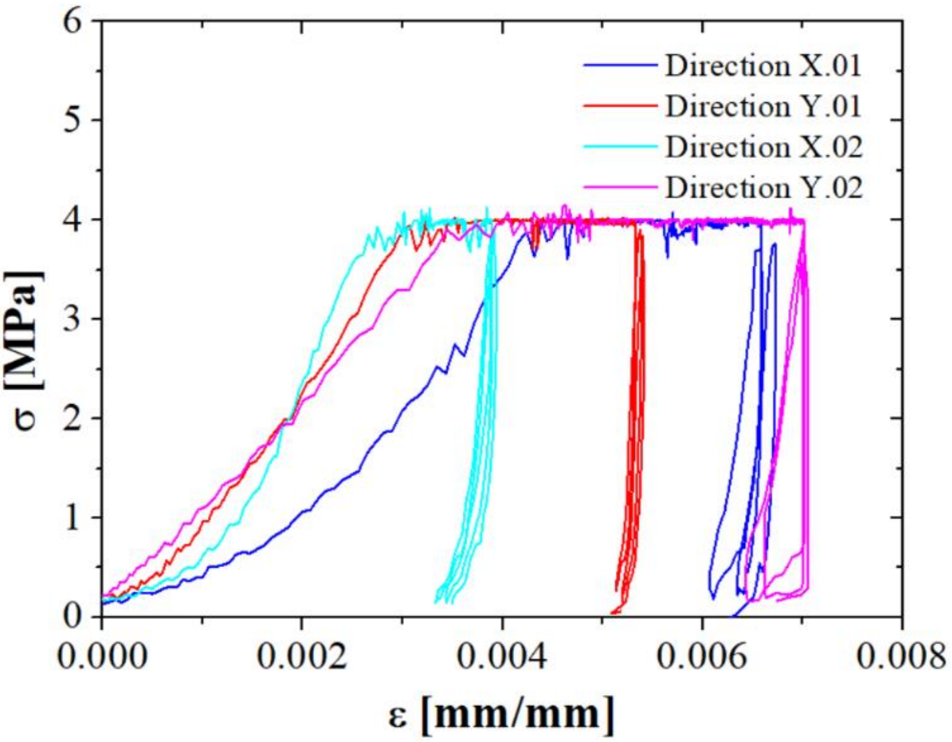

Figure 5-56 – Test series S10.HT.CBI – Stress-strain curves

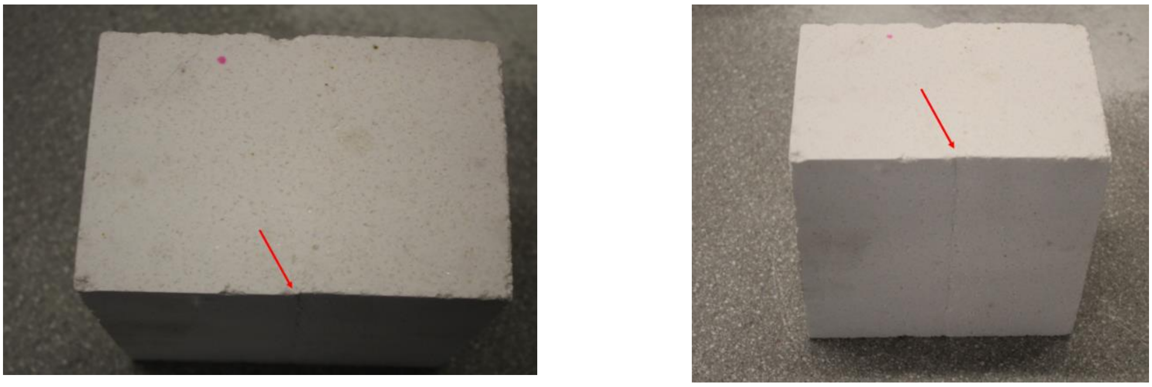
a)
b)

Figure 5-57 – Test series S09.HT.CBJ – Different creep strains due brick's height imperfections: a) upper view; b) front view

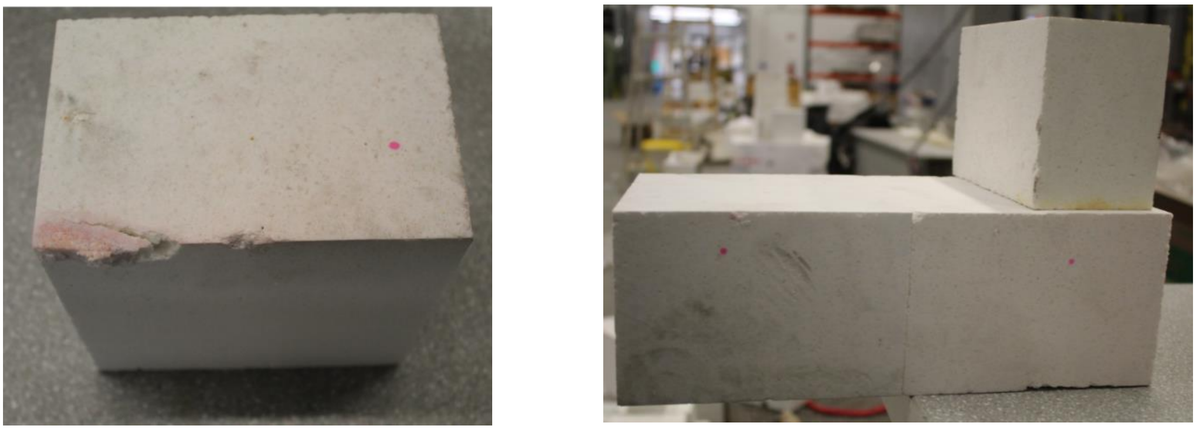

a) b)

Figure 5-58 – Test series S09.HT.CBJ – Failure at the head joint: a) Crushing; b) Bricks sticked together

As noticed in test series S09.HT.CBJ, the shear failure observed in the brick situated in the edge of the wall also happened. The chamfers in the linings of the moveable plungers (**Figure 5-5**d) resulted from a non-homogeneous load distribution in this brick that led to shear failure associated to creep.

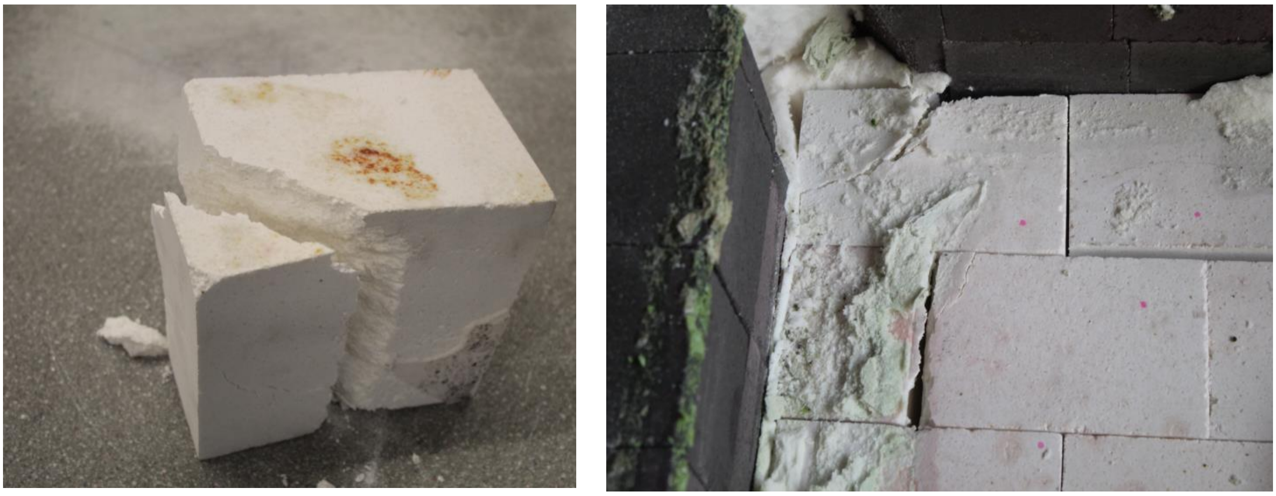

a) b)

Figure 5-59 – Test series S09.HT.CBJ – Shear failure associated to creep at the brick adjacent to the plunger chamfers

The reaction between the rockwool used for insulating and the alumina spinel brick was more significant in this test. The molten insulation got in touch with the specimen and some pits of corrosion were observed in the surface of the specimens, as shown in **Figure 5-60**. However, it does not affect the thermomechanical behaviour of the specimen.

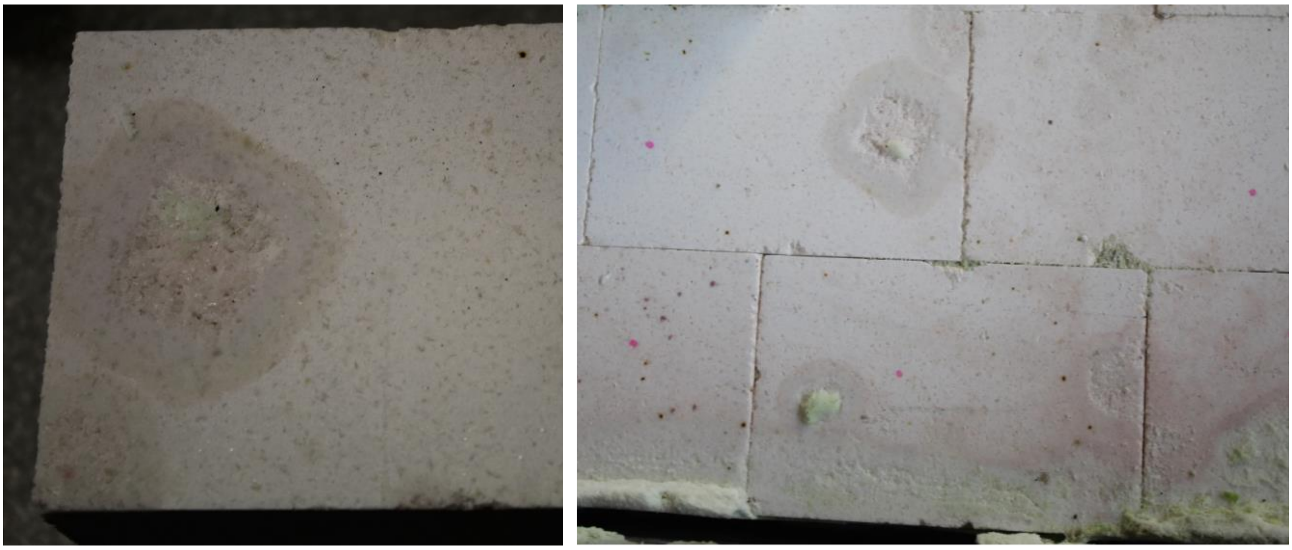

a) b)

Figure 5-60 – Test series S09.HT.CBJ – Reaction between alumina-spinel bricks and rockwool insulation

5.5.7 Test series S11.HT.RBI

The refractory masonry was characterized under uniaxial and biaxial loading at high temperature in the test series S09.HT.CBJ and S10.HT.CBI. However, in service conditions the refractory linings experience relaxation. Therefore, this test series S11.HT.RBI aims to characterize the wallets under biaxial relaxation.

The typical temperature evolution obtained for test series S11.HT.RBI is given in **Figure 5-61**. The temperatures measured in the hot face were around 1460 ºC during the relaxation test. The centre of the cold face was around 1300 ºC. Due to the heat loses in the edges of the specimen, the thermocouples located at the edges of the cold face measured temperatures around 1150ºC.

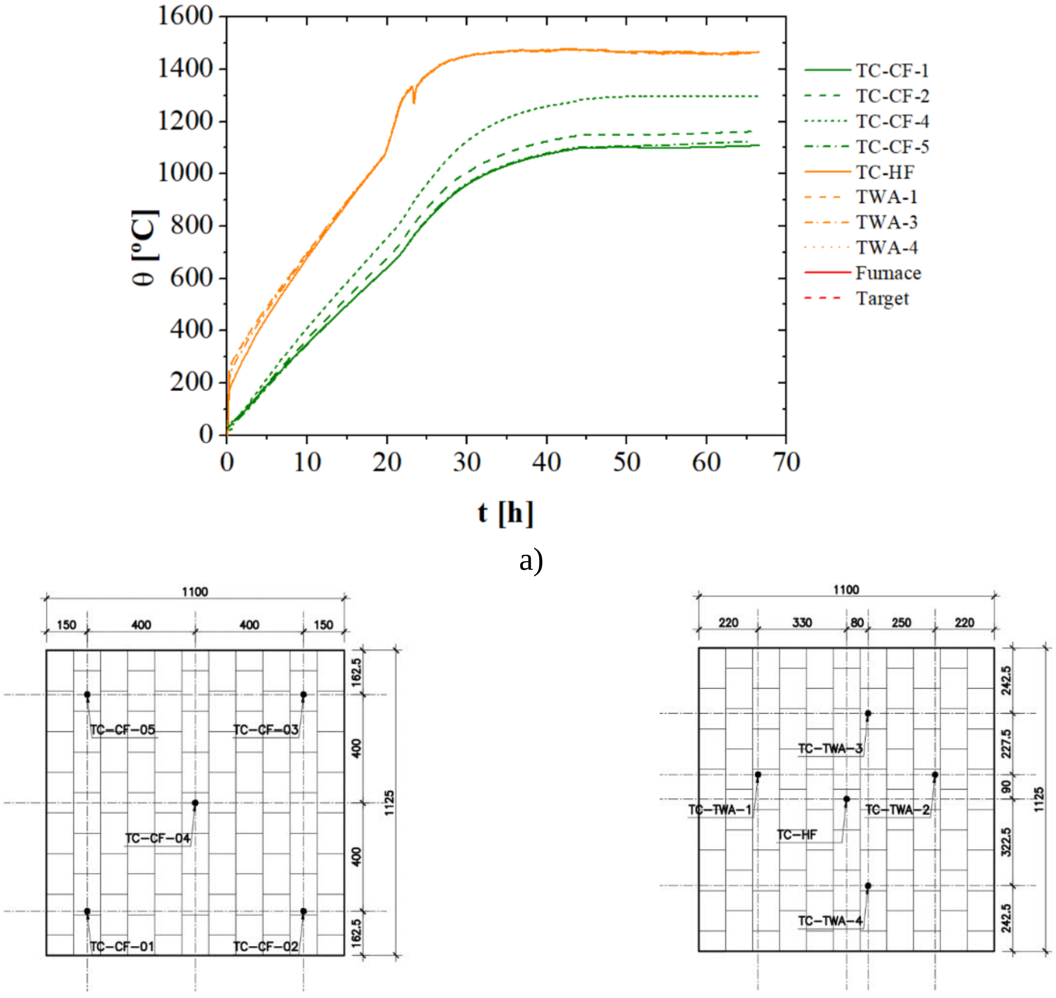

a)

b) c)

Figure 5-61 – Test series S11.HT.RBI – Temperatures

The displacements and strains measured for the specimen S11.HT.RBI.01 are presented in **Figure 5-62**. The measurements of the LVDTs confirmed that no significant displacements happened during the relaxation stage. The location of the LVDTs is given in **Figure 5-62**c.

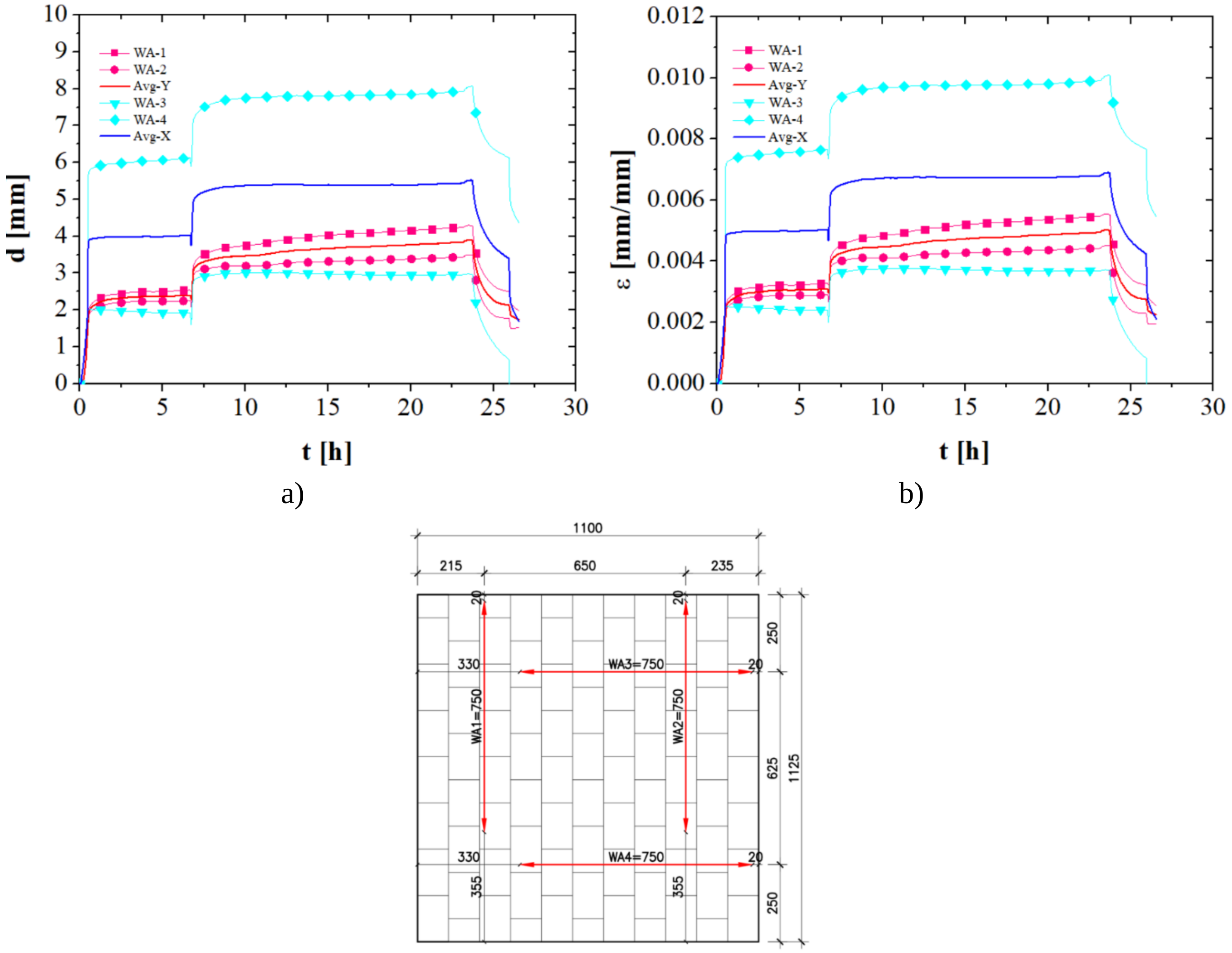

a)

b)

c)

Figure 5-62 – Test series S11.HT.RBI – a) In-plane displacements; b) Strains; LVDTs location

The evolution of forces and stresses measured during the relaxation tests are given in **Figure 5-63**. When the controller of the hydraulic jacks blocks their positions the relaxation process starts. The forces (and stresses) measured in the specimens drops significantly. Taking specimen S11.HT.RBI.01 as an example, the forces decrease from 505.2 kN (direction X) and 597.2 (direction Y) to 286.0 kN and 337.1 kN, respectively, in 30 minutes. After one hour, the forces reach 240.6 kN and 272.4 kN. The rate of forces relief decreases during the relaxation process.

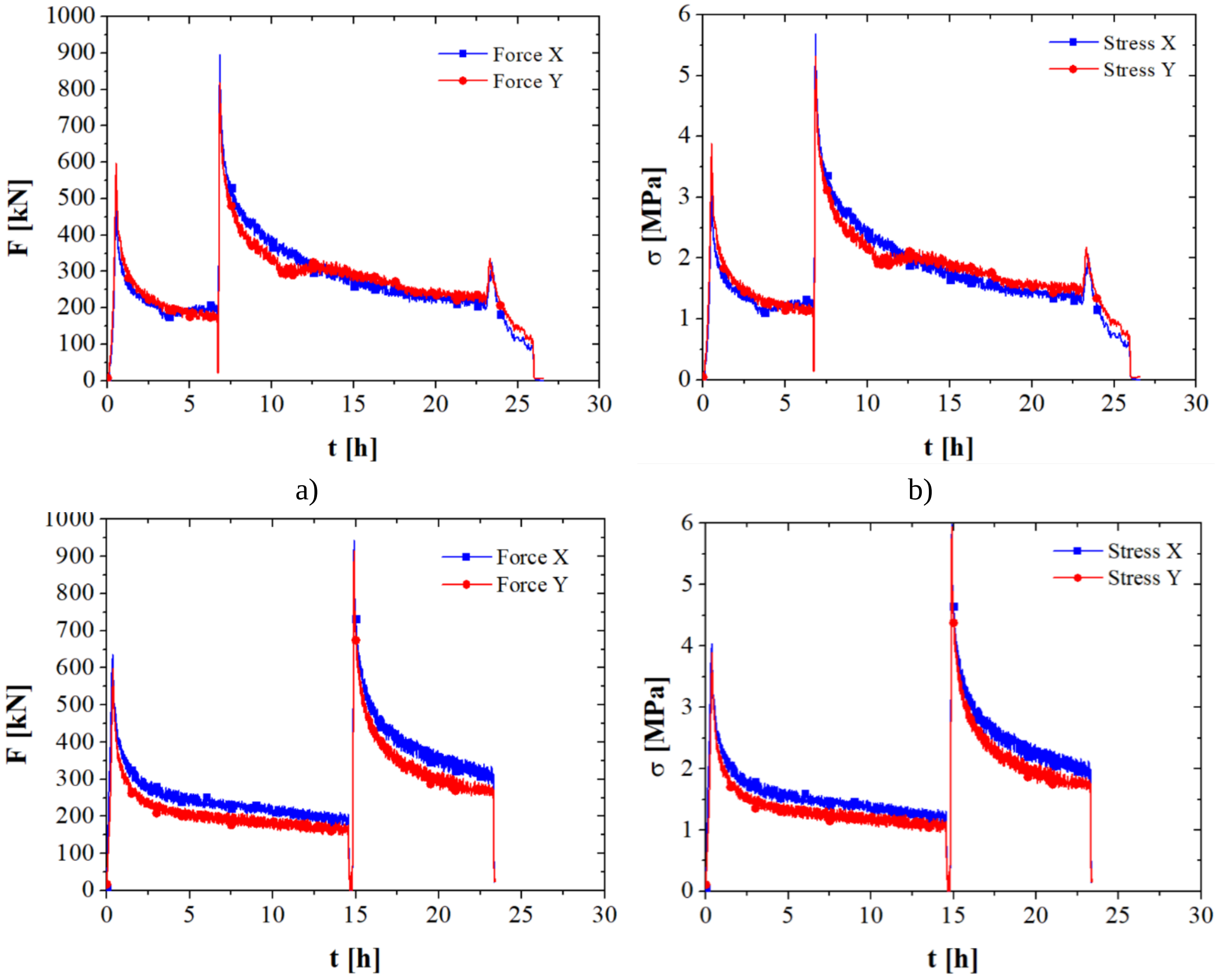

a)
b)
c)
d)

Figure 5-63 – Test results of Series S11.HT.RBI: a) Forces S11.HT.RBI.01; b) Stresses S11.HT.RBI.01; c) Forces S11.HT.RBI.02; d) Stresses S11.HT.RBI.02

It was not possible to keep the same test procedure for the second stage of the test due to circulations restrictions imposed by the Austrian authorities in the moment of executing test S11.HT.RBI.02. However, the first 6.5 hours of both tests were similar. **Figure 5-64** presents the comparison of the force evolution in specimens S11.HT.RBI.02 and S11.HT.RBI.02, a small scattering was observed. The stress-strain curves are presented in **Figure 5-65**

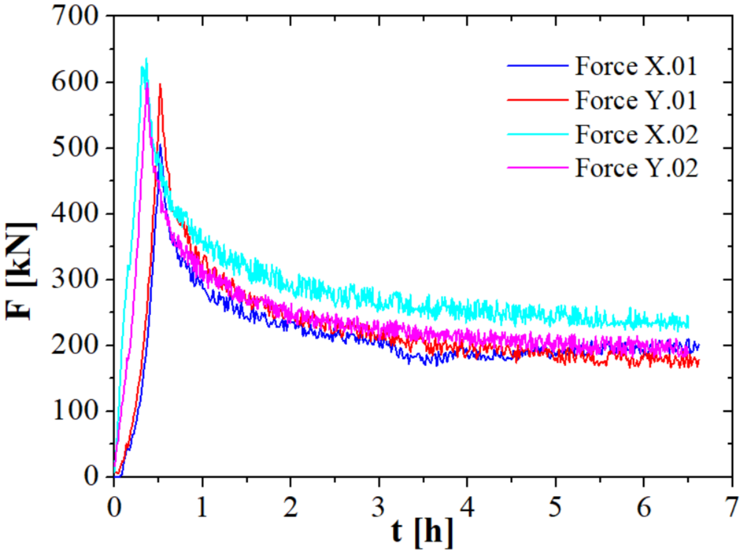

Figure 5-64 – Comparison between specimen S11.HT.RBI.02 and S11.HT.RBI.02

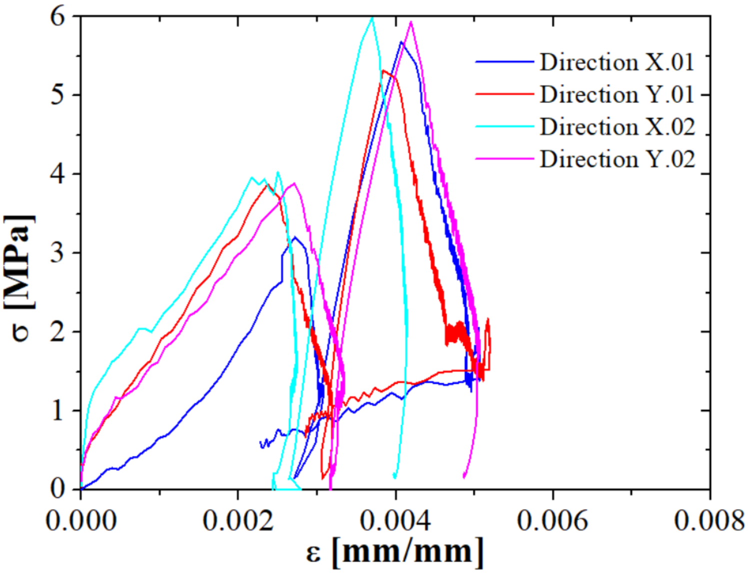

Figure 5-65 – Test series S11.HT.RBI – Stress-strain curves: a) S11.HT.RBI.01; b) S11.HT.RBI.02

5.6 Final remarks

This chapter aimed to assess the thermomechanical behaviour of refractory masonry under biaxial loading. To achieve this task, several tests were performed at ambient and high temperature. At ambient temperature, the specimens were tested under: *i*) uniaxial loading in the direction of the bed joints; *ii*) uniaxial loading in the direction of the head joints, and *iii*) biaxial loading. At high temperatures the specimens were tested for: *i*) uniaxial creep in the direction of the bed joints, *ii*) biaxial creep, and *iii*) biaxial relaxation. The experimental results obtained in this test series are being used to validate the numerical models of Chapter 6.

Test series S06.AT.LBJ aimed to assess the mechanical behaviour of dry-stacked masonry loaded in the direction of the bed joints with restrained deformation in the direction of the head joints. Three load cycles were applied to the specimens. As observed in S02.AT.CIC the crushing of initially non-plane surfaces of the bricks caused by the mechanical load was observed. Residual strains were observed after the first load cycle. The crushing of the surfaces resulted in the increasing of the contact area of the bricks and consequently the increase of the wall’s stiffness.

Test series S07.AT.LHJ had the same goal of test series S06.AT.LBJ, but the wall was loaded in the direction of the head joints with restrained thermal elongation in the direction of the bed joints. Three load cycles were considered. The residual strains and the increasing of the wall’s stiffness with the applied load was also observed. The strain level was lower when compared to the previous series, as the number of joints was smaller and the head joints have a stiffer behaviour than the bed joints.

Test series S08.AT.LBI evaluated the mechanical behaviour of the specimens under biaxial loading. When the strains are compared to the strains obtained in the previous series (S06.AT.LBJ and S07.AT.LHJ) it is possible to identify that the friction between the plungers and the specimens leads to reductions in the strain level.

The goal of test series S09.HT.LBJ was to assess the creep behaviour of dry-stacked masonry loaded in the bed joints’ direction. The temperature fields were measured along the test and the temperature evolution may be used for the calibration of numerical heat transfer analyses. The creep effects led to a significantly increasing in the strains, when the test results are compared to S06.AT.LBJ.

Test series S10.HT.CBI tested the creep behaviour of specimens loaded in biaxial conditions. The creep effects led to a significant increase of the strains, when the test results are compared to S08.AT.LBI. The analysis of the stress-strain curves allowed to observe that the creep strain during the holding stage is similar in both directions.

Test series S11.HT.RBI was designed to evaluate the relaxation effects of dry-stacked masonry under biaxial compression. The evolution of stresses along the test time allowed to identify the relaxation in the wallet. The experimental result indicated that the relaxation was similar in the direction of the bed joints and head joints.

In spite of the small load level, all tested specimens presented some cracks in the bricks, as observed in the uniaxial experimental campaign. Most of the cracks were located at the cross joints, caused by bricks’ height imperfection (Ngapeya *et al,* 2018). The specimens loaded in the head joints shown some spalling in these joints, as a result of stress concentrations.

6 NUMERICAL SIMULATIONS

An extensive numerical investigation for developing finite element models capable of simulating the thermal and mechanical response of dry-stacked masonry walls at ambient and high temperatures is detailed in this chapter. The experimental results presented in the previous chapters are being used for validating the developed models. The developed numerical models must comprise the several non-linearities observed experimentally, as the joint closure and joint opening, crushing in compression, cracking in tension and creep. Additionally, the materials' properties were taken as temperature dependent.

A large number of mechanical simulations with three-dimensional finite element models were carried out using the commercial software Abaqus (Abaqus User Manual, 2014). Heat transfer analysis were also performed to determine the evolution of the temperature fields in the specimens. The model geometry, the finite elements properties, the material modelling, the boundary and loading conditions, the analysis procedure are presented and discussed in the details in the following sections. The validation of the numerical predictions against the experimental results is duly addressed and discussed. Finally, the numerical simulation of a simplified steel ladle is presented.

6.1 Model geometry

The thermomechanical analysis of the masonry structures encompassed different possible techniques. In the micro-modelling approach, the units and mortar have been modelled as continuum elements and the interfaces between bricks and mortar (or between bricks and bricks) as discontinuous elements. In the macro-modelling approach, the units and the interfaces were represented by continuous elements (Lourenço et al, 2011; Pereira *et al,* 2015). Homogenization techniques may be also used to simulate the masonry (Ali *et al,* 2020; Ali *et al,* 2019; Gasser *et al,* 2013), in which a homogeneous equivalent material is used to represent the masonry. The micro-modelling approach leads to more accurate results, but its main drawback is the large computational resources required to run the analysis (Ngapeya *et al,* 2018; Ali *et al,* 2020). Nevertheless, this approach provides detailed results on the behaviour of the bricks and joints and, therefore, was adopted in this study.

The commercial software Abaqus was used to simulate the thermomechanical response of dry stacked masonry walls tested in this doctoral thesis, from ambient temperature up to 1500ºC. The model geometry was based on the dimensions of the specimens (**Figure 4-9** and **Figure 5-9**) and is presented in **Figure 6-1**. The nomenclature adopted in the FE models of the walls is analogous to the ones from the experimental campaign presented in the previous chapters. Further information concerning the specimens used for the numerical study, test procedures, test instrumentation and test results is provided in Chapter 4 and 5.

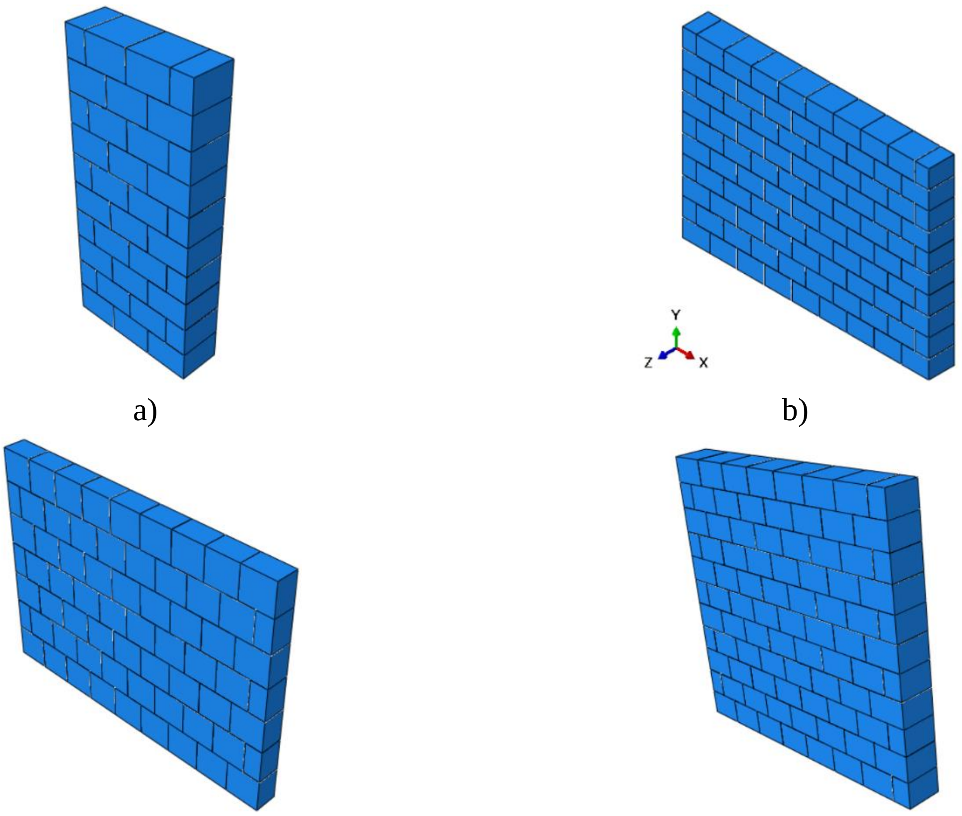

a) b)

c) d)

Figure 6-1 – 3D numerical models for the dry-stacked walls: a) S01.AT.LBC; b) S02.AT.CIC to S04.HT.RTE; c) S05.HT.LL10; d) S06.AT.LJB to S11.HT.RBI

6.2 FE model

The software Abaqus/CAE (Abaqus User’s Manual, 2014) is widely used to simulate the thermomechanical behaviour of structures with material and geometric nonlinear behaviour. Thus, the software was extensively used in numerical studies of refractory linings and masonry structures at high temperatures (Ali *et al*, 2020; Oliveira *et al*, 2021; Ali *et al*, 2019; Zahra and Dhanasekar, 2018; Hou *et al*, 2018; Santos *et al*, 2018; Jin *et al*, 2016; Gasser *et al*, 2004; Nguyen *et al*, 2009). The software is able to perform heat transfer analysis at transient or steady-state conditions and mechanical analysis comparing: *i*) material non-linearities, *ii*) geometric non-linearities; *iii*) plasticity; and *iv*) creep. Therefore, this software was chosen for the numerical research.

In the mechanical analysis, the bricks were modelled by using solid elements (C3D8R). These elements are defined as a continuous (C) three-dimensional (3D), hexahedral and eight-node (8) brick element with reduced integration (R), hourglass control and linear interpolation (**Figure 6-2**a). The element has three degrees of freedom per node, the translations in the directions X, Y and Z. The C3D8R elements are widely used in numerical simulations for complex nonlinear analysis comprising contact, plasticity, creep and large strains.

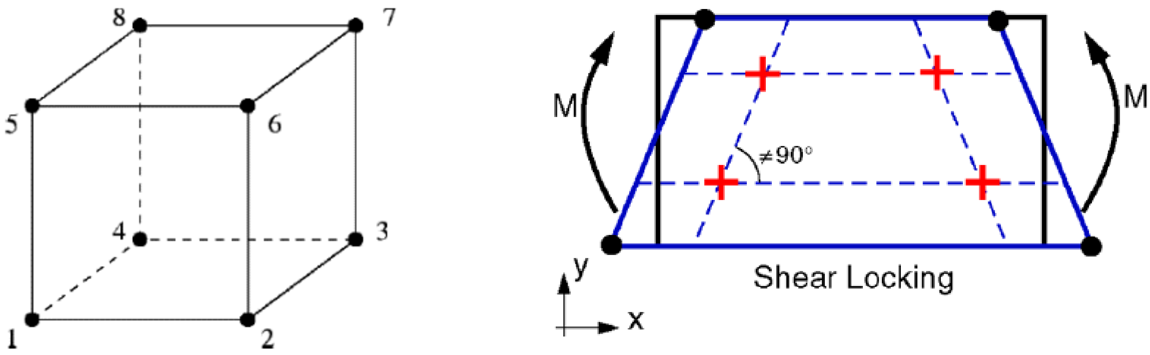

a) b)

Figure 6-2 – Finite Elements: a) Scheme of the C3D8R elements (Abaqus Manual); b) Shear locking (Abaqus Manual)

The C3D8R elements uses reduced integration to calculate the element stiffness with only one integration location per element, reducing the computational time for analysis and to avoid shear locking (**Figure 6-2**b). According to Laim (2013), the shear locking may result in the overestimation of the load capacity and the reduction in the predicted strains in bending dominated problems. For the heat transfer analysis an 8-node linear heat transfer brick was used (DC3D8).

The finite element mesh significantly influences the accuracy of the numerical predictions. The masonry walls were discretized using 8-node solid elements. The final mesh was generated automatically by Abaqus software and was rather refined (280 elements per brick and 140 elements per half brick). The influence of the finite element size on the thermomechanical behaviour of the masonry walls was evaluated, 30mm, 20mm and 10mm elements were used in the mesh study. It was found that the 20mm × 20mm × 20mm elements led to adequate simulation results.

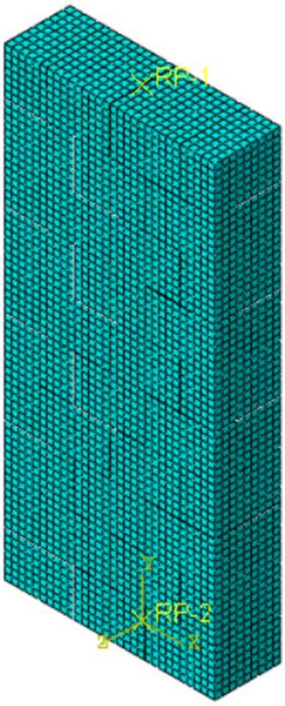

Figure 6-3 – Mesh details

As observed in the experimental setup, the masonry support and the loading were applied on rigid elements aiming to distribute the concentrated load from the hydraulic actuator uniformly on the top and bottom surfaces of the wall. A hard contact was assumed between the masonry and the rigid elements, in other words a perfect contact condition was used, consequently, there is no overclosure or clearance between these surfaces. Suitable boundary conditions were applied at the bottom and top surfaces of the masonry, to represent the boundary conditions provided by the experimental setup.

The developed finite element model comprised two analyses that were performed consecutively for each variation increment of external conditions: *i*) heat transfer analysis, and *ii*) mechanical analysis. The heat transfer analysis aims to determine the temperature fields in the wall throughout the test. The results of this analysis are used as input on the mechanical analysis. The mechanical analysis aims to simulate the structural behaviour of the dry-stacked masonry walls. For the tests performed at ambient temperature only the mechanical analysis was performed and temperature was inputted as pre-determined value.

In the heat transfer analysis, the model was fed with the thermal properties (taken as temperature-dependent) and density of the alumina spinel brick. The initial temperature of the system and the gas temperature of the furnace throughout the test were inputted in the analysis. The analysis account all of the three modes of heat transfer: convection, conduction and radiation. At the exposed and non-exposed face, the radiation was represented as a surface radiation and the convection was represented as a surface film condition. Due to the thermal insulation material used in the experimental system, adiabatic surfaces were considered between the wall and the reaction slab, the lateral masonry columns and the loading beam. Consequently, all heat losses took place on the non-exposed face. The exposed wall's surface was assumed to be, in each instant, at a constant temperature. This was confirmed by thermocouples installed in the tested specimens. Therefore, the temperature was considered to vary only through the thickness of the wall.

In the mechanical analysis, the model was fed with the bricks' Young's modulus, thermal elongation coefficient, density, compressive strength, tensile strength and creep parameters, taken as temperature-dependent. The temperature fields generated in the heat transfer analysis were inputted in the mechanical analysis, therefore, the software uses the temperatures in each element to calculate the thermal strains and the variations in the mechanical properties.

6.3 Material behaviour

The material modelling comprised all the non-linearities observed in the material's behaviour. The materials thermal and mechanical properties were measured within the scope of ATHOR Project (Samadi *et al,* 2020; Teixeira *et al,* 2019; Vitiello, 2021). The goal of the numerical simulations was to reproduce the thermomechanical behaviour of the tested specimens as faithfully as possible, therefore a duly characterization of the material is required.

6.3.1 Thermophysical properties

The correct modelling of the thermophysical properties of the alumina spinel brick is essential for the predictions of the temperature fields developed in the specimen and, consequently, for the accuracy of the mechanical analysis. The specific heat, thermal conductivity, density, emissivity and convection coefficient used in the numerical simulations are being presented in this section.

The specific heat (c_p) was calculated based on the chemical composition of the material (**Table 3-1**) (Vitiello, 2021) and it is being presented in **Figure 6-4**. The material was fired during the production; therefore, the moisture content was taken as 0%. An increasing on the specific heat is observed within the temperature.

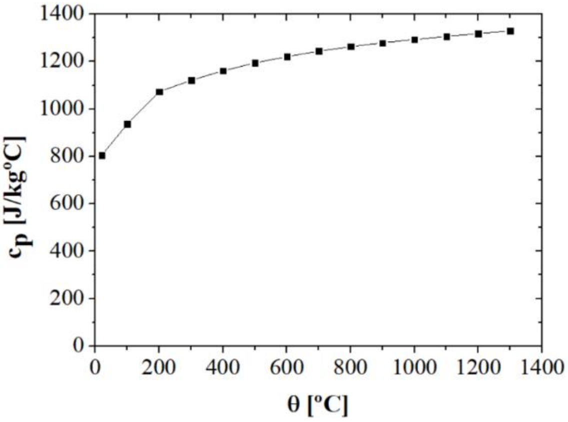

Figure 6-4 – Specific heat of the alumina spinel brick (Vitiello, 2021)

The thermal conductivity (λ) of the alumina spinel brick was measured by the laser-flash technique (**Figure 2-6**) (Vitiello, 2021) and it is being presented in **Figure 6-5**. A reduction is observed in the conductivity within the increasing of the temperature.

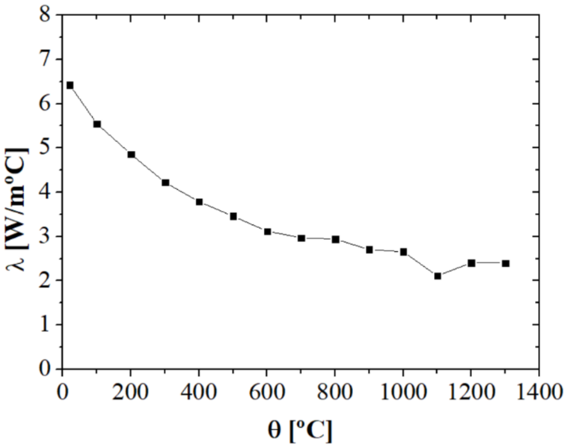

Figure 6-5 – Thermal conductivity of the alumina spinel brick (Vitiello, 2021)

The variation of the density (ρ) of the alumina spinel brick is not influenced by water losses as the brick is fired during the production (moisture of 0%). Therefore, the density was taken as not temperature-dependant. The density was measured experimentally.

$$\rho = 3130 \text{ kg/m}^3$$

The resultant emissivity (ε_{res}) of the alumina spinel brick was taken as 0.18 and considered constant with the temperature. The convection coefficient (h) was taken as 25 W/m^{2o}C, constant with the temperature, as suggested in EN-1996-1-2 (2005).

6.3.2 Mechanical properties

The mechanical properties used in the numerical simulations are being presented in this section, namely, the thermal elongation, the Young's modulus, the concrete damage parameters and the creep parameters. As observed experimentally in Chapter 3 and 4, the plasticity effects are more evidenced for the tests performed from ambient temperature up to 1100 ºC. On the other hand, the visco-plastic effects are more significant for the tests performed at temperatures higher than 1100 ºC, as observed by Samadi *et al.* (2020).

In Abaqus, the coupling of the concrete damage plasticity model with a creep model requires the development of a new constitutive law using UMAT (a subroutine developed by the user to describe the material behaviour). The development of this constitutive law is outside of the scope of this doctoral research. Thus, the CPD model was used to represent the test series S01.AT.LBC, S02.AT.CIC, S03.HT.LL8, S04.HT.RTE, S05.HT.LL10, S06.AT.LJB, S07.AT.LHJ and S08.AT.LBI. A creep model was used for the other test series.

The thermal elongation (Δl/l) of the alumina spinel brick was experimentally measured by (Kaczmarek *et al,* 2019) and it is presented in **Figure 6-6**. It is possible to observe an almost linear behaviour of the material (CTE = 8.8 x 10^{-6}/ºC).

The Young's modulus (E) of the alumina spinel brick was measured experimentally by ultrasonic technique (**Figure 2-3**c) and it is presented in **Figure 6-7** (Kaczmarek *et al,* 2019). More detailed information on the materials Young's modulus is given at Chapter 2.

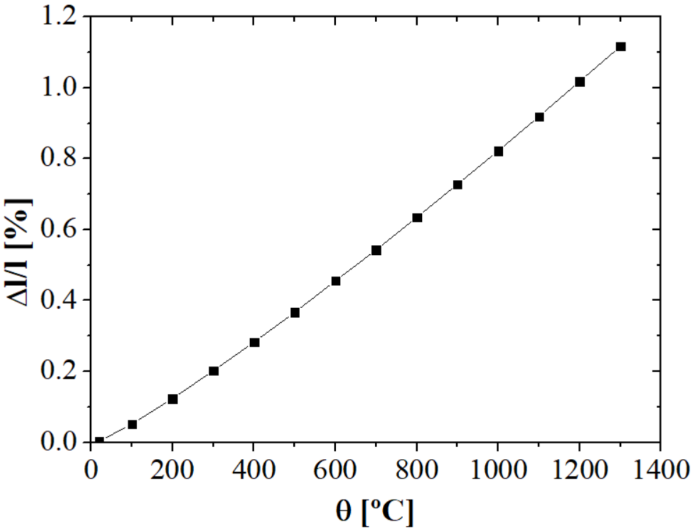

Figure 6-6 – Thermal elongation of the alumina spinel brick (Kaczmarek *et al,* 2019)

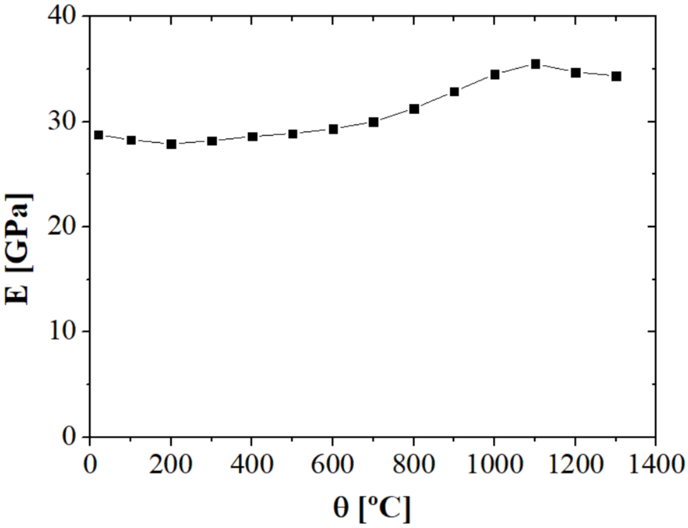

Figure 6-7 – Young's modulus of the alumina spinel brick (Kaczmarek *et al*, 2019)

6.3.3 Concrete Damage Plasticity

The CDP (Concrete Damage Plasticity) model assumes that failure under compressive crushing and tensile cracking is defined by damage plasticity, using the concept of isotropic damage evolution for representing the inelastic behaviour of concrete like materials. The CDP model is a modification of the Drucker-Prager model (Lubliner *et al* 1989, Lee *et al* 1998), however the failure surface's shape, in the deviatory plane, does not need to be a circle. The shape of the failure surfaces is defined by the parameter K_c: the ratio of the distances between the hydrostatic axis and, respectively, the compression meridian and the tension meridian in the deviatory plane K_c was taken as 0.667. The dilation angle (ψ) was taken as 20º, the eccentricity (ϵ) as 0.10, the ratio of the initial equibiaxial compressive yield stress to initial uniaxial compressive stress as 1.16 and the viscosity parameter as 0.02. These parameters were taken as non-temperature-dependent. The compressive and tensile strengths of the material were taken as temperature dependent (**Figure 6-8**). The material properties used in the numerical models were presented in Section 2.1. The CPD model was used to simulate test series S01.AT.LBC, S02.AT.CIC, S03.HT.LL8, S04.HT.RTE, S05.HT.LL10, S06.AT.LJB, S07.AT.LHJ and S08.AT.LBI. It should be noted that creep was not included in these models.

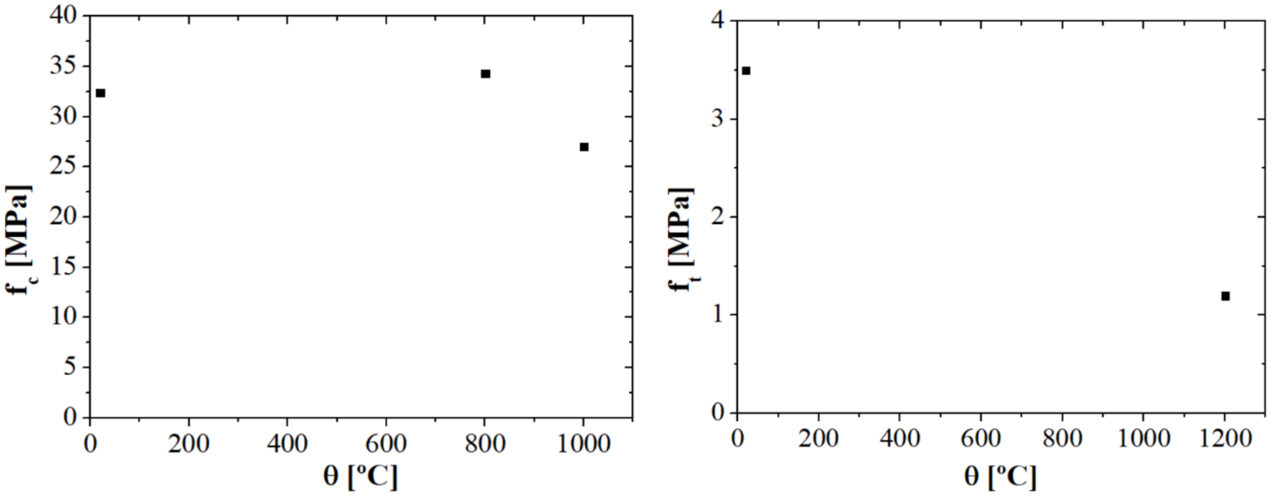

a) b)

Figure 6-8 – Mechanical properties of the alumina spinel: a) Compressive strength (Oliveira *et al* 2019); b) Tensile strength (Kaczmarek *et al*, 2019)

6.3.4 Creep

The strain hardening form of the Norton-Bailey creep law is being used to represent the creep strains in the material. The experimental results provided by (Samadi *et al*, 2020) evidences the three-stage creep curves of the alumina spinel material. However, the present study is mainly focused on the primary creep stage. The creep strain rate may be obtained by:

$$\dot{\varepsilon}_{cr} = K(T)\ \sigma^{n}\ \varepsilon^{a}_{cr}$$

where σ denotes the compressive stress, $\dot{\varepsilon}_{cr}$ is the creep strain rate, ε_{cr} is the creep strain, *K(T)* is a temperature dependent value, *n* is the stress exponent and *a* is the strain exponent. The parameters *K(T)*, *a* and *n* were inversely identified by (Samadi *et al*, 2020) and are being presented in **Table 6-1**. The compressive loads are dominating in the problem, thus, the compressive creep parameters are used.

The Norton-Bailey creep law was used to represent test series S09.HT.CBJ, S10.HT.CBI and S11.HT.RBI. It should be noted that the CDP was not used in these models, as the software does not allow the coupling of Norton-Bailey creep and CPD without using UMAT.

Table 6-1 – Compressive creep parameters (Samadi *et al*, 2020)

Temperature (ºC)	**n**	**a**	**Log (K/MPa^{-n})**
1300	4.25	-2.73	-14.41
1400	5.80	-2.65	-13.90
1500	2.00	-1.97	-9.79

6.4 Contact conditions

The joints play an important role on the behaviour of dry-stacked masonry and they were modelled with surface-to-surface contact properties. The joints' normal behaviour was represented by a pressure-overclosure relation. In this formulation the contact stiffness increases with the overclosure of the joint, resulting in a suitable representation of the behaviour of the dry joints. The behaviour of the dry-stacked masonry varies with the size of the specimen (Zahra and Dhanasekar, 2018), consequently, different relations were used to represent masonry with different dimensions. The general formulation of Eq. 1, provided by Thanoon *et al* (2013), was used to model the joint behaviour. The DIC technique was used to assess the average joint behaviour and the adopted curves are shown in **Figure 6-9**.

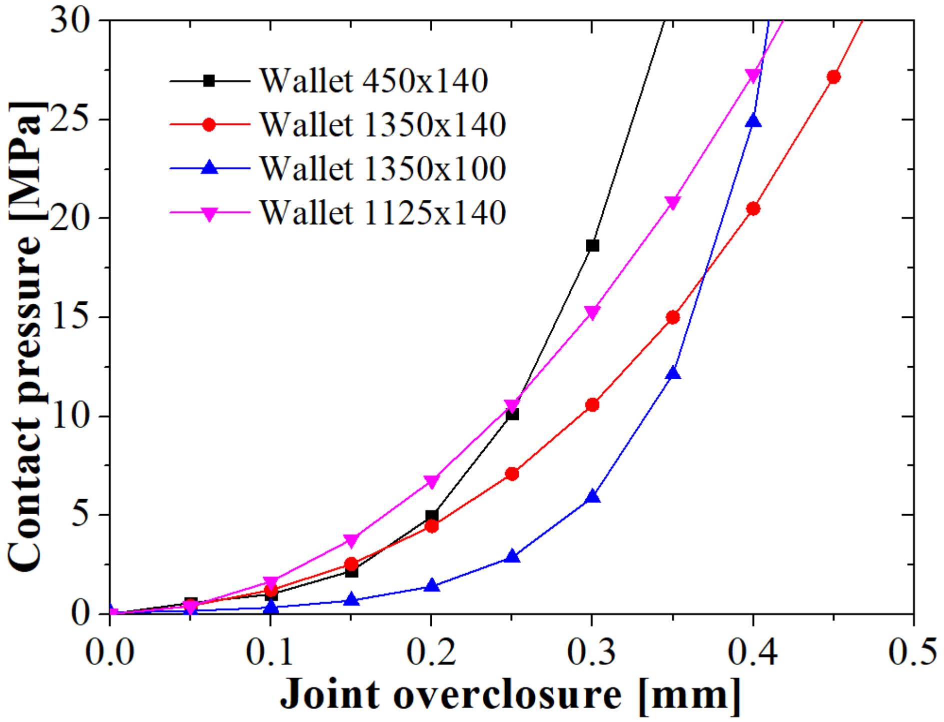

Figure 6-9 – Contact pressure-overclosure relations used for different walls dimensions.

The tangential behaviour was represented by the penalty friction formulation, in which sliding is governed by the friction coefficient. The friction coefficient of the alumina bricks as a function of the temperature was obtained experimentally, as shown in Chapter 3 (**Table 3-8**).

Table 6-2 – Friction coefficient values for dry joints and different temperatures

Temperature [ºC]	Friction Coefficient [-]
20	0.598
300	0.498
600	0.510
900	0.530

6.5 Validation of the finite element model

This section presents a comparison between the numerical and experimental results. The stress-strain curves, displacement evolution, temperature fields and failure modes obtained experimentally and numerically are compared and analysed. At the end of this section, results are discussed and analysed.

6.5.1 Test series S01.AT.LBC

Figure 6-10a shows the comparison of the stress-strain curves, for specimens S01.AT.LBC, obtained in the experimental and numerical tests. The curve from the FEA analysis fits closely with the experimental ones. As explained before, specimen S01.AT.LBC.02 was submitted to a significant uneven stress distribution, therefore, the experimental curve was expected to be much lower than the other two specimens. The good agreement between the experimental and numerical results ensures the adequacy of the developed finite element model. The developed model is able to represent all of the three stages described in section 3.1: *i*) joint closure; *ii*) linear behaviour; *iii*) plastic behaviour and failure. Besides the stress-strain curves, also the failure mode was compared.

The failure mode observed experimentally and numerically is compared in Figure 6-10b, where it is possible to observe a similar behaviour, the brick in the centre of the fifth masonry course crushed. Moreover, it was possible to identify a pattern of head joint opening in the rows bellow and above the crushing area, due to the restraint to lateral movement provided by the top and bottom supports. The developed model represents with great accuracy the evolution of the secant Young’s modulus of the wall’s masonry. The failure mode and compressive strength was also predicted accurately.

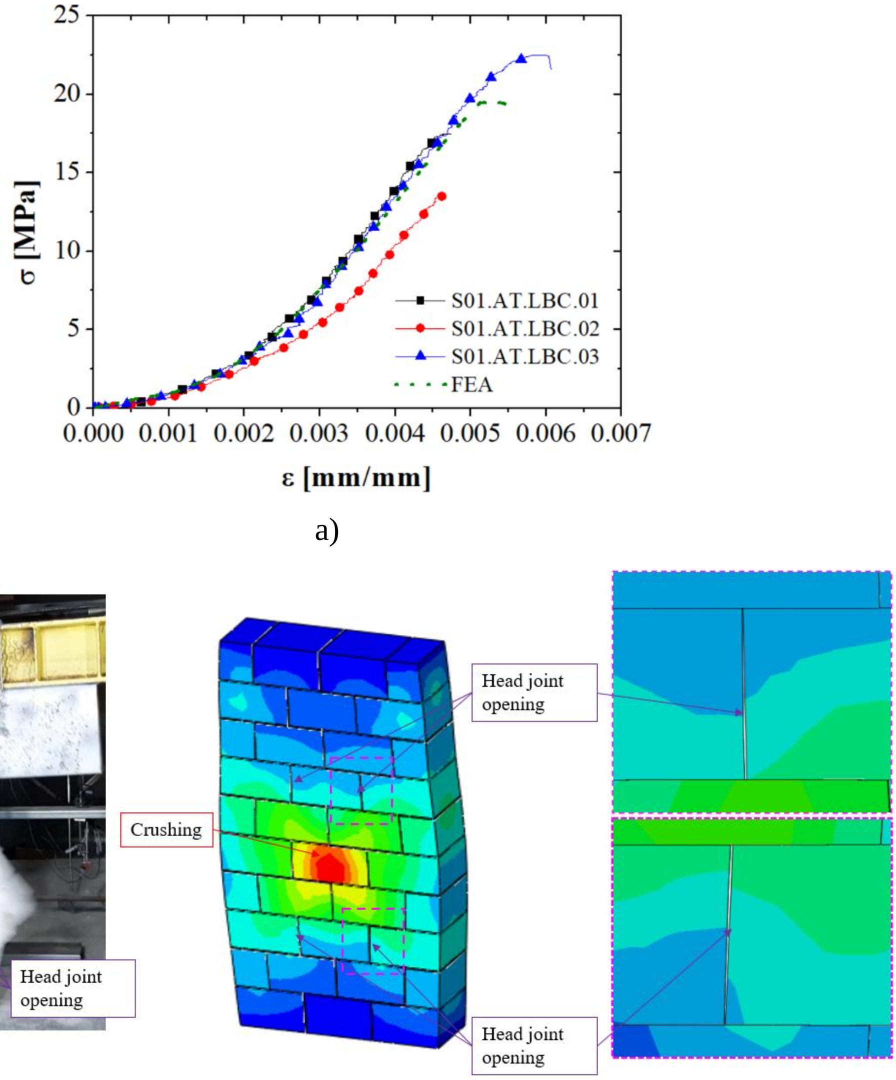

a)

b)

Figure 6-10 – Validation of the numerical model – test series S01.AT.LBC: a) Stress-Strain curve; b) Comparison of failure modes

6.5.2 Test series S02.AT.CIC

Figure 6-11a shows the comparison of the stress-strain curves, for specimens S02.AT.CIC, obtained from the experimental tests and finite element analysis. The curve from the FEA analysis fits in the envelop defined by the loading curves of the experimental results. An acceptable agreement between the experimental and numerical results was found. Only the loading stage of the test was simulated, the developed numerical model was not able to perform the unloading stage of the test, due to limitations on the software that does not allow modifications on the pressure-overclosure relation in function of the load and unload cycles. The evolution of the secant Young's modulus of the masonry in terms of the compressive stresses are presented in **Figure 6-11**b. An increase on the stiffness of the specimens is observed with the stress level.

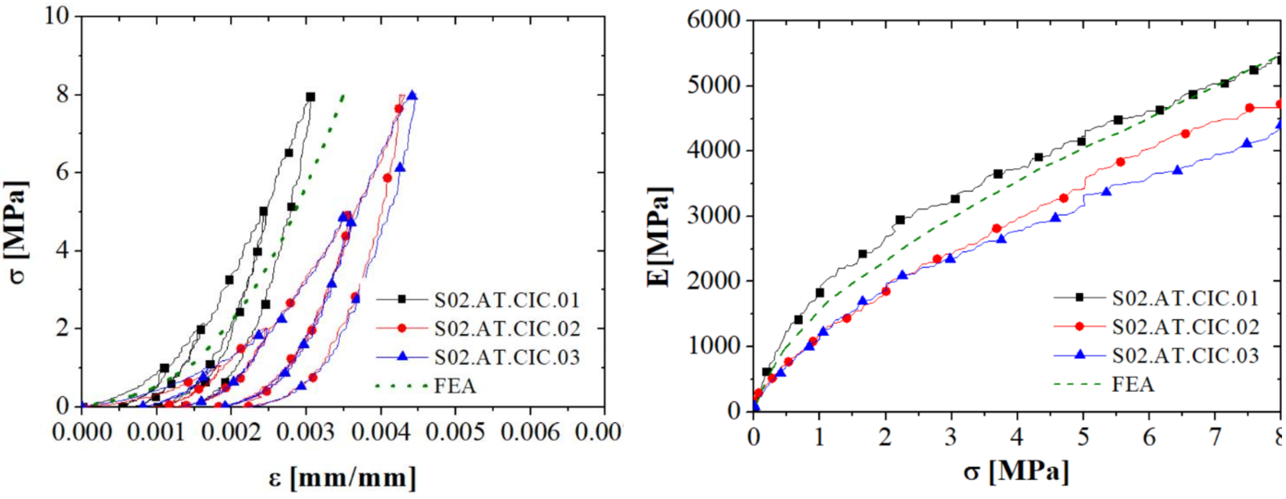

a) b)

Figure 6-11 – Validation of the numerical model – test series S02.AT.CIC: a) stress-strain curves, b) evolution of secant Young's modulus of the masonry with the stress

The developed model represents with great accuracy the evolution of the secant Young's modulus of the masonry of the wall, validating the joint-closure curve used to represent the interfaces. The accurate prediction of the evolution of secant Young's modulus of the masonry with stress indicates that the future numerical models created based on this one should be able to represent the stresses developed in the refractory linings due to the restrained thermal elongation.

6.5.3 Test series S03.HT.LL8

Figure 6-12a shows the comparison of temperatures obtained from the experimental and numerical tests for test series S03.HT.LL8. The curves presented in orange and magenta are the measured temperatures in the hot face (HF) and in the cold face (CF), respectively. The maximum (Max), minimum (Min) and average (Avg) measured values in each face are presented. The purple dashed lined stands for the beginning of the heating. The temperatures calculated by the finite element analysis in the hot face (HF.FEA) and cold face (CF.FEA) are presented in blue and green, respectively. The temperature curves of the FEA analysis fit closely with the average of the measured temperatures. This good agreement and accuracy ensure the adequacy of the developed finite element model for the heat transfer analysis.

The model was able to represent accurately the evolution of the temperatures in the exposed and non-exposed face of the wall. The comparison of the in-plane displacements obtained experimentally and numerically are presented in **Figure 6-12**b. The developed model is able to represent all stages of the test, including the effects of the thermal elongation on the masonry walls. The differences between the numerical and experimental in-plane displacements, in the interval from 20 to 45 minutes, may have been caused by rotation of the load application beam on its longitudinal axis, induced by the beginning of the thermal bowing of the wall.

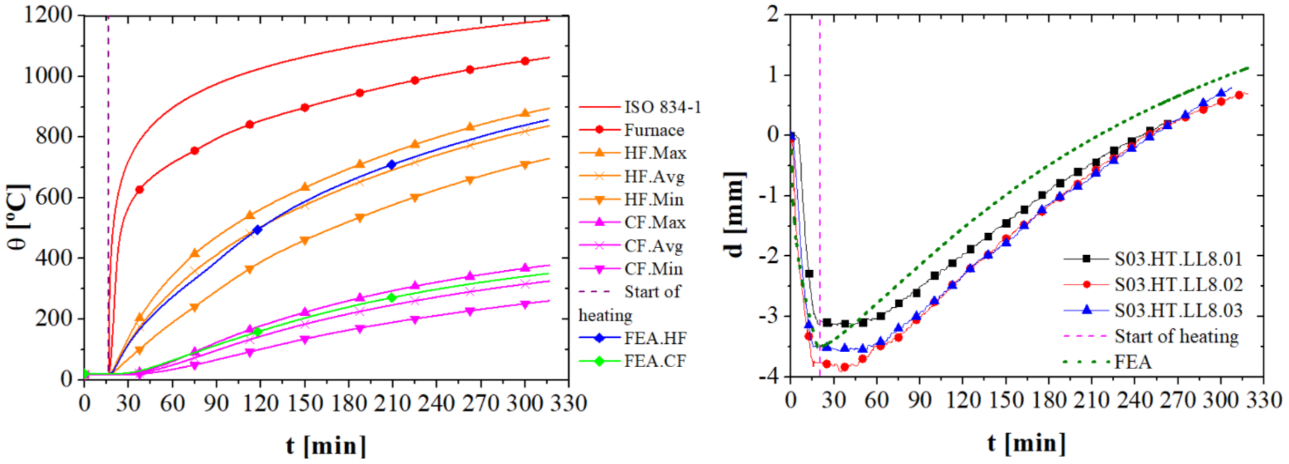

a) b)

Figure 6-12 – Validation of the numerical model – test series S03.HT.LL8: a) Temperatures; b) In-plane displacements

The results of the heat transfer analysis allow us to validate the thermal properties used in the numerical models. These parameters may be used for future simulations of the temperature fields in industrial vessels. The results of the mechanical analysis validate the mechanical properties and the joints parameters used for this temperature range.

6.5.4 Test series S04.HT.RTE

Figure 6-13 shows the comparison of the in-plane displacements and stresses obtained in the experimental and numerical tests for test series S04.HT.RTE. The curves of the FEA analysis fit closely with the experimental ones. This good agreement between the experimental and numerical results once more ensures the validity of the developed finite element model. There is a difference in the numerical and experimental reactions (**Figure 6-13**b), between 20 and 45 minutes. In the experimental curves it is possible to observe a plateau between 20 and 45 minutes before the reaction force starts increasing. This may have been caused by slightly pressure drop in the hydraulic system.

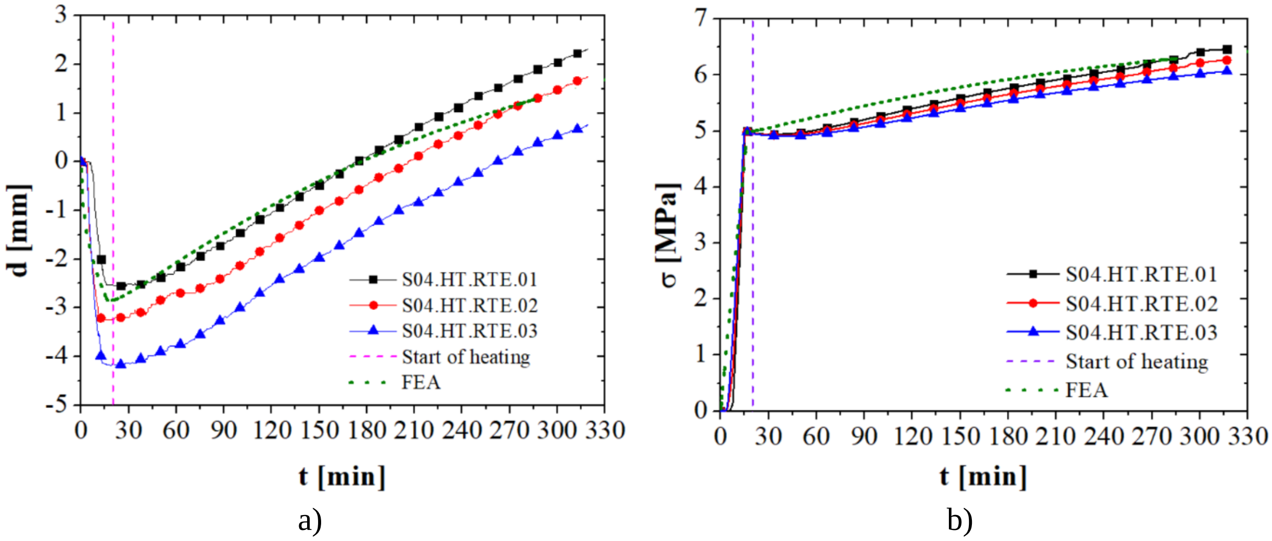

a) b)

Figure 6-13 – Validation of the numerical model – test series S04.HT.RTE: a) In-plane displacements; b) Stresses

Once more the results of the mechanical analysis validate the mechanical properties and the joints parameters used for this temperature range. Therefore, these parameters may be used for future simulations of refractory linings under similar conditions.

6.5.5 Test series S05.HT.LL10

Figure 6-14a shows the comparison of temperatures obtained in the experimental and numerical tests for test series S05.HT.LL10. As in the previous heat transfer analyses, the temperatures predicted in the exposed and non-exposed face by the FEA model are in good agreement with the average of the measured temperature. The smaller thickness of the specimens tested in this series (100 mm) results in a faster temperature evolution both in exposed and non-exposed face, when compared to test series S03.HT.LL08 and S04.HT.RTE (140 mm thickness). The comparison of the in-plane displacements obtained experimentally and numerically are presented in **Figure 6-14**b. A compressive stress of 10 MPa was applied during the first 20 minutes of the test, and the average displacements measured in the tests and predicted by the numerical model are in good agreement.

At 20 minutes the furnace was turned on and the temperatures started to rise. Therefore, a positive strain rate was observed in the specimen. At the beginning of the heating, the strain rate developed in the numerical model was slightly higher than the one observed in the numerical model. A good agreement in temperatures and displacements was observed between the experimental and numerical results, for all stages of the test.

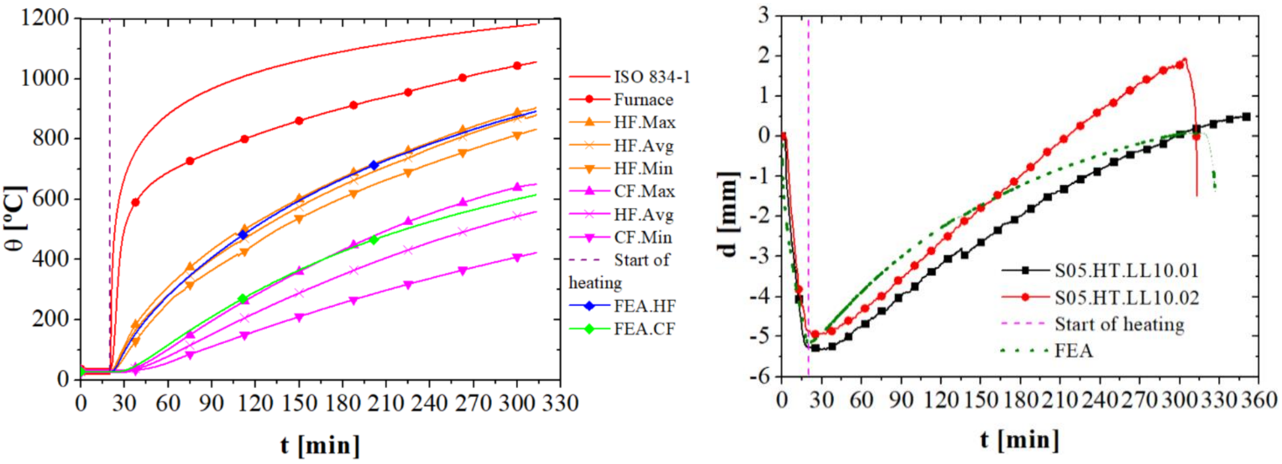

a) b)

Figure 6-14 – Validation of the numerical model – test series S05.HT.LL10: a) Temperatures; b) In-plane displacements

In case of specimen S05.HT.LL10.02, failure of the wall was observed. The thermal gradient through the thickness of the wall led to the thermal bowing of the wall, therefore, significant out of plane displacements were observed in the specimen, with failure ultimately, as shown in **Figure 6-15**.

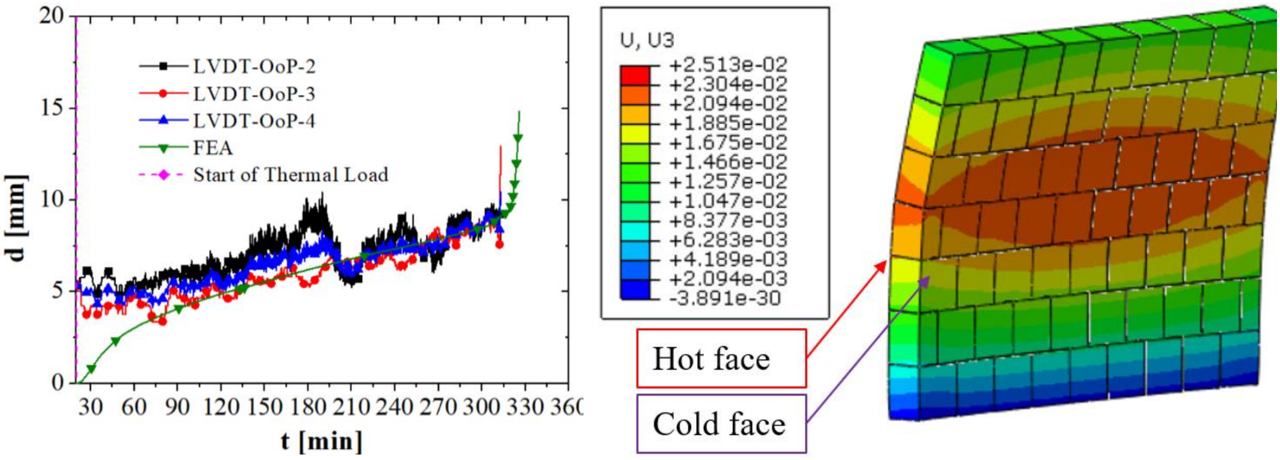

a) b)

Figure 6-15 – Out-of-plane displacements: a) Comparison between numerical and experimental results, b) Out-of-plane displacements fields at 300 minutes

Figure 6-16 shows the stresses in the vertical direction and the plastic strains developed in the wall. The results clearly show that the effects of load eccentricity caused by the thermal bowing of the wall led to a significant stress concentration in the cold face of the wall. Significant plastic strains are developed in this face, and the crushing of the bricks are observed. Thus, the developed model is able to represent all stages of the test, including the effects of thermal elongation on the masonry specimens and the failure of the wall caused by eccentricity due to thermal bowing.

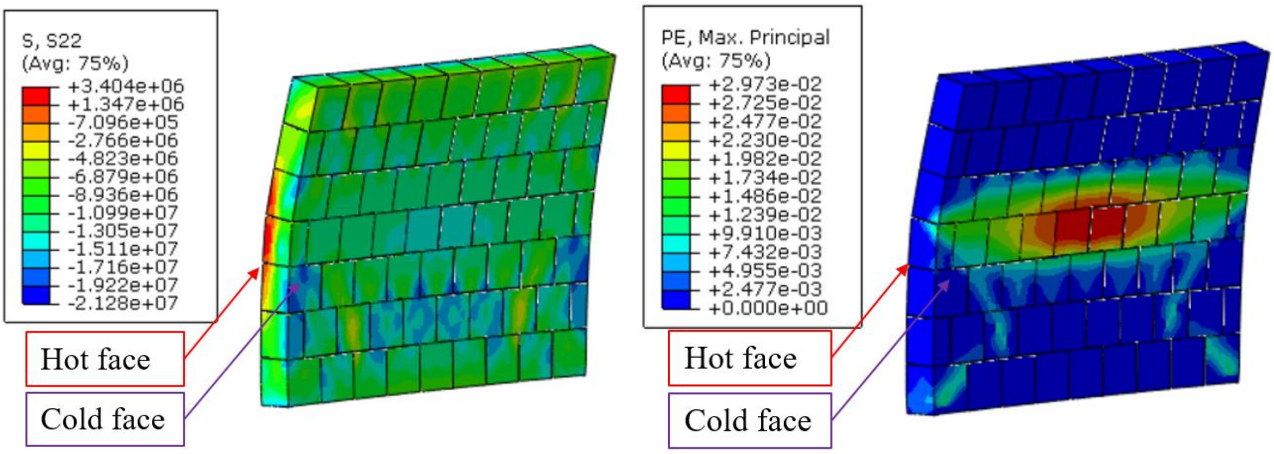

a) b)

Figure 6-16 – Numerical predictions by the end of the tests: a) Vertical stresses; b) Plastic strains

6.5.6 Test series S06.AT.LBJ

Figure 6-17 shows the comparison of the stress-strain curves, for specimens S06.AT.LBJ, obtained from the experimental tests and finite element analysis. The curve from the FEA analysis fits closely with the loading curves obtained experimentally. A good agreement between the experimental and numerical results was found. As in test series S02.AT.CIC, only the loading stage of the test was simulated, the developed numerical model was not able to perform the unloading stage of the test, due to limitations on the software that did not allow modifications on the pressure-overclosure relation as a function of the load and unload cycles. The displacement fields are shown for different load levels in **Figure 6-17**, it is possible to identify that the biggest part of the displacements is caused by the joint closure, as large displacements were obtained for relatively small load levels.

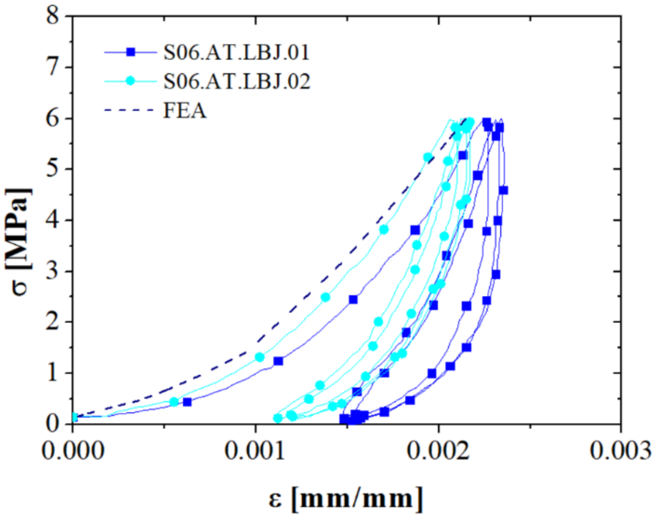

Figure 6-17 – Validation of the numerical model – test series S06.AT.LBJ

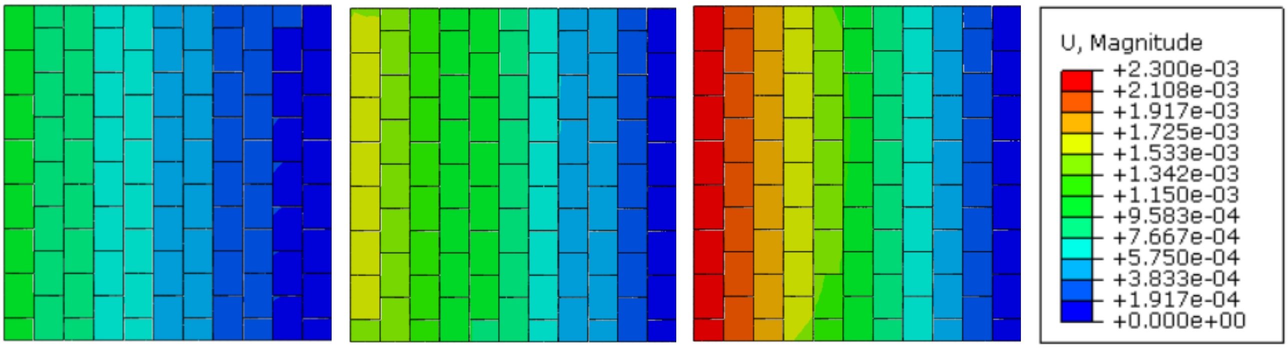

a) b) c) d)

Figure 6-18 – S06.AT.LBJ - Displacement fields for different load levels: a) 20% (1.2 MPa); b) 50% (3 MPa); c) 100% (6 MPa); d) Displacements in m

6.5.7 Test series S07.AT.LHJ

The comparison of the stress-strain curves, for specimens S07.AT.LHJ, obtained from the experimental tests and finite element analysis is presented in **Figure 6-19**. The curve from the FEA analysis fits in the envelope defined between the two loading curves obtained experimentally. The good agreement between the experimental and numerical results ensures the validation of the developed numerical model.

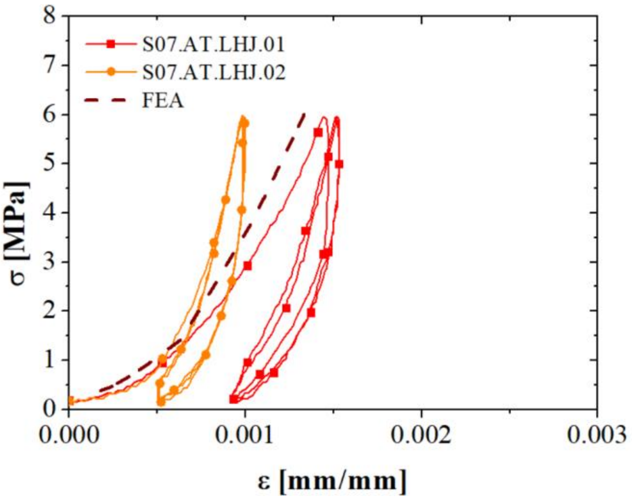

Figure 6-19 – Validation of the numerical model – test series S07.AT.LHJ

The displacement fields for the load levels of 1.2 MPa, 3.0 MPa and 6.0 MPa are shown in **Figure 6-20**. As observed in the previous test, the main part of the measured displacements was caused by the joints closure.

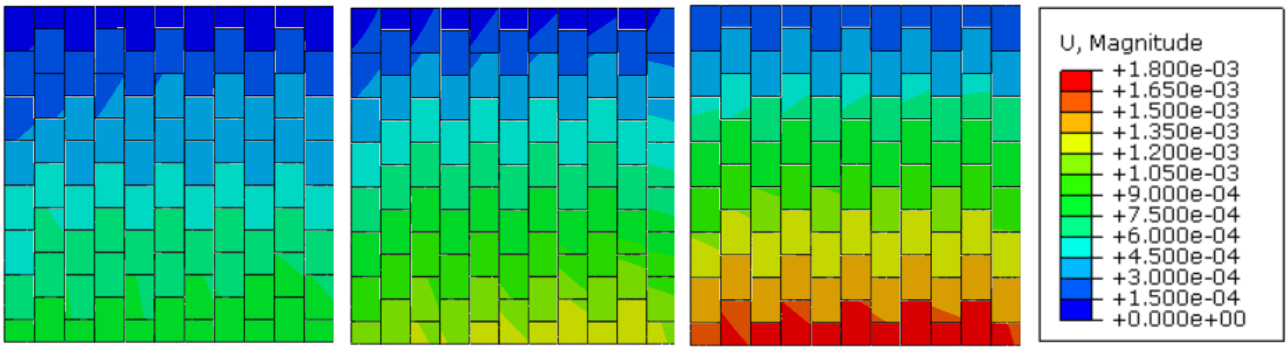

a) b) c) d)

Figure 6-20 – S07.AT.LHJ - Displacement fields for different load levels: a) 20% (1.2 MPa); b) 50% (3 MPa); c) 100% (6 MPa); d) Displacements in m

6.5.8 Test series S08.AT.LBI

Figure 6-21 shows the comparison of the stress-strain curves, for specimens S06.AT.LBJ, obtained from the experimental tests and finite element analysis. The curve from the FEA analysis fits closely with the loading curves obtained experimentally. A great agreement between the experimental and numerical results was found. As in test series S02.AT.CIC, only the loading stage of the test was simulated. An increase of the stiffness of the specimens was observed with the stress level, as a result of the increase of the contact area between the bricks.

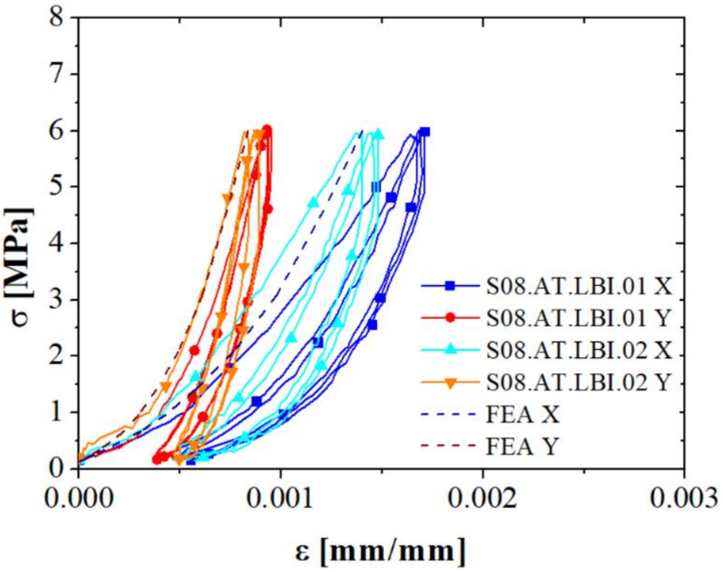

Figure 6-21 – Validation of the numerical model – test series S08.AT.LBI

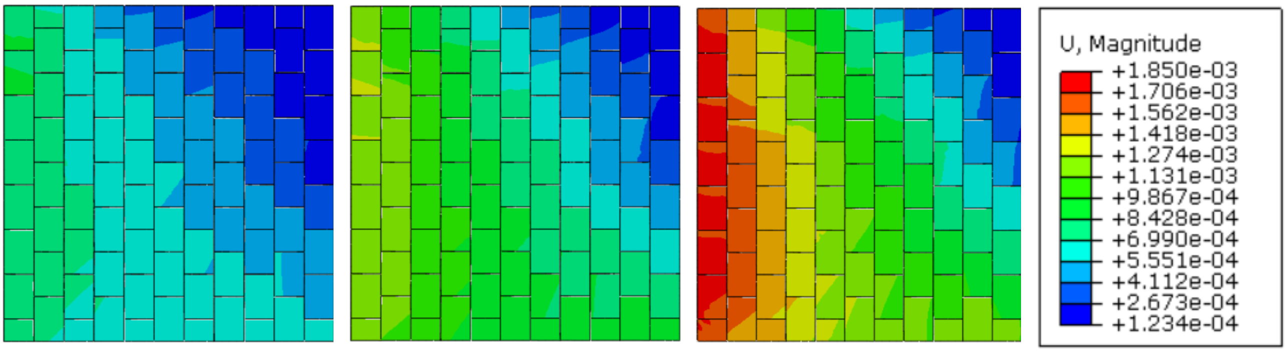

a) b) c) d)

Figure 6-22 – S08.AT.LBI - Displacement fields for different load levels: a) 20% (1.2 MPa); b) 50% (3 MPa); c) 100% (6 MPa); d) Displacements in m

6.5.9 Preliminary test at high temperature

Preliminary test at high temperature was performed at 1200ºC because the furnace was not able to reach the desired temperature. However, the experimental results allowed the identification of a small creep strain. The temperature field in the specimen is shown in **Figure 6-23**.

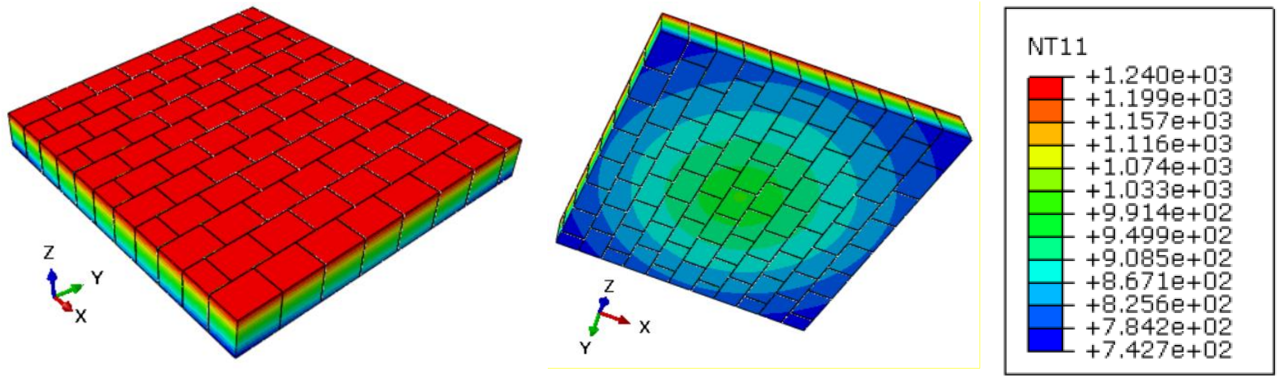

a) b) c)

Figure 6-23 – Temperature distribution – Preliminary Test at high temperature: a) hot face, b) cold face, c) temperatures in ºC

The stress-strain curve of the test is given in **Figure 6-24**. A good agreement was observed between the experimental and numerical predictions. It is possible to identify that the creep is small for this temperature range.

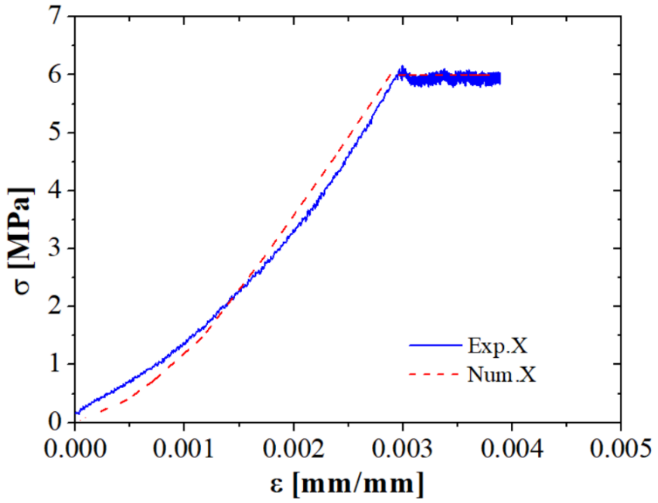

Figure 6-24 – Validation of the numerical model – Preliminary Test at high temperature

6.5.10 Test series S09.HT.CBJ

The validation of the numerical model of the test series S09.HT.CBJ performed at 1500ºC is shown in this section. The temperature distribution in the wall is presented in **Figure 6-25**. The temperatures in the hot face during the test was approximately 1465 ºC. In the cold face, the temperature measured in the centre was 1300 ºC and in the borders around 1115 ºC. The temperature gradient at the cold face is caused by the non-homogeneous insulation conditions of the bottom of the press.

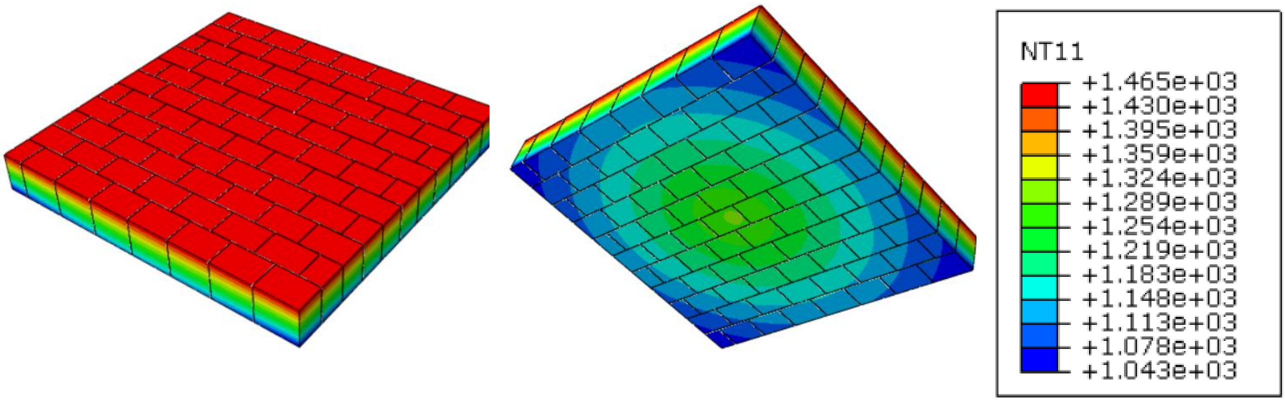

a) b) c)

Figure 6-25 – Temperature distribution– test series S09.HT.CBJ: a) hot face, b) cold face; c) temperatures (ºC)

The comparison of the experimental and numerical stress-strain curves for specimens S09.HT.CBJ, is shown in **Figure 6-26**. The numerical predictions fit the loading curve obtained experimentally with an acceptable agreement. The creep parameters used led to good results, however, the characterization of the creep properties for 1200 ºC and 1100 ºC are strongly recommended to increase the database of the material and improve the quality of future simulations. Moreover, the characterization of the joint closure curves at high temperatures are important to analyse their effect on the behaviour of dry-stacked masonries.

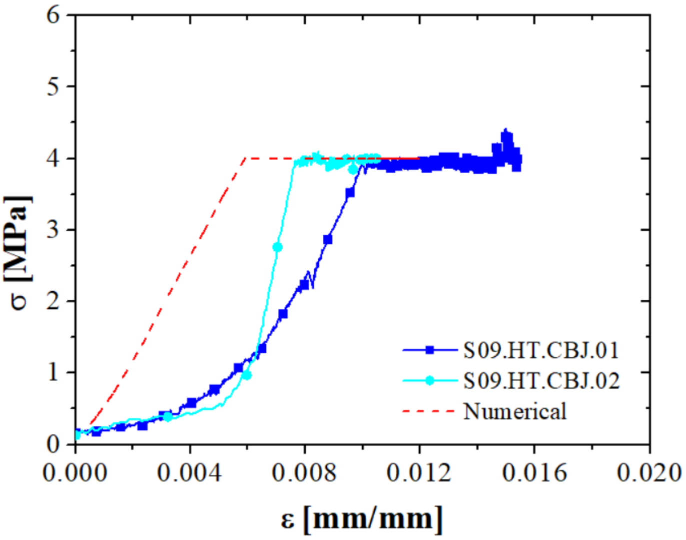

Figure 6-26 – Validation of the numerical model – test series S09.HT.CBJ

The analysis of the stress distribution in the wall (**Figure 6-27**) shown that the main part of the load is being transmitted by the bottom part of the wall. This phenomenon is caused because the creep strains are higher in the top face, due to the temperature distribution, resulting in a reduction of the stiffness of the specimen in this area.

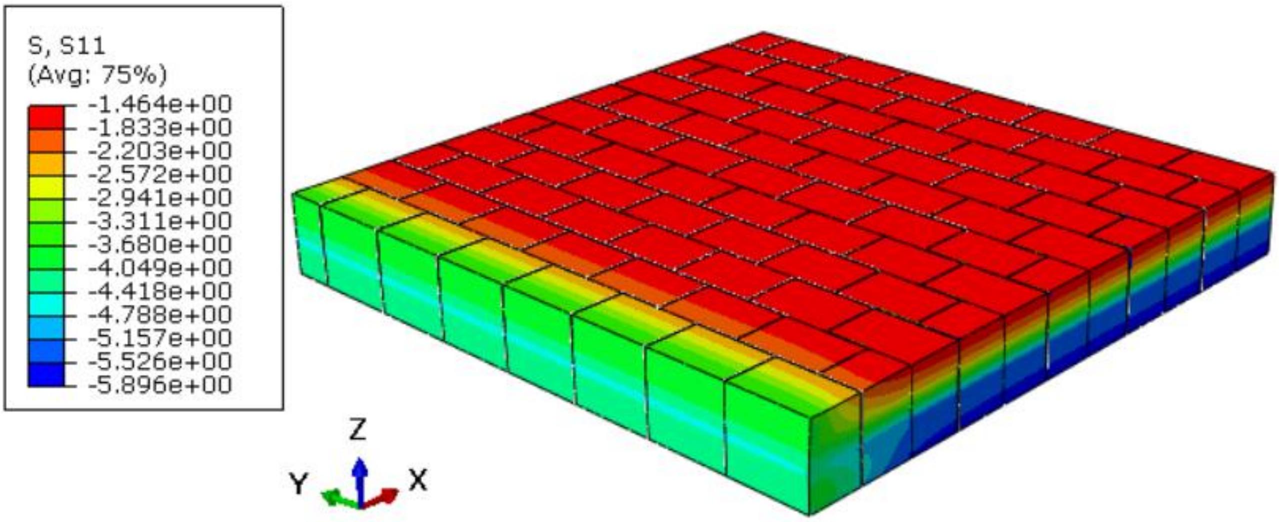

Figure 6-27 – Stress distribution – test series S09.HT.CBJ: direction X (MPa)

The micro-modelling of the masonry allows the detailed study of the joint behaviour. **Figure 6-28** presents the normal pressure and the overclosure of the joints, respectively. The analysis of the joint behaviour allows to reach the same conclusions: the contact pressure is higher in the bottom of the specimen. The joints overclosure is also greater in this area.

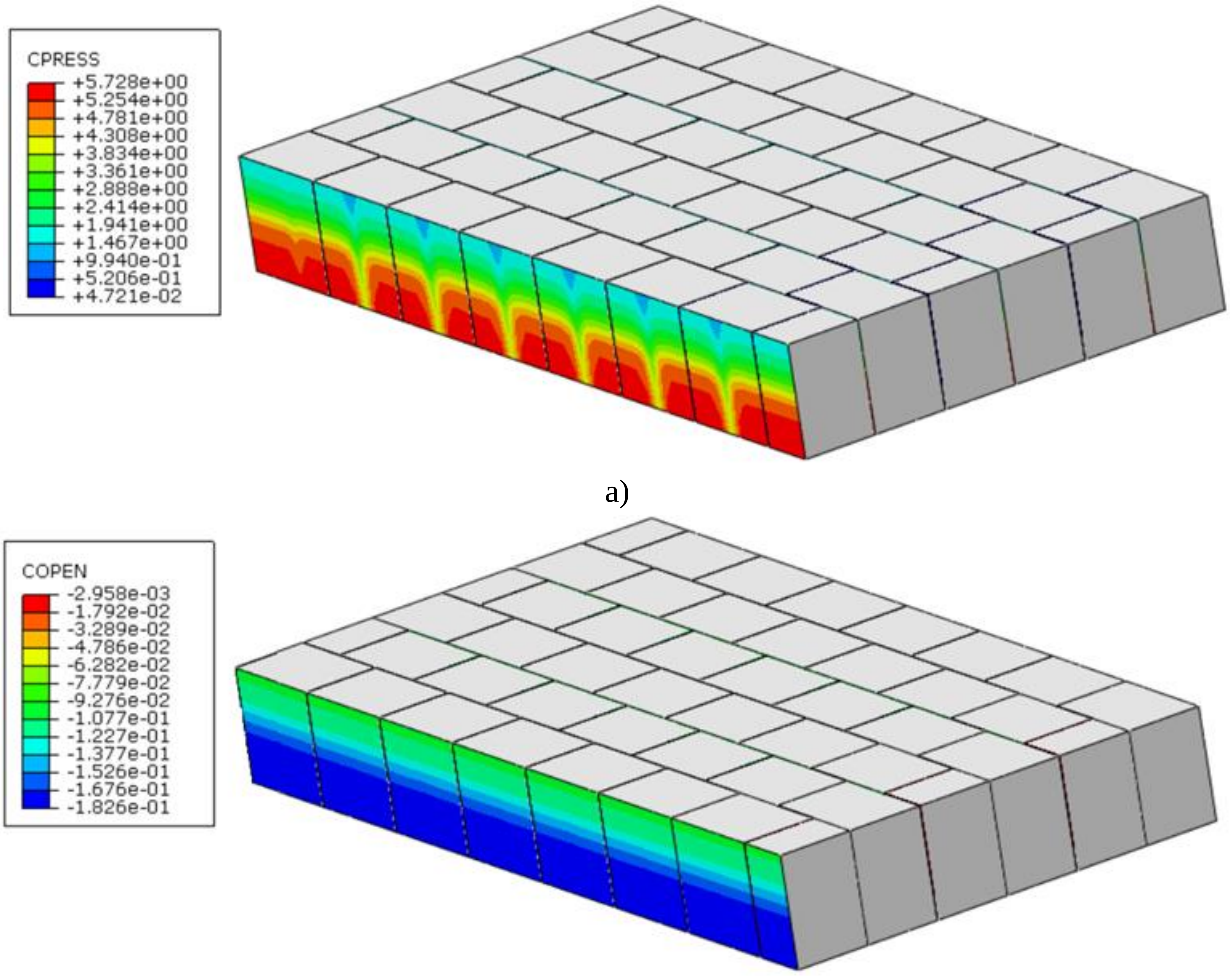

a)

b)

Figure 6-28 – Joint states – test series S09.HT.CBJ a) Joint normal pressure, b) Joint opening/overclosure

6.5.11 Test series S10.HT.CBI

The validation of test series S10.HT.CBI is given in **Figure 6-29** in terms of stress-strain curves. The numerical and experimental results are in good agreement during the loading stage and part of the hold stage. However, by the end of the test, the numerical predictions are indicating significantly higher strains. This disagreement may have been caused by the lack of characterization of the creep parameters for the temperatures of 1000ºC, 1100 ºC and 1200ºC.

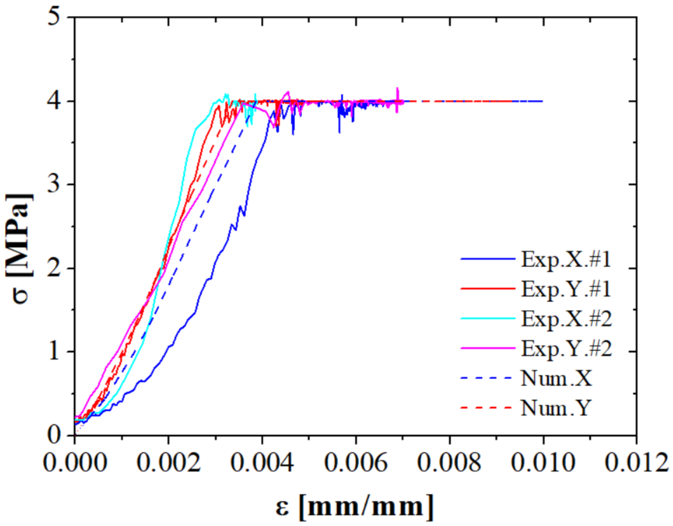

Figure 6-29 – Validation of the numerical model – Test series S10.HT.CBI

The plot of the minimum principal stresses in the specimen is given in **Figure 6-30**. As in the previous cases, the biggest part of the mechanical load is being supported by the cold face of the specimen. The visco-plastic strains developed in the specimen are more significant in the hot face, and consequently, this part of the structure experiences a higher stiffness reduction (**Figure 6-31**).

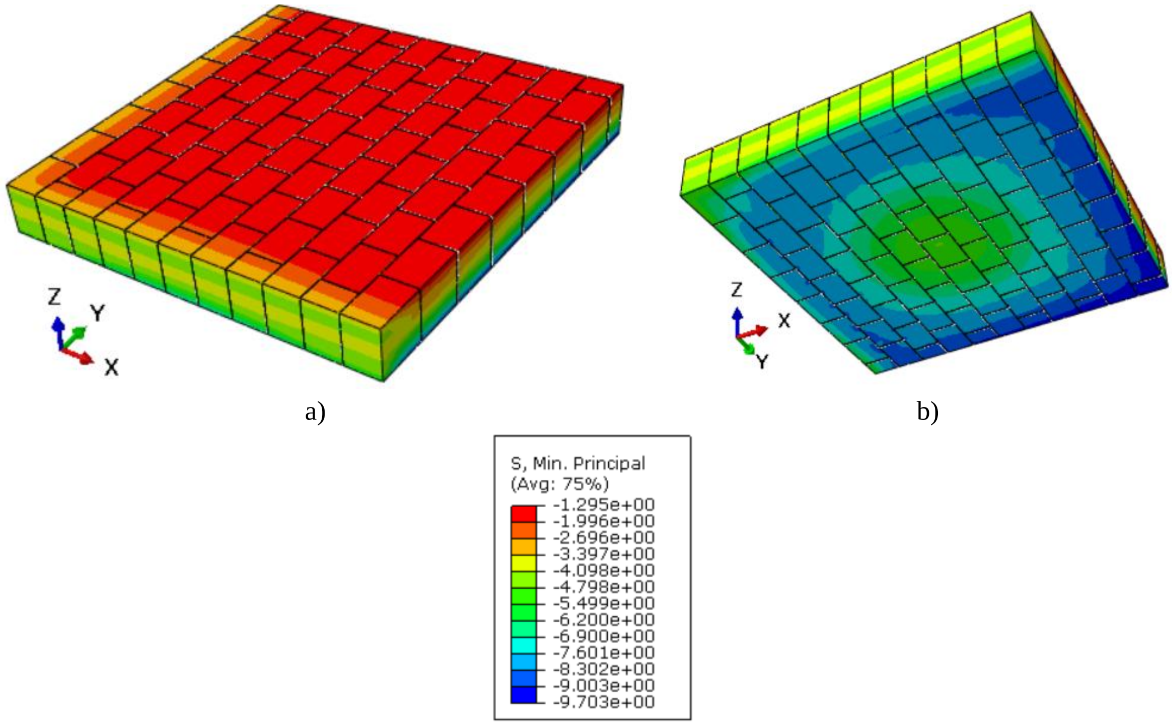

a)

b)

c)

Figure 6-30 – Stress distribution in the specimen – Test series S10.HT.CBI: a) hot face, b) cold face c) Stresses in MPa

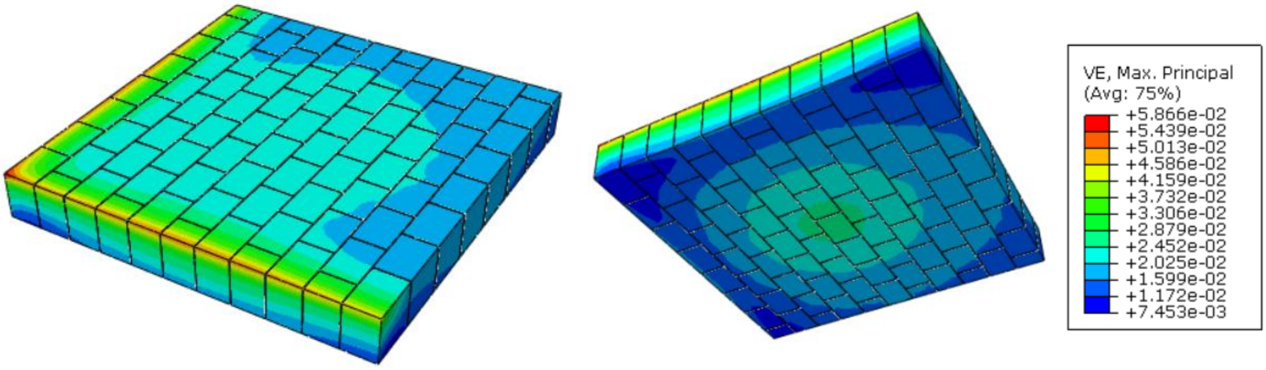

a) b) c)

Figure 6-31 – Viscoplastic strains in the specimen – Test series S10.HT.CBI: a) hot face, b) cold face; c) strains (mm/mm)

6.5.12 Test series S11.HT.RBI

For test series S11.HT.RBI, the temperature distribution in the wall is similar to the one presented in **Figure 6-25**. As in the previous tests, the temperatures in the hot face were around 1465 ºC. In the cold face, the temperature measured in the centre was 1300 ºC and in the borders around 1115 ºC.

The comparison of the experimental and numerical results in terms of forces versus time is given in **Figure 6-32**. The numerical model is able to represent the reduction of the forces caused by relaxation with a great agreement. As stated before, the characterization of the creep properties for 1200 ºC and 1100 ºC is strongly recommended to increase the database of the material and improve the quality of the future simulations.

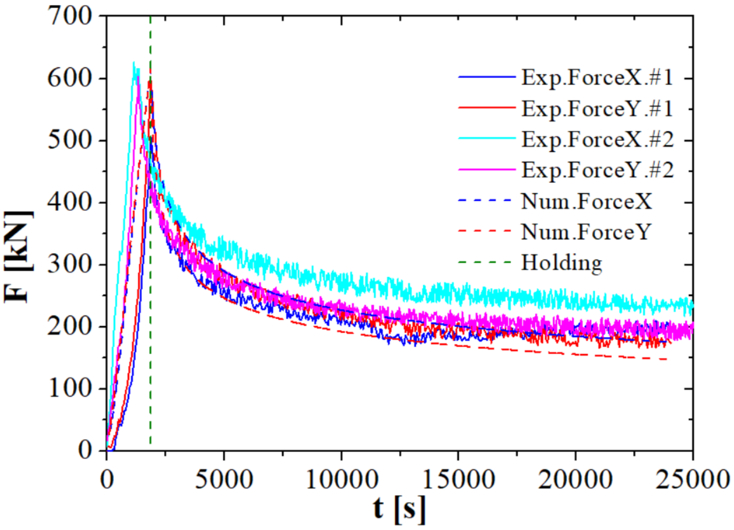

Figure 6-32 – Validation of the numerical model – Test series S11.HT.RBI

The relaxation is defined by the reduction of the mechanical stresses in the lining caused by the increase of the viscoplastic strains. The total strain is composed by the elastic, thermal and visco-plastic strain components. The mechanical load was applied to the specimens when temperature fields were stabilized (steady-state), therefore, there was no significant variation of the thermal strains. The visco-plastic strains increase during the test due to creep, and consequently, the elastic strains decreased in the same proportion. **Figure 6-33** presents the plot of stresses (directions X and Y) and viscoplastic strains by the end of the load stage and by the end of the test.

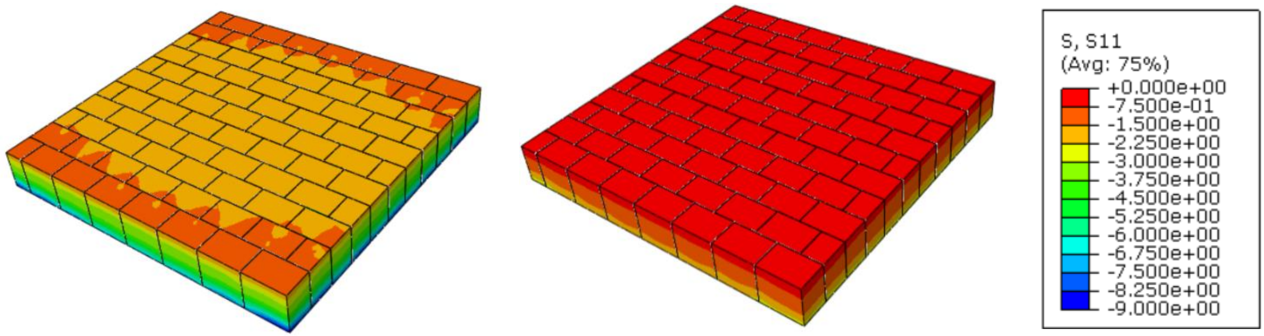

End of load stage (t=1850s)

End of test (t=24000s)

[MPa]

a)

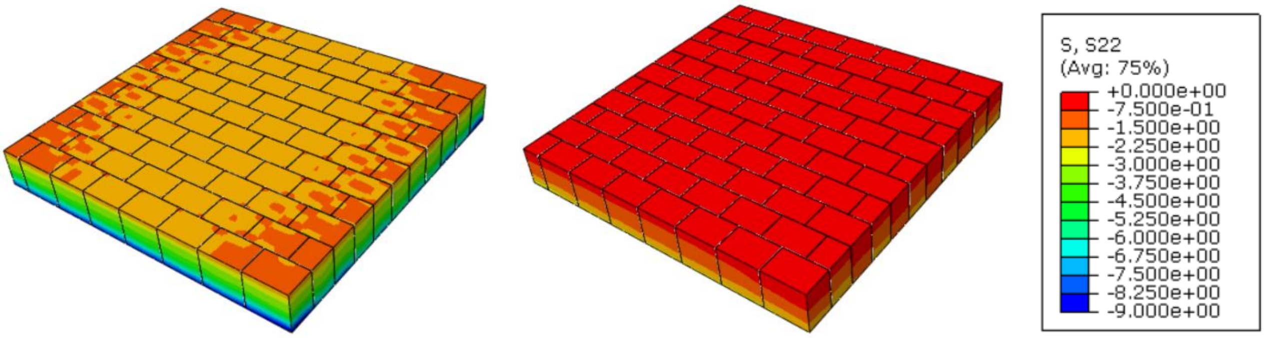

End of load stage (t=1850s)

End of test (t=24000s)

[MPa]

b)

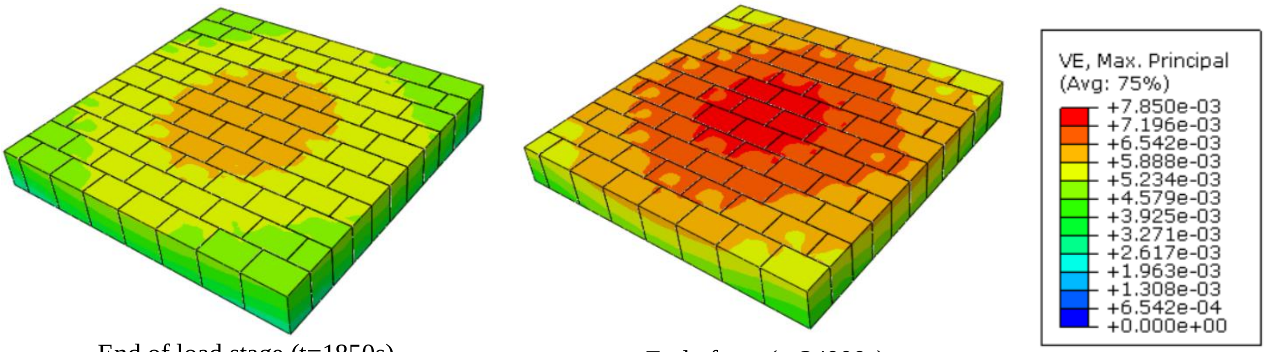

End of load stage (t=1850s)

End of test (t=24000s)

c)

Figure 6-33 – Minimum principal strain –Test series S11.HT.RBI: a) Stresses direction X, b) Stresses direction Y; c) Viscoplastic strains

6.6 Numerical simulation of a steel ladle

This section presents a numerical simulation of a steel ladle under a full operational cycle. The geometry of the steel ladle is shown in **Figure 6-34**. The vessel is composed by a 140 mm thick working lining (alumina spinel), a 40 mm safety lining (bauxite layer), a 35 mm thick insulation lining (fire clay), a 5 mm insulation board (medium density) and a 40 mm thick steel shell. Aiming to reduce the computational time, the ladle was modelled as 15 degrees periodic slice with axisymmetric boundary conditions. The bottom of the model was simply supported, and no restrictions were applied to the upper face.

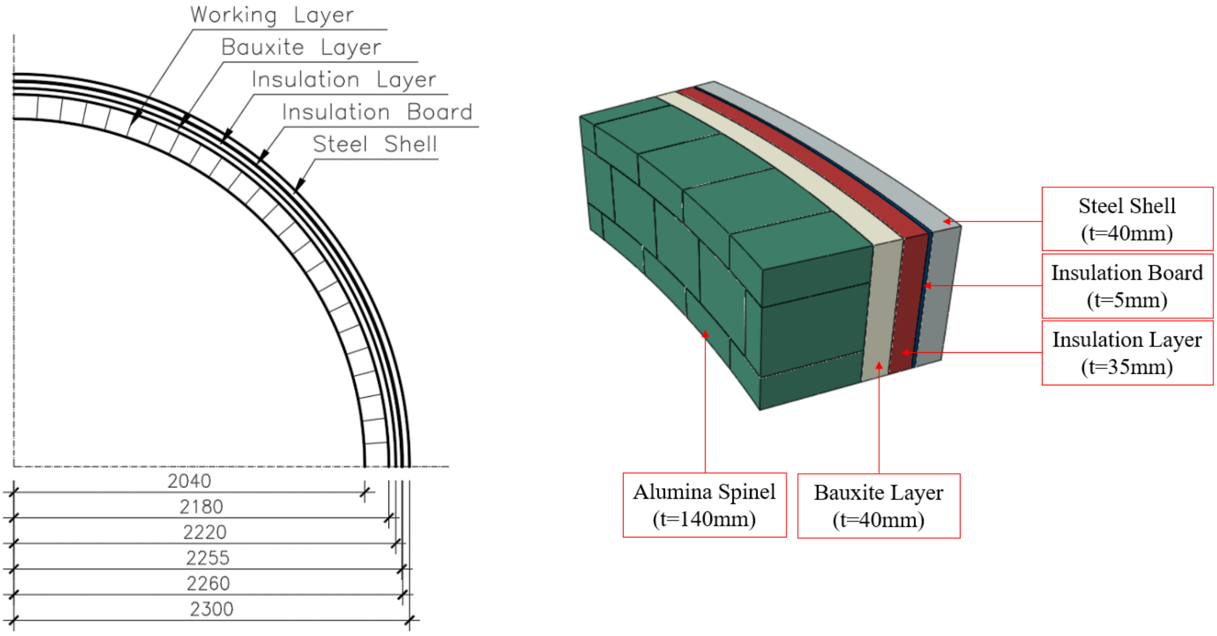

a) b)

Figure 6-34 – Details of the steel ladle: a) Dimensions of the ladle, b) Details of the model

The steel ladle was submitted to a thermal cycle composed by: *i*) pre-heating from 40 ºC to 600 ºC in one hour; ii) pre-heating from 600 ºC to 1050 ºC in 13 hours; *iii*) dwell time of 2 hours at 1050 ºC; *iv*) steel pouring and treatment for 2.5 hours, in this period the temperature of the molten steel decreases from 1650 ºC to 1550ºC; *v*) waiting time at 400 ºC for 2 hours. The thermal cycle is detailed in **Figure 6-35**. The emissivity of the alumina spinel and the steel shell was taken as 0.70. The convection coefficient was taken as 8 W/m^{2}ºC.

The density and thermal elongation coefficient of the used materials were taken as non-temperature dependent and are presented in **Table 6-4**. The specific heat and the thermal conductivity are given in **Figure 6-36**. The Young's moduli are detailed in **Figure 6-37** (Ali *et al*, 2021; Vitiello, 2021).

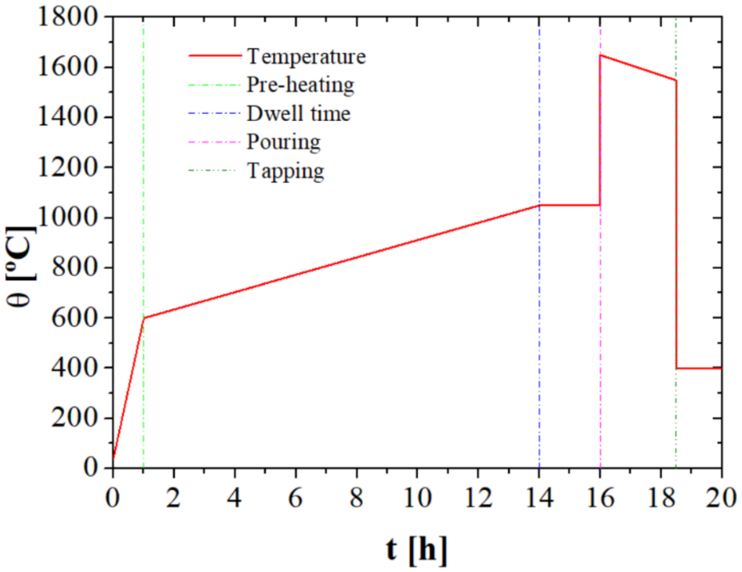

Figure 6-35 – Thermal cycle of the steel ladle

Table 6-3 – Alumina spinel mechanical properties obtained by compressive tests

Temperature [°C]	Poisson Ration	Young Modulus [MPa]
20	0.2	41 340
800	0.2	36 256
1000	0.2	23 25
1200	0.2	21 432
1300	0.2	10 50
1400	0.2	6 972
1500	0.2	6 503

Table 6-4 – Materials properties

Properties	Alumina Spinel	Bauxite	Fire Clay	Insulation Board	Steel
Density [kg/m^3]	3130	2680	857	998	7850
Thermal elongation coefficient [/ºC]	7.4×10^{-6}	7.8×10^{-6}	6.4×10^{-6}	9.3×10^{-6}	1.33×10^{-5}

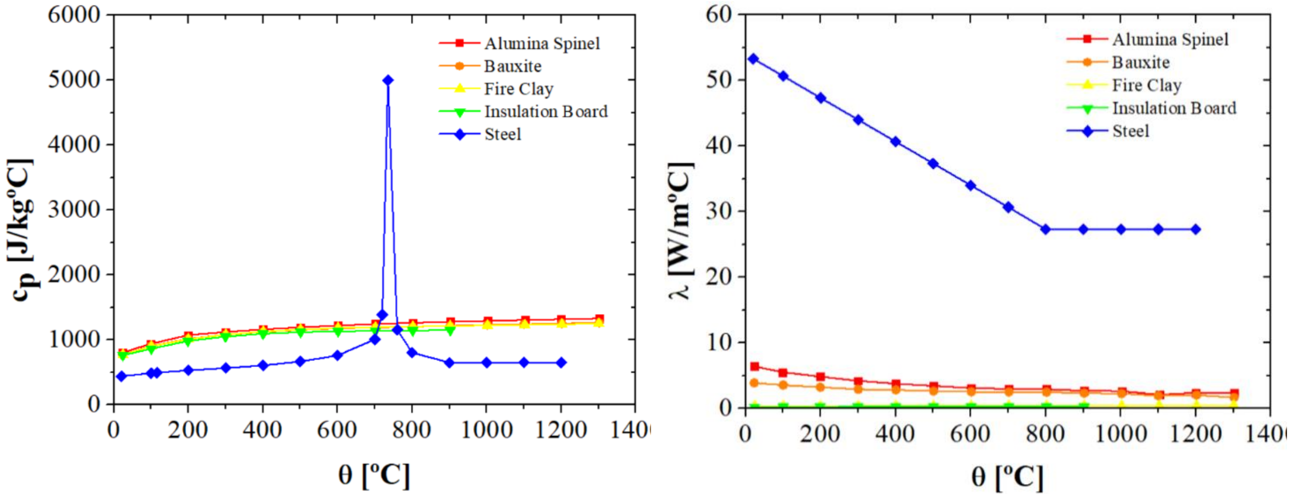

a) b)

Figure 6-36 – Thermal properties of the materials: a) Specific heat; b) Thermal conductivity

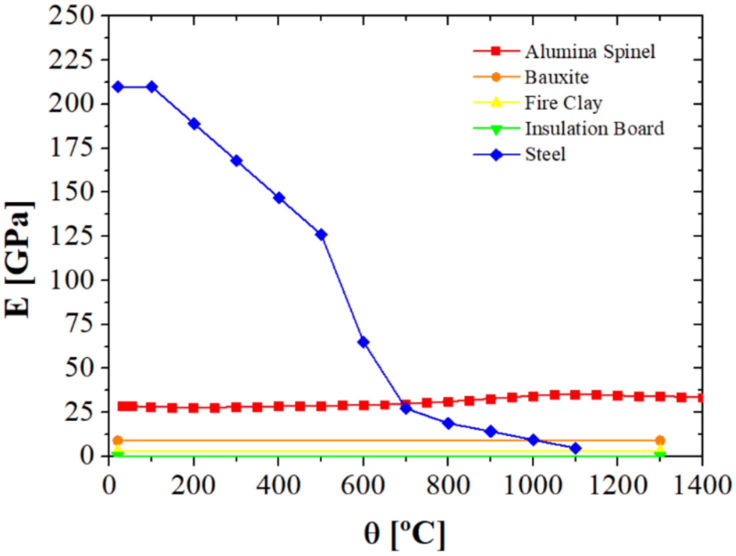

Figure 6-37 – Materials Young's modulus

6.6.1 Numerical model

A micro-modelling approach was chosen to represent the steel ladle. The bricks of the working lining were modelled separately and surface-to-surface contact interactions were used to represent their interactions. The masonry layers of the safety lining (bauxite) and insulation lining (fireclay) are built with thin-layer mortar, and they were assumed and modelled as a homogeneous material and their Young's moduli were calculated according to EN 1996-1-1 (2005). The general arrangement of the model is given **Figure 6-38**a. A sequentially coupled analysis was done. The DC3D8 elements were used for the heat transfer and the elements C3D8R for the mechanical analysis. The elements had approximately 20 mm. The adopted mesh is given in **Figure 6-38**b.

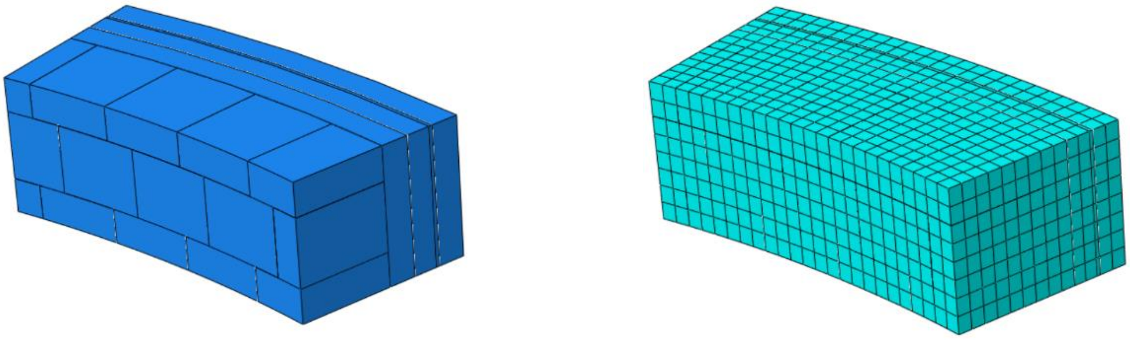

a) b)

Figure 6-38 – Details of the model: a) General arrangement, b) Mesh

The numerical simulations aimed to evaluate the influence of the material modelling (elastic and visco-plastic), the joints modelling (hard contact and pressure-overclosure) and the technique used to obtain the Young's modulus (ultrasonic measurements and compressive tests). **Table 6-5** summarizes the performed simulations.

Table 6-5 – Materials properties

Model	Material Modelling	Joints	Young modulus
MAE.NJ.EUS	Elastic	Hard contact	Ultrasonic measurements
MAE.WJ.EUS	Elastic	Pressure-overclosure	Ultrasonic measurements
MAV.WJ.EUS	Visco-plastic	Pressure-overclosure	Ultrasonic measurements
MAV.WJ.ECT	Visco-plastic	Pressure-overclosure	Compressive tests

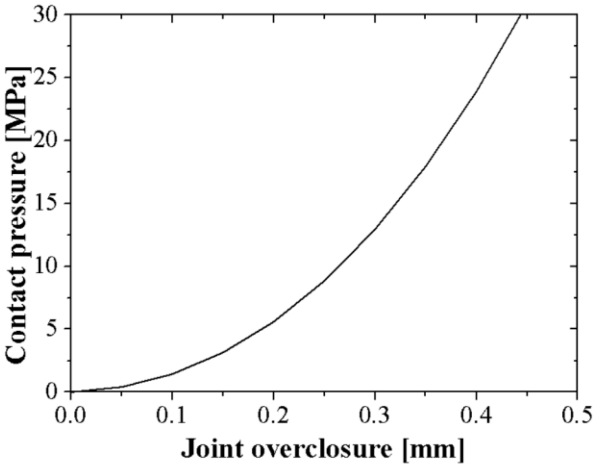

Figure 6-39 – Joint pressure-overclosure curve

6.6.2 Results

The results of the analyses are presented in this section. The temperature fields are shown and analysed in detail. Lastly, the mechanical stresses developed in the refractory linings are presented and discussed.

6.6.2.1 Temperature fields

The temperature distribution obtained in the ladle is given in **Figure 6-40**. The maximum temperature obtained in the working lining is 1603 ºC at 16.3 h and 889 ºC at 19.24 h, for the hot (P01) and cold (P02) face, respectively. The points P03 and P04 are submitted to temperatures up to 798 ºC at 19.5 h and 351 ºC at 20.1 h, respectively. The temperatures in the steel shell reach 260 ºC by the end of the first cycle. The temperature gradient between P05 and P06 is negligible, due to the elevated thermal conductivity of the steel shell. **Figure 6-41** presents the temperatures is the ladle immediately before the pouring and tapping.

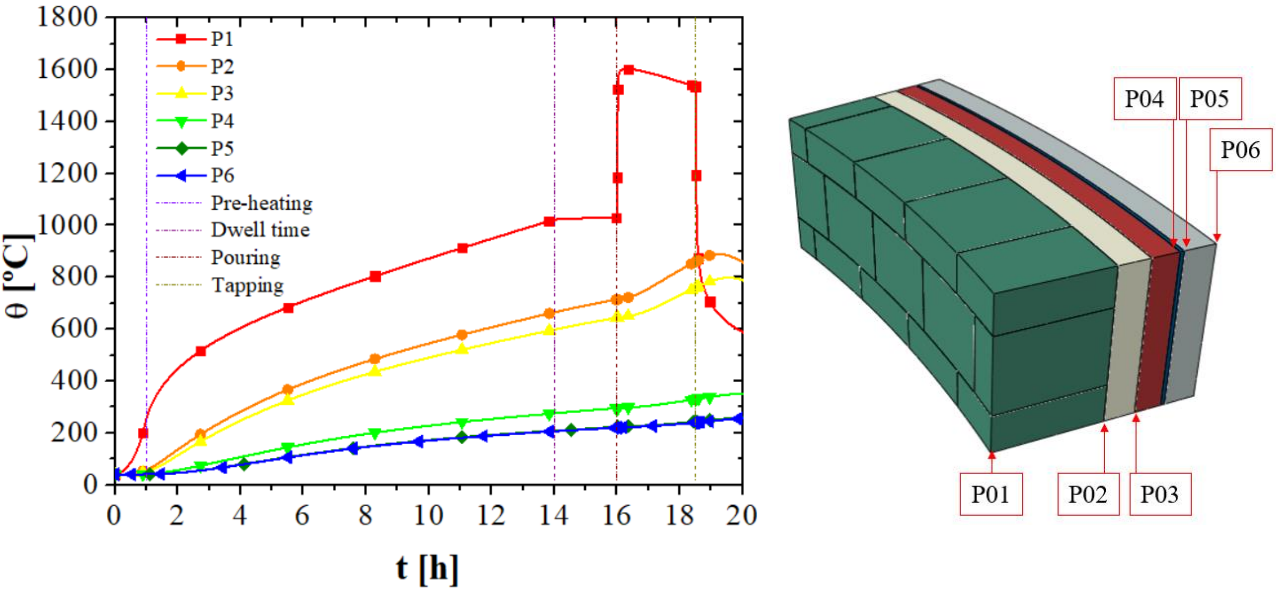

a) b)

Figure 6-40 – Thermal response of the ladle: a) Temperatures, b) Location of the points

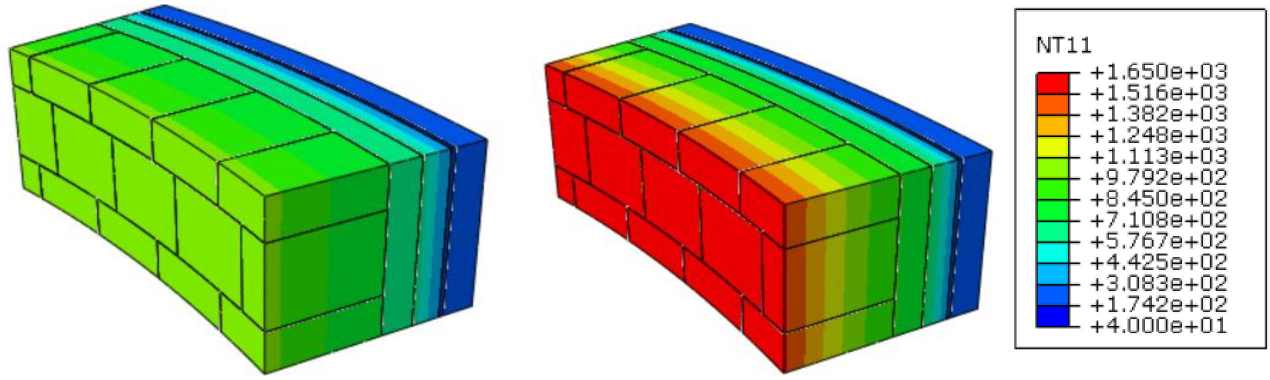

a) b) c)

Figure 6-41 – Temperatures in the ladle: a) Immediately before pouring, b) Immediately before tapping; c) Legend [in ºC]

6.6.2.2 Stress fields

The joints play an important role in dry-stacked refractory masonries reducing the stiffness of the linings and consequently reducing the compressive stresses developed in the working layer and the tensile stresses in the steel shell. The influence of the joints in a fully elastic model is being studied in this section. **Figure 6-42** presents the stresses predicted by the numerical models of a isotropic ladle and a ladle with joints. A significant reduction of the stresses is observed in the model with the presence of the joints. When the joints are included in the analysis, the maximum compressive stress in the hot face of the working lining decreases from 304 MPa to 132 MPa, in the cold face the compressive stress decreases from 96 MPa to 24 MPa. The tensile stresses in the steel shell decreases from 463 MPa to 194 MPa. The stresses are plot in **Figure 6-43** for both models.

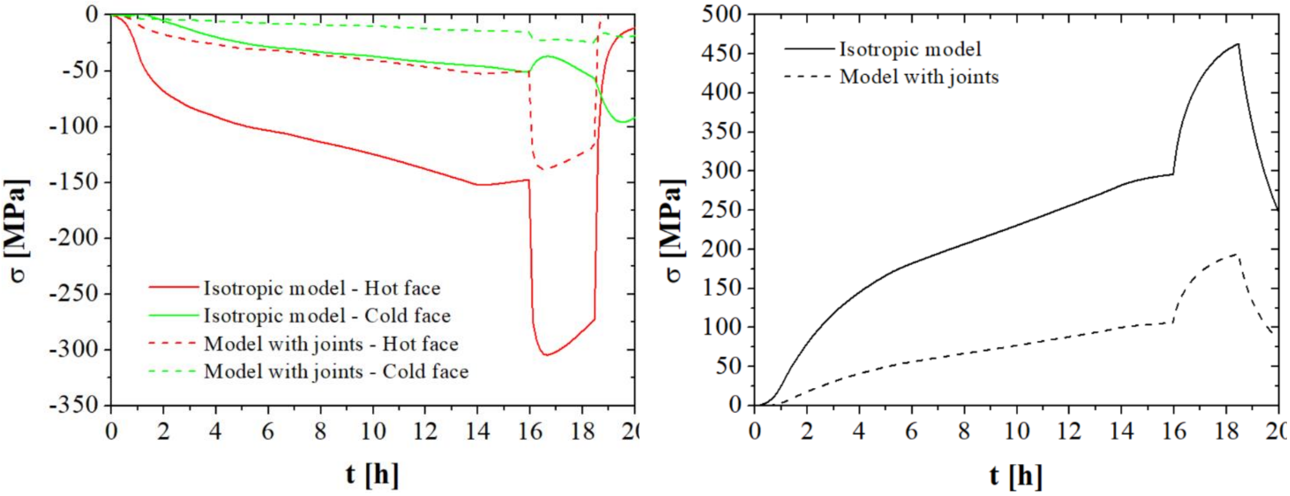

a) b)

Figure 6-42 – Influence of the joints in the stresses developed in the ladle in a fully elastic model: a) Refractory lining; b) Steel Shell

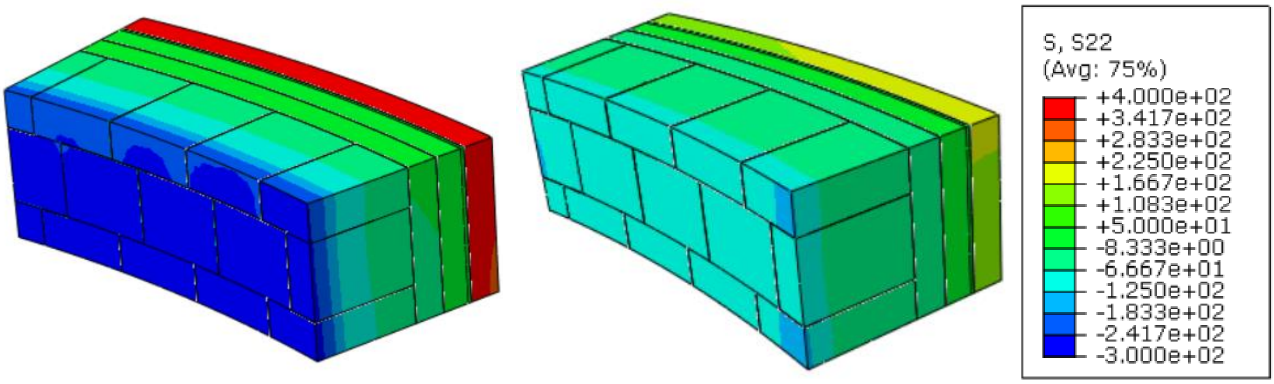

a) b) c)

Figure 6-43 – Tangential stresses in the ladle: a) Isotropic model; b) Model with joins; c) Legend [MPa]

In spite of the significant reduction, the stresses developed in the refractory lining are several times higher than the material’s compressive strength. Additionally, the stresses developed in the steel shell would lead to the yielding of the material. To have a better idea of the behaviour of the steel ladle, it is necessary to include de visco-plastic effects caused by creep.

The influence of the creep strains in the stresses developed in the steel ladle are presented in **Figure 6-44**. The accounting of creep in the model results in a considerable stresses relief in the vessel. Due to the relaxation, the maximum compressive stress in the hot face of the working lining decreases from 132 MPa in the elastic model to 52 MPa in the visco-plastic model.

As observed in the numerical simulations presented in 6.5.10, 6.5.11 and 6.5.12, the creep strains in the hot face results in a slightly increase of the stresses in the cold face. This phenomenon was also observed in the simulation of the ladle, the visco-plastic strains resulted in an increasing of the compressive stresses in the cold face from 24 MPa to 31 MPa. The tensile stresses in the steel shell decreased from 194 MPa to 106 MPa.

The Young’s modulus of the refractory materials may be obtained by compressive tests or by ultrasonic measurements. As stated by Andreev and Zinngrebe (2009), above 1200 ºC it is possible to observe the weakening of the material in compressive tests, this weakening is not seen in the dynamic measurements of the Young’s modulus. The material is influenced by micro plastic events, which are responsible for the greater part of the deviations observed between both techniques (van Mier, 1996; Nazaret *et al*, 2006). **Figure 6-45** shows the comparison of the stresses developed in the ladle for models accounting the Young’s modulus obtained by ultra-sonic technique and by compressive tests. It is possible to identify a slight reduction of the stresses in hot face from 52 MPa (ultra-sonic) to 42

MPa (compressive tests). The reduction of the stresses in the cold face and in the steel shell are not significant.

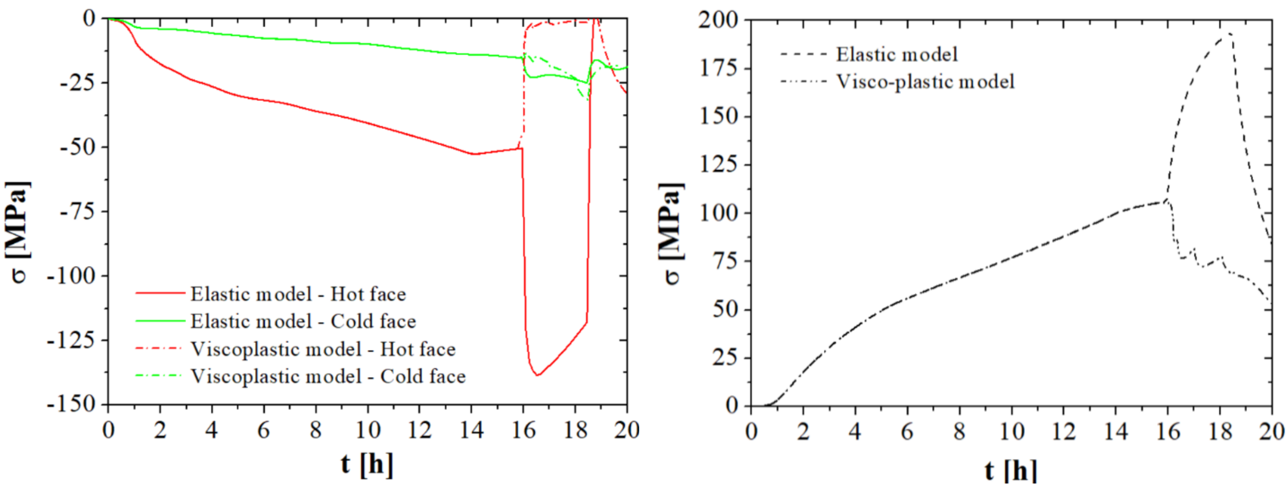

a) b)

Figure 6-44 – Influence of the creep in the stresses developed in the ladle with joints: a) Refractory lining; b) Steel Shell

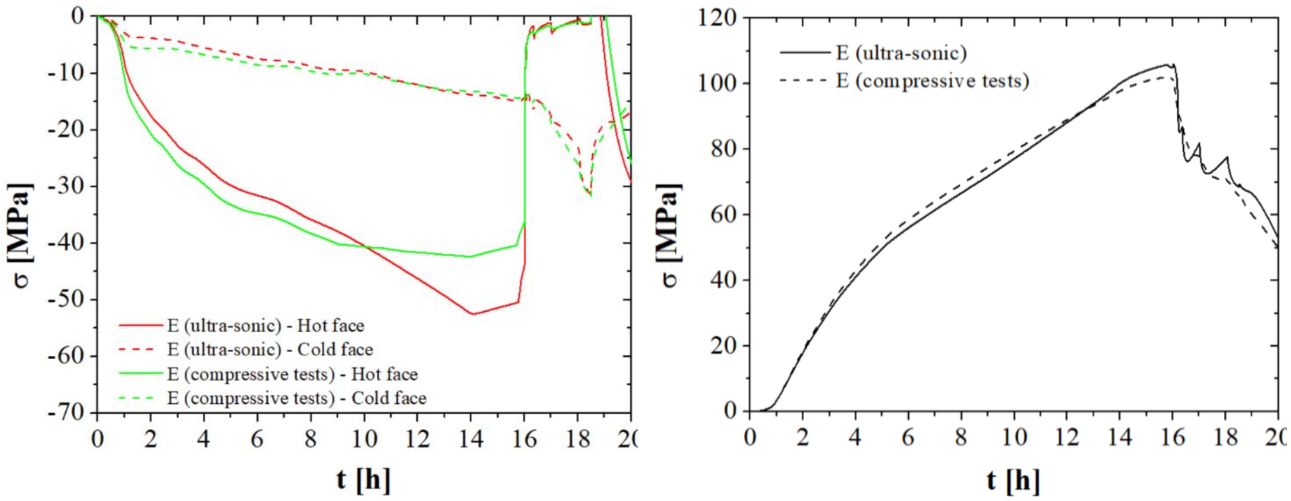

a) b)

Figure 6-45 – Influence of the Young modulus in the stresses developed in the ladle: a) Refractory lining; b) Steel Shell

6.6.3 Conclusions of the numerical simulation of a steel ladle

Based on the numerical studies presented in this section, it was possible to draw the following conclusions:

- The account of the joint behaviour is really important to lead for reliable results of the stresses in the steel ladle. The model is sensible to the joint thickness curve used, therefore, it should be correctly determined based on compression tests in masonry wallets, as compressive tests in two stacked bricks may result in the underestimation of the joint closure curve.
- The visco-plastic strains developed in the working lining results in significant relief of the stresses (relaxation). Therefore, the creep properties of the material should be characterized under different temperatures, from 1000 ºC to 1500 ºC.
- The measurement of the Young’s modulus by the ultrasonic technique results in values slightly bigger than the ones obtained at the compressive tests, mostly for high temperatures. The ultrasonic technique does not account the effects of the micro plastic events that happen in the material’s microstructure. Thus, the use of the ultra-sonic measurements may result in the overestimation of the stresses in the ladle.

6.7 Final remarks

An extensive numerical investigation for developing finite element models capable of simulating the thermal and mechanical response of dry-stacked masonry walls at ambient and high temperatures was detailed in this chapter. The developed numerical models included the several non-linearities observed experimentally, as the joint closure and joint opening, crushing in compression, cracking in tension and creep.

The models were developed using the software Abaqus (Abaqus User Manual). The micro-modelling approach was adopted, therefore, the units were modelled separately and connected to each other by surface-to-surface contact interactions. This technique was chosen as it is reported in the literature to have more accurate results. The mechanical and thermal properties used in the numerical models were experimentally measured within the scope of the ATHOR Project.

The validation of the developed finite element models was presented. The numerical predictions of heat transfer and the mechanical analyses were compared with the experimental results and a good agreement was observed.

The heat transfer analyses were validated in terms of temperatures in the exposed and non-exposed. The numerical model is able to predict with great accuracy the temperature evolution in the specimen. The accurate distribution of temperatures in the model is important to ensure the quality of the results provided by the mechanical analysis, as the properties of the material are temperature-dependent. The heat flux was also calculated during the heat transfer analysis, it is an important parameter to estimate the thermal efficiency of the industrial vessels and to optimize their design reducing the heat loses.

The mechanical analyses were validated in terms of displacements (in-plane and out-of-plane), forces and failure modes. The developed models were able to accurately predict the behaviour of dry-stacked refractory masonry under uniaxial and biaxial loads both at ambient and high temperatures. The structural response and the failure mode of the models are in good agreement with the experimental observation.

The thermomechanical characterization of the alumina spinel brick, including the evaluation of the material compressive strength presented in Chapter 3, tensile strength (Kaczmarek *et al*, 2019), Young's modulus (Kaczmarek *et al*, 2019), thermal elongation (Kaczmarek *et al*, 2019), specific heat and thermal conductivity (Vitiello, 2021) and creep parameters (Samadi *et al*, 2020) led to reliable data base that may be used to analyse and design refractory linings with this material.

The CDP model was suitable to represent the mechanical behaviour of refractory masonries at ambient and intermediate temperatures (up to 1100ºC, where creep effects are not significant). Nevertheless, due to the service conditions of refractory linings, where the temperatures in service may reach up to 1650 ºC, the Norton-Bailey creep law should be used. Coupling of the CDP model with some creep law, such as Norton-Bailey, is required to represent the mechanical behaviour of refractory masonry under a large range of temperatures, from ambient up to the service temperatures.

The micro-modelling technique adopted led to good predictions of the behaviour of masonry at ambient and high temperatures. This technique requires more computational resources when compared to the macro-modelling and homogenization techniques. However, it has greater accuracy and it gives detailed information on the joint's behaviour. The use of homogenization techniques may overcome the drawback of the micro-modelling technique, being more suitable for modelling refractory linings at industrial scale.

The formulation recommended by Thanoon *et al* (2013) presents the evolution of the compressive stresses in the wall in terms of joint closure. The formulation was proven to be suitable to model the normal behaviour of dry joints presenting good results for the loading stage of the tests. However, this formulation may not be used to represent the residual strains on the unloading stage and, consequently, different models must be used to represent the loading and unloading of masonry.

The use of the Norton-Bailey creep law led to good results in the numerical models. The models were validated against experimental results and a good agreement was observed between them. This creep law is able to represent the behaviour of the refractory lining under uniaxial creep, biaxial creep and biaxial relaxation. Nevertheless, the development of asymmetric creep models is recommended (Teixeira *et al*, 2020).

7 CONCLUSIONS AND FUTURE WORK

This section intends to gather all the major conclusions observed within this work, and it is structured according to the work presented in this document.

7.1 The behaviour of refractory masonry under uniaxial conditions

The characterization of dry-stacked refractory masonry under uniaxial loading was presented in Chapter 4. The masonry walls have been characterized at ambient and high temperatures under diverse loading conditions. The following conclusions were drawn from the experimental research:

- As reported in the literature, refractory materials have a highly heterogeneous behaviour resulting in considerable scatter on their properties, which was observed in the experimental results. The heterogeneous behaviour of the refractories should be taken into account in the design of the linings, increasing the safety factors of the structures or using the most unfavourable values for the analysis.
- The test series S01.AT.LBC has characterized the loadbearing capacity of the specimens at ambient temperature. It was possible to identify three different stages of the stress-strain curves: *i*) joint closing state; *ii*) linear behaviour; and *iii*) plastic behaviour and failure. In the first stage, the stress-strain curve had a parabolic shape, the contact area between the bricks increased with the applied load and consequently the in-plane stiffness of the wallet increased as well. The second stage was evidenced by a linear behaviour on the stress-strain curve, at this stage the contact area between the bricks stops to increase, and consequently, the stiffness of the wallet. In the third stage the plastic effects started to rise, the cracks in the specimen led to a reduction on the wall’s stiffness and a brittle failure was observed.
- The test series S02.AT.CIC has evaluated the behaviour of the walls under cyclic loading. Four load cycles with increasing load level were applied to the specimens. The crushing of the initial non-plane bricks’ surfaces caused by the mechanical loading were observed and evidenced by the residual strains obtained after each load cycle. The residual strains increased with the load level. The crushing of the non-plane brick’s surfaces increased the contact area between the bricks, and consequently the wall’s in-plane stiffness. In spite of the small loading level applied to the specimen, some cracks were found in the bricks, caused by the non-uniformity on the load and support conditions of the bricks.
- Test series S03.HT.LL8, S04.HT.RTE and S05.HT.LL10 have been tested at high temperatures. A small scattering on the temperature measurements in the furnace was obtained, mostly caused by different insulation conditions of the experimental setup, however it has no significant impact on the test results. Additionally, some scatter was obtained in the readings of the thermocouples embedded in the bricks. The position of the thermocouples may have

changed during the casting procedure, therefore, they were maybe at slightly different positions from the wanted. Nevertheless, a relatively homogenous temperature distribution was found in the wall. Due to the high thermal capacity of the specimens, the furnace was not able to follow the standard fire curve (ISO 834-1, 1999).

- In test series S03.HT.LL8, the specimens have been tested under a constant load level of 8 MPa. The mechanical load was applied at ambient temperature and a negative displacement was observed, due to joint closure and bricks' strains. When the furnace was turned on a positive strain rate was observed with the heating. The effects of the thermal elongation surpassed the effects of the mechanical loading after 248 minutes in average. A small scattering on the displacements was found during the test. In spite of the small load level applied to test series, cracks were observed in the wall by the end of the tests, caused by the non-uniformity of the loading and support conditions of the bricks. Head joints opening were also observed.
- Test series S04.HT.RTE has been tested with restrained thermal elongation. A mechanical load of 5MPa was applied at ambient temperature, the hydraulic jack was blocked at its current position and the furnace was turned on. The restrained thermal elongation led to a reaction force that increased the stress level on the specimens. By the end of the tests, an average increasing of 1.25 MPa was observed in the load. Cracks and head joint opening observed in S03.HT.LL8 were also detected. A relatively small scattering was found in the displacement and reaction forces evolution.
- In test series S05.HT.LL10 the specimens with higher slenderness ratio have been tested under a load level of 10 MPa and wall failure at high temperatures was observed. The thermal bowing of the specimen, caused by the temperature gradient across the wall's thickness, resulted in eccentricity in the load application and led to failure of the specimen S05.HT.LL10.02.
- The limitations of the uniaxial experimental setup didn't allow to reach the service temperatures of the industrial linings in the experimental campaign. The service temperatures of the working lining of steel ladles is usually around 1650 ºC. The maximum temperature measured in the specimens were around 900 ºC.

7.2 The behaviour of refractory masonry under biaxial conditions

The characterization of dry-stacked refractory masonry under biaxial loading was presented in Chapter 5. The masonry walls were characterized at ambient and high temperatures under diverse loading conditions. The testing temperature was similar to the service temperature of refractory linings. The following conclusions could have been drawn from this experimental research:

- Test series S06.AT.LBJ aimed to assess the mechanical behaviour of dry-stacked masonry loaded in the direction of the bed joints with restrained thermal elongation in the direction of the head joints. Three loading cycles were applied to the specimens. As observed in S02.AT.CIC the crushing of the initially non-plane surfaces of the bricks caused by the mechanical load was observed. Residual strains were observed after the first loading cycle. The crushing of the surfaces resulted in an increasing of the contact area of the bricks and consequently in an increasing in the wall stiffness.

- Test series S07.AT.LHJ had the same goal of test series S06.AT.LBJ, but the wall was loaded in the direction of the head joints with restrained thermal elongation in the direction of the bed joints. Three load cycles were considered. The residual strains and the increasing of the wall stiffness with the applied load was also observed. The strain level was lower when compared to the previous series, as the number of joints was lower and the head joints have a stiffer behaviour (less compressibility) than the bed joints.
- Test series S08.AT.LBI has evaluated the mechanical behaviour of the specimens under biaxial loading. When the strains are compared to the strains obtained in the previous series (S06.AT.LBJ and S07.AT.LHJ) it is possible to identify that the friction between the plungers and the specimens leads to reductions in the strain level.
- The goal of test series S09.HT.LBJ was to assess the creep behaviour of dry-stacked masonry loaded in the bed joints' direction. The temperature fields were measured along the test and the temperature evolution may be used for the calibration of numerical heat transfer analyses. The creep effects led to a significantly increasing in the strains, when the test results are compared to S01.AT.LBJ.
- Test series S10.HT.CBI has tested the creep behaviour of specimens loaded in biaxial directions. The creep effects led to a significant increasing of the strains, when the test results are compared to S03.AT.LBI. The analysis of the stress-strain curves allowed to observe that the creep strain during the holding stage is similar in both directions.
- Test series S11.HT.RBI was designed to evaluate the relaxation effects of dry-stacked masonry under biaxial compression. The evolution of stresses along the test time allowed to identify the relaxation in the wallet. The experimental result indicated that the relaxation was similar in the direction of the bed joints and head joints.
- In spite of the small load level, all tested specimens presented some cracks in the bricks, as observed in the uniaxial experimental campaign. Most of the cracks were located at the cross joints, caused by bricks' height imperfection (Ngapeya *et al*, 2018). The specimens loaded in the head joints shown some spalling in these joints, as a result of stress concentrations

7.3 The numerical modelling of refractory linings

The development of numerical models to simulate the thermal and mechanical response of dry-stacked refractory masonry at ambient and high temperatures were presented in Chapter 6. The models included several non-linearities: material dependent properties, joint closure and opening, crush in compression, crack in tensile and creep. The Abaqus software was used and the micro-modelling technique was chosen due to its accuracy. The developed models were validated against the experimental results presented in Chapter 4 and 5. The following conclusions were drawn from the numerical research:

- The heat transfer analyses predicted the temperature distribution in the specimen with great accuracy. The thermal properties obtained experimentally (Vitiello, 2021) were validated. The accurate temperature distribution in the model is important to guarantee the quality of the results provided by the mechanical analysis. The numerical models were able to predict the heat flux in the system, which is an important parameter to optimize the thermal efficiency of the vessels.
- The mechanical analyses have been validated in terms of displacements (in-plane and out-of-plane), forces and failure modes. It was observed that the developed models were able to predict the behaviour of dry-stacked masonry with great accuracy. The models were validated both at ambient and high temperatures, under uniaxial and biaxial loading conditions.
- The thermomechanical characterization of the alumina spinel brick performed within the scope of the ATHOR Project led to a reliable data base that may be used for the design and optimization of refractory linings composed by this material. The following properties were obtained: tensile strength (Kaczmarek *et al*, 2019), Young's modulus (Kaczmarek *et al*, 2019), thermal elongation (Kaczmarek *et al*, 2019), specific heat and thermal conductivity (Vitiello, 2021) and creep parameters (Samadi *et al*, 2020).
- The CDP model was able to represent the mechanical behaviour of dry-stacked refractory masonries from ambient temperature up to 1000 ºC (when the creep effects are not significant). However, in service conditions the temperature may reach up to 1650 ºC, therefore, a constitutive model that takes creep into account shall be used. Coupling of the CDP model with some creep law, such as Norton-Bailey, would be interesting to represent the mechanical behaviour of refractory masonry under a large range of temperatures, from ambient up to the service temperatures.
- The micro-modelling approach resulted in a good representation of the behaviour of dry-stacked refractory masonry. This technique has a great accuracy however it requires more computational resources. The homogenization technique is an approach that overcomes the

high computation costs of the micro-modelling, being more suitable to represent the refractory linings at industrial scale.

- The formulation recommended by Thanoon *et al* (2013) to represent the compressive stress in the lining in terms of joint closure was suitable to represent dry-stacked refractory masonry.
- The Norton-Bailey creep law led to excellent results in the numerical models. Only the compressive creep properties were used in the present study. The models were validated against experimental results and a good agreement was observed. This creep law is able to represent the behaviour of the refractory lining under uniaxial creep, biaxial creep and biaxial relaxation. Nevertheless, the development of asymmetric creep models is recommended (Teixeira *et al*, 2020).

7.4 Recommendations for the design of industrial vessels

Based on the conclusion drawn from this doctoral thesis a few recommendations for the design of industrial vessels and their refractory linings are addressed:

- The materials used in the industrial vessels shall be fully characterized under a large temperature range. The specific heat, thermal conductivity, density, Young's modulus, compressive strength, fracture energy and creep parameters shall be experimentally identified.
- The joint behaviour should be characterized from small wallets, not from two stacked bricks. It was observed that the classical joint closure test performed in two stacked bricks may result in an under estimation of the average joint thickness.
- The fabrication process shall aim to minimize the dimensions' tolerances of the bricks. It was observed that high fabrication tolerances may result in thick joints, which results in non-homogeneous support and loading conditions of the bricks. This condition reduces the load-bearing capacity of the bricks and results in several cracks mostly located at the cross-joints. Additionally, the thick joints are prone to the penetration of the slag and steel.
- The numerical models shall be validated against experiments performed in conditions similar to the service ones (the temperature range and the load level).
- The numerical models shall represent the joint behaviour accordingly. Homogenization techniques or the micro-modelling shall be preferably used. The use of isotropic models would result in unreal stress levels in the refractory lining (several times higher than its compressive strength) and high von Misses stresses in the steel shell.

- The numerical models shall take into account the viscosity effects caused by creep in the working lining and slag line. The relaxation of the hot face of these layers leads to a significant stress reduction in the lining and in the steel shell, resulting in more realistic stresses.
- During the assemblage of the linings, the bricks shall be sorted and bricks with approximately the same height shall be used in the same course. This process results in the reduction of the number of thick joints. The bricks that present significant dimensions errors shall be discarded.

7.5 Future work

This doctoral thesis is a step forward in the direction of the characterization of dry-stacked refractory masonry, however there is still much more work to be done and new aspects to be discovered. Some relevant aspects that may be considered in future experimental work, along with the gaps in this field of knowledge that need further investigation are the following:

- Characterization of the alumina spinel brick under biaxial and triaxial loading aiming to generate experimental results for the accounting of the effects of multiaxial loading in the materials' behaviour. As reported in the literature, concrete-like materials exhibit an increase in capacity under biaxial and triaxial loading.
- Characterization of the tangent Young's modulus of the material by compressive tests at different temperatures to be used in simulations instead of the ultrasonic values. As reported in this thesis, the use of the Young's modulus obtained by the ultrasonic test may result in the overestimation of the compressive stresses in refractory linings.
- Experimental characterization of the joint closure's behaviour at high temperatures to evaluate the effects of temperature in the joints behaviour.
- Characterization of the joints tangential behaviour by triplet shear tests to evaluate the influence of the normal stresses in the friction angle of the joint.
- Characterization of the creep parameters for the alumina spinel brick at 1000 ºC, 1100 ºC and 1200 ºC will increase the database of the material and improve the quality of the developed numerical models.
- Characterization of refractory linings under biaxial loading with restrained thermal elongation will generate experimental results that may be used for the further validation of the developed models. The characterization of refractory linings under biaxial loading with different expansion joints can also be done.

Moreover, future numerical studies are also required to help us to better understand the behaviour of refractory masonry, some recommendations are presented:

- Development of a constitutive model that couples CDP and creep would be really useful to the design of refractory linings.
- Development of asymmetric creep models (tensile and compression) taking into account the three creep stages. As reported in the literature, the tensile and compression creep behaviour is quite different, therefore, asymmetric creep models are necessary to simulate the linings with greater accuracy.
- Development of models to account the joint degradation effects under cyclic loads.
- Development of subroutines to account the effects of the hysteresis in the material's Young's modulus caused by heating and cooling cycles: lead to a more realistic numerical predictions of the simulations of the different service cycles of the vessel.
- Instrumentation of an industrial ladle aiming to analyse the thermal and mechanical behaviour of the vessel in service conditions.

FREFERENCES

1. Abaqus User Manual (2014), Dassault Systems Simulia Corporation, USA.
2. Abdou, L. Saada, R.A., Meftah, F., Mebarki, A. (2006) . "*Experimental investigations of the joint-mortar behaviour*". Mechanics Research Communications, 33:370-384.
3. Agaajani S (2015). "*Development and Investigation of a New Dry-Stacked Wall System*". PhD thesis. University of Luxembourg.
4. Al Nahhas, F, Ami Saada R, Bonnet G, Delmotte P. (2007). "*Resistance to fire of walls constituted by hollow blocks: Experiments and thermal modelling*". Applied Thermal Engineering, 27(1):258-267.
5. Ali M, Sayet T, Gasser A, Blond E. (2019). "*Thermomechanical modelling of refractory mortarless masonry wall subjected to biaxial compression*". Unified Int Tech Conf Refractories, Yokohama – Japan,
6. Ali M, Sayet T, Gasser A, Blond E. (2020). *"Transient thermo-mechanical analysis of steel ladle refractory linings using mechanical homogenization approach"*. Ceramics, 2:171–188.
7. Ali M, Sayet T, Gasser A, Blond E. (2021). *"Computational Homogenization of Elastic-Viscoplastic Refractor Masonry with Dry Joints*". International Journal of Mechanical Sciences, 196:106275.
8. Allaoui S, Rekik A, Gasser A, Blond E, Andreev K. (2018). "*Digital image correlation measurements of mortarless joint closure in refractory masonries"*. Constr Build Mater, 162:334–344.
9. Andreev K, Zinngreve, E. (2009). "*Compressive Behaviour of ACS torpedo bricks*". 11th Unified International Technical Conference on Refractories, UNITECR, Oct. 13-16.
10. Andreev K, Sinnema S, Rekik A, Allaoui S, Blond E, Gasser A. (2012). *"Compressive behaviour of dry joints in refractory ceramic masonry*". Constr Build Mater, 34: 402–8.
11. Andreini, M., Caciolai, M., La Mendola, S., Mazziotti, L., Sassu, M. (2015). *"Mechanical behavior of masonry materials at high temperatures*". Fire and Materials, 39:41–57.
12. Bakunov VS, Belyakov AV. (2000). *"Role of structural characteristics in high-temperature creep of ceramics*". Refract Ind Ceram, 41:349–55.

13. Belrhiti Y, Dupre JC, Pop O, Germaneau A, Doumalin P, Huger M, et al. (2017). *"Combination of Brazilian test and digital image correlation for mechanical characterization of refractory materials*". J Eur Ceram Soc,37:2285–93.
14. Besnard, G. Hild, F., Roux, S. (2006). "*"Finite-Element" Displacement Fields Analysis from Digital Images: Application to Portevin–Le Châtelier Bands*". Experimental Mechanics 46(6).
15. Brulin J, Blond E, de Bilbao E, Rekik A, Landreau M, Gasser A, Colleville Y. (2020). "*Methodology for brick/mortar interface strength characterization at high temperature*". Constr Build Mater, 256: 120565.
16. Buhr, A. and Lachmund, H. (2016). *"Dream Ladle Lining*", VDEh Proceedings, 9th International Symposium Refractory Technology: Steel Ladle Lining.
17. Byrne S. (1979). *"Fire resistance of load-bearing masonry walls"*. Fire Technology 15(3):180-188.
18. Callister D, Callister Jr D. (2001). *"Fundamentals of materials science and engineering*". John Wiley & Sons, Inc.
19. Ceylantekin R, Aksel C. (2012). *"The comparison of mechanical behavior of MgO-MgAl2O4 with MgO-ZrO2 and MgO-MgAl2O4-ZrSiO4 composite refractories*". Ceram Int, 38(2):1409–16.
20. Czechowski J, Gerle A, Podworny J, Dahlem E. (2015) *"Investigation of the testing parameters influencing the cold crushing strength testing results of refractory materials*". Refract Worldforum, 7:105–12.
21. Dahlem E, Clasen S, Dannert C. (2015) "*Investigation of the factors influencing the bulk density and open porosity testing results for refractory materials"*. Refract. Worldforum, 7:95–104.
22. Dhanasekar M, Chandrasekaran V, Grubits SJ, (1994) "*A numerical model for thermal bowing of masonry walls*". 10th IB2MaC, pp. 1093-1102.
23. Dupre JC, Doumalin P, Belrhiti Y, Khlifi I, Pop O, Huger M. (2018) "*Detection of cracks in refractory materials by an enhanced digital image correlation technique*". J Mater Sci, 53:977–93.

24. European Committee for Standardization (CEN) (2002) EN 1052-3 “*Methods of test for masonry - Part 3: Determination of initial shear strength”*, Brussels, Belgium.
25. European Committee for Standardisation. EN 1996-1.1 (2005), “*Eurocode 6 – Design of masonry structures, Part 1.1: General rules for reinforced and unreinforced masonry structures”*, Brussels, Belgium.
26. European Committee for Standardisation. EN 1996-1.2 (2005), “*Eurocode 6 – Design of masonry structures, Part 1.2: General rules Structural Fire Design”*, Brussels, Belgium.
27. European Committee for Standardisation. EN 993-1 (2019) “*Methods of test for dense shaped refractory products. Determination of bulk density, apparent porosity and true porosity”* Brussels, Belgium.
28. European Committee for Standardisation. EN 993-5 (2018) “*Methods of test for dense shaped refractory products - Part 5: Determination of cold crushing strength”*. Brussels, Belgium.
29. European Committee for Standardisation. EN 993-9 (1997) *“Methods of testing dense shaped refractory products - Part 9: Determination of creep in compression*”. Brussels, Belgium
30. European Committee for Standardisation. EN ISO 12677:2011 (2014) “*Chemical analysis of refractory products by X-ray fluorescence (XRF). Fused cast-bead method*”. Brussels, Belgium.
31. Gasser, A., Terny-Rebeyrotte, K., Boisse, P. (2004) *“Modelling of joint effects on refractory lining behaviour*”. J Mater: Des Appl, 218(1):19–28.
32. Gasser A, Genty F, Daniel JL, Chen L. “*Influence of different masonry designs of bottom linings”*. In: 13th Unified International Technical Conference on Refractories (UNITECR); 2013. p. 775–80.
33. Glaser, B.; Görnerup, M.; Sichen, D. “*Fluid Flow and Heat Transfer in the Ladle during Teeming*”. Steel Res.Int. 2011, 82, 827–835.
34. Gruber D, Harmuth h, “*Simulation of molding of refractory bricks*”, Adv. Sci. Technol. 70 (2010) 167–172.
35. Haach V. G. (2009), “*Development of a design method for reinforced masonry subjected to in-plane loading based on experimental and numerical analysis”*. PhD Thesis. University of Minho, Portugal.

36. Heindl R.A., Mong L.E., *“Young's modulus of elasticity, strength, and extensibility of refractories in tension*”, J. Res. Natl. Bur. Stand. 17 (1936) 463–482.
37. Heller, K. Bullock. A. (2001) *“Refractories Manufacturing NESHAP: Industry Profile, Methodology, and Economic Impact Analysis”.* Research Triangle Institute. 52 p.
38. Hou A., Jin S., Harmuth H., Gruber D. (2018) *“A method for steel ladle lining optimization applying thermomechanical modeling and taguchi approaches*”, J. Miner. Met. Mater. Soc. 70 (11) (2018) 2449–2456
39. Hubalkova J. , Stoyan D., (2003) *“On a qualitative relationship between degree of inhomogeneity and cold crushing strength of refractory castables*”, Cement Concr. Res.33 (2003) 747–753
40. Fruehan, R.J., Wakelin, D.H. (1998) *“Making, Shaping and Treating of Steel: Ironmaking Volume*”. United States Steel Corp;
41. International Organization for Standardization. ISO 12677:2011 *“Chemical analysis of refractory products by X-ray fluorescence (XRF) — Fused cast-bead method*”. Geneva, Switzerland.
42. International Organization for Standardization. ISO 834-1:1999 *“Fire resistance tests – elements of building construction, Part 1: general requirements*”. Geneva, Switzerland.
43. European Committee for Standardisation. EN 1402-1:2003 *“Unshaped refractory products - Part 1: Introduction and classification”* Brussels, Belgium.
44. Jaafar MS, Alwathaf AH, Thanoon WAM, Noorzaei J, Abdulkadir MR. (2006) *“Characteristic of interlocking mortarless block masonry under compression*”. In: Proceedings of ICE, construction materials, UK, vol. 159 (3), p. 111–7
45. Jin S., Harmuth H., Gruber D., (2014) *“Compressive creep testing of refractories at elevated loads—device, material law and evaluation techniques*”, J. Eur. Ceram. Soc. 34, 4037–4042,
46. Jin S., Gruber D., Harmuth H., Rössler R. (2016) *“Thermomechanical failure modeling and investigation into lining optimization for a Ruhrstahl Heraeus snorkel*”, Eng. Fail. Anal. 62 254–262

47. Kaczmarek R, Dupre JC, Doumalin P, Pop IO, Teixeira LB, Gillibert J, et al. (2019). *“Thermomechanical behaviour of an alumina spinel refractory for steel ladle applications”*. In: Unified International Technical Conference of Refractories, Yokohama - Japan; p. 422–5.
48. Khlifi I. *“Optimisation of optical methods for strain field measurements dedicated to the characterisation of the fracture behaviour of refractories: application to magnesia based materials*”. Material chemistry. PhD Thesis, University of Limoges; 2019. p. 182
49. Kumar P., Kodur V.K.R. (2017) *“Modeling the behavior of load bearing concrete walls under fire exposure*”. Construction and Building Materials, 154, pp. 993–1003
50. O. Knacke, O. Kubaschewski, and K. Hesselmann, (1977) *“Thermal Chemical Properties of Inorganic Substances*”, 2nd Ed. Springer Verlag.
51. Laim, L. (2013) *“Experimental and numerical analysis on the structural behaviour of cold-formed steel beams subjected to fire*” Fire Safety Engineering. PhD Thesis, University of Coimbra; p. 377
52. Lawrence S., Gnanakrishnan N. (1987) *“The Fire Resistance of Masonry Walls - An Overview”* First National Structural Engineering Conference, Melbourne, Australia, pp 431-437
53. Lee J. and Fenves G. L. (1998) *“Plastic-damage model for cyclic loading of concrete structures*”. J. Eng. Mech. 124 (8), pp 892-900.
54. Lopes, R., Rodrigues, J. P. C., Pereira, J. M., Lourenço, P. B. (2017) “*Experimental research on structural concrete masonry walls subjected to fire*”, IFireSS 2017 – 2nd International Fire Safety Symposium, Naples, Italy
55. Lopes R. (2017). *“Fire behaviour of structural masonry walls of vertical hollowed concrete blocks”.* MSc Thesis on Urban Fire Safety. University of Coimbra, Portugal.
56. Lourenço PB, Mendes N, Ramos LF, Oliveira DV. (2011) *“Analysis of masonry structures without box behavior*”. Int J Arch Heritage;5:369–82.
57. Lubliner J., Oliver J., Oller S. and Onate E. (1989) “*A plastic-damage model for concrete*”. Int. J. Solids Struct.,25(3), pp 299–329.
58. Madias, J. A (2018) *“Review on Recycling of Refractories for the Iron and Steel Industry”.* AISTech Proceedings. p 3271 - 3279

59. Melo C.C. , Moraes A.L.I., Rocco F.O. , Montilha F.S. , Canto R.B. , (2018) *“A validation procedure for numerical models of ceramic powder pressing*”, J. Eur. Ceram. Soc. 38 2928–2936
60. Mukhopadhyay S., Dana K., Moitra S., Basumallick S, Mukhopadhyay TK. (2016) *“Thermal and thermomechanical characteristics of monolithic refractory composite matrix containing surface-modified graphite*”. Ceram Int;42(5):6015–24.
61. Musante L, Martorello LF, Galliano PG, Cavalieri AL, Martinez AG. (2012) *“Mechanical behaviour of MgO-C refractory bricks evaluated by stress-strain curves”*. Ceram Int 38(5):4035–47
62. Nadjai A., O'Garra M., Ali F. A., Laverty D. (2003), *“Finite element modelling of compartment masonry walls in fire”*. Computer and Structures 81, pp 1923–1930
63. Nadjai A., O'Garra M., Ali F. A., Laverty D. (2003), “*A numerical model for the behaviour of masonry under elevated temperatures”* Fire and Materials, 27-4, pp. 163-182
64. Nath M, Tripathi HS. *“Thermo-mechanical behavior of Al2O3-Cr2O3refractories: effect of TiO2”*. Ceram Int 2015;41(2):3109–15.
65. Nguyen T. D., Meftah F. (2012) *“Behavior of clay hollow-brick masonry walls during fire. Part 1: Experimental analysis”*. Fire Safety Journal, 52, pp 55-64
66. Nguyen T.D., Meftah F. (2014), *“Behavior of hollow clay brick masonry walls during fire. Part 2: 3D finite element modeling and spalling assessment”*. Fire Safety Journal, 66, pp. 35–45
67. Ngapeya G, Waldmann D, Scholzen F. (2018) *“Impact of the height imperfections of masonry blocks on the load bearing capacity of dry-stack masonry walls”*. Constr Build Mater 2018;165:898–913
68. Nguyen T, Blond E, Gasser A, Prietl T. (2009) *“Mechanical homogenisation of masonry wall without mortar”*. Eur J Mech – A/Solids ;28(3):535–544
69. O’Meagher A. J., Bennetts I. D. (1991) *“Modelling of Concrete Walls in Fire”*. Fire Safety Journal, 17, pp 315-335

70. Oliveira R, Rodrigues JP, Pereira JM. (2019) *“The characterization of joint behaviour in mortarless refractory masonry”.* In: Proceedings of the Unified International Technical Conference of Refractories, Yokohama, Japan; 2019. p. 612–4.
71. Oliveira R, Rodrigues JPC, Pereira J, Lourenço PB, Lopes R. (2021) *“Experimental and numerical analysis on the structural fire behaviour of three-cell hollowed concrete masonry walls”.* Eng Struct 2021;228:111439.
72. Pereira J. M., Campos J., Lourenço P.B. (2015) *“Masonry infill walls under blast loading using confined underwater blast wave generators (WBWG)”.* Engineering Structures, 92, pp. 69–83
73. Poirier J, Rigaud M. (2017) *“Corrosion of Refractories: The Fundamentals*”. F.I.R.E Compendium Series; 450 pages.
74. Prietl T, Zach O, Studnicka H. *“The evaluation of refractory linings thermomechanical properties”.* Erzmetall – World Metall 2006;59:127–32.
75. Prietl T. *“Ermittlung materialspezifischer Kennwerte von feuerfesten Werkstoffen und Zustellungen unter uni- und biaxialen Lastbedingungen für die Nichteisenmetallindustrie*”. PhD Thesis. University of Leoben; 2006. p. 192.
76. Ramanenka D, Stjernberg J, Eriksson K, Jonsen P. (2014) *“Modelling of refractory brick furniture in rotary-kiln using finite element approach*”. In: 11th World Congress on Computational Mechanics (WCCM XI), Barcelona – Spain, pp. 1199-1210
77. Ramanenkaa D, Antti M-L, Gustafsson G, Jonsen P. (2017) *“Characterization of high-alumina refractory bricks and modelling of hot rotary kiln behaviour”.* Eng Fail Anal 2017;79:852–64.
78. Rekik, A., Gasser, A. (2016) “*Numerical homogenization model for effective creep properties of microcracked masonry*”. International Journal of Solids and Structures 102-103 297-320
79. Rekik. A., Allaoui, S. Gasser, A., Blond, E. Andreev, K., Sinnema, S. (2015) *“Experiments and nonlinear homogenization sustaining mean-field theories for refractory mortarless masonry: The classical secant procedure and its improved variants”.* European Journal of Mechanics A/Solids 49 67-81
80. Rekik, A.; Nguyen, T.T.N.; Gasser, A. (2016) *“Multi-level modeling of viscoelastic microcracked masonry”.* Int. J. Solids Struct. 2016, 81, 63–83.

81. Rigaud, M. (2004) *“Trends in the Steel Industry and Developments of New Refractory Materials*”, Tehran International Conference on Refractories, 2004, p. 164 – 174
82. RILEM TC 200-HTC, (2007). *“Recommendation of RILEM TC 200-HTC: mechanical concrete properties at high temperatures — modeling and applications. Part 1: introduction — general presentation”*, Materials and Structures, Vol. 40 pp. 841–853.
83. RILEM TC 200-HTC, (2007). *“Recommendation of RILEM TC 200-HTC: mechanical concrete properties at high temperatures—modeling and applications. Part 2: stress–strain relation”,* Materials and Structures, Vol. 40, pp. 855–864.
84. Sakshi (2021) *“Steel plant in India”* https://english.sakshi.com/news/andhrapradesh/fire-accident-vizag-steel-plant-100-tonnes-hot-metal-fell-down-127886
85. Samadi, S. Jin, S. Gruber, D., Harmuth, H.. *“Statistical study of compressive creep parameters of an alumina spinel refractory”*. Ceram Int 2020;46(10):14662–8
86. Samadi, S. Jin, S. Gruber, D., Harmuth, H.. *“A comparison of two damage models for inverse identification of Mode I fracture parameters: Case study of a refractory ceramic*”. International Journal of Mechanical Science 197 (2021) 106345
87. Santos, M.F.; Moreira, M.H.; Campos, M.G.G.; Pelissari, P.I.B.G.B.; Angélico, R.A.; Sako, E.Y.; Sinnema, S.; Pandolfelli, V.C. (2018) *“Enhanced numerical tool to evaluate steel ladle thermal losses*”. Ceram. Int. 2018, 44, 12831–12840.
88. Seven Refractories (2021, October 17). “*Steel ladle*”. https://www.sevenrefractories.com/
89. Shields, TJ. O’Connor, DJ. Silcock, GWH. Donegan, HA. (1988) *“Thermal bowing of a model brickwork panel”*, Proceedings of 8th International Brick/Block Masonry Conference, Dublin, Vol. 2, pp. 846–856.
90. Shubin V. (2001) *“Mechanical effects on the lining of rotary cement kilns*”. Refract Ind Ceram 42(5–6):245–50.
91. Sinnema S, Tesselaar W, Siebring R, (2017) *“Bridging the Gap between Refractory Supplier and the Refractory User in the Steel Plant – real Value-in-Use”,* Refractories World Forum vol. 9(3):71-75
92. Stuppfler A, Dahlem E. (2015) *“Investigation of the parameters influencing the refractoriness under load (RuL) testing results for refractory materials*”. Refract. Worldforum 2015;7:87–93.

93. Sugita, K. (2008) *“Historical Overview of Refractory Technology in the Steel Industry*”. Nippon Steel Technical Report, p. 8 – 17
94. Teixeira L, Gillibert J, Blond E, Sayet T. (2019) *“Creep characterization of refractory materials at high temperatures using the Integrated Digital Image Correlation*”. In: Unified International Technical Conference of Refractories, Yokohama - Japan; 2019. p. 899–902.
95. Teixeira L, Samadi S, Gillibert J, Jin S, Sayet T, Gruber D, et al. (2020) *“Experimental investigation of the tension and compression creep behavior of alumina-spinel refractories at high temperatures*”. Ceramics 2020;3(3):372–83.
96. Thanoon W, Alwathaf A, Noorzaei J, Jaafar M, Abdulkadir M. (2008) *“Finite element analysis of interlocking mortarless hollow block masonry prism*”. Comput Struct;86:520–8
97. Themines, D. Comportement des mac¸onneries. Sollac report, Dunkerque, France, 1994
98. The Spec (2021). “*Blast furnace failure”.* https://www.thespec.com/news/hamilton-region/2019/05/30/arcelormittal-dofasco-hands-over-details-about-blast-furnace-failure-to-ministry.html
99. Vitiello, D., Smith, D., Nait-Ali, B., Doyen-Tessier, N., Tonessen, T. Laim, L., Rebouillat, L. (2019) *“Thermal properties characterization of refractory materials used in the insulation layer of steel ladles*”. Unified Int Tech Conf Refractories, Yokohama - Japan 2019:205–8.
100. Vitiello, D. (2021) *“Thermo-physical properties of insulating refractory materials*”. Material chemistry. PhD Thesis, University of Limoges; 2021. p. 136
101. Xia, Z.; Zhang, Y.; Ellyin, F. (2003) *“A unified periodical boundary conditions for representative volume elements of composites and applications*I. Int. J. Solids Struct, 40, 1907–1921.
102. Yellishetty, M., Ranjith, P., Tharumarajah, A. (2010) *“Iron ore and steel production trends and material flows in the world:Is this really sustainable?”* Resources, Conservation and Recycling 54 (2010) 1084-1094
103. Yilmaz, S. (2003) *“Thermomechanical Modelling for Refractory Lining of a Steel Ladle Lifted by Crane*”. Steel Res. Int., 74, 485–490
104. Zahra T, Dhanasekar M. (2018). *“ Characterisation and strategies for mitigation of the contact surface unevenness in dry-stack masonry*”. Constr Build Mater;169: 612–28.

105. ZKG (2021, October 17). #*Rotary Cement Kiln*". https://www.zkg.de/)

APPENDIX A – INDUSTRIAL APPLICATION OF REFRACTORY CERAMICS

Refractory Type	General Characteristics	Application
Silica	High strength at high temperatures, residual expansion, low specific gravity, high expansion coefficient at low temperatures, low expansion coefficient at high temperatures	Glass tank crown, copper refining furnace, electric arc furnace roof
Fused silica	Low thermal expansion coefficient, high thermal shock resistance, low thermal conductivity, low specific gravity, low specific heat	Coke oven, hot stove, soaking pit, glass tank crown
Chamotte (fireclay)	Low thermal expansion coefficient, low thermal conductivity, low specific gravity, low specific heat, low strength at high temperatures, less slag penetration	Ladle, runner, sleeve, coke oven, annealing furnace, blast furnace hot stove, reheating furnace, soaking pit
Alumina	High refractoriness, high mechanical strength, high slag resistance, high specific gravity, relatively high thermal conductivity	Hot stove, stopper head, sleeve, soaking pit cover, reheating furnace, glass tank, high-temperature kiln
High alumina	High refractoriness, high mechanical strength, high slag resistance, high specific gravity, relatively high thermal conductivity	Slide gate, aluminium melting furnace, skid rail, ladle, incinerator, reheating furnace hearth, skid rail, ladle, incinerator
Roseki	Low thermal expansion coefficient, high thermal shock resistance, low thermal conductivity, low specific gravity, low specific heat	Ladle, runner, sleeve, coke oven, annealing furnace, blast furnace hot stove, reheating furnace, soaking pit
Zircon	High thermal shock resistance, high slag resistance, high specific gravity	Ladle, nozzle, stopper head, sleeve
Zirconia	High melting point, low wettability against molten metal, low thermal conductivity, high corrosion resistance, high specific gravity	Nozzle for continuous casting, glass tank, high-temperature furnace, crucible
Alumina zirconia silica	High slag resistance, high corrosion resistance against molten glass	Glass tank, incinerator, ladle, nozzle for continuous casting
Lime	High slag resistance, low hydration resistance	Special refining surface
Magnesia	High refractoriness, relatively low strength at high temperature, high basic slag resistance, low thermal shock resistance, low durability at high humidity	Hot-metal mixer, secondary refining vessel, rotary kiln, checker chamber of glass tank, electric arc furnace

Refractory Type	General Characteristics	Application
Magnesia-chrome	High refractoriness, high refractoriness under load, high basic slag resistance, relatively good thermal shock resistance (low MgO bricks), high strength at high temperature (direct bonded and fusion cast)	Hot-metal mixer, electric arc furnace, secondary refining vessel, nonferrous refining furnace, rotary cement kiln, lime and dolomite kiln, copper furnace, ladle, checker chamber for glass tank, slag line of electric arc furnace, degasser for copper, nonferrous smelter
Chrome	High refractoriness, low strength at high temperature, low thermal resistance	Buffer brick between acid and basic brick
Dolomite	High refractoriness, high refractoriness under load, high basic slag resistance, low durability in high humidity, high thermal expansion coefficient	Basic oxygen furnace, electric arc furnace, secondary refining vessel, rotary cement kiln
Spinel	High thermal shock resistance, high strength at high temperatures, high slag resistance	Rotary cement kiln, ladle
Carbon	High refractoriness, high slag resistance, low oxidation resistance	Blast furnace hearth, electric arc furnace
Silicon carbide	High refractoriness, high strength at high temperature, high thermal conductivity, high thermal shock resistance, reduced oxidation resistance at high temperature, high slag resistance	Incinerator
Silicon carbide graphite	High refractoriness, high strength at high temperature, high thermal conductivity, high thermal shock resistance	Kiln furniture, blast furnace
Silicon carbide Containing	High corrosion resistance against low iron oxide, high strength at high temperatures, high thermal shock resistance	Ladle, blast furnace, electric arc, torpedo ladle, iron ladle
Magnesia-carbon	High slag resistance, high thermal shock resistance	Basic oxygen furnace, electric arc furnace, ladle
Alumina-carbon	High refractoriness, high thermal shock resistance, high corrosion resistance	Submerged entry nozzle and slide gate

APPENDIX B – SUMMARY OF STANDARDS

Europeans Standards

Standard	Title
EN 993-1:1995	Methods of test for dense shaped refractory products - Determination of bulk density, apparent porosity and true porosity
EN 993-2:1995	Methods of test for dense shaped refractory products - Determination of true density
EN 993-3:1997	Methods of test for dense shaped refractory products - Test methods for carbon-containing refractories
EN 993-4:1995	Methods of test for dense shaped refractory products - Determination of permeability to gases
EN 993-5: 2018	Methods of test for dense shaped refractory products - Determination of cold crushing strength
EN 993-6:1995	Methods of test for dense shaped refractory products - Determination of modulus of rupture at ambient temperature
EN 993-7:2000	Methods of test for dense shaped refractory products - Determination of modulus of rupture at elevated temperatures
EN 993-8:1997	Methods of test for dense shaped refractory products - Determination of refractoriness-under-load
EN 993-9:1997	Methods of test for dense shaped refractory products - Determination of creep in compression
EN 993-10:1998	Methods of test for dense shaped refractory products - Determination of permanent change in dimensions on heating
EN 993-11:2007	Methods of test for dense shaped refractory products - Determination of resistance to thermal shock
EN 993-12:1997	Methods of test for dense shaped refractory products - Determination of pyrometric cone equivalent (refractoriness)
EN 993-13:1995	Methods of test for dense shaped refractory products - Specification for pyrometric reference cones for laboratory use
EN 993-14:1998	Methods of test for dense shaped refractory products - Determination of thermal conductivity by the hot-wire (cross-array) method
EN 993-15:2005	Methods of test for dense shaped refractory products - Determination of thermal conductivity by the hot wire (parallel) method
EN 993-16:1995	Methods of test for dense shaped refractory products - Determination of resistance to sulfuric acid
EN 993-17:1999	Methods of test for dense shaped refractory products - Determination of bulk density of granular materials by the mercury method with vacuum
EN 993-18:2002	Methods of test for dense shaped refractory products - Determination of bulk density of granular materials by the water method with vacuum
DIN 51068:2008-11	Testing of ceramic raw and basic materials - Determination of resistance to thermal shock - Water quenching method for refractory bricks
EN 1094-1:2008	Insulating refractory products - Part 1: Terminology, classification and methods of test for high temperature insulation wool products

Standard	Title
EN 1094-2:1998	Insulating refractory products - Part 2: Classification of shaped products (ISO 2245:1990 modified)
EN 1094-4:1995	Insulating refractory products - Part 4: Determination of bulk density and true porosity
EN 1094-6:1998	Insulating refractory products - Part 6: Determination of permanent change in dimensions of shaped products on heating (ISO 2477:1987, modified)
EN 1094-8:2005	Insulating refractory products - Part 8: Terminology for alkaline earth silicate (AES) wools
EN 1094-9:2005	Insulating refractory products - Part 9: Methods of test for alkaline earth silicate (AES) wool products
EN 1402-1:2003	Unshaped refractory products - Part 1: Introduction and classification
EN 1402-2:2003	Unshaped refractory products - Part 2: Sampling for testing
EN 1402-3:2003	Unshaped refractory products - Part 3: Characterization as received
EN 1402-4:2003	Unshaped refractory products - Part 4: Determination of consistency of castables
EN 1402-5:2003	Unshaped refractory products - Part 5: Preparation and treatment of test pieces
EN 1402-6:2003	Unshaped refractory products - Part 6: Measurement of physical properties
EN 1402-7:2003	Unshaped refractory products - Part 7: Tests on pre-formed shapes /.
EN 1402-8:2003	Unshaped refractory products - Part 8: Determination of complementary properties
EN 12475-4:1998	Classification of dense shaped refractory products - Part 4: Special products
EN 12698:2005	Chemical analysis of nitride bonded silicon carbide refractories
EN 12698-1:2007	Chemical analysis of nitride bonded silicon carbide refractories - Part 1: Chemical methods
EN 12698-2:2007	Chemical analysis of nitride bonded silicon carbide refractories - Part 2: XRD methods
EN 14945:2005	Refractory products and materials - Spectrometric determination of chromium (VI) in chrome bearing refractories, before and after use

International Organization for Standardization

Standards	Title
ISO 836:2001	Terminology for refractories
ISO 10635:1999	Refractory products - Methods of test for ceramic fibre products
ISO 16835:2014	Refractory products - Determination of thermal expansion
ISO 12676:2000	Refractory products - Determination of resistance to carbon monoxide
ISO 1893:2007	Refractory products - Determination of refractoriness under load - Differential method with rising temperature
ISO/WD 23071	Refractory products - Determination of reduced species in carbon containing refractories by XRD
ISO 528:1983	Refractory products - Determination of pyrometric cone equivalent (refractoriness)
ISO 5013:1985	Refractory products - Determination of modulus of rupture at elevated temperatures
ISO 3187:1989	Refractory products - Determination of creep in compression
ISO 10080:1990	Refractory products - Classification of dense, shaped acid-resisting products
ISO 5018:1983	Refractory materials - Determination of true density
ISO 8894-1:2010	Refractory materials - Determination of thermal conductivity - Part 1: Hot-wire methods (cross-array and resistance thermometer)
ISO 8894-2:2007	Refractory materials - Determination of thermal conductivity - Part 2: Hot-wire method (parallel)
ISO 8840:1987	Refractory materials - Determination of bulk density of granular materials (grain density)
ISO 16349:2015	Refractory materials - Determination of abrasion resistance at elevated temperature
ISO/AWI 22605	Refractories - Determination of Young’s modulus (MOE)at elevated temperatures by impulse excitation of vibration
ISO/CD 21736	Refractories - Determination of thermal shock resistance
ISO 5017:2013	Dense shaped refractory products - Determination of bulk density, apparent porosity and true porosity

ASTM International Standards

Standard	Title
ASTM C1161 - 18	Standard Test Method for Flexural Strength of Advanced Ceramics at Ambient Temperature
ASTM C1211 - 18	Standard Test Method for Flexural Strength of Advanced Ceramics at Elevated Temperatures
ASTM C1368 - 18	Standard Test Method for Determination of Slow Crack Growth Parameters of Advanced Ceramics by Constant Stress Rate Strength Testing at Ambient Temperature
ASTM C1465 – 08 (2013)	Standard Test Method for Determination of Slow Crack Growth Parameters of Advanced Ceramics by Constant Stress-Rate Flexural Testing at Elevated Temperatures
ASTM C1576 – 05 (2017)	Standard Test Method for Determination of Slow Crack Growth Parameters of Advanced Ceramics by Constant Stress Flexural Testing (Stress Rupture) at Ambient Temperature
ASTM C1684 - 18	Standard Test Method for Flexural Strength of Advanced Ceramics at Ambient Temperature—Cylindrical Rod Strength
ASTM C1834 - 16	Standard Test Method for Determination of Slow Crack Growth Parameters of Advanced Ceramics by Constant Stress Flexural Testing (Stress Rupture) at Elevated Temperatures
ASTM C1424 – 10 (2015)	Standard Test Method for Monotonic Compressive Strength of Advanced Ceramics at Ambient Temperature
ASTM C1273 - 15	Standard Test Method for Tensile Strength of Monolithic Advanced Ceramics at Ambient Temperatures
ASTM C1291 - 18	Standard Test Method for Elevated Temperature Tensile Creep Strain, Creep Strain Rate, and Creep Time to Failure for Monolithic Advanced Ceramics
ASTM C1366 – 04 (2013)	Standard Test Method for Tensile Strength of Monolithic Advanced Ceramics at Elevated Temperatures
ASTM C1361 – 10 (2015)	Standard Practice for Constant-Amplitude, Axial, Tension-Tension Cyclic Fatigue of Advanced Ceramics at Ambient Temperatures
ASTM C1499 - 15	Standard Test Method for Monotonic Equibiaxial Flexural Strength of Advanced Ceramics at Ambient Temperature
ASTM C1323 - 16	Standard Test Method for Ultimate Strength of Advanced Ceramics with Diametrally Compressed C-Ring Specimens at Ambient Temperature
ASTM C1198 – 09 (2013)	Standard Test Method for Dynamic Young's Modulus, Shear Modulus, and Poisson's Ratio for Advanced Ceramics by Sonic Resonance
ASTM C1259 - 15	Standard Test Method for Dynamic Young’s Modulus, Shear Modulus, and Poisson’s Ratio for Advanced Ceramics by Impulse Excitation of Vibration
ASTM C1495 - 16	Standard Test Method for Effect of Surface Grinding on Flexure Strength of Advanced Ceramics
ASTM C1470 – 06 (2013)	Standard Guide for Testing the Thermal Properties of Advanced Ceramics
ASTM C1525 – 04 (2013)	Standard Test Method for Determination of Thermal Shock Resistance for Advanced Ceramics by Water Quenching
ASTM C1421 - 18	Standard Test Methods for Determination of Fracture Toughness of Advanced Ceramics at Ambient Temperature